GREEN SYNTHESIS AND CHARACTERIZATION OF COPPER OXIDE AND ZINC OXIDE NANOPARTICLES DERIVED FROM AQUEOUS MANGOSTEEN (GARCINIA MANGOSTANA) LEAF EXTRCAT FOR PALM OIL MILL EFFLUENT (POME) TREATMENT

By

CHAN YU BIN

A dissertation submitted to the Department of Chemical Science,
Faculty of Science,
Universiti Tunku Abdul Rahman,
in partial fulfillment of the requirements for the degree of
Doctor of Philosophy in Science
March 2025

© 2025 CHAN YU BIN. All rights reserved.

This thesis is submitted in partial fulfilment of the requirements for the degree of Doctor of Philosophy (Science) at Universiti Tunku Abdul Rahman (UTAR). This thesis represents the work of the author, except where due acknowledgment has been made in the text. No part of this thesis may be reproduced, stored, or transmitted in any form or by any means, whether electronic, mechanical, photocopying, recording, or otherwise, without the prior written permission of the author or UTAR, in accordance with UTAR's Intellectual Property Policy.

ABSTRACT

GREEN SYNTHESIS AND CHARACTERIZATION OF COPPER OXIDE AND ZINC OXIDE NANOPARTICLES DERIVED FROM AQUEOUS MANGOSTEEN (*GARCINIA MANGOSTANA*) LEAF EXTRACT FOR PALM OIL MILL EFFLUENT (POME) TREATMENT

Chan Yu Bin

Green synthesis of nanomaterials using plant extracts offers a sustainable and eco-friendly alternative to conventional methods. In this study, copper oxide (CuO), zinc oxide (ZnO), and zinc oxide-copper oxide (ZnO-CuO) nanomaterials were successfully synthesized using mangosteen (*Garcinia mangostana*) leaf extract (MLE). The synthesis process was optimized based on key parameters such as MLE concentration, calcination temperature, and the Zn-to-Cu ratio. The synthesized nanomaterials were characterized using a range of analytical tools to assess their physicochemical properties.

The optimized CuO, ZnO and ZnO-CuO nanomaterials were chosen in inhibiting selected bacteria using Broth macrodilution assay and treating palm oil mill effluent (POME) at different conditions under light-emitting diode (LED). In preliminary *in vitro* antibacterial study, MLE-mediated synthesized CuO nanoparticles (NPs) and ZnO NPs calcinated at 500^{o}C and 0.05 g/mL MLE-mediated synthesized 70ZnO-30CuO nanocomposites (NCs) calcinated at 500^{o}C were chosen due to their small crystalline size. The average particle sizes of the

synthesized nanomaterials were 14.31 nm ± 5.368, 29.61 nm ± 12.573 and 23.09 nm ± 10.656 and mostly spherical structure.

The ZnO NPs demonstrated the highest antibacterial efficacy with minimum inhibitory concentrations (MIC) of 15.63 µg/mL (*Staphylococcus aureus*, *Bacillus subtilis*), 62.50 µg/mL (*Escherichia coli*), and 125.00 µg/mL (*Klebsiella pneumoniae*). ZnO-CuO NCs ranked second, with MICs of 62.50 µg/mL, 62.50 µg/mL, 250.00 µg/mL, and 125.00 µg/mL, respectively. CuO NPs were the least effective, showing higher MICs of 250.00 µg/mL, 125.00 µg/mL, 125.00 µg/mL, and 500.00 µg/mL. For POME treatment, ZnO NPs calcinated at 400°C achieved the best performance with COD and AN removal efficiencies at 54.05% ± 0.03 and 38.72% ± 0.00, respectively, using 50 mg of NPs under 120 min of blue LED exposure. In contrast, 150 mg of CuO NPs and ZnO-CuO NCs were required for optimal photodegradation under blue LED for 150 min, achieving COD and AN removal efficiencies of 58.58% ± 0.02 and 38.86% ± 0.01 (CuO NPs) and 59.72% ± 0.02 and 27.80% ± 0.01 (ZnO-CuO NCs), respectively.

In conclusion, this study demonstrates the potential of MLE-mediated green synthesis of nanomaterials as a sustainable approach for producing effective photocatalyst and antibacterial agents. ZnO NPs, in particular, exhibit high promise for environmental and biomedical applications. This study introduced a sustainable and environmentally friendly approach to MLE-based nanomaterial synthesis. Additionally, it offered a viable alternative method of bacterial inhibition and a treatment for POME. Moreover, the use of treated POME shown good agricultural development. This study proposed breakthroughs in scientific knowledge of

nanomaterial synthesis, antibacterial and photocatalysis mechanisms. This work has a significant contribution to science and society as the results have far-reaching implications for sustainable development, public health and environmental protection – all of which are parallel to the sixth and twelfth sustainable development goals.

Keywords: Copper oxide; green synthesis; mangosteen leaf; nanoparticles; zinc oxide

Subject Area: QD146-197 Inorganic Chemistry

ACKNOWLEDGEMENT

First and foremost, I would like to express my deepest gratitude to my supervisor, Dr. Mohammod Aminuzzaman**,** for his valuable guidance, constant support, and encouragement throughout the course of my PhD journey. His expertise and insightful advice have been crucial to the success of this project.

I am also deeply thankful to Dr. Tey Lai Hock, Prof. Md. Akhtaruzzaman and Dr. Yip Foo Win**,** whose input and feedback have significantly enriched my research. Their expertise and willingness to assist me at every stage of my study were instrumental to the completion of this work.

In addition, I extend my sincere thanks to the faculty members of Universiti Tunku Abdul Rahman for their support and for providing the facilities necessary for my research. Special thanks go to the laboratory staff for their technical support and cooperation.

I would also like to express my heartfelt gratitude to my family and friends, whose unwavering support and encouragement have been my constant motivation. Their belief in me provided the strength I needed to complete this journey.

Finally, I acknowledge the financial support from UTARRF (IPSR/RMC/UTARRF/202-C2/M01), which made this research possible.

To everyone who contributed to this thesis, directly or indirectly, I am truly grateful.

TABLE OF CONTENTS

LIST OF TABLES

LIST OF FIGURES

Figures **Page**

Figures **Page**

Figures **Page**

Figures **Page**

Figures **Page**

LIST OF ABBREVIATIONS/NOTATIONS/GLOSSARY OF TERMS

$\bullet HO_2$	Hydroperoxyl radical
•OH	Hydroxyl radical
$\bullet O_2^-$	Superoxide radical
AOP	Auto oxidation process
Ag	Silver
Ag_2SO_4	Silver sulfate
AN	Ammoniacal nitrogen
Au	Gold
BOD	Biochemical oxygen demand
C	Carbon
CB	Conduction band
COD	Chemical oxygen demand
Cl^-	Chloride ion
$Cr_2O_7^{2-}$	Dichromate ion
Cr^{3+}	Trivalent chromium ion

Cu	Copper
Cu^{2+}	Copper (II) ions
CuO NPs	Copper oxide nanoparticles
$Cu(NO_3)_2 \cdot 3H_2O$	Copper nitrate trihydrate
DMSO	Dimethyl sulfoxide
DNA	Deoxyribonucleic acid
e_{CB}^-	Electrons in conduction band
E_{CB}	Bottom conduction band energy
E_g	Energy bandgap
E_{VB}	Top valance band energy
e^-/h^+	Electron-hole
EDX	Energy dispersive X-ray
FDA	Food and Drug Administration
FE-SEM	Field emission scanning electron microscopy
FT-IR	Fourier transform infrared
GRAS	Generally recognized as safe

H^+	Hydrogen ion
h_{VB}^+	Holes at valence band
H_2O_2	Hydrogen peroxide
$HgSO_4$	Mercuric sulphate
HR-COD	High range chemical oxygen demand
HR-TEM	High-resolution transmission electron microscopy
H_2SO_4	Sulphuric acid
IUPAC	International Union of Pure and Applied Chemistry
KHP, $KC_8H_5O_4$	Potassium hydrogen phthalate
$K_2Cr_2O_7$	Potassium dichromate
LED	Light-emitting diode
LR-COD	Low range chemical oxygen demand
MIC	Minimum inhibition concentration
MLE	Mangosteen leaf extract
MO	Metal oxide
NB	Nutrient broth

NCs	Nanocomposites
NHE	Normal hydrogen electrode
NiO	Nickel oxide
NPs	Nanoparticles
O	Oxygen
OH^-	Hydroxide ion
POME	Palm oil mill effluent
ROS	Reactive oxygen species
SE	Standard error
SHSTI	Shoot height stress tolerance index
SnO	Tin oxide
SPR	Surface plasmon resonance
TiO_2	Titanium doixode
UV-Vis	Ultraviolet-visible
VB	Valence band
XPS	X-ray photoelectron spectroscopy

XRD	X-ray powder diffraction
ZOI	Zone of inhibition
Zn	Zinc
Zn^{2+}	Zinc (II) ions
$Zn(NO_3)_2 \cdot 6H_2O$	Zinc nitrate hexahydrate
ZnO NPs	Zinc oxide nanoparticles
ZnO-CuO NCs	Zinc oxide-copper oxide nanocomposites

CHAPTER 1

INTRODUCTION

1.1 Background Study

The rapidly developing field of nanotechnology is widely applied in the fields of optics, electronics, biomedicine, nano-electronics, and material sciences (Balakrishnan et al., 2020; Hoseinpour and Ghaemi, 2018; Vladimirovna Zaitseva and Alexandrovna Zemlyanova, 2020). By having an atomic size or molecular aggregates smaller than 100 nm (Abbes et al., 2021; Ammulu et al., 2021; Hassan et al., 2021; Sajjad et al., 2021; Sana et al., 2020), nanomaterials are regarded as a distinct and intermediate matter state between their individual atoms and bulk material (Dawadi et al., 2020). These nanomaterials are modified from the fundamental elements by changing both their atomic and molecular properties (Sabir et al., 2014). Researchers are becoming increasingly interested in nanomaterials because of its unusual physicochemical features and high surface area to volume ratio (Abbes et al., 2021; Ammulu et al., 2021; Greene et al., 2020; Hassan et al., 2021; Rajendran et al., 2021; Sobańska et al., 2021). The production of nanomaterials has been reported by using conventional method, such as hydrothermal method, sol-gel synthesis, laser ablation, microwave assistance, precipitation, spray pyrolysis, sputter deposition, and solvothermal (Basit et al.,

2023; Droepenu et al., 2022; Khatoon et al., 2023; Mallikarjunaswamy et al., 2020; Narath et al., 2021; Nguyen et al., 2023; Shaba et al., 2021). Although the nanomaterials synthesized by physical or chemical methods have a specific size and shape (Sajjad et al., 2021), these methods are costly (Aminuzzaman et al., 2018; Aminuzzaman et al., 2019; Aminuzzaman et al., 2021; Georgia et al., 2023; Rajendran et al., 2021), time-consuming (Georgia et al., 2023), technically complex (Aminuzzaman et al., 2018; Fawcett et al., 2017), low materials conversion and reaction rates (Ammulu et al., 2021; Fawcett et al., 2017), high energy requirements (Abbes et al., 2021; Fawcett et al., 2017; Khan et al., 2020), hazardous chemicals used (Abbes et al., 2021; Aminuzzaman et al., 2021; Khan et al., 2020; A. Khan et al., 2021; Ammulu et al., 2021) and toxic byproducts produced (Georgia et al., 2023; Ogunyemi et al., 2020; Prasanth et al., 2019). Therefore, public is becoming more concerned about the development of high-yielding, economical (Abbes et al., 2021; Ammulu et al., 2021; Hassan et al., 2021; A. Khan et al., 2021; Sharma et al., 2021) and environmentally friendly (Abbes et al., 2021; Aminuzzaman et al., 2019; Ogunyemi et al., 2020; Prasanth et al., 2019; Sharma et al., 2021) approaches for synthesizing nanomaterials.

The discovery of antibiotics in the middle of the 20th century has had a significant impact on medicine (Shabatina et al., 2022; Singh et al., 2020). Bacteria, on the other hand, are resistant to almost all antibiotics due to the overuse and abuse of these drugs (Amaro et al., 2021; Niño-Martínez et al., 2019; Shabatina et al., 2022; Singh et al., 2020). Despite the constant introduction of novel antibiotics to the market, the rate of manufacture cannot keep up with the rate at which bacteria

resistant to multiple drugs are emerging (Shabatina et al., 2022). As a result, it has become a public health concern of the 21st on a worldwide scale for the outbreaks of multiple antibiotics resistance pathogenic bacteria (Hoseinzadeh et al., 2016). The WHO has confirmed that bacterial infections cause millions of deaths globally each year (Gajic et al., 2022; Khameneh et al., 2019; Singh et al., 2020). Although new antibiotics are continuously introduce to market, the rate of production is insufficient to address the rate of emergence of bacteria (Shabatina et al., 2022). Consequently, the pathogenic bacteria outbreaks due to the development of resistance to general antibiotics becomes the alarming public health issue of 21st century at global level (Hoseinzadeh et al., 2016). It has now a challenging problem for human health and all living organisms (Vindhya and Kavitha, 2023). It has become a worldwide problem in treating infectious diseases (Salayová et al., 2021), whereby costly treatment is needed and mortality might increase if treated without correct antibiotics (Helba et al., 2013). It is also expensive and time-consuming in combating bacteria and leads to patient dissatisfaction (Alavi et al., 2019). Hence, research has turned to nanomaterials as an alternative solution (Niño-Martínez et al., 2019) due to nanoparticles (NPs) has different mode of action in inhibiting bacteria by direct contacting with bacteria cell wall without the need of cell penetration (Wang et al., 2017) and alter the biochemical pathways *via* the organelles destruction, eventually leads to bacteria cell death (Singh et al., 2020).

Clean water scarcity has become the major issue in worldwide and it is needed to maintain the healthy living things (Akpomie et al., 2023; Mahmod et al., 2023). The dissolved contaminants are easily transported in water and poses direct

serious long-term toxic threat (Zelekew et al., 2023), eco-toxicity and environmental toxicity (Nguyen et al., 2023). Thus, it is important to have an effective and proper water treatment (Sidik et al., 2023). Also, reuse and recycle of waste- and polluted water has become a needs for utilizing of water in all around of world to meet the clean water demand (Amirian et al., 2017). Conventional methods, such as physical (floatation and membrane filtration), chemical (Fenton oxidation and ozonation), biological treatment (aerobic and anaerobic bioreactors, enzymatic removal, phytoremediation and bioremediation), physiochemical (coagulation-flocculation and ultrasonication), recirculation and evaporation methods has been used for reclaiming clean water from waste- and polluted water (Cheng et al., 2021; Mahmod et al., 2021; Ng et al., 2019; Obayomi et al., 2023; Saputera, Amri, Mukti, et al., 2021; Saputera, Amri, Daiyan, et al., 2021; Mojiri et al., 2020; Mrabet et al., 2021; Pavithra et al., 2020; Shadi et al., 2020; Singh et al., 2021; Vaidh et al., 2022; Zandsalimi et al., 2019). However, several drawbacks from conventional methods were reported, which including long operation period, high energy consumption, costly and generation of sludge which requires secondary treatment. Moreover, the organic pollutants has complex organic molecular configuration, poor biodegradability and high noxiousness which makes conventional methods not effective in treating wastewater (Obayomi et al., 2023; Puasa et al., 2021; Saputera, Amri, Mukti, et al., 2021; Saputera, Amri, Daiyan, et al., 2021; Sidik et al., 2023; Azadi et al., 2020). In response to this situation, the water purification method has switched to by using nanomaterials as they are being

reported to have excellent adsorptive and photocatalytic properties (Nguyen et al., 2023).

1.2 Problem Statements

The traditional synthesis of nanomaterials often depends on hazardous chemicals, posing significant risks to both the environment and public health. The increasing awareness of these dangers has led researchers to explore greener alternatives for nanomaterial production. One promising approach is the use of plant extracts, which offer a safer, eco-friendly option for synthesizing nanomaterials. However, while these green synthesis methods reduce the reliance on toxic chemicals, they present a new set of challenges. Achieving the desired physicochemical properties such as size, shape, stability, and functionality is critical for the effective application of nanomaterials in various fields. These properties can be highly dependent on the specific nature of the plant extracts employed, complicating efforts to optimize synthesis protocols.

The treatment of bacterial infections remains a major concern for human and environmental health. Traditional antimicrobial therapies are often expensive, have extended recovery periods, and exhibit diminishing efficacy, leading to patient dissatisfaction. Nanomaterials offer a promising alternative due to their multifunctional antibacterial mechanisms, such as the physical disruption of bacterial cell membranes, the generation of reactive oxygen species (ROS), and the interference with bacterial metabolic pathways. These properties make

nanomaterials a strong candidate for overcoming bacterial resistance, providing a potentially more robust and sustainable solution for infection control.

In Malaysia, the palm oil industry commonly uses open ponding systems to treat palm oil mill effluent (POME), a process that is both cost-effective and widely adopted. However, this method often fails to fully degrade the effluent, leading to severe environmental contamination and ecological degradation. Recently, nanomaterials have gained attention for their photocatalytic capabilities under UV and visible light, offering an innovative approach to purify POME. Despite this potential, research on the effectiveness of these nanomaterials in degrading toxic compounds has yielded inconsistent results, largely due to variations in nanomaterial composition and different experimental conditions. Addressing these discrepancies is critical for advancing the practical application of nanotechnology in environmental remediation.

1.3 Objectives

The objectives of this study were stated as below:

1. To synthesize copper oxide nanoparticles (CuO NPs) zinc oxide nanoparticles (ZnO NPs) and zinc oxide-copper oxide nanocomposites (ZnO-CuO NCs) using an eco-friendly approach with mangosteen (*Garcinia mangostana*) leaf extract (MLE) as the reducing and stabilizing agent.

2. To determine the optimal conditions for the synthesis of CuO, ZnO and ZnO-CuO nanomaterials mediated by MLE, and to comprehensively characterize their physicochemical properties with various analytical techniques [such as ultraviolet-visible (UV-Vis) spectrophotometry, Fourier transform infrared (FT-IR) spectrophotometry, X-ray diffractometer, field emission scanning electron microscopy (FE-SEM) with energy dispersive X-ray (EDX) analysis, high-resolution transmission electron microscopy (HR-TEM), and X-ray photoelectron spectroscopy (XPS)].
3. To assess the preliminary *in vitro* antibacterial effectiveness of the optimized nanomaterials against Gram-positive and Gram-negative bacteria, providing quantitative data on their efficacy.
4. To optimize the photodegradation of chemical oxygen demand (COD) and ammoniacal nitrogen (AN) in POME using the synthesized CuO, ZnO and ZnO-CuO nanomaterials.

1.4 Significance of Study

Various parts of the mangosteen plant, such as the stem, seed, peel, bark, rind, and pericarp, have been widely used as natural reducing, capping, and stabilizing agents in the green synthesis of metal and metal oxide (MO) NPs, including silver (Ag), gold (Au), and ZnO. However, there is a notable gap in the literature regarding the use of mangosteen leaves in the green synthesis of ZnO NPs.

Additionally, no studies have reported for the green synthesis of CuO NPs or ZnO-CuO NCs using mangosteen leaves or other plant components. This study will address this gap by exploring the use of MLE in the green synthesis of these nanomaterials.

Nanomaterials synthesized from various parts of the mangosteen plant have demonstrated antimicrobial, dye photodegradation, and antioxidant activities. However, their potential for treating POME has not yet been investigated. This study will evaluate the effectiveness of these green-synthesized nanomaterials in degrading harmful substances in POME, offering a new application for mangosteen-derived nanomaterials in environmental remediation.

In terms of antibacterial activity, the disk diffusion assay is commonly used to assess the preliminary antimicrobial efficacy of nanomaterials qualitatively. However, there is limited literature reporting quantitative results for the antibacterial activity of green-synthesized nanomaterials. This study will fill that gap by providing quantitative data on the antibacterial effectiveness of the synthesized CuO, ZnO, and ZnO-CuO nanomaterials.

Lastly, while polychromatic light sources such as UV and visible light are commonly used in POME treatment, their effectiveness in reducing COD has shown inconsistent results (Chai et al., 2019; Kanakaraju et al., 2017; Lam et al., 2018; Phang et al., 2021; Puasa et al., 2021; Sidik et al., 2023). This study will explore the use of blue light-emitting diode (LED) as an alternative. LEDs are more economical due to their longer lifespan (up to 50,000 hours compared to 9,000 hours for UV lamps) and higher photon energy, particularly in the blue light

spectrum. The use of blue LED in this study may offer a more efficient and cost-effective solution for photodegrading harmful substances in POME.

1.5 Scope of Study

In this study, CuO, ZnO and ZnO-CuO nanomaterials were green synthesized using MLE. The synthesis process was optimized in a stepwise manner by varying the MLE concentration, calcination temperature, and salt precursor ratios. The synthesized nanomaterials were characterized using a range of analytical techniques, including UV-Vis spectrophotometry, FT-IR spectrophotometry, X-ray diffractometer, FE-SEM with EDX analysis, HR-TEM and XPS. The physicochemical properties of the nanomaterials, including optical properties, functional groups, crystalline structure, morphology, elemental composition, and surface oxidation, were thoroughly examined.

Following characterization, the preliminary antibacterial activity of the optimized CuO, ZnO and ZnO-CuO nanomaterials was assessed using a macro-dilution assay to determine their minimum inhibition concentration (MIC) against Gram-positive bacteria (*Staphylococcus aureus* ATCC BAA-1026 and *Bacillus subtilis* ATCC 6633) and Gram-negative bacteria (*Escherichia coli* ATCC 25922 and *Klebsiella pneumoniae* ATCC 13883).

Finally, the efficacy of the optimized nanomaterials in treating POME was evaluated. The treatment parameters were systematically optimized, including the use of mono- and polychromatic LEDs, nanomaterial loading, POME volume,

POME concentration, and photo-degradation duration. The quality of the treated POME was assessed by measuring COD, AN and phytotoxicity.

CHAPTER 2

LITERATURE REVIEW

2.1 Nanomaterials

Nanomaterials properties are first described scientifically by Michael Faraday and it can date back to 9th century when Ag and Au of NPs were used in Mesopotamia age (Patra and Baek, 2014). The small size of nanomaterials are highly reactive with prominent physical properties with the presence of a large number constituting atoms can be found around on the surface of the particles (Vaseem et al., 2010). Different from their bulk form, nanomaterials are able to provide a new and promising solution due to its unique features (Greene et al., 2020; Imani and Safaei, 2019; Sobańska et al., 2021) in light scattering properties, including surface plasmon resonance (SPR), surface-enhanced Rayleigh scattering and surface-enhanced Raman (Dauthal and Mukhopadhyay, 2016). By having distinct physicochemical and morphological properties (Khatoon et al., 2023), nanomaterials are commonly utilized in photocatalysis, environmental remediation and energy storage (Nisticò, 2023). Moreover, with similar size to biomolecules (Vaseem et al., 2010) and having great dispersity, stability, solubility and bio-efficiency under metabolic condition (Jameel et al., 2020; You et al., 2021), nanomaterials are reported to be low in toxicity (Jameel et al., 2020). Therefore,

nanomaterials can be useful in biomedical field and human health care (Fredericks et al., 2020; Imani and Safaei, 2019; Khan et al., 2020; Lee et al., 2020; Nisticò, 2023; Sobańska et al., 2021) including in drug delivery, antibacterial, cell imaging and bio-sensing (Nguyen et al., 2023; Sana et al., 2020; H. Wang et al., 2021; You et al., 2021). Additionally, nanomaterials are widely applied in pharmaceuticals as disinfectants, fillers and drugs to tackle against bacteria (Takele et al., 2023). Besides, some of the nanomaterials, such as ZnO, has recognized as non-toxic and contain some important mineral elements which are beneficial to human body (Siddiqi et al., 2018). The properties and applications of CuO NPs, ZnO NPs and ZnO-CuO NCs is summarized in **Table 2.1**.

Table 2.1: Summarization of CuO NPs, ZnO NPs and ZnO-CuO NCs properties with their applications.

Nanomaterials	CuO NPs	ZnO NPs	ZnO-CuO NCs
Semiconductor type	*p*	*n*	*p-n*
Properties	• Non toxic • Commonly found in nature • Outstanding in electrical and optical properties with unique selective catalytic activity • Good in magnetic phase, antioxidant, and antimicrobial characteristics	• Less toxic • High stability • Simple to prepare • Environmentally friendly • Growth in various structure • Outstanding optical, semiconducting, and piezoelectric capabilities.	• Effective in electron-hole (e^-/h^+) pair separation • Improve structural, morphological, and surface properties • Evenly size distribution, • Non-dispersive and non-aggregative • Superior loading separation efficiency • Can extend the light response to visible light range

Continue

Nanomaterials	CuO NPs	ZnO NPs	ZnO-CuO NCs
Applications	Electrical, electronic, photoctalysts, biomedical and sensor technologies	Electrical, electronic, skin protection and hygiene, photoctalysts, biomedical and sensor technologies	Electrical, electronic, photoctalysts and sensor technologies

2.1.1 CuO

Research in both basic and applied sciences has focused on CuO compounds in the copper-oxygen planes in high-temperature superconductors (Habibi and Karimi, 2014; Nithya et al., 2014). It is a *p*-type semiconductor with unique electrical, magnetic, and optical characteristics, and a small bandgap between 1.20 eV and 2.00 eV (Basit et al., 2023; Dien et al., 2023; Li et al., 2023; Mubeen et al., 2023; Nguyen et al., 2023; Oudah et al., 2020; Phang et al., 2021; Takele et al., 2023; Verma and Khan, 2019; Vindhya and Kavitha, 2023; Waris et al., 2020; Bandekar et al., 2020). Copper NPs can be easily oxidized into CuO with excellent robustness, chemical stability, and charge separation and their shelf life is longer compared to other organic antimicrobial agents (Amin et al., 2021; Li et al., 2023). As a result, it is widely used in catalytic processes, photovoltaic applications, and photo-degradation reactions (Basit et al., 2023; Dien et al., 2023; Li et al., 2023; Slobodchikov et al., 2023). However, CuO's fast e^-/h^+ pair recombination, results in low photocatalytic efficiency (Dien et al., 2023).

The CuO NPs have gained a lot of attention lately (Cuong et al., 2022). The production of CuO NPs is one of the more promising MO NPs because it is less expensive than other Nobel metals (Amin et al., 2021; Ruda et al., 2019) and its stability makes it easy to combine with polymers (Siddiqi and Husen, 2020). These multifunctional members of the copper compound family have special properties (Nithya et al., 2014; Selvanathan et al., 2021; Waris et al., 2020), including non-toxicity, high natural abundance (Oudah et al., 2020), high-

temperature superconductivity, electron correlation effects, spin dynamics and unique selective catalytic activity (Saravanan and Sivasankar, 2016). In light of this, CuO NPs have outstanding electrical and optical, magnetic phase, antioxidant and antimicrobial characteristics (Sharma et al., 2021; Siddiqi and Husen, 2020; Waris et al., 2020) which is useful in, anti-cancer, biomedical imaging, drug and cellular deliveries, wound healing, disease treatment and act as the heterogeneous catalysis (Amin et al., 2021; Hamid et al., 2021; Siddiqui, Ansari, Chauhan, et al., 2021; Waris et al., 2020). Additionally, a wide range of fields has the potential to benefit from the use of CuO NPs, including energy storage devices, supercapacitors, magnetic storage media, gas sensors, gas sensors, high-temperature semiconductors, catalytic processes, nano-fluid, environmental remediation, batteries, biosensors, photo-catalysis, and magneto-resistant materials (Cuong et al., 2022; Slobodchikov et al., 2023; Vindhya and Kavitha, 2023; Waris et al., 2020).

2.1.2 ZnO

ZnO is an *n*-type semiconductor (Basit et al., 2023; Dien et al., 2023; Hitkari et al., 2022; Mansoor Al-Saeedi et al., 2022; Mubeen et al., 2023; Nguyen et al., 2023; Sakib et al., 2019; Takele et al., 2023; Vibitha et al., 2020) that appears as an insoluble white powder in water which is seldom found in nature (Naseer et al., 2020; Shaba et al., 2021). ZnO has a band gap energy of 3.30 –3.37 eV at room temperature, a high exciton binding energy (60 meV), strong bonds (Abbes et al.,

2021; Dien et al., 2023; Hitkari et al., 2022; Kaningini et al., 2022; Mansoor Al-Saeedi et al., 2022; Mubeen et al., 2023; Nguyen et al., 2023; Puasa et al., 2021; Rajendran et al., 2021; Sajjad et al., 2021; Siddiqui, Ansari, Ansari, et al., 2021; Vibitha et al., 2020), and good chemical, photo- and thermal stability (Aminuzzaman et al., 2019). ZnO also has excellent chemical immovability, resistivity control, piezoelectric and pyroelectric capabilities, strong quantum field, flexible morphologies, exceptional electrical and optical properties, and a great isoelectric point of 9.3 – 9.8 (Lei et al., 2017; Basavalingiah et al., 2019; Mallikarjunaswamy et al., 2020; Ng et al., 2019). ZnO also shows significant green emission after thermal treatment under reducing atmosphere and considered as a phosphorescence exhibiting materials (Mallikarjunaswamy et al., 2020). Furthermore, the United States Food and Drug Administration (FDA) has classified ZnO as a chemical that is "generally recognized as safe" (GRAS) (Naseer et al., 2020; Nguyen et al., 2023; Sana et al., 2020; Shaba et al., 2021; You et al., 2021). It is advised that individuals consume 10 mg of ZnO per day (Nguyen et al., 2023). ZnO's aforementioned properties make it a popular choice for use in biomedical, biological, catalyst, sensor, energy storage, optoelectronic devices (Droepenu et al., 2022; Kaningini et al., 2022; Mubeen et al., 2023; Naseer et al., 2020; Ng et al., 2019; Sana et al., 2020), antibacterial (Kumar et al., 2020; Mubeen et al., 2023; Velsankar et al., 2020; H. Wang et al., 2021), anti-fungal, UV radiation blocking (Abbes et al., 2021; Kumar et al., 2020; Naseer et al., 2020; Sajjad et al., 2021; Velsankar et al., 2020), anti-inflammatory, wound healing and anti-cancerous (Kumar et al., 2020). Although ZnO is safe for environmental application (Ng et

al., 2019), its broad energy bandgap and high rate of recombination of photo-generated charge carriers requires UV light to carry out photodegradation. Moreover, high potential in photo-corrosion, low capacity for visible light absorption high, short lifetime (due to photo-catalyst leaching and dissolution during irradiation) and mild electrostatic repulsion force in water restricts its photocatalytic activity (Dien et al., 2023; Li et al., 2023; Mubeen et al., 2023; Puasa et al., 2021; Zelekew et al., 2023).

The rubber industry was the first to use nano-sized ZnO (Saravanan and Sivasankar, 2016). It has been widely researched to enhance the polymer performance of rubber composites by increasing rubber toughness and intensity, antiaging, and other properties (Ogunyemi et al., 2020; Sajjad et al., 2021; Saravanan and Sivasankar, 2016). It is affordable, simple to make, environmentally beneficial and very stable (Takele et al., 2023). The ZnO NPs may grow into a variety of nanostructures, including nanowires, nano-rods, nanotubes, nano-belts and other complex morphologies (Aminuzzaman et al., 2018). Their sizes, shapes, and orientations can also regulate their distinctive optical, semiconducting, and piezoelectric capabilities (Jaithon et al., 2024; Sivakumar et al., 2018). The ZnO NPs is essential MO NPs that have distinct physicochemical properties (Jiang et al., 2018). They are widely used in a variety of applications, including solar cells, photocatalysis, photoluminescence, varistors, photodetectors, and sensors (Jaithon et al., 2024; Naseer et al., 2020), as well as in the food processing, cosmetics, textile (Jaithon et al., 2024; Jindaruk et al., 2023) and agriculture (Jaithon et al., 2024) industries. Furthermore, ZnO NPs may show the desirable

properties of resistance to UV and light, deodorant (Jiang et al., 2018; Velsankar et al., 2020), and antibacterial (Jaithon et al., 2024; Jindaruk et al., 2023; Mallikarjunaswamy et al., 2020; Ogunyemi et al., 2020; Sajjad et al., 2021; Rajendran et al., 2021). In contrast to other metal particles like Ag and Au, ZnO NPs can actively remain under intracellular conditions, changing insulin resistance and further regulating lipid, carbohydrate, protein and chronic inflammation through enzymatic oxidative stress (You et al., 2021). Also, it has been observed that ZnO NPs are relatively cheap, less poisonous (Cao et al., 2019; Jiang et al., 2018; Sana et al., 2020; Senthilkumar et al., 2017a; You et al., 2021), readily absorbed by the body (Jiang et al., 2018; Sivakumar et al., 2018), bio-safe and biocompatible (Jindaruk et al., 2023; Senthilkumar et al., 2017a; Sivakumar et al., 2018). Therefore, ZnO NPs can provide superior alternatives for a range of biological applications (Vaseem et al., 2010), drug delivery (Mallikarjunaswamy et al., 2020; Rajendran et al., 2021; Senthilkumar et al., 2017a), bio-imaging, cancer curing (Jindaruk et al., 2023; Mallikarjunaswamy et al., 2020) and biomedical applications (Jiang et al., 2018; Jindaruk et al., 2023; Naseer et al., 2020; Sana et al., 2020; Senthilkumar et al., 2017a).

2.1.3 ZnO-CuO

In the design and modelling of low energy bandgap heterojunction nanomaterials, the addition of impurities to individual semiconductors is crucial (Li et al., 2023). The produced heterojunction semiconductors favorable feasibility and

effectiveness in e^-/h^+ pair separation can enhance photo-catalysis (Li et al., 2023; Mrabet et al., 2023). In comparison to single semiconductor MO NPs, such as ZnO and CuO, mixing has drawn much more interest due to its superior applicability in electrical, electronic and sensor technologies. Combining semiconductor metal oxides is essential in many real-world applications because of their improved and customizable structural, morphological, and surface properties (Basit et al., 2023; Nguyen et al., 2023). The *p*-*n* heterojunction nanocomposites (NCs) exhibit a homogeneous size distribution, non-dispersive, non-aggregative and non-agglomerative characteristics (Bandekar et al., 2020), superior loading separation efficiency, increased surface area (Basit et al., 2023) and is able to extend the light response to visible light range (Dien et al., 2023). These properties enhance their optical and electronic properties, thereby expanding their applications, particularly in environmental remediation (Basit et al., 2023; Dien et al., 2023). Among the *p*-*n* type heterojunction semiconductors, researchers have emphasis on ZnO-CuO NCs because copper can readily overlap *d*-electrons with the valence bond of ZnO (Das and Srivastava, 2017; Khan et al., 2017) once their interfaces contact with each other (Mubeen et al., 2023). Moreover, CuO is good in separating and transferring photo-excited electrons from the higher conduction band to the lower valance band, makes it an ideal metal oxide to form NCs with ZnO. Thus, ZnO-CuO NCs is reported having great performance as photo-catalyst with its large surface area and simple synthesis methods (Dien et al., 2023; Mubeen et al., 2023).

2.2 Nanomaterials Synthesis Techniques

When synthesizing nanomaterials, the synthesized particles must have a consistent size and shape using a simple method. The primary problem in the absence of a stabilizer is the agglomeration of small particles that precipitate in the solution due to the high surface-to-volume ratio of nanomaterials. As a result, it's important to get ready the stable colloids for nanomaterials growth (Vaseem et al., 2010). However, process parameters (Singh et al., 2018), the kinetics of the process between metal ion precursors and reducing agents, and the adsorption kinetics between stabilizing agents and nanomaterials (Shah et al., 2015) all have an impact on the size, shape stability and physicochemical attributes of nanomaterials.

Nanomaterials can be prepared using physical, chemical or green syntheses (Abbes et al., 2021; Basit et al., 2023; Cuong et al., 2022; Droepenu et al., 2022; Hassan et al., 2021; Salayová et al., 2021). The two primary categories of nanomaterials synthesis methods are top-down and bottom-up, as illustrated in **Figure 2.1**. While molecules are formed into nanomaterials in the bottom-up technique, bulk materials are broken down into nanomaterials in the top-down approach (Ammulu et al., 2021; Cuong et al., 2022; Dawadi et al., 2020; Lee et al., 2020; Waris et al., 2020). Nevertheless, the top-down method is rarely employed because of its high cost, surface structure imperfections and potential for serious crystallographic damage to nanomaterials (Dawadi et al., 2020; Lee et al., 2020). However, when internal stress is imposed in a bottom-up manner, surface flaws and contaminations may arise even though the products' chemical composition is more

consistent. If not well regulated, these constraints will eventually have an impact on the uses of the nanomaterials synthesized and have a significant impact on their physicochemical characteristics (Lee et al., 2020).

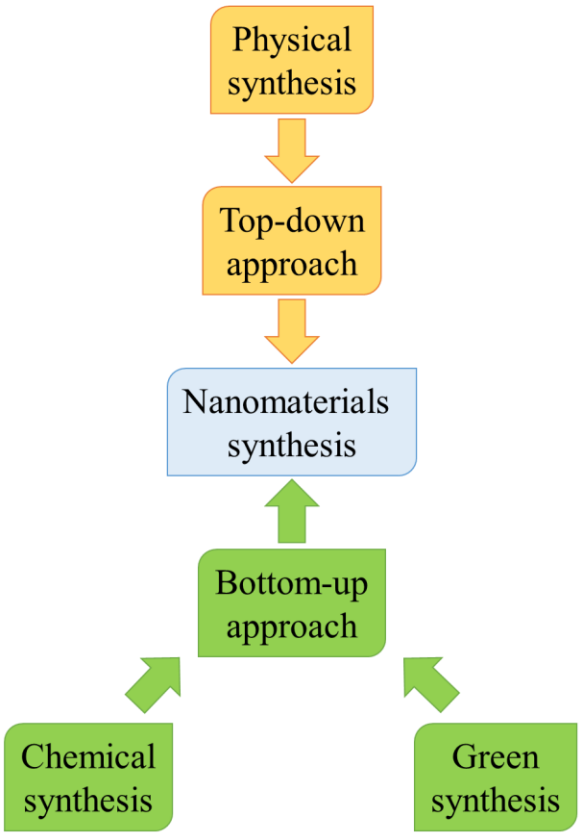

Figure 2.1: Synthesis of nanomaterials methods with different approaches (Ammulu et al., 2021; Cuong et al., 2022; Dawadi et al., 2020; Lee et al., 2020; Waris et al., 2020).

2.2.1 Physical and Chemical Syntheses

Physical synthesis, which includes lithography, machining and milling, uses mechanical forces to break down bulk particles or atom beams to create ultra-thin and very pure nanomaterials. Conversely, in the process of producing

nanomaterials, chemical synthesis includes the creation of ions through chemical processes. Common techniques for chemically synthesizing nanoparticles include chemical vapor deposition, liquid phase approach, sol-gel method, colloidal method and electrodeposition (Droepenu et al., 2022; Hassan et al., 2021; Jameel et al., 2020). Both approaches are the most often used (Vaseem et al., 2010) and chemical synthesis allows for the quick production of huge quantities of NPs (Ingale and Chaudhari, 2013). Therefore, the chemically and physically synthesized nanomaterials are not appropriate for use in catalytic (Basit et al., 2023) or medicinal (Takele et al., 2023) applications.

2.2.2 Green Synthesis

According to International Union of Pure and Applied Chemistry (IUPAC) green chemistry is defined as the preparation of chemical products without utilizing or generating harmful substances to living things and the environment. The center of green chemistry is surrounded by 12 principles (**Figure 2.2**) in describing the correct way of a chemical should be produced and applied in a green approach to achieve reduction in materials usage and environment pollution (Mutlu and Barner, 2022).

Principles of green chemistry	Prevent waste
	Maximize atom economy
	Design less hazardous chemical syntheses
	Design safer chemicals and products
	Use safer solvents and reaction conditions
	Increase energy efficiency
	Use renewable feedstocks
	Avoid chemcial derivaties
	Use catalysts, not stoichiometic reagents
	Design chemicals andproducts to degrade after use
	Analyze in real time to prevent pollution
	Minimize the potential for accidents

Figure 2.2: The 12 principles of green chemistry as stated in United States Environmental Protection Agency (Mutlu and Barner, 2022).

The public's concern about the development of economical and environmentally friendly methods for synthesizing nanomaterials is growing these days (Aminuzzaman et al., 2019; Hassan et al., 2021; A. Khan et al., 2021; Abbes et al., 2021; Ogunyemi et al., 2020; Sharma et al., 2021; Ammulu et al., 2021; Prasanth et al., 2019). When it comes to synthesizing nanomaterials, green synthesis is a straightforward process (Basit et al., 2023; Jameel et al., 2020; A. Khan et al., 2021; Prasanth et al., 2019; Septiningrum et al., 2024; Siddiqi and Husen, 2020) that requires less energy to start the reaction and uses fewer chemicals than conventional approaches (Hassan et al., 2021; Jameel et al., 2020; Sana et al., 2020), resulted in producing the less harmful byproducts (Abbes et al., 2021; Ahn et al., 2022; Basit et al., 2023; Georgia et al., 2023; Septiningrum et al., 2024). Also, green synthesis is feasible to carry out at physiological pH, temperature,

and pressure and decreases the cost of synthesizing nanomaterials. Thus, it is convenient in scaling up to prepare nanomaterials with regulated toxicity (Jameel et al., 2020; Sana et al., 2020; Basavalingiah et al., 2019; Siddiqi and Husen, 2020; Souri et al., 2019). The main challenges to synthesizing nanomaterials through green synthesis are related to morphology, composition, structure, size, and the presence of a capping agent, as these aspects determine how nanomaterials are used in industrial and biological applications (Hoseinpour and Ghaemi, 2018; Jameel et al., 2020). **Figure 2.3** outlines the benefits of synthesizing nanomaterials by adopting green synthesis.

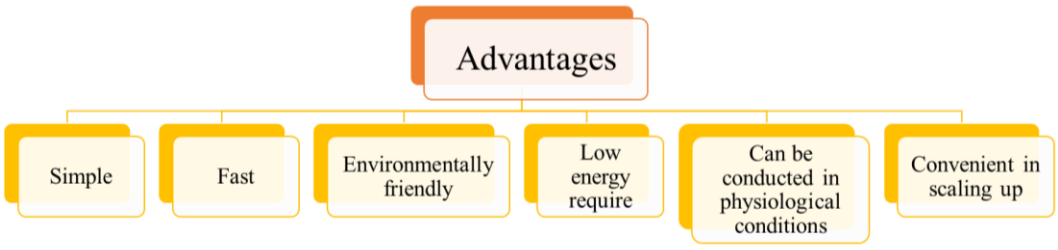

Figure 2.3: Summarization of advantages in synthesizing nanomaterials by using green synthesis.

2.3 Plant Extract Mediated Green Synthesis

In general, microbes, plant extracts, viruses, fungi, yeasts, microalgae and macro-algae can all be used to carry out the green synthesis of nanomaterials (Khalafi et al., 2019; Koopi and Buazar, 2018; Sepahvand et al., 2020; Abbes et al., 2021; Ammulu et al., 2021; Hassan et al., 2021; Rajendran et al., 2021; Septiningrum et al., 2024; Sharma et al., 2021). Among the aforementioned

biological entities, plant extracts are more dependable, straightforward and environmental friendly than other biological entities when it comes to green synthesis of nanomaterials (Vijayaraghavan and Ashokkumar, 2017; Haneefa et al., 2017; Khan et al., 2020). Because plants are non-pathogenic and their phytochemicals are highly controlled assembly, they offer a superior platform for the production of nanomaterials (Kumar et al., 2019). Plant-mediated green synthesis also presents several benefits over other biological materials for the synthesis of nanomaterials. These include the ability for one-pot synthesizing NPs, as well as robustness, eco-friendliness, natural capping and reducing agents, ease of availability, safety, cost-effectiveness, suitable for large scale synthesis without requiring cell cultures (Ahn et al., 2022; Khan et al., 2020; A. Khan et al., 2021; Phang et al., 2021; Aminuzzaman et al., 2021; Kureshi et al., 2021; Waris et al., 2020).

Plants can be used either in their live form or dead/inactive form in green synthesizing nanomaterials (Dauthal and Mukhopadhyay, 2016; Prasanth et al., 2019; Vijayaraghavan and Ashokkumar, 2017). When green synthesizing nanomaterials, plant components such flowers, leaves, stems, roots, and seeds are often used (Efenberger-Szmechtyk et al., 2020; Shammout and Awwad, 2021; Vijayaraghavan and Ashokkumar, 2017). With the presence of primary and secondary metabolites in plants (Ahn et al., 2022), such as amino acids, phenols, aldehydes, ketones, carboxylic acids, nitrogenous compounds (Jameel et al., 2020), flavonoids, alkaloids, terpenoids, (Kureshi et al., 2021) and pigments (Kumar et al., 2020), metals are accumulated and subsequently capped, stabilized or reduced into

nanomaterials intracellularly (Ahn et al., 2022; Jameel et al., 2020; Singh et al., 2018; Vijayaraghavan and Ashokkumar, 2017). Plant-based nanomaterials synthesis is a simple process that may be accomplished in a few minutes to several hours by adding the plant extracts with metal salt solution (Ammulu et al., 2021) or by using less or non-harmful chemicals (Kumar et al., 2017) at room temperature. The green synthesis employing plant extracts have been reported as the simple and alternative way to synthesize nanomaterials (Haneefa et al., 2017; Khan et al., 2020). Hence, it has been reported in wide range of applications, which including agriculture, food industry and medicine (Naseer et al., 2020).

2.3.1 CuO NPs

Calcination temperature applied in green synthesizing plant extract-mediated CuO NPs reported was in between 100^{o}C and 900^{o}C, whereas 500^{o}C and 600^{o}C were the common calcination temperature applied (**Table 2.2**). Although most of the article reported the green-synthesized CuO NPs were in spherical shape, CuO NPs green synthesized using *Muntingia calabura* leaf (Selvanathan et al., 2021) and *Momordica charantia* fruit (Qamar et al., 2020) extracts were reported in rod shape. Moreover, *Cedrus deodara* leaf extract-mediated synthesized CuO NPs was in irregular shape reported in Ramzan et al. study (2021) (Ramzan et al., 2021). Furthermore, calcination temperature applied significantly altered the plant extract-mediated synthesized CuO NPs. In Hamid et al. study (2021), *Fumaria indica* extract-mediated synthesized CuO NPs changed from cluster at low

calcination temperature (100^{o}C and 300^{o}C) to flake at high calcination temperature (600^{o}C and 900^{o}C) (Hamid et al., 2021). Structural changes in CuO NPs also observed in Verma and Khan study as *Prunus amygdalus* pericarp extract-mediated synthesized CuO NPs was in flake form when calcinated at 400^{o}C and 500^{o}C, while it was in spherical form when calcinated at 600^{o}C (Verma and Khan, 2019). The particle size of plant extract-mediated synthesized CuO NPs varied in different studies with the smallest CuO NPs obtained through the green synthesized *Punica granatum* peel extract at 12 nm (Siddiqui, Ansari, Chauhan, et al., 2021). Meanwhile, biggest CuO NPs was reported by black tea powder and coffee powder extracts at 35 – 65 nm (Fardood and Ramazani, 2018) and 20 – 60 mm (Fardood and Ramazani, 2016), respectively. Indeed, calcination temperature utilized in green synthesis affected the CuO NPs particles size. In Hamid et al. study (2021), particle size of CuO NPs green synthesized using *F. indica* plant extract increased 41.67% from 24 mm to 58 mm when they increased the calcination temperature applied from 100^{o}C to 900^{o}C (Hamid et al., 2021).

Table 2.2: CuO NPs synthesized by different plant extracts with their calcination temperature applied, structural properties and applications.

Plant extracts	Calcination temperatures (^oC)	Morphologies	Particles sizes (nm)	Applications	References
Coriandrum sativum leaf	350	Spherical	25	Photocatalytic activity	(Basit et al., 2023)
Annona glabra leaf	500	Quasi-spherical	14 – 27	Antibacterial, photocatalytic and antioxidant activities	(Nguyen et al., 2023)
Zingiber officinale rhizome	-	-	-	Antibacterial activity	(Takele et al., 2023)
Annona muricata leaf	500	Spherical	30	Antibacterial, photocatalytic, antioxidant, antifungal activities	(Vindhya and Kavitha, 2023)

Continue

Plant extracts	Calcination temperatures (^oC)	Morphologies	Particles sizes (nm)	Applications	References
Dovyalis caffra leaf	400	Spherical	-	Antioxidant and anticancer activities	(Adeyemi et al., 2022)
Bougainvillea flower	-	Spherical	5 – 20	Antifungal activity	(Shammout and Awwad, 2021)
Aloe barbadensis flower	-	Spherical	-	-	(Sharma et al., 2021)
M. calabura leaf	400	Rod	Length = 79 – 90 Thickness = 23	-	(Selvanathan et al., 2021)

Continue

Plant extracts	Calcination temperatures (^oC)	Morphologies	Particles sizes (nm)	Applications	References
Stachys. lavandulifolia flower	-	Spherical	20 – 35	Catalytic activity	(Veisi et al., 2021)
F. indica plant	100 300 600 900	Cluster Flake	24 33 41 58	Antibacterial and antioxidant activities	(Hamid et al., 2021)
M. charantia fruit	-	Rod	Length = 400 – 500 Thickness = 61	Antibacterial, antifungal and antiviral activities	(Qamar et al., 2020)

Continue

Plant extracts	Calcination temperatures (^oC)	Morphologies	Particles sizes (nm)	Applications	References
C. deodara leaf	500	Irregular	-	Antibacterial activity	(Ramzan et al., 2021)
P. granatum peel	300	Spherical	12	Antibacterial activity	(Siddiqui, Ansari, Chauhan, et al., 2021)
P. amygdalus pericarp	400	Flake	-	-	(Verma and Khan, 2019)
	500				
	600	Spherical			
Black tea powder	600	Spherical	35 – 65	-	(Fardood and Ramazani, 2018)
Coffee powder	600	Spherical	20 – 60	-	(Fardood and Ramazani, 2016)

From the literature review, the articles reported on the utilization of plant extract-mediated synthesized CuO NPs in photocatalytic activity are quite limited. A 50 mL of methylene blue dye solution did not decolourize effectively under sunlight for 110 min using 5 mg of *C. sativum* leaf extract-mediated synthesized ZnO NPs in Basit et al. study (2023) (Basit et al., 2023). Similar result was observed in Nguyen et al. study (2023) as only 13.37% degradation efficiency in 50 mL of 10 ppm methylene blue dye solution under sunlight for 2.5 h using *A. glabra* leaf extract-mediated synthesized CuO NPs (Nguyen et al., 2023). In contrast, although degradation efficiency of *A. muricata* leaf extract-mediated synthesized CuO NPs was not mentioned in the study, Vindhya and Kavitha reported that their CuO NPs was able to decolourized 100 mL of 100 ppm methylene blue dye solution under sunlight for 2 h (Vindhya and Kavitha, 2023).

On the other hand, antibacterial activity of the CuO NPs green synthesized by plant extract was determined in 47.06% among the recent published articles (Hamid et al., 2021; Nguyen et al., 2023; Qamar et al., 2020; Ramzan et al., 2021; Siddiqui, Ansari, Chauhan, et al., 2021; Takele et al., 2023; Vindhya and Kavitha, 2023). In Vindhya and Kavitha study, *A. muricata* leaf extract-mediated synthesized CuO NPs has better bactericidal effect against *Pseudomonas aeruginosa* compared to *S. aureus*. The zone of inhibition (ZOI) of *P. aeruginosa* was 11.0 mm and 16.0 mm, while *S. aureus* was not detected and 11.0 mm, at 500 µg and 1000 µg, respectively (Vindhya and Kavitha, 2023). In another work by Hamid et al. using *F. indica* plant extract-mediated synthesized CuO NPs at 100, 300, 600 and 900^{o}C have better bactericidal effect against Gram-negative bacteria

(*E. coli* and *K. pneumonia*) compared to Gram-positive bacteria (*S. aureus* and *Staphylococcus epidermidis*). Among the tested bacteria, *K. pneumonia* has the largest ZOI at 0.0 – 5.0 mm, followed by *E. coli* (ZOI at 2.0 – 4.3 mm), *S. aureus* (ZOI at 1.1 – 4.5 mm) and the smallest ZOI was recorded for *S. epidermidis* at 0.0 – 4.0 mm. In their study, it was also shown that nanomaterial's bactericidal effect was affected by its particle size. A smaller CuO NPs has better bactericidal effect compared to those with larger size (Hamid et al., 2021). Furthermore, at 150.00 µg/mL of *C. deodara* leaf extract-mediated synthesized CuO NPs, highest ZOI was recorded for *E. coli* for 29.0 mm, whereas ZOI recorded for *S. aureus*, *Salmonella enterica* (Gram-negative bacteria) and *Listeria monocytogenes* (Gram-positive bacteria) were lower than 25.0 mm in Ramzan et al. study (2021) using disc diffusion assay (Ramzan et al., 2021). Same antibacterial assay mentioned in Ramzan et al. study (2021), Siddiqui et al. study (2021) shown similar result whereby 20.0 mm of ZOI was recorded against *E. coli* using *P. granatum* peel extract-mediated synthesized CuO NPs (Siddiqui, Ansari, Chauhan, et al., 2021).

As for Gram-positive bacteria (*S. aureus*, *Streptococcus mutans*, *Streptococcus pyogenes*, *Streptococcus viridians*, *S. epidermidis*, *Corynebacterium xerosis* and *Bacillus. cereus*), it was well inhibited by *M. charantia* fruit extract-mediated synthesized CuO NPs with ZOI recorded at 23.0 – 31.7 mm. For Gram-negative bacteria (*E. coli*, *K. pneumonia*, *P. aeruginosa* and *Proteus vulgaris*), it has the ZOI at 24.7 – 26.3 mm (Qamar et al., 2020). On the other hand, *A. glabra* leaf extract-mediated synthesized CuO NPs in Nguyen et al. study (2023) shown comparable bactericidal effect against tested Gram-positive bacteria (*B. cereus* and

S. aureus) and Gram-negative bacteria (*P. aeruginosa* and *E. coli*), with the ZOI recorded at 18.7 – 19.7 mm, respectively (Nguyen et al., 2023). Similarly, *Z. officinale* rhizome extract-mediated synthesized CuO NPs has comparable bactericidal effect against *E. coli* and *S. aureus* as their minimal concentration in inhibiting were 12.50 mg/mL using MIC assay using disc diffusion method in Takele et al. study (2023) (Takele et al., 2023).

2.3.2 ZnO NPs

ZnO NPs green synthesized using different plant extracts with their calcination temperature applied, structural properties and applications were tabulated in **Table 2.3**. Generally, calcination temperature applied in green synthesizing ZnO NPs by plant extract reported was in between 200^{o}C and 900^{o}C. Most of the articles reported that the green-synthesized ZnO NPs using different plant extracts were in spherical, partially spherical or spheroid shape. There were also some articles reported that the synthesized NPs in irregular cube, hexagonal, rod or mixture of several shapes. The particle size of green-synthesized ZnO NPs was vary with different authors. In Naseer et al. study (2020), *Melia azedarach* leaf extract-mediated ZnO NPs was as small as in 3 nm (Naseer et al., 2020), while Mazli et al. study (2020) reported *Aloe vera* leaf extract-mediated synthesized ZnO NPs was in 100 – 900 nm (Mazli et al., 2020). Particle size of plant extract-mediated synthesized ZnO NPs increased when higher calcination temperature was applied. In Yusoff et al. study (2020), around two fold of increment in particle size was

obtained when black tea powder extract-mediated ZnO NPs was calcinated from 500^{o}C to 900^{o}C (Yusoff et al., 2020). Moreover, in Akbarian et al study, the particle size distribution of *Camellia sinensis* L. leaf extract-mediated synthesized ZnO NPs also affected by the calcination temperature applied. Wider particle size distribution was observed at 550^{o}C (13 – 28 mm) compared to 400^{o}C (17 – 25 mm) (Akbarian et al., 2019).

.

Table 2.3: ZnO NPs synthesized by different plant extracts with their calcination temperature applied, structural properties and applications.

Plant extracts	Calcination temperatures (°C)	Morphologies	Particles sizes (nm)	Applications	References
C. sativum leaf	350	Irregular	55	Photocatalytic activity	(Basit et al., 2023)
A. glabra leaf	500	Mixture of spherical and rectangular	13 – 24	Antibacterial, photocatalytic and antioxidant activities	(Nguyen et al., 2023)
Z. officinale rhizome	-	-	-	Antibacterial activity	(Takele et al., 2023)
D. caffra leaf	400	Hexagonal rod	-	Antioxidant and anticancer activities	(Adeyemi et al., 2022)

Continue

Plant extracts	Calcination temperatures (°C)	Morphologies	Particles sizes (nm)	Applications	References
Verbascum sinaiticum leaf	500	Spherical	-	Photocatalytic and catalytic reduction activities	(Bekru et al., 2022)
A. muricata L. leaf	450	Quasi-spherical	20 – 50	Antibacterial activity	(Selvanathan et al., 2022)
Mulberry fruit	600	Spherical	252	Antioxidant activity	(Abbes et al., 2021)
Cinnamomum tamala leaf	500	Polygonal	35	Photocatalytic activity	(Narath et al., 2021)
Rubus fairholmianus root	-	Spherical	1 – 100	Antibacterial activity	(Rajendran et al., 2021)

Continue

Plant extracts	Calcination temperatures (°C)	Morphologies	Particles sizes (nm)	Applications	References
Dendropanax morbifera	-	Spheroid	146	Anti-obesity activity	(You et al., 2021)
Lippia adoensis leaf	400	Mixture of spherical and hexagonal	19	Antibacterial activity	(Demissie et al., 2020)
Aegle marmelos pulp	500	Hexagonal	20	Antibacterial, photocatalytic and antioxidant activities	(Mallikarjunaswamy et al., 2020)
A. vera leaf	900	Cube	100 – 900	Electrochemical performance	(Mazli et al., 2020)
Ocimum. gratissimum leaf	250 400	Spherical	-	-	(Mfon et al., 2020)

Continue

Plant extracts	Calcination temperatures (°C)	Morphologies	Particles sizes (nm)	Applications	References
Cassia fistula leaf	-	Spherical	68	Antibacterial activity	(Naseer et al., 2020)
M. azedarach leaf	-	Spherical	3	Antibacterial activity	
Crotalaria verrucosa leaf	400	Hexagonal	16 – 38	Antibacterial and anticancer activities	(Sana et al., 2020)
	500		80 – 430		
Black tea powder	700	Irregular	90 – 570	Electrochemical performance	(Yusoff et al., 2020)
	900		150 – 880		
C. sinensis L. leaf	400	Spherical	17 – 25	Antibacterial, anticancer, antioxidant and hemolytic activities	(Akbarian et al., 2019)
	550		13 – 28		

Continue

Plant extracts	Calcination temperatures (°C)	Morphologies	Particles sizes (nm)	Applications	References
Hylocereus polyrhizus peel	450	Spherical	5 – 100	Photocatalytic activity	(Aminuzzaman et al., 2019)
Cardiospermum halicacabum leaf	-	Hexagonal	48 – 55	Antibacterial activity	(Nithya and Kalyanasundharam, 2019)
Hibiscus sabdariffa flower	400	Spherical	5 – 40	Photocatalytic activity	(Soto-Robles et al., 2019)
Vaccinium arctostaphylos L. fruit	-	Spherical	23	Antibacterial activity	(Mohammadi-Aloucheh et al., 2018a)

Continue

Plant extracts	Calcination temperatures (°C)	Morphologies	Particles sizes (nm)	Applications	References
Mentha longifolia leaf	-	Spherical	24	Antibacterial activity	(Mohammadi-Aloucheh et al., 2018b)
Abutilon indicum leaf	200	Spheroid	-	Antibacterial, photocatalytic, anticancer, antioxidant, antifungal activities	(Khan et al., 2017)
Tectona grandis L. leaf	400	Partially spherical	54	Antibacterial, antioxidant, anticancer and anti-arthritic activities	(Senthilkumar et al., 2017a)

Among the articles, 80.00% of authors applied green-synthesized ZnO NPs in photocatalytic and/or *in vitro* antibacterial activities. In Basit et al. study (2023), 5 mg of *C. sativum* leaf extract-mediated synthesized ZnO NPs did not decolourize significantly 50 mL of 0.000015 M methylene blue dye solution under sunlight for 110 min (Basit et al., 2023). A degradation efficiency of 95.02% was achieved using *A. glabra* leaf extract-mediated synthesized ZnO NPs in 50 mL of 10 ppm methylene blue dye solution under sunlight for 180 min in Nguyen et al. study (2023) (Nguyen et al., 2023). The degradation efficiency of 5 mg *C. tamala* leaf extract-mediated synthesized ZnO NPs has 87.45% on the 50 mL of 0.1 M methylene blue dye solution under direct sunlight for 90 min in Narath et al. study (2021) (Narath et al., 2021). In Aminuzzaman et al. study (2019), 95.00% of degradation efficiency was recorded using 50 mg of *H. polyrhizus* peel extract-mediated synthesized ZnO NPs on 20 ppm of 50 mL methylene blue dye solution under sunlight exposure for 120 min (Aminuzzaman et al., 2019). Full degradation on 5 ppm of 100 mL methylene blue dye solution was observed after 60 min of visible light irradiation in Mallikarjunaswamy et al. study (2020) using 30 mg of ZnO NPs green synthesized from *A. marmelos* pulp extract (Mallikarjunaswamy et al., 2020). According to Soto-Rables et al. study (2019), more concentrated *H. sabdariffa* flower extract (1%, 4% and 8%) in green synthesizing ZnO NPs was able to improve photocatalytic performance on 15 ppm of 200 mL methylene blue dye solution from 87.00% to 95.00% under UV lamp exposure for 90 min (Soto-Robles et al., 2019). Although degradation efficiency on acid black 234 dye solution was not mentioned in Khan et al. study (2017), *A. indicum* leaf extract-

mediated synthesized ZnO NPs was significant decolourized dye solution under sunlight exposure for 100 min (Khan et al., 2017). In contrast, only 24.00% of 120 mL of 10 ppm methylene blue dye solution was degraded using 20 mg of *V. sinaiticum* leaf extract-mediated synthesized ZnO NPs under halogen lamp for 105 min in Bekru et al. study (2022) (Bekru et al., 2022).

Disc and well diffusion assays are popularly applied in determining *in vitro* antibacterial activity of green-synthesized ZnO NPs. A simple *in vitro* antibacterial study was done by Rajendran et al. study (2021) and the MIC assay result shown that their *R. fairholmianus* root extract-mediated synthesized ZnO NPs was at 337.86 µg/mL (Rajendran et al., 2021). The 150 mg/mL of *Annona muricata* L. leaf extract-mediated synthesized ZnO NPs dissolved in dimethyl sulfoxide (DMSO) reported by Selvanathan et al. study (2022) effectively inhibit the growth of *B. subtilis*, *S. aureus*, *K. pneumoniae* and *P. aeruginosa* (Gram-negative bacteria). The ZOI recorded for the tested bacteria were 16.7 mm, 11.7 mm, 12.0 mm and 17.0 mm, respectively (Selvanathan et al., 2022). Similarly, *T. grandis* L. leaf extract-mediated ZnO NPs bactericidal effect was comparable in Gram-positive bacteria (*S. aureus* and *B. subtilis*) and Gram-negative bacteria (*E. coli* and *Salmonella paratyphi*) in Senthilkumar et al. study (2017a). The difference of ZOI between tested bacteria was less than 4.00 mm (Senthilkumar et al., 2017a). Moreover, this phenomena also similarly observed in Mallikarjunaswamy et al. study (2020) in using *A. marmelos* pulp extract-mediated synthesized ZnO NPs against the tested bacteria (Mallikarjunaswamy et al., 2020). Furthermore, 128 µg/mL of *V. arctostaphylos* L. fruit extract-mediated synthesized ZnO NPs has

similar comparable bactericidal effect against *E. coli* (32.10%) and *S. aureus* (34.40%) in Mohammadi-Aloucheh et al. study (2018a) (Mohammadi-Aloucheh et al., 2018a).

In Demissie et al. study (2020), concentration of *L. adoensis* (Koseret) leaf extract in green synthesis did not affect the bactericidal effect of ZnO NPs. Although their ZnO NPs was effective in inhibiting the growth of *S. aureus* (ZOI in between 7.0 – 9.0 mm), ZOI of *Enterococcus faecalis* (Gram-positive bacteria), *E. coli* and *K. pneumonia* were comparable with each other in between 6.0 mm and 8.0 mm (Demissie et al., 2020). However, concentration of *C. halicacabum* leaf extract in green synthesizing ZnO NPs significantly affected the ZOI observed in *B. subtilis*, *S. aureus*, *E. coli* and *P. aeruginosa* in Nithya and Kalyanasndharam study. In their study, 0.6% *C. halicacabum* leaf extract-mediated ZnO NPs has largest ZOI (19.0 – 21.0 mm), followed by 0.4% *C. halicacabum* leaf extract-mediated synthesized ZnO NPs (16.0 – 19.0 mm) and the least was 0.2% *C. halicacabum* leaf extract-mediated synthesized ZnO NPs (13.0 – 16.0 mm) (Nithya et al., 2014). In Sana et al. study (2020), *C. verrucosa* leaf extract-mediated synthesized ZnO NPs has less bactericidal effect against *E. coli* (ZOI in between 9.0 mm and 15.0 mm) compared to *P. vulgaris* (Gram-negative bacteria, ZOI in between 11.0 mm and 17.0 mm), *K. pneumoniae* (ZOI in between 10.0 mm and 17.0 mm) and *S. aureus* (ZOI in between 11.0 mm and 18.0 mm) at 25, 50 and 100 µg/mL, respectively (Sana et al., 2020). Similar results were observed in Khan et al. study (2017), as the ZOI on *E. coli* was the smallest (6.0 mm) compared to *S. aureus* (10.0 mm), *Klebsiella* (13.00 mm) and *B. subtilis* (15.0 mm). Their ZOI

results were supported by MIC results due to *A. indicum* leaf extract-mediated synthesized ZnO NPs was less sensitive to *E. coli* (1.01 mg/mL) compared to *S. aureus* (0.99 mg/mL), *Klebsiella* (0.10 mg/mL) and *B. subtilis* (0.06 mg/mL) (Khan et al., 2017).

MIC assay using disc diffusion method was applied and their result shown that lower concentration of *Z. officinale* rhizome extract-mediated synthesized ZnO NPs was needed to inhibit *E. coli* (12.50 mg/mL) compared to *S. aureus* (15.00 mg/mL) in Takele et al. study (2023) (Takele et al., 2023). In Naseer et al. study (2020), ZnO NPs green synthesized using *C. fistula* leaf and *M. azedarach* leaf extracts were more effective in inhibiting Gram-negative bacteria (*E. coli*) than Gram-positive bacteria (*S. aureus*). In both ZnO NPs concentration at 10 µL and 200 µL, the earlier has the ZOI in between 20.00 mm and 44.00 mm, while the later ZOI was in between 14.0 mm and 38.0 mm, respectively (Naseer et al., 2020). Furthermore, less healthy *E. coli* (26.13%) was found in Mohammadi-Aloucheh et al. study (2018b) compared to *S. aureus* (34.10%) using 128 µg/mL of *M. longifolia* leaf extract-mediated synthesized ZnO NPs (Mohammadi-Aloucheh et al., 2018b). However, *B. cereus* (Gram-positive bacteria) has the best bactericidal effect using *A. glabra* leaf extract-mediated synthesized ZnO NPs (ZOI at 21.8 mm) compared to *P. aeruginosa* (ZOI at 14.9 mm), *E. coli* (ZOI at 20.1 mm) and *S. aureus* (ZOI at 19.8 mm) in Nguyen et al. study (2023) (Nguyen et al., 2023). Moreover, 0.50, 1.00 and 2.00 mg/mL of ZnO NPs green synthesized using *C. sinensis* L. leaf extract did not inhibit the growth of Gram-negative bacteria (*E. coli* and *K. pneumonia*) as no ZOI were observed. On the other hand, ZOI in between 0.0 mm

and 15.0 mm were recorded in Gram-positive bacteria (*S. aureus* and *B. subtilis*) using 0.50, 1.00 and 2.00 mg/mL of *C. sinensis* L. extract mediated-ZnO NPs. Interestingly, ZnO NPs calcinated at high temperature (550^{o}C) was more effective in inhibiting tested Gram-positive bacteria (3.0 – 15.0 mm) compared to it low temperature (400^{o}C) calcinated one (0.0 – 13.0 mm) (Akbarian et al., 2019).

2.3.3 ZnO-CuO NCs

Calcination temperature and Zn-to-Cu ratio applied, structural properties and applications of different plant extract-mediated ZnO-CuO NCs were tabulated in **Table 2.4**. Calcination temperature applied in green synthesizing ZnO-CuO NCs by plant extract reported was in small range, between 350^{o}C and 500^{o}C. Moreover, spherical shape of plant extract-mediated ZnO-CuO NCs was commonly reported in articles (50.00%), while others reported in irregular or plate shape. The smallest particle size of ZnO-CuO NCs was reported to be 11 nm in Basit et al. study (2023) using *C. sativum* leaf extract (Basit et al., 2023), whereas largest *Sambucus nigra* L. shoot extract-mediated synthesized ZnO-CuO NCs in Cao et al. study (2021) in the range of 30 – 130 nm (Cao et al., 2021).

Table 2.4: ZnO-CuO NCs synthesized by different plant extracts with their calcination temperature and Zn-to-Cu ratio applied, structural properties and applications.

Plant extracts	Calcination temperatures (^oC)	Zn-to-Cu ratio	Morphologies	Particles sizes (nm)	Applications	References
C. sativum leaf	350	60:40	Irregular	11	Photocatalytic activity	(Basit et al., 2023)
A. glabra leaf	500	30:70 50:50 70:30	Spherical	16 – 35	Antibacterial, photocatalytic and antioxidant activities	(Nguyen et al., 2023)
Z. officinale rhizome	-	80:20 90:10	-	-	Antibacterial activity	(Takele et al., 2023)
D. caffra leaf	400	80:20	Spherical	20 – 32	Antioxidant and anticancer activities	(Adeyemi et al., 2022)

Continue

Plant extracts	Calcination temperatures (^oC)	Zn-to-Cu ratio	Morphologies	Particles sizes (nm)	Applications	References
V. sinaiticum leaf	500	50:50 70:30 90:10	Plate	-	Photocatalytic and catalytic reduction activities	(Bekru et al., 2022)
S. nigra L. shoot	400	65:35	Spherical	30 – 130	Anticancer activity	(Cao et al., 2021)
Calotropis gigantea leaf	300	75:25	-	-	Antibacterial activity	(Govindasamy et al., 2020)

Continue

Plant extracts	Calcination temperatures (°C)	Zn-to-Cu ratio	Morphologies	Particles sizes (nm)	Applications	References
C. gigantea leaf	500	50:50	Irregular	10 – 40	Antibacterial and photocatalytic activities	(Rajith Kumar et al., 2020)
A. barbadensis leaf	350	50:50	Spherical	-	Photocatalytic activity	(Vibitha et al., 2020)
V. arctostaphylos L. fruit	-	90:10 95:5	-	-	Antibacterial activity	(Mohammadi-Aloucheh et al., 2018a)

Continue

Plant extracts	Calcination temperatures (^oC)	Zn-to-Cu ratio	Morphologies	Particles sizes (nm)	Applications	References
M. longifolia leaf	-	90:10 95:5	Spherical	-	Antibacterial activity	(Mohammadi-Aloucheh et al., 2018b)
Theobroma cacao bark	400	75:25	Spherical	20 – 50	-	(Yulizar et al., 2018)

A 75.00% of the studies discussed the use of synthesized ZnO-CuO NCs mediated by plant extracts for photocatalytic and/or antibacterial purposes. In the Basit et al. research, 5 mg of *C. sativum* leaf extract-mediated synthesized 60ZnO-40CuO NCs successfully decolored 50 mL of 0.000015 M methylene blue dye solution under sunshine for 110 min, in contrast to its pure ZnO NPs and CuO NPs (Basit et al., 2023). Furthermore, 50 mg of *C. gigantea* leaf extract-mediated synthesized 50ZnO-50CuO NCs decolorized 97.93% of 100 mL 5 ppm of methylene blue dye solution, according to a research by Rajith Kumar et al. study (Rajith Kumar et al., 2020). But according to Nguyen et al.'s work, only 70ZnO-30CuO NCs mediated using *A. glabra* leaf extract degraded as well as its ZnO NPs (95.02%) in 50 mL of a 10 ppm methylene blue dye solution after 180 min under sunlight irradiation. In contrast, 30ZnO-70CuO and 50ZnO-50CuO NCs had a lower degradation efficiency in methylene blue dye solution than pure ZnO NPs, with respective values of 21.49% and 77.64%. On the other hand, the methylene blue dye solution degradation efficiency of all their synthesized ZnO-CuO NCs mediated by *A. glabra* leaf extract is greater than that of their pure CuO NPs (13.37%) (Nguyen et al., 2023). In Vibitha et al. study (2020), a 60 mg of 50ZnO-50CuO NCs green synthesized using *A. barbadensis* leaf extract was only able to degrade 100 mL of 0.00001 M methyl orange dye solution to 44.90% under 60 min exposure of UV light (Vibitha et al., 2020).

According to a research by Nguyen et al. (2023), 50ZnO-50CuO NCs synthesized using *A. glabra* leaf extract had a greater bactericidal impact on Gram-positive bacteria (*B. cereus* and *S. aureus*) than Gram-negative bacteria (*P.*

aeruginosa and *E. coli*). For *B. cereus*, *S. aureus*, *P. aeruginosa* and *E. coli*, the corresponding ZOI values were 21.0, 19.2, 13.4, and 17.3 mm. In comparison to its pure ZnO NPs and CuO NPs, 50ZnO-50CuO NCs had a lower bactericidal activity against tested bacteria (Nguyen et al., 2023). However, in the study by Govindasamy et al., the synthesized 75ZnO-25CuO NCs mediated by *C. gigantea* leaf extract were most sensitive to *P. aeruginosa* (0.16 mg/mL), followed by *S. aureus*, *E. coli* and *K. pneumonia*. The MIC for all of the microorganisms that were later tested was 0.63 mg/mL (Govindasamy et al., 2020). Furthermore, the Ranjith Kumar et al. study (2015) found that *C. gigantea* leaf extract-mediated synthesized 50ZnO-50CuO NCs were more efficient in suppressing *E. coli* (7.7 mm and 9.1 mm) than *S. aureus* (6.7 mm and 8.3 mm) at increasing NCs concentration from 500 µg/mL to 1000 µg/mL (Ranjith Kumar et al., 2015).

The bactericidal action of ZnO-CuO NCs synthesized using Z. *officinale* rhizome extract is superior to that of pure ZnO NPs and CuO NPs. ZnO-CuO NCs inhibited *S. aureus* and *E. coli* more effectively than its pure NPs at varying NCs concentrations (6.25 – 50.00 mg/mL). In particular, when tested against bacteria, 80ZnO-20CuO NCs have a higher ZOI than 90ZnO-10CuO NCs. The earlier ZOI in *S. aureus* was observed between 0.0 mm and 20.0 mm, whereas the latter one was recorded between 0.0 mm and 15.5 mm. In contrast, ZOI measured in *E. coli* employing NCs with more Zn ranged from 0.0 – 16.0 mm, whereas NCs with lesser Zn ranged from 0.0 – 14.5 mm (Takele et al., 2023). Similarly, the bactericidal effect of 128 µg/mL of ZnO-CuO NCs green synthesized utilizing fruit extract from *V. arctostaphylos* L. was superior to that of the same dose of pure ZnO NPs. The

vitality of *S. aureus* and *E. coli* against ZnO-CuO NCs and pure ZnO NPs was 14.90 – 18.20%, 12.10 – 15.70% and 34.40%, respectively. ZnO-CuO NCs inhibited *S aureus* more effectively than *E. coli* in their investigation. In particular, compared to 90ZnO-10CuO NCs, 95ZnO-5CuO NCs are less viable against tested bacteria. *E. coli* and *S. aureus*. The earlier were 18.20% and 15.70%, while the latter one were 14.90% and 12.10%, respectively (Mohammadi-Aloucheh et al., 2018a). Similar result and observation was reported by the previous authors using 128 µg/mL of *M. longifolia* leaf extract-mediated synthesized ZnO-CuO NCs. The viability of *E. coli* and *S aureus* for the 95ZnO-5CuO NCs were 21.80% and 13.76%, while the 90ZnO-10CuO NCs were 17.10% and 10.16%, respectively (Mohammadi-Aloucheh et al., 2018b).

2.4 *Garcinia mangostana* L.

Mangosteen, also known as *Garcinia mangostana* L., is a kind of indigenous evergreen tree that is native to tropical regions like Thailand, Indonesia and Malaysia (Ahn et al., 2022; Hiew et al., 2021; Huang et al., 2021; Jaithon et al., 2024; Mohd Basri et al., 2021; Mulyono et al., 2021; Syahputra et al., 2021). It is a member of the Clusiacae family, is known as the "fruit queen" because of its unsurpassed flavor and fragrance (Aizat et al., 2019; de Jesus Matos Viégas et al., 2018; Hiew et al., 2021; Syahputra et al., 2021). In 2017, the global production of mangosteen was close to 700,000 tones (Aizat et al., 2019), where it is most widely and economically eaten in Southeast Asia (Aminuzzaman et al., 2018).

Although it has a brownish-white taproot (Andani et al., 2021), mangosteen plant has an inadequate root structure leads it to absorb nutrients and water more slowly. Mangosteen plants also have modest rates of cell cutting in shoot meristems and photosynthesis. The mangosteen plant has a protracted juvenile stage and grows slowly (Syahputra et al., 2021). It matures slowly and produces its first fruit between the ages of 9 – 20 (Abdumutalovna and Urmanovna, 2021). The height of a mature mangosteen tree can vary from 6 – 25 m. The green, thick and cylindrical stalk mangosteen leaf has an oval form and a tapering tip, with it is around 20 – 25 cm in length and 6 – 9 cm in breadth. The mangosteen plant, which has a solitary blossom and is androgynous, has 1 – 2 cm long axillae. Mangosteen fruit has a spherical, 6 – 8 cm diameter, purplish-brown hue (Aminuzzaman et al., 2018; Andani et al., 2021; Mohd Basri et al., 2021; Mulyono et al., 2021). In fact, the fruit size and weight are not directly proportional (Mulyono et al., 2021). The fruit is white and soft with slightly sour taste (Aminuzzaman et al., 2018). Within each mangosteen fruit, there are five to seven seeds, each yellowish-spherical, 2 cm in diameter (Andani et al., 2021). The seeds of the mangosteen are apomictically. Their development is asexual, resulting in little genetic variety, and they inherit features from their female parents genetically (Syahputra et al., 2021).

Terpene, xanthones, anthocyanins, flavonoids, polyphenols and tannins are among the many phytochemicals found in mangosteen (Ahn et al., 2022; Aizat et al., 2019; Andani et al., 2021; Diniatik and Anggraeni, 2021; Huang et al., 2021; Jassim et al., 2021; Mohd Basri et al., 2021; Septiningrum et al., 2024). Xanthone is the phytochemicals with the highest degree of antioxidant activity (Ahn et al.,

2022; Diniatik and Anggraeni, 2021; Septiningrum et al., 2024), particularly in the rind of mangosteen (Hiew et al., 2021; Huang et al., 2021; Septiningrum et al., 2024). These primary and secondary bioactive compounds are reported act as reducing agents in forming NPs (Septiningrum et al., 2024). The identified xanthone fraction contains both α- and γ-mangostin as major components. The majority of studies concentrate on the structure and extraction of xanthones from the heartwood, stem, seed, and hull or pericarp of mangosteen fruits (Obolskiy et al., 2009). Both 1,5,8-trihydroxy-3-methoxy-2-(3-methylbut-2-enyl) xanthone and 1,6-dihydroxy-3-methoxy-2-(3-methyl-2-buthenyl) xanthone (**Figure 2.4**) are the xanthones reported found in mangosteen leaves (Obolskiy et al., 2009).

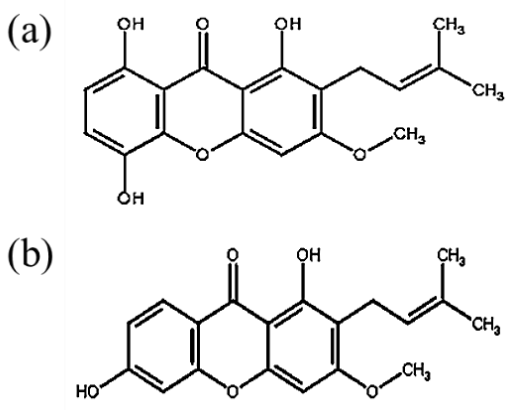

Figure 2.4: Chemical structure of (a) 1,5,8-trihydroxy-3-methoxy-2-(3-methylbut-2-enyl) xanthone and (b) 1,6-dihydroxy-3-methoxy-2-(3-methyl-2-buthenyl) xanthone.

Mangosteen is reported with various different medical benefits, such as anti-HIV, anti-ulcer (Ahn et al., 2022), cardioprotective, anti-carcinogenic (Georgia et al., 2023), anti-allergic, anti-convulsants (Mohd Basri et al., 2021), anti-leukemic activity (de Jesus Matos Viégas et al., 2018), anti-tumor, anti-diabetic,

anti-plasmodial, immunity increment, hepatoprotective function, antioxidant, antimicrobial, anti-inflammatory (Abdumutalovna and Urmanovna, 2021; Ahn et al., 2022; Andani et al., 2021; de Jesus Matos Viégas et al., 2018; Diniatik and Anggraeni, 2021; Georgia et al., 2023; Hiew et al., 2021; Huang et al., 2021; Jassim et al., 2021; Mohd Basri et al., 2021) properties. Mangosteen has also been shown to be helpful in treating of hypertension and arthritis, and the improvement of lymphatic system strength (Huang et al., 2021; Syahputra et al., 2021; Abdumutalovna and Urmanovna, 2021). Additionally, the mangosteen shell is reported being utilized in treating skin infections, wounds, inflammation (Jaithon et al., 2024), cancer, diabetes and diarrhea (Georgia et al., 2023).

2.4.1 Green Synthesized of Nanomaterials Using Mangosteen Plant Parts

Nanomaterials green synthesized using mangosteen plant parts with their structural properties and applications were tabulated in **Table 2.5**. Among the articles, more than half the authors (54.84%) reported the used of mangosteen plant in green synthesizing Ag NPs, followed by Au NPs with 22.58% reported by authors, ZnO NPs (12.90%) and other nanomaterials (9.68%). Biological activities (antibacterial, antifungal, antioxidant and anticancer activities) were the most discussed by different authors (64.52%), while the remaining applications were related to catalytic activities (35.48%). Although numerous applications were applied by the mangosteen derived nanomaterials, author were only focusing on

photocatalytic and *in vitro* antibacterial activities as both applications were related to the current study.

Particularly, mangosteen extract-mediated (peel and pericarp) ZnO NPs was reported spherical shape with particle size in between 5 nm and 321 nm. On the other hand, flower-shaped ZnO NPs green synthesized from mangosteen peel and seed extracts was also obtained with large particle size in between 92 nm and 334 nm. Most of the ZnO NPs was applied in photocatalytic activity. In Kuruppu et al. study (2020), 5 mg of mangosteen seed extract-mediated synthesized ZnO NPs has better degradation efficiency (92.00%) than 5 mg of ZnO NPs green synthesized using mangosteen peel extract (85.00%) in 25 mL of 5 ppm methylene blue dye solution concentration at pH 4 under sunlight for 150 min (Kuruppu et al., 2020). Moreover, 99.00% of 50 mL of malachite green dye solution at 10 ppm was reported in Aminuzzaman et al. study (2018) by 50 mg of ZnO NPs under sunlight for 180 min (Aminuzzaman et al., 2018). Only Jaithon et al. study (2024) reported antibacterial activity of ethanolic mangosteen peel extract-mediated synthesized ZnO NPs using MIC assay. In their study, ZnO NPs was more effective in inhibiting plant pathogen bacteria (*Ralstonia solanacearum* and *Xanthomonas axonopodis* pv. *citri*) than human pathogen bacteria (*S. aureus* and methicillin-*S. aureus*). This is due to half-maximal inhibitory concentration for the earlier was smaller (2.09 mg/mL and 2.12 mg/mL) than the later (5.21 mg/mL and 5.43 mg/mL) as shown in their study (Jaithon et al., 2024).

Table 2.5: Nanomaterials green synthesized by different mangosteen extracts with their structural properties and applications.

Nanomaterials	Mangosteen extracts	Morphologies	Particles sizes (nm)	Applications	References
Ag NPs	Pericarp	Spherical	69	Detection of mercury (III) ions, catalytic, antioxidant, antibacterial and anticancer activities	(Jamila et al., 2021)
	Pericarp	Spherical	5 – 23	Antifungal activity	(Le et al., 2021)
	Rind	-	-	Antibacterial activity	(Manju et al., 2021)
	Peel	Spherical	20 – 30	Detection of iron (III) ions	(Trang et al., 2021)
	Peel	-	-	Antibacterial activity	(Alkhuriji et al., 2020)

Continue

Nanomaterials	Mangosteen extracts	Morphologies	Particles sizes (nm)	Applications	References
Ag NPs	Peel	Spherical	62 – 94	Fluorescence quenching and photocatalytic activities	(Perera et al., 2020)
	Seed	Spherical	47 – 291	Fluorescence quenching and photocatalytic activities	(Perera et al., 2020)
	Peel	Spherical	25 – 50	Anticancer activity	(Lee et al., 2019)
	Rind	Spherical	23	Antibacterial activity	(Nishanthi et al., 2019)
	Rind	Spherical	30 – 50	Antibacterial and antioxidant activities	(Rajakannu et al., 2015)

Continue

Nanomaterials	Mangosteen extracts	Morphologies	Particles sizes (nm)	Applications	References
Ag NPs	Rind	Spherical	20 – 50	Antibacterial and antifungal activities	(Karthiga et al., 2012)
	Leaf	Spherical	25	Antibacterial activity	(Gupta et al., 2015)
	Stem	-	15 – 20	Antibacterial activity	(Karthiga, 2018)
	Bark	Spherical	65	Antibacterial and larvicidal activities	(Karthiga et al., 2018)
	Bark	Spherical	12 – 15	Anticancer activity	(Zhang and Xiao, 2018)

Continue

Nanomaterials	Mangosteen extracts	Morphologies	Particles sizes (nm)	Applications	References
Ag NPs	Pericarp	Dumbbell	129 – 248	Anticancer activity	(J. S. Park et al., 2017)
	Leaf	Spherical	6 – 57	Antibacterial activity	(Veerasamy et al., 2011)
	Peel	-	15 – 125	Antibacterial, antioxidant, anti-inflammatory and wound healing activities	(Jassim et al., 2021)
Au NPs	Peel	Spherical	75 – 130	Dye fixing	(Sivakavinesan et al., 2021)
	Rind	Spherical	20 – 40	Antibacterial activity	(Nishanthi et al., 2019)

Continue

Nanomaterials	Mangosteen extracts	Morphologies	Particles sizes (nm)	Applications	References
Au NPs	Peel	Spherical	47	-	(Lee et al., 2017)
	Pericarp	Spherical	54 – 132	Anticancer activity	(J. S. Park et al., 2017)
	Peel	Spherical	32	-	(Lee et al., 2016)
	Rind	Spherical	25 – 60	Antibacterial activity	(Nishanthi and Palani, 2016)

Continue

Nanomaterials	Mangosteen extracts	Morphologies	Particles sizes (nm)	Applications	References
ZnO NPs	Peel	Spherical	321	Antibacterial activity and rice growth promotion	(Jaithon et al., 2024)[1]
	Peel	Flower	92 – 247	Phytofabrication, photocatalytic, fluorescence quenching and photoluminescence activities	(Kuruppu et al., 2020)
	Seed	Flower	233 – 334	Phytofabrication, photocatalytic, fluorescence quenching and photoluminescence activities	
	Pericarp	Spherical	5 – 45	Photocatalytic activity	(Aminuzzaman et al., 2018)

[1]Ethanolic extract.

Continue

Nanomaterials	Mangosteen extracts	Morphologies	Particles sizes (nm)	Applications	References
Silver/titanium dioxide (Ag/TiO_2)	Pericarp	Spherical	19	Photocatalytic activity	(Septiningrum et al., 2024)
Selenium (Se)	Pericarp	-	-	Antibacterial, antifungal and antioxidant activities	(Benitha et al., 2021)
Platinium (Pt)	Rind	Spherical	20 – 25	Antibacterial activity	(Nishanthi et al., 2019)

2.5 Bacteria

Bacteria are microscopic, single-celled organisms that have evolved a sophisticated and complex cell envelope to enable them to transmit nutrients *via* their outer membrane and expel waste from their interiors while surviving in harsh environments. Christian Gramme developed a staining technique in 1884 that enabled him to categorize bacteria into two categories: Gram-positive and Gram-negative bacteria (Silhavy et al., 2010). **Table 2.6** provides an overview of the structural variations in cell membranes between Gram-positive and Gram-negative bacteria.

Table 2.6: Structural differences in cell membrane between Gram-positive and Gram-negative bacteria (Panawala, 2017; Slavin et al., 2017; Steward, 2019).

Cell membrane structure	Gram-positive bacteria	Gram-negative bacteria
Outer membrane	Present	Absent
Peptidoglycan layer	Thick	Thin
Periplasmic space	Absent	Present
Cell wall thickness	20 – 80 nm	5 – 10 nm
Cell wall smoothness	Smooth	Waxy
Lipopolysaccharide content	Absent	Present
Outer lipid membrane	Absent	Present
O-specific side chains	Absent	Present

Continue

Cell membrane structure	Gram-positive bacteria	Gram-negative bacteria
Teichoic acid	Present	Absent
Lipoteichoic acid	Present	Absent
Example	*S. aureus* and *B. subtilis*	*E. coli* and *K. pneumoniae*

As discussed in previous subchapter, disc and well diffusion assays were commonly applied in testing bactericidal effect of green synthesized nanomaterials against Gram-positive and Gram-negative bacteria. Although in different studies there are difference in the effectiveness against Gram-positive and Gram-negative bacteria, the information about minimum concentration of green synthesized nanomaterial required to inhibit the growth of bacteria was seldom reported. Without repeating the aforementioned study detailed, bactericidal effect of nanomaterials (ZnO NPs, CuO NPs and ZnO-CuO NCs) green synthesized using the extract of *R. fairholmianus* root (Rajendran et al., 2021), *A. indicum* leaf (Khan et al., 2017), *Z. officinale* rhizome (Takele et al., 2023) and *C. gigantea* leaf (Govindasamy et al., 2020) were tested by MIC assay.

2.6 POME

POME refers to the wastewater that is released from the palm oil production mill's final stage and cannot be readily or quickly treated again before being

dumped into the mill's internal drain system (Igwe and Onyegbado, 2007). The POME is composed of various liquids, dirties, residual oil, and suspended particles. It has an acidic pH of 3.5 – 4.2, is dark, viscous and smells bad (Agustina et al., 2021; Charles and Chin, 2018; Mahmod et al., 2023; Puasa et al., 2021; Ratnasari et al., 2021; Saputera, Amri, Daiyan, et al., 2021; Sidik et al., 2023; Sin et al., 2019). The high concentration of phenolic chemicals, pectin, tannin, carotene and lignin in POME is responsible for its brownish color. Additionally, it has substantial concentrations of inorganic minerals, free organic acids, carbohydrates, and amino acids (Akhbari et al., 2020; Chai et al., 2019; Mahmod et al., 2021; Mahmod et al., 2023; Obayomi et al., 2023). In Malaysia, the POME composition mainly included water (95.00%), oil (1.00%), suspended solids (2.00%) and dissolved solids (2.00%). The untreated POME is a very high-strength waste with high organic load, resulting in high biological oxygen demand (BOD) and COD in the range of 8200 to 43750 mg/L and 15000 to 100000 mg/L (Agustina et al., 2021; Ghazali et al., 2019; Mahmod et al., 2021; Ng et al., 2019; Obayomi et al., 2023; Puasa et al., 2021; Osman et al., 2020; Ratnasari et al., 2021; Saputera, Amri, Mukti, et al., 2021; Saputera, Amri, Daiyan, et al., 2021), respectively. Therefore, direct discharge of POME to the water bodies is inhabitable for aquatic life as the water oxygen content rapidly depletes with the presence of organic and nutritional elements (Akhbari et al., 2020; Cheng et al., 2021; Mahmod et al., 2023; Obayomi et al., 2023; Puasa et al., 2021; Saputera, Amri, Daiyan, et al., 2021; Sidik et al., 2023). Moreover, the discharged POME reduces the clarity of rivers which impacts the permeability of sunlight which in turn adversely affects the fragile aquatic ecosystem (Charles and

Chin, 2018). In addition, POME contains significant amount of nitrogenous matter 520 mg/L of total nitrogen and 613 mg/L of ammoniacal nitrogen, respectively (Ratnasari et al., 2021). The disadvantages of the traditional methods for recovering clean water from POME have been discussed in **Section 1.2**. As a result, scientists are developing alternative methods for treating POME effectively (Obayomi et al., 2023; Puasa et al., 2021; Saputera, Amri, Mukti, et al., 2021; Saputera, Amri, Daiyan, et al., 2021; Sidik et al., 2023).

Malaysia produces a significant amount of POME per year (Osman et al., 2020). An estimated 0.5 – 0.8 tons of POME may be produced from one ton of palm fruit bunches with an organic matter concentration of 5 kg/t (Akhbari et al., 2020; Phang et al., 2021). According to different research, every ton of crude palm oil produces 2.5 – 3.5 tons of POME (Mahmod et al., 2021; Osman et al., 2020). This resulted in Malaysia's 2017 POME discharge of 74 million metric tons (Charles and Chin, 2018). POME treatment is costly and challenging (Osman et al., 2020), particularly for large-scale manufacturing of oil palm industry (Osaigbovo et al., 2007). The simplest and least expensive method of handling POME is to release the wastewater into a neighboring area or river (Osman et al., 2020; Osaigbovo et al., 2007). In Malaysia, the traditional approach of treating POME is an open ponding system. However, it takes a lot of time and space and cannot clean extremely contaminated water (Aqilah Mohd Razali et al., 2020). Furthermore, the treated POME in the Madaki and Seng study is still capable of having negative environmental impacts (Osman et al., 2020). As a result, a more stringent discharge

limits is set by Department of Environment in 2015 must be followed by palm oil mills, as shown in **Table 2.7** (Zainal et al., 2017).

Table 2.7: Discharge limits of POME based on Malaysia Department of Environment (Zainal et al., 2017).

Physicochemical characteristics	Current standard discharge limit (DOE, 1982)	Future standard discharge limit (DOE, 2015)
pH	5.0 – 9.0	5.0 – 9.0
BOD	100.00 mg/L	20.00 mg/L
COD	100.00 mg/L	-
AN	-	-

2.6.1 Photocatalyst

Photocatalysis is often used in degrading organic pollutants due to its effectiveness and low cost. Harmful pollutants are degraded into harmless byproducts (particularly carbon dioxide and water) when photo-catalyst is exposed under UV or visible light during wastewater remediation (Septiningrum et al., 2024). Photocatalyst is a non-toxic, cheap and reliable material which offers excellent performance in photo-degradation, especially metal oxides heterogeneous photocatalysts. The metal oxides heterogeneous photo-catalysts, such as ZnO, CuO, titanium dioxide (TiO_2), nickel oxide (NiO) and tin oxide (SnO), are potentially applied in removing organic pollutants during wastewater treatment (Dien et al.,

2023; Mrabet et al., 2023). Homogeneous and heterogeneous catalysis have their own advantages and disadvantages. High activity and selectivity are exhibited by homogenous catalysts, but purification is needed to regain them from products. On the other hand, heterogeneous catalysts are stable and easy to recover, however they have low catalytic activity and require long reaction duration. According to reports, the NPs demonstrated the facile separability and longevity of heterogeneous catalysts in addition to having the activity and selectivity of homogeneous catalysts (Parapat et al., 2022).

2.6.2 COD Determination

COD is an important parameter in determining the organic load in the water sample by measuring the amount of oxygen required chemically to decompose organic matter in the collected water sample (Amouei et al., 2021; Kolb et al., 2017; Li et al., 2017; Wiyantoko et al., 2020). Comparing to BOD, COD is superior representative of organic matter because COD requires short duration (2 h) and is able to provide oxidation state of the organic matters. Therefore, COD determination is more famous than BOD (Li et al., 2017). According to ISO 6060 and ISO 15705, when an oxidant is applied to a water or sludge sample under specific conditions, the mass concentration of oxygen that results is equal to the quantity of dichromate ions ($Cr_2O_7^{2-}$) ingested by dissolved and suspended materials (Geerdink et al., 2017; Li et al., 2017). The former method (reflux digestion and titration) is commonly applied for a wide range of samples using

excess of potassium dichromate ($K_2Cr_2O_7$) titrated against ferrous ammonium sulfate with the presence of ferroin as an indicator. Meanwhile, latter method (seal digestion and spectrometry) is measuring the absorbance of trivalent chromium ion (Cr^{3+}) after the samples are oxidized by $K_2Cr_2O_7$ (Li et al., 2017).

The earliest COD testing method were developed approximately 150 years ago by observing the colour changes of permanganate solution after adding to water samples. In 1925 – 1930, dichromate was started to be used as oxidant in oxidizing organic matter although the results were not promising. In 1949, dichromate procedure was applied by Moore et al. in analyzing the wastewater by refluxing the sample for 2 h using $Cr_2O_7^{2-}$ in 50% sulphuric acid (H_2SO_4) solution at 145 – 150^oC. It resulted in around 90% of the organic matter and most of the chloride ions (Cl^-) were oxidized. Later in 1951, Moore et al. applied small amount of silver sulfate (Ag_2SO_4) to the water sample to catalyze the oxidation and resulted in nearly qualitative results even with the presence of inert compounds, such as carboxylic acids and aliphatic alcohols. The addition of mercuric sulphate ($HgSO_4$) to the mixture of H_2SO_4 and $Cr_2O_7^{2-}$ reagent demonstrated by Dobbs et al. in 1963 was able to reduce Cl^- oxidation during the COD digestion, which meant separate Cl^- determination was no longer required (Geerdink et al., 2017). In 1970, the use of $K_2Cr_2O_7$ in oxidizing organic matter in the water sample was internationally applied as standard method (Kolb et al., 2017).

Conventionally, COD can be determined using $K_2Cr_2O_7$ or potassium permanganate. The earlier method is mainly used in accessing moderate or heavy polluted water bodies (such as sewage and wastewater), while the latter method is

used in determining low-leveled COD values water bodies (such as surface water and river water) (Li et al., 2017). During the COD testing, $K_2Cr_2O_7$ is used as strong oxidizer under acidic (H_2SO_4) and hot conditions with Ag_2SO_4 as catalyst to decompose all the organic materials in the water sample for 2 h. The potassium hydrogen phthalate (KHP, $KC_8H_5O_4$) is commonly used to represent the organic matters in testing the procedure. During the 2 h of COD digestion, the organic matters are oxidized by $Cr_2O_7^{2-}$ at 148^{o}C, while Cl^- are oxidized into chlorine. The Cl^- interference is mitigated by the addition of $HgSO_4$ (Geerdink et al., 2017; Kolb et al., 2017; Li et al., 2017; Wiyantoko et al., 2020). At the end of the COD testing, the organic matters are decomposed into carbon dioxide and water, while the nitrogenous compounds are converted into ammonia before forming nitrite and nitrate (Amouei et al., 2021). **Equations 1 – 3** represent the chemical reactions involved during the COD determination (Geerdink et al., 2017; Li et al., 2017).

$$2KC_8H_5O_4 + 10K_2Cr_2O_7 + 41H_2SO_4 \rightleftharpoons 16CO_2 + 46H_2O + 10Cr_2(SO_4)_3 + 11K_2SO_4 \quad (1)$$

$$Cr_2O_7^{2-} + 6Cl^- + 14H^+ \rightleftharpoons 3Cl_2 + 2Cr^{3+} + 7H_2O \quad (2)$$

$$Hg^{2+} + 2Cl^- \rightleftharpoons HgCl_2 \quad (3)$$

2.6.3 AN Determination

Nitrogen is an essential compound for all living and present as organic nitrogen, nitrate, nitride and ammonia in natural water. On the other hand, nitrogen is present in the form of organic nitrogen and ammonium in raw wastewater. High

concentration of ammonium in water will lead to algal bloom resulting in oxygen depletion, subsequently threatening the aquatic life (Jeong et al., 2013; Varghese et al., 2023). The harmful contaminant ammonia which may directly kill individuals and disturb the balance of water ecological systems is measured as AN. Oxygen demand level is often determined in conventional treatment. Therefore, AN has received special attention in the biological wastewater treatment. AN can be conventionally removed using biological, physical, chemical or combination of these methods. In particular, auto oxidation process (AOP) involving photocatalytic processes are reported to be utilized in industrial wastewater treatment (Patil et al., 2021).

Nessler's methods is the common colorimeter in determining ammonium concentration. Nessler's method was first developed in 1856 and is able to apply in analyzing water with low concentration of ammonium (0.025 – 5.0 mg/L). In Nessler's method, yellow-brownish compound is formed when potassium, mercury and iodine reacted with ammonium through Nesslerization (**Equation 4**) in alkaline medium. At the end of the reaction, the yellow colour intensity of the mixture is measured using spectrophotometer at the wavelength in the range of 410 – 425 nm, whereby the intensity of the colour is proportional to the concentration of ammonium in the sample (Jeong et al., 2013; Utomo et al., 2023; Varghese et al., 2023).

$$2[HgI_4]^{2-} + NH_3 + 3OH^- \rightleftharpoons Hg_2ONH_2I + 2H_2O + 7I^- \quad (4)$$

2.6.4 POME Treatment Using Nanomaterials

POME treatment using nanomaterials are seldom reported in literature review. In **Table 2.8**, UV lamp was commonly used as light source in photodegrading harmful substances in POME and removal efficiency of COD was the only parameter reported in different articles. Although some articles reported COD removal efficiency was able to achieve more than 90.00%, the mode of photo-catalytic performance of nanomaterials was 60.59%. Meanwhile, 30.00% articles reported COD removal efficiency were below 50.00%. This shown that optimization process is needed in utilizing nanomaterials in treating POME to achieve optimized harmful substances' removal efficiency.

Phang et al. study (2021) demonstrated 0.5 g/L of *Carica papaya* L. peel extract-mediated synthesized CuO NPs in 300 mL of POME under UV light for 3 h shown 66.00% of COD removal efficiency was achieved (Phang et al., 2021). On the other hand, 0.3 g/L of *Cymbopogon citratus* plant extract-mediated synthesized ZnO NPs recorded highest COD removal efficiency in POME (75.40%) under UV light for 60 min, followed by 0.1 g/L of ZnO NPs (71.80%) and 0.5 g/L of ZnO NPs (70.86%) in Sidik et al. study (2023) (Sidik et al., 2023). However, as compared to 0.5 g/L of polyethylene glycol coated ZnO NPs, lower COD removal efficiency in POME was observed using 0.5 g/L of *C. citratus* plant extract-mediated synthesized ZnO NPs (60.67%) under UV light for 15 min in Puasa et al. study (2021). The earlier ZnO NPs recorded COD removal efficiency for 68.31% (Puasa et al., 2021). On the other hand, COD removal efficiency in POME was

optimized using different ZnO NPs loading in Kanakaraju et al. study (2017). They found that highest COD removal efficiency was recorded using 2.0 g/L of ZnO NPs (60.50%), followed by 1.0 g/L of ZnO NPs (~ 45.00%), 4.0 g/L of ZnO NPs (36.60%) and 0.5 g/L of ZnO NPs (26.30%). Their POME degradation study was carried out under sunlight irradiation for 300 min (Kanakaraju et al., 2017). A, 82.00% of COD removal efficiency was achieved by 1.0 g/L of *Hibiscus rosasinensis* leaf extract-mediated synthesized ZnO NPs in 400 mL of POME under UV light for 240 min reported by Chai et al. study (2019) (Chai et al., 2019). Better COD removal efficiency was observed at 96.00% in Lam et al. study (2018) when they used 1.0 g/L of flower-shape ZnO NPs to photodegrade POME under UV light for just 120 min (Lam et al., 2018).

Table 2.8: Photocatalytic performance of nanomaterials in POME treatment under different conditions.

Nanomaterials	Conditions				COD removal efficiency (%)	References
	Light sources	Nanomaterials loading (g/L)	POME volume (mL)	Duration (min)		
CuO NPs	UV light	0.50	300	180	66.00	(Phang et al., 2021)
		0.10			71.80	
	UV light	0.30	-	60	75.40	(Sidik et al., 2023)
		0.50			70.86	
ZnO NPs	UV light	0.50	-	15	[1]68.31	(Puasa et al., 2021)
					60.67	
	UV light	1.00	400	240	82.00	(Chai et al., 2019)
	UV light	1.00	400	120	96.00	(Lam et al., 2018)

[1]Polyethylene glycol coated ZnO NPs.

Continue

Nanomaterials	Conditions				COD removal efficiency (%)	References
	Light sources	Nanomaterials loading (g/L)	POME volume (mL)	Duration (min)		
ZnO NPs	Sunlight	0.50	150	300	26.30	(Kanakaraju et al., 2017)
		1.00			~ 45.00	
		2.00			60.50	
		4.00			36.60	
TiO_2 NPs	Sunlight	0.02	150	300	54.30	
		~0.06			~75.00	
		0.10			88.50	
		0.20			40.00	

Continue

Nanomaterials	Conditions				COD removal efficiency (%)	References
	Light sources	Nanomaterials loading (g/L)	POME volume (mL)	Duration (min)		
TiO_2 NPs	UV light	2.50	250	240	23.00	(Tan et al., 2014)
		5.00			43.00	
		10.00			26.00	
TiO_2-biosilica NPs	Xenon lamp	1.00	500	240	47.00	(Putri et al., 2022)
WO_3-ZnO NCs	UV light	1.00	500	240	68.30	(Sin et al., 2019)
Nb_2O_5-ZnO NCs	UV light	1.00	500	240	91.70	
La-Ca NPs	UV light	3.00	200	300	55.46	(Ghazali et al., 2019)

CHAPTER 3

MATERIALS AND METHODS

3.1 Layout of The Study

The mangosteen leaf aqueous extract was prepared for green synthesizing nanomaterials. Only calcination temperature was optimized in green synthesizing ZnO NPs and CuO NPs as both nanomaterials are commonly green synthesized by researchers and frequently reported in literature review. For ZnO-CuO NCs, the conditions in green synthesizing nanomaterials were optimized by altering mangosteen leaf aqueous concentration (1 – 5 g/mL), calcination temperature (200 – 600^{o}C) and precursor loading ratio [zinc (Zn) salt:copper (Cu) salt; 3.2:0.8 – 2.0:2.0]. The physicochemical properties of green-synthesized nanomaterials were characterized using UV-Vis spectrophotometer, FT-IR spectrophotometer, X-ray diffractometer and FE-SEM with EDX analyzer. Meanwhile, HR-TEM and XPS spectrometer were only used to characterize the selected green-synthesized nanomaterials of ZnO, CuO and ZnO-CuO based on the physicochemical properties determined by aforementioned analytical tools. Next, macro-dilution assay was used in accessing the antibacterial activity of the ideal green-synthesized ZnO, CuO and ZnO-CuO nanomaterials by using Gram-positive (*S. aureus* ATCC BAA-1026 and *B. subtilis* ATCC 6633) and Gram-negative (*E. coli* ATCC 25922

and *K. pneumoniae* ATCC 13883) bacteria and their MIC were reported. Last but not least, the ideal green-synthesized ZnO, CuO and ZnO-CuO nanomaterials were applied in treating POME. The effect in utilizing different LED irradiation (blue LED representing monochromatic and white LED representing polychromatic light, respectively), nanomaterials loading (50 – 200 mg), POME volume (100 – 200 mL), POME concentration (1.6× – 12.5× dilution) and photo-degradation duration (0 – 2.5 h) were carried out to determine the optimized condition in treating POME and their COD and AN were reported, respectively. Phytotoxicity study was then carried out to determine the effect of treated POME on the mung bean seeds growth. The procedure layout of the study was shown in **Figure 3.1**.

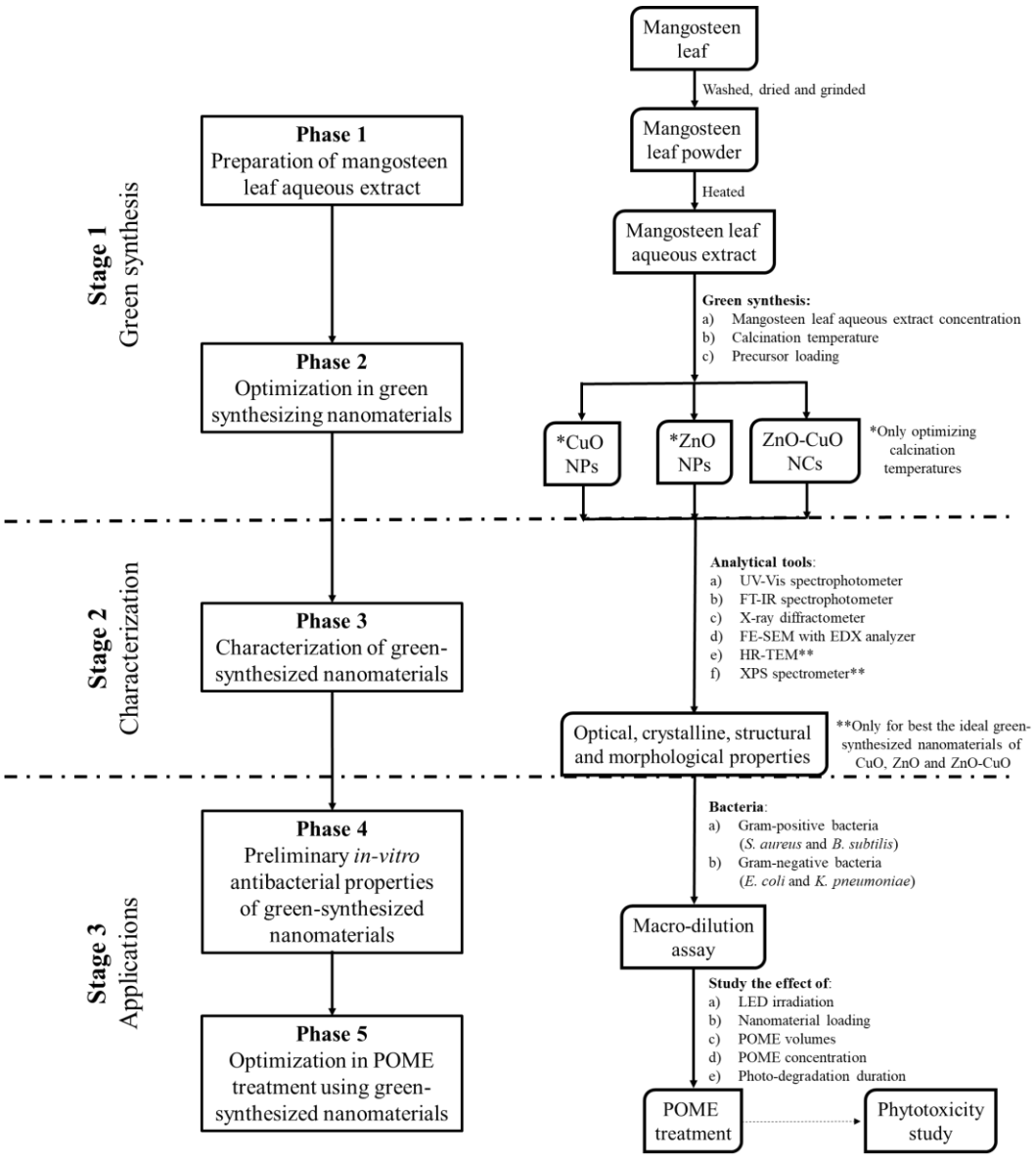

Figure 3.1: The procedure layout of the study was divided into three stages: (1) green synthesis of nanomaterials, (2) their characterization and (3) applications. The nanomaterials (CuO NPs, ZnO NPs and ZnO-CuO NCs) were green synthesized and optimized by altering the reaction conditions. Then, the green-synthesized nanomaterials were characterized by using different analytical tools to select the suitable green-synthesized nanomaterials (CuO NPs, ZnO NPs and ZnO-CuO NCs) for preliminary *in vitro* antibacterial activity and POME treatment including phytotoxicity study, based on their physicochemical properties.

3.2 Chemicals and Materials

The mangosteen leaves were gathered from Kampar, Malaysia's neighborhoods. Without further purification, 97.00% purity of copper nitrate trihydrate [$Cu(NO_3)_2 \cdot 3H_2O$] and 98.50% purity of zinc nitrate hexahydrate [$Zn(NO_3)_2 \cdot 6H_2O$] were utilized after being acquired from HiMedia Laboratories Pvt. Ltd. (Nashik, India) and HmbG (Hamburg, Germany), respectively. POME sample taken from Selangor and was kept in an airtight container to prevent deterioration during shipping.

Nutrient broth (NB) and high purity of ampicillin sodium salt was purchased from HiMedia Laboratories Pvt. Ltd. (Nashik, India) and Bio Basic Canada Inc, respectively, Gram-positive (*S. aureus* ATCC BAA-1026 and *B. subtilis* ATCC 6633) and Gram-negative (*E. coli* ATCC 25922 and *K. pneumoniae* ATCC 13883) bacteria were obtained from Faculty of Sciences, Universiti Tunku Abdul Rahman (UTAR), Malaysia. All the glassware were washed with deionized water and dried in an oven before use.

A mini light meter manufactured by Uni-Trend Technology, China was purchased to determine the light intensity of the LEDs. Meanwhile, the low range (LR-COD, 3 – 150 mg/L) and high range (HR-COD, 20 – 1500 mg/mL) COD digestion vials bought from HACH manufactured in Thailand for COD analysis. On the other hand, Nessler's reagent, mineral stabilizer and polyvinyl alcohol dispersing agent purchased from HACH in United States of America for NH_3-N

analysis. Mung bean seeds used in phytotoxicity study was bought from Econsave nearby.

3.3 Aqueous MLE Preparation

The MLE preparation was adapted from Chan et al.'s work (Chan et al., 2023; Chan et al., 2022). The leaves were thoroughly rinsed with tap water to eliminate the dust and dried in an oven for two days before put into a vacuum oven for another 8 h. The dried leaves were ground through a grinder to obtain a fine powder. After that, 1.0 g of powder was added with 100 mL of deionized water and heated with stirring for 20 min at 70 – 80^{o}C to create 0.01 g/mL of aqueous leaf extract. Then, the aqueous leaf extract was vacuum-filtered and the reddish-brown MLE was obtained. The 0.02, 0.03, 0.04 and 0.05 g/mL of aqueous MLE were prepared according to the aforementioned procedure. The prepared aqueous MLE were utilized for green synthesizing nanomaterials.

The bacteria colonies were transferred to sterilized NB and incubated at 35 – 37^{o}C for overnight. The culture was adjusted to 1 – 2 × 10^{8} CFU/mL with sterilized NB photo-metrically (absorbance reading in the range of 0.08 – 0.10 at 600 nm). The bacterial suspension was further diluted in sterilized NB to obtain 1 – 2 × 10^{5} CFU/mL. The bacterial suspension of *S. aureus* ATCC BAA-1026, *B. subtilis* ATCC 6633, *E. coli* ATCC 25922 and *K. pneumoniae* ATCC 13883 were ready to be used based on the above mentioned procedure.

The POME was diluted to allow the penetration of light for degradation. The 200 mL of 12.5 diluted POME was made ready by using 16 mL of POME with 84 mL of distilled water. Similar approach was applied in preparing two-fold dilutions of POME (1.6, 3.1 and 6.3 diluted) and volume (100, 200 and 400 mL) of POME by altering the volume ratio of POME-to-distilled water.

3.4 Green Synthesis of Nanomaterials

As shown in **Figure 3.2**, green synthesis of nanomaterials (CuO NPs, ZnO NPs and ZnO-CuO NCs) was modified and adapted from Chan et al. work (Chan et al., 2023; Chan et al., 2022).

3.4.1 CuO NPs and ZnO NPs

A 30 mL of 0.05 g/mL aqueous MLE was heated and stirred at 70 – 80°C. Then, 2.0 g of $Cu(NO_3)_2 \cdot 3H_2O$ was added and the heating and stirring at 70 – 80°C were continued until a dark brown paste was formed. The dark brown paste was transferred to a ceramic crucible and calcined at 200°C for 2 h in a muffle furnace to obtain the black CuO powder. Green synthesis of ZnO NPs was similar to the above mentioned step by using 50 mL of 0.04 g/mL aqueous MLE and 4.0 g of $Zn(NO_3)_2 \cdot 6H_2O$ to obtain the white ZnO powder. The effect of calcination temperature on the CuO NPs and ZnO NPs physicochemical properties was determined by altering the calcination temperature (200, 300, 400 and 500°C) during the green synthesis.

3.4.2 ZnO-CuO NCs

The green synthesis of ZnO-CuO NCs was optimized by changing the reaction parameters, including aqueous MLE concentration, calcination temperature and Zn-to-Cu ratio.

3.4.2.1 Aqueous MLE Concentrations

The 50 mL of aqueous MLE (0.01, 0.02, 0.03, 0.04 and 0.05 g/mL) were mixed separately with 2.8 g of $Zn(NO_3)_2 \cdot 6H_2O$ and 1.2 g of $Cu(NO_3)_2 \cdot 3H_2O$. Immediately, greenish brown solution was formed and continue heating at 70 – 80^oC with constant stirring until the formation of a dark brown paste. The paste was then cooled to room temperature and calcinated at 500^oC for 2 h by using the Muffle furnace to obtain fine black-blue ZnO-CuO powder.

3.4.2.2 Calcination Temperatures

After the selection of the optimized aqueous MLE concentration at 0.05 g/mL, the synthesis of ZnO-CuO NCs was repeated using 2.8 g $Zn(NO_3)_2 \cdot 6H_2O$ and 1.2 g of $Cu(NO_3)_2 \cdot 3H_2O$. The cooled dark brown paste was calcinated at 200, 300, 400 and 500^oC for 2 h.

3.4.2.3 Zn-to-Cu Ratios

After the selection of the optimized aqueous MLE concentration at 0.05 g/mL and calcination temperature at 500^{o}C, the synthesis steps was repeated using different weight ratio of $Zn(NO_3)_2 \cdot 6H_2O$ and $Cu(NO_3)_2 \cdot 3H_2O$, including 3.2:0.8, 2.8:1.2, 2.4:1.6 and 2.0:2.0. With the formation of dark brown paste, these synthesized products were then calcinated at 500^{o}C for 2 h.

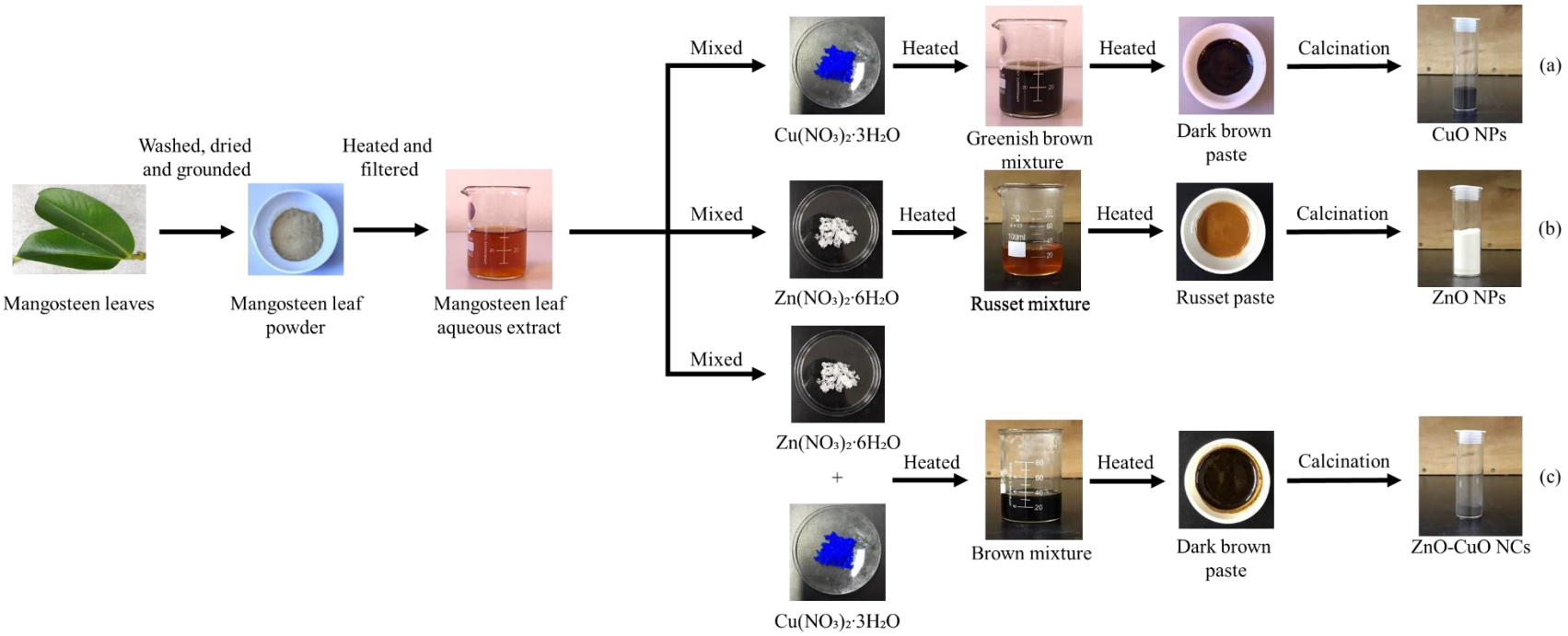

Figure 3.2: The green synthesis pathway of (a) CuO NPs, (b) ZnO NPs and (c) ZnO-CuO NCs by using aqueous MLE as natural reducing and stabilizing agents. Green synthesis conditions, including aqueous MLE concentration (0.01 – 0.05 g/mL), calcination temperature (200 – 600^{o}C) and Zn-to-Cu ratio (80:20 – 50:50), were altered to obtain the optimized physicochemical properties of ZnO-CuO NCs. Meanwhile, different calcination temperatures (200 – 600^{o}C) were applied in green synthesizing of ZnO NPs and CuO NPs.

3.5 Characterization of Nanomaterials

Various analytical tools were used in analyzing physicochemical properties of MLE mediated-synthesized nanomaterials, including UV-Vis spectrophotometer, FT-IR spectrophotometer, X-ray diffractometer, FE-SEM with an EDX analyzer, HR-TEM and XPS.

3.5.1 UV-Vis Analysis and Energy Bandgap Study

Thermo Scientific GENESYS 10S UV-Vis spectrophotometer used to detect the CuO NPs, ZnO NPs and ZnO-CuO NCs absorption spectra. Energy bandgap is inversely related to absorbance of nanomaterials. Thus, energy bandgap of the synthesized nanomaterials were plotted and best fitted using $(\alpha h\nu)^n$ versus $h\nu$ from the Tauc's approach (Mubeen et al., 2023) as in **Equation 5**.

$$\alpha h\nu = \mathrm{A}\left(h\nu - E_g\right)^n \quad (5)$$

where,

α = Absorption coefficient

A = Constant

E_g = Energy bandgap (eV)

h = Planck's constant (6.626×10^{-34} Js)

n = Exponential factor of electronic transition

(n = ½, for indirect transition; n = 2, for direct transition)

Suitable nanomaterials (CuO NPs, ZnO NPs and ZnO-CuO NCs) were selected in determining their photocatalytic performance for POME treatment by considering the redox potential of hydroxyl (•OH, 2.59 eV) and superoxide radicals ($\bullet O_2^-$, -0.16 eV) (Nguyen et al., 2023). The positon of bottom conduction band energy and top valence band energy were calculated against normal hydrogen electrode (NHE) based on Mulliken electronegativity theory (Mrabet et al., 2023; Mubeen et al., 2023; Nguyen et al., 2023), in **Equation 6** and **Equation** 7, respectively.

$$E_{CB} = \chi - E_e - 0.5E_g \quad (6)$$

$$E_{VB} = \chi - E_e + 0.5E_g \quad (7)$$

where,

E_{CB} = Bottom conduction band energy (eV)

E_{VB} = Top valence band energy (eV)

χ = Absolute electronegativity of semiconductor (eV)

(CuO = 5.80 eV, ZnO = 5.79 eV)

E_e = Free electron energy in the hydrogen scale (4.5 eV)

E_g = Energy bandgap of nanomaterials (eV)

3.5.2 FT-IR Analysis

The FT-IR (Perkin Elmer RX1 spectrophotometer) study was carried out at room temperature in the range of 4000 – 400 cm^{-1} with resolution of 4 cm^{-1} by using potassium bromide pellets. The calculated and experimental *v*(M-O) band of

synthesized nanomaterials using Hooke's Law expression (Pavia et al., 2015) as shown in **Equation 8**.

$$\nu = 4.12\sqrt{\frac{K}{\mu}} \quad (8)$$

where,

ν = Frequency (cm^{-1})

K = Force constant (5×10^5 dynes/cm)

μ = Masses of atoms (g)

3.5.3 XRD Analysis

X-ray powder diffraction (XRD) patterns was taken by X-ray diffractometer (Shimadzu XRD 6000, Kyoto, Japan) operating in continuous scanning mode at 40 kV/30 mA and 0.02 min^{-1} with Cu Kα radiation (λ = 1.5406 Å) in the 2θ range from 10 – 80°. By using the XRD data obtained, the synthesized nanomaterials' average crystalline size, dislocation density and micro strain was calculated based on Debye-Scherrer's (**Equation 9**), Williamson-Smallman's (**Equation 10**) and micro strain (**Equation 11**) relation formulae (Chan et al., 2023; Hitkari et al., 2022), respectively.

$$D = \frac{0.94\lambda}{\beta\cos\theta} \quad (9)$$

$$\delta = \frac{1}{D^2} \quad (10)$$

$$\varepsilon = \frac{\beta\cos\theta}{4} \quad (11)$$

where,

D = Crystalline size (nm)

δ = Dislocation density ($\times 10^{14}$ cm^{-1})

ε = Micro strain ($\times 10^{-4}$)

λ = Wavelength of X-ray

β = Full-width half-maximum (FWHM) of peak

θ = Bragg angle

3.5.4 FE-SEM with EDX and HR-TEM Analyses

A FE-SEM (JEOL JSM-6710F, Kyoto, Japan) with an EDX analyzer (X-max, 150 Oxford Instruments) used to examine the morphology and elemental composition of CuO NPs, ZnO NPs and ZnO-CuO NCs. Additionally, HR-TEM (JEOL JEM-3010) were utilized for selected MLE mediated-synthesized CuO, ZnO and ZnO-CuO nanomaterials.

3.5.5 XPS Analysis

XPS (Perkin Elmer PHI5600, ULVAC-PHI, Inc, Waltham, MA, USA) were utilized for surface oxidation state of selected MLE mediated-synthesized CuO, ZnO and ZnO-CuO nanomaterials.

3.6 Applications

The selected CuO NPs, ZnO NPs and ZnO-CuO NCs were utilized in preliminary *in vitro* antibacterial activity using broth macrodilution inhibiting Gram-positive (*S. aureus* and *B. subtilis*) and Gram-negative (*E. coli* and *K. pneumoniae*) bacteria. Additionally, they were also used in POME treatment by optimizing the treatment conditions (selection of LEDs, nanomaterials loading, POME volume, POME concentration and photodegradation duration) and phytotoxicity study was carried out using mung bean seeds.

3.6.1 Preliminary *in vitro* Antibacterial Activity

As shown in **Figure 3.3**, broth dilution assay was used and adapted from European Committee for Antimicrobial Susceptibility Testing (EUCAST) of the European Society of Clinical Microbiology and Infectious Diseases (ESCMID) discussion document at 2003 (European Committee for Antimicrobial Susceptibility Testing of the European Society of Clinical Microbiology and Infectious Diseases, 2003). The bacteria colonies were transferred to sterilized NB and incubated at 35 – 37°C for overnight. The culture was adjusted to $1 – 2 \times 10^8$ CFU/mL with sterilized NB photo-metrically (absorbance reading in the range of 0.08 – 0.10 at 600 nm). The bacterial suspension was further diluted in sterilized NB to obtain $1 – 2 \times 10^5$ CFU/mL^{-1}. Two-fold dilutions of green-synthesized nanomaterial suspensions (1000.00, 500.00, 250.00, 125.00, 62.50, 31.25 and 15.63

μg/mL) and antibiotic (Ampicillin sodium salt solution, 100.00, 50.00, 25.00, 12.50, 6.25, 3.13 and 1.56 μg/mL) in sterilized NB were dispensed in sterilized tubes and inoculated with $1 – 2 \times 10^5$ CFU/mL bacterial suspension. After incubation at 35 – 37°C for overnight, the visible bacterial growth in tubes were examined by turbidity with the MIC. The study was carried out in triplicates.

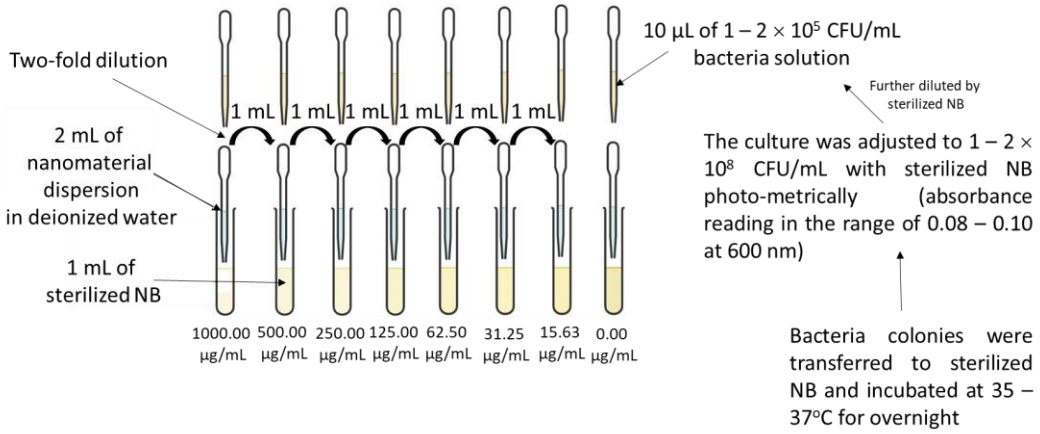

Figure 3.3: Broth macrodilution assay performed in this study to identify the preliminary *in vitro* antibacterial activity of nanomaterials.

3.6.2 Photocatalytic Performance in POME Treatment

The light intensity of LEDs was determine in unit lux and converted to mW/cm^2 by multiplying 0.0001. As shown in **Figure 3.4**, the photocatalytic performance of selected green-synthesized nanomaterials (ZnO NPs, CuO NPs and ZnO-CuO NCs) was determined by COD and AN removal efficiencies, respectively in POME treatment, slightly modified from Phang et al. study (2021) (Phang et al., 2021). The untreated and treated POME was centrifuged at 6000 rpm for 30 min to separate the nanomaterials from the suspension for COD and AN

value determination. The COD and AN removal efficiencies (in percentage) using green-synthesized nanomaterials was triplicated and determined by **Equation 12** and **Equation 13**, respectively.

$$\text{COD removal (\%)} = \frac{\text{COD}_\text{i} - \text{COD}_\text{f}}{\text{COD}_\text{i}} \times 100\% \quad (12)$$

$$\text{AN removal (\%)} = \frac{\text{AN}_\text{i} - \text{AN}_\text{f}}{\text{AN}_\text{i}} \times 100\% \quad (13)$$

where,

i = initial value of parameter in mg/L

f = final value of parameter after photo-degradation in mg/L

A 2 mL of untreated and treated POME were withdrawn for COD value determination. The withdrawn solutions were added to HR-COD or LR-COD digestion vials, followed by digestion at 150^{o}C for 2 h using a HACH DRB 200 COD digital reactor (HACH Company, Germany). Meanwhile, 2 mL of distilled water was added to COD digestion vials to act as blank solution for reference (Phang et al., 2021). The COD values were measured using DR3900 digital reactor without RFID (HACH Company, Germany) with program 435 or 430.

On the other hands, 25 mL of untreated and treated POME were withdrawn for AN value determination. Then, three drops of mineral stabilizer were added and subsequently covered and shaken to mix the solution homogeneously. Another three drops of polyvinyl alcohol dispersing agent were added and covered and mixed. Subsequently, 1 mL of Nessler's reagent was added to the mixture and shake homogenously again before allowing the mixture to stand for 1 min. Similarly, a

blank solution as reference was prepared using the aforementioned steps by using 25 mL of distilled water (Jeong et al., 2013). The AN values were measured using DR3900 digital reactor without RFID (HACH Company, Germany) with program 380.

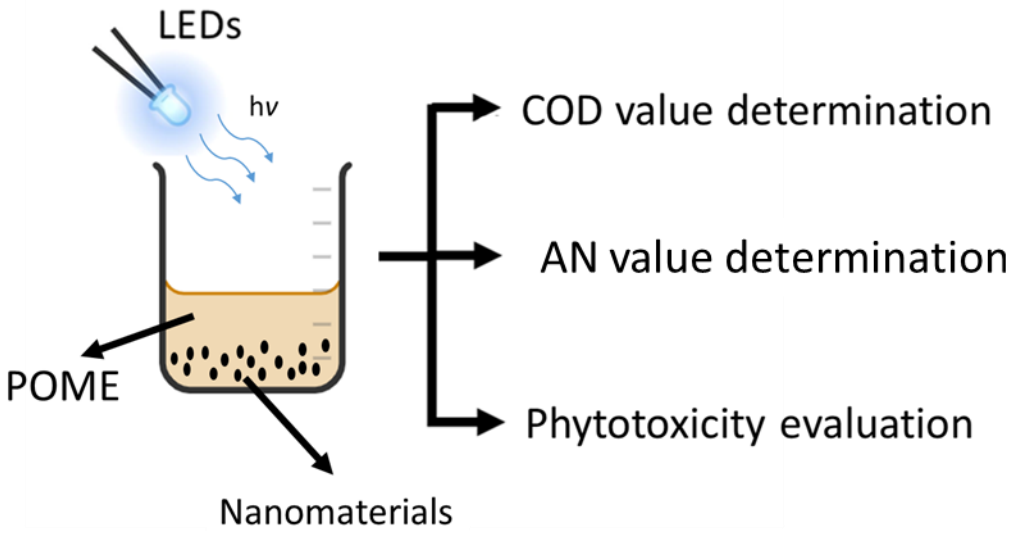

Figure 3.4: Simplified POME treatment using nanomaterial under LEDs exposure. COD, AN and phytotoxicity of the treated POME were determined after treatment. The POME treatment method was modified from Phang et al. study (2021)(Phang et al., 2021).

3.6.2.1 Selection of LEDs

The 12.5 × diluted POME was added with 100.0 mg of nanomaterial and stirred in dark for 50 min to achieve adsorption-desorption equilibrium between POME and nanomaterials. Then, the suspension was exposed to blue and white LEDs (4 W in power and voltage in 220 V and 50 Hz), respectively for 2 h.

3.6.2.2 Nanomaterial Loadings

The photocatalytic performance of 12.5 × diluted POME was repeated by exposing the 50, 100, 150 and 200 mg of nanomaterials, respectively, under blue LED exposure for 2 h.

3.6.2.3 POME Volumes

The photocatalytic performance of 12.5 × diluted POME was repeated by using the optimized nanomaterials loading with different volume of POME (100, 200, 300 and 400 mL) under blue LED exposure for 2 h. The selected POME volumes can effectively develop the treatment method in a controlled, efficient and scalable manner.

3.6.2.4 POME Concentrations

The photocatalytic performance of POME was repeated by using two-fold dilutions of POME (1.6 ×, 3.1 ×, 6.3 × and 12.5 × diluted) under blue LED exposure for 2 h with the optimized nanomaterials loading and POME volume.

3.6.2.5 Photodegradation Durations

After selecting blue LED as light source, optimized nanomaterials loading and POME volume, the treated diluted POME at passing edge was selected to extend the photo-degradation duration (up to 3 h) by repeating the same procedure to determine whether it could be fulfilled to the Department of Environment Malaysia regulation. Their COD and AN values were taken for every 30 min interval.

3.6.2.6 Phytotoxicity Study

As shown in **Figure 3.5**, the mung bean seeds were used to test the phytotoxicity of 12.5 × diluted POME samples before and after photocatalytic degradation. The mung bean seeds (healthy, uniform-sized seeds were utilized) were soaked in distilled water for 12 h before to the experiment, and they were then carefully cleaned with distilled water. Next, ten randomly chosen mung bean seeds and cotton pads were uniformly distributed within each sterilized petri dish (diameter in 90 mm). For seven straight days at room temperature, three distinct sets of petri dishes were set up and immersed in 5 mL of tap water (control) and 5 mL of POME solutions (before and after photo-degradation) at a predefined interval of 12 h (Phang et al., 2021). Following a 7 days period, the germination percentage (**Equation 14**), shoot height stress tolerance index (SHSTI, **Equation 15**) and shoot

phytotoxicity percentage (**Equation 16**) were carried out (Sen et al., 2016; Swarnakar, 2020) to determine the phytotoxicity of the POME samples.

$$\text{Germination (\%)} = \frac{\text{Germinated seeds}}{\text{Total seeds}} \times 100\% \quad (14)$$

$$\text{SHSTI} = \frac{\text{SH}_\text{s}}{S\text{H}_\text{c}} \times 100\% \quad (15)$$

$$\text{Shoot phytotoxicity (\%)} = \frac{\text{SH}_\text{c} - \text{SH}_\text{s}}{\text{SH}_\text{c}} \times 100\% \quad (16)$$

where,

SH_s = shoot height of sample (cm)

SH_c = shoot height of control (cm)

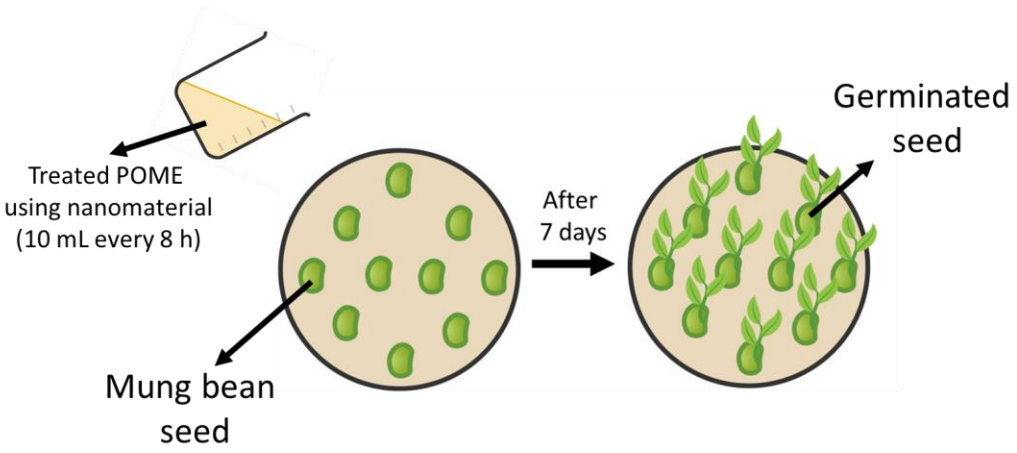

Figure 3.5: Simplified phytotoxicity evaluation of treated POME by determining the shoot length of mung bean seeds. This method was modified from Phang et al. study (2021) (Phang et al., 2021).

3.7 Statistical Analysis

COD and AN removal efficiencies, phytotoxicity and preliminary *in vitro* antibacterial study by CuO NPs, ZnO NPs and ZnO-CuO NCs were presented in mean ± standard error (SE). Two-way ANOVA analysis and post hoc Tukey test were performed to compare the pollutants removal efficiencies within different selected nanomaterials (LEDs selection and nanomaterials loading). Meanwhile, one-way ANOVA analysis and post hoc Tukey test were performed to compare the pollutants removal efficiencies within selected nanomaterials with preliminary *in vitro* antibacterial study and different photo-degradation parameters (POME volume, POME concentration and photo-degradation duration). Both ANOVA analyses were using Microsoft Excel 2013 by setting p-value < 0.05 as a significant criterion, respectively.

CHAPTER 4

RESULTS

4.1 Physicochemical Properties of Nanomaterials

Physicochemical properties of nanomaterials were analyzed by using various analytical tools and described as below.

4.1.1 UV-Vis Analysis and Energy Bandgap Study

The MLE absorbance was located at 479 cm^{-1} as shown in **Figure 4.1**. The absorbance of nanomaterials were shifted to higher wavelength (bathochromic shift) when higher MLE concentration or calcination temperature were applied as shown in **Tables 4.1** and **4.2**. The CuO NPs' absorbance shifted from 344 nm to 522 nm (**Figure 4.2**), while the absorbance of ZnO NPs were shifted from 368 nm to 373 nm (**Figure 4.3**) when the calcination temperature increased. For 70ZnO-30CuO NCs, their absorbance rose from 344 nm to 375 nm (**Figure 4.4**) and 369 nm to 373 nm (**Figure 4.5**), respectively. However, location of absorbance was not greatly affected by the CuO ratio in ZnO-CuO NCs as their absorbance were in the range of 371 – 373 nm (**Figure 4.6**).

Energy bandgap of nanomaterials decreased with higher MLE concentration and calcination temperature. Energy bandgap of CuO NPs and ZnO NPs (**Table 4.1**) decreased from 3.41 eV to 3.14 eV and 3.46 eV to 2.79 eV, respectively at elevated calcination temperature. However, CuO NPs energy bandgap increased to 3.23 eV when calcinated at 600^{o}C. Interestingly, energy bandgap of CuO NPs were larger than its bulk size and ZnO NPs. On the other hand, energy bandgap of 70ZnO-30CuO NCs (**Table 4.2**) decreased from 3.60 eV to 2.57 eV (at increasing MLE concentration) and 3.44 eV to 2.08 eV (at increasing calcination temperature), respectively. In contrast, energy bandgap of the ZnO-CuO NCs decreased (from 3.44 eV to 2.08 eV) as more Cu available in ZnO-CuO NCs. Among the nanomaterials calcinated at different temperatures, 70ZnO-30CuO NCs had the lower energy bandgap (3.44 – 2.08 eV) compared to CuO NPs (3.41 – 3.14 eV) and ZnO NPs (3.46 – 2.79 eV).

CuO NPs synthesized using 0.05 g/mL of MLE calcinated at 500^{o}C for 2 h do not have the best crystalline properties and it had the lowest energy bandgap (3.14 eV) with the radicals generation are thermodynamically favoured to it (E_{CB} = -0.27 eV and E_{VB} = 2.87 eV) among the green-synthesized CuO NPs (**Figure 4.7**). On the other hand, ZnO NPs synthesized using 0.04 g/mL of MLE calcinated at 400^{o}C for 2 h was studied for its photocatalytic performance in POME treatment. Although it is not having the lowest energy bandgap (3.27 eV), among the synthesized NPs, it had the minimal E_{CB} (-0.35 eV) and E_{VB} (2.93 eV) in fulfilling the radicals generation for photocatalytic performance (**Figure 4.8**). Instead of having relative small crystalline size (16.79 nm), it had the largest dislocation

density (38.98 × 10^{14} cm^{-1}) and micro strain (2.13 × 10^{-4}) among the green synthesized ZnO NPs. Nonetheless, 70ZnO-30CuO NCs green synthesized using 0.05 g/mL of MLE calcinated at 500ºC for 2 h was chosen as it had the lowest energy bandgap (2.57 eV) with the generation of radicals which are thermodynamically favoured to it (ZnO: E_{CB} = -0.23 eV, E_{VB} = 2.81 eV; CuO: E_{CB} = -0.22 eV, E_{VB} = 2.86 eV) as shown in **Figure 4.9**. Moreover, it had the best crystalline properties among the green synthesized ZnO-CuO NCs with the smallest crystalline size (18.17 nm) as well as largest dislocation density (161.37 × 10^{14} cm^{-1}) and micro strain (2.77 × 10^{-4}).

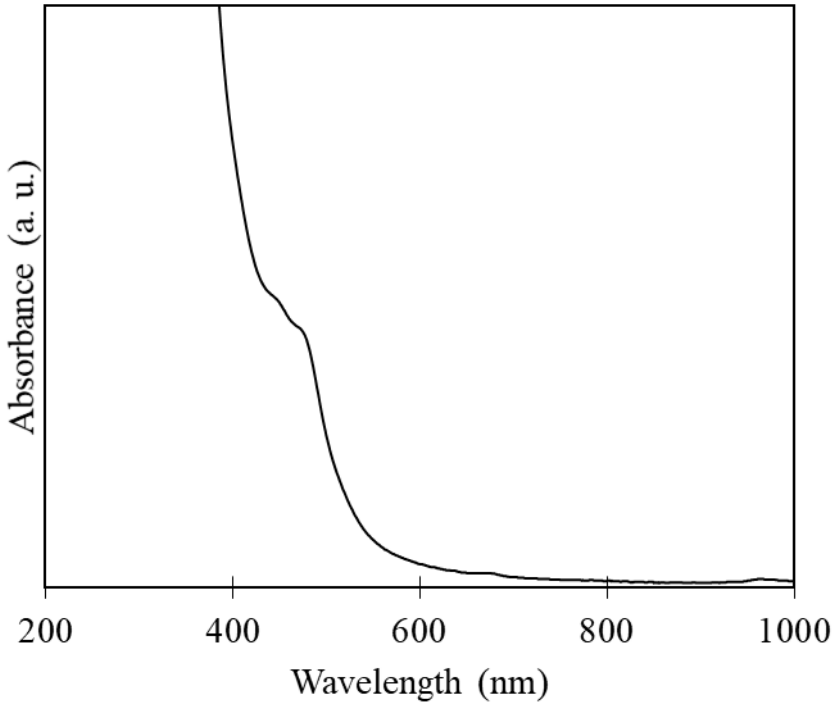

Figure 4.1: UV-Vis spectrum of MLE.

Table 4.1: Summarization of optical properties of CuO NPs and ZnO NPs green synthesized at different calcination temperatures.

Nanomaterials	Parameters					Wavelength (nm)	Energy bandgap (eV)
	MLE concentrations (g/mL)	Calcination temperatures (°C)	Zn precursor loadings (g)	Cu precursor loadings (g)	Zn-to-Cu ratios		
CuO NPs	0.05	200	-	2.0	-	344	3.41
	0.05	300	-	2.0	-	378	3.30
	0.05	400	-	2.0	-	376	3.26
	0.05	500	-	2.0	-	367	3.14
	0.05	600	-	2.0	-	522	3.23
ZnO NPs	0.04	200	4.0	-	-	368	3.46
	0.04	300	4.0	-	-	367	3.37
	0.04	400	4.0	-	-	368	3.27
	0.04	500	4.0	-	-	373	2.80
	0.04	600	4.0	-	-	372	2.79

Table 4.2: Summarization of optical properties of ZnO-CuO NCs green synthesized at different conditions.

Nanomaterials	Parameters					Wavelength (nm)	Energy bandgap (eV)
	MLE concentrations (g/mL)	Calcination temperatures (°C)	Zn precursor loadings (g)	Cu precursor loadings (g)	Zn-to-Cu ratios		
ZnO-CuO NCs	0.01	500	2.8	1.2	70:30	344	3.60
	0.02	500	2.8	1.2	70:30	374	3.31
	0.03	500	2.8	1.2	70:30	375	2.70
	0.04	500	2.8	1.2	70:30	373	2.61
	[1]0.05	500	2.8	1.2	70:30	373	2.57
	0.05	200	2.8	1.2	70:30	369	3.44
	0.05	300	2.8	1.2	70:30	369	3.31
	0.05	400	2.8	1.2	70:30	372	3.27
	0.05	[1]500	2.8	1.2	70:30	373	2.57
	0.05	600	2.8	1.2	70:30	373	2.08
	0.05	500	3.2	0.8	80:20	371	2.69
	0.05	500	2.8	1.2	[1]70:30	373	2.57

[1]ZnO-CuO NCs green synthesized in same conditions.

Continue

Nanomaterials	Parameters					Wavelength (nm)	Energy bandgap (eV)
	MLE concentrations (g/mL)	Calcination temperatures (°C)	Zn precursor loadings (g)	Cu precursor loadings (g)	Zn-to-Cu ratios		
ZnO-CuO NCs	0.05	500	2.4	1.6	60:40	371	2.57
	0.05	500	2.0	2.0	50:50	373	2.77

[1]ZnO-CuO NCs green synthesized in same conditions.

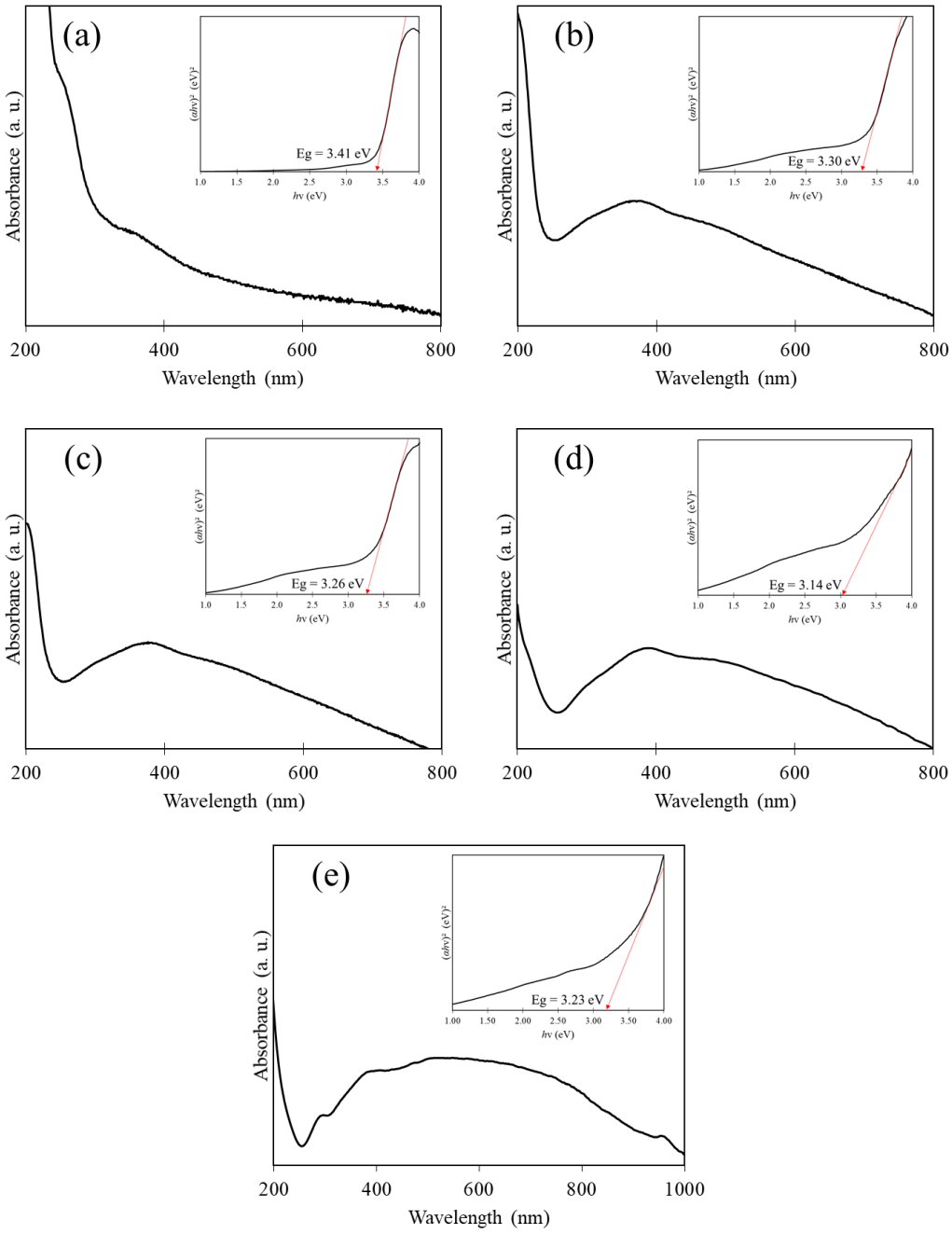

Figure 4.2: UV-Vis and Tauc's plot approach spectra of CuO NPs green synthesized calcinated (a) 200°C, (b) 300°C, (c) 400°C, (d) 500°C and (e) 600°C for 2 h using 0.05 g/mL of MLE.

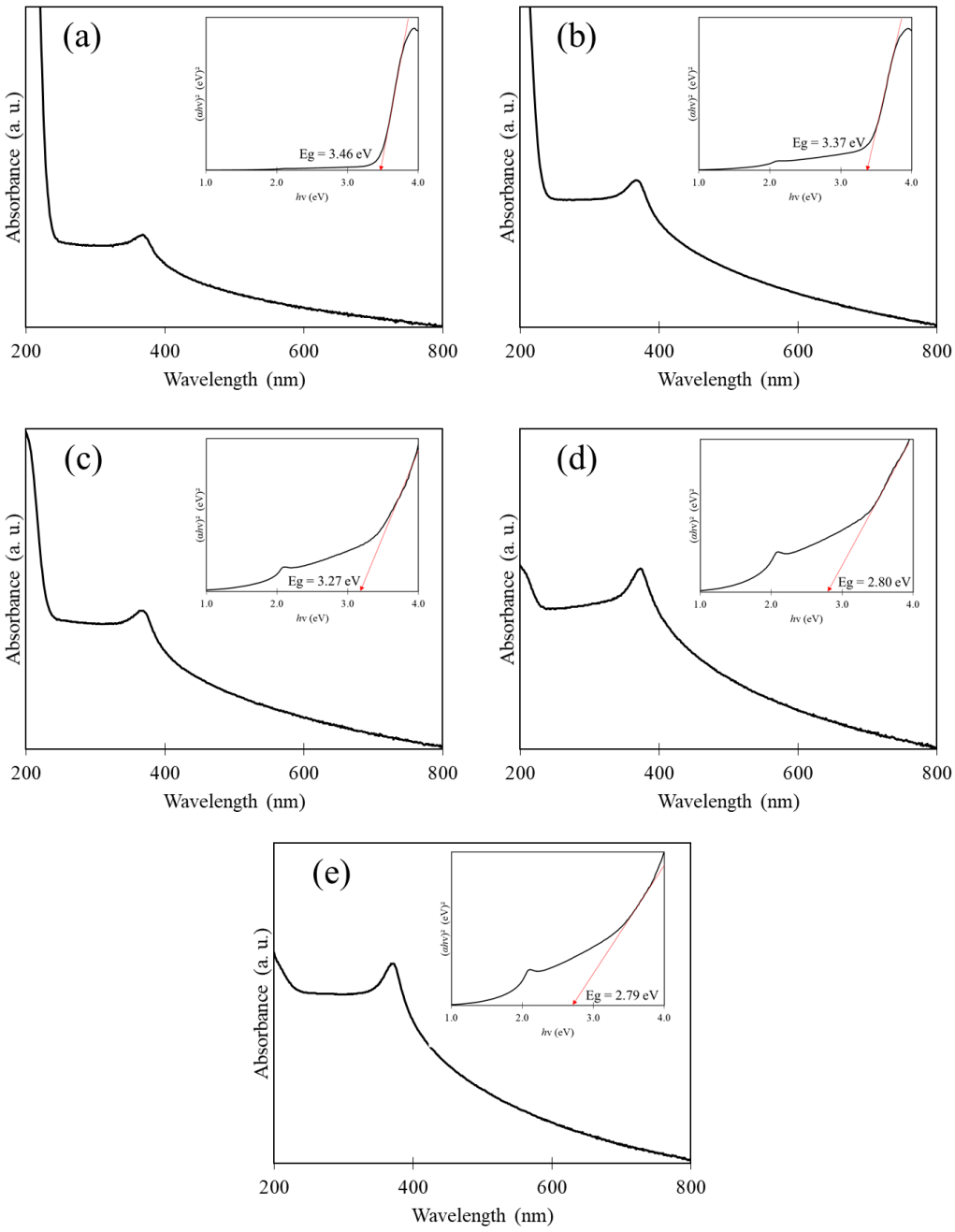

Figure 4.3: UV-Vis and Tauc's plot approach spectra of ZnO NPs green synthesized calcinated (a) 200°C, (b) 300°C, (c) 400°C, (d) 500°C and (e) 600°C for 2 h using 0.04 g/mL of MLE.

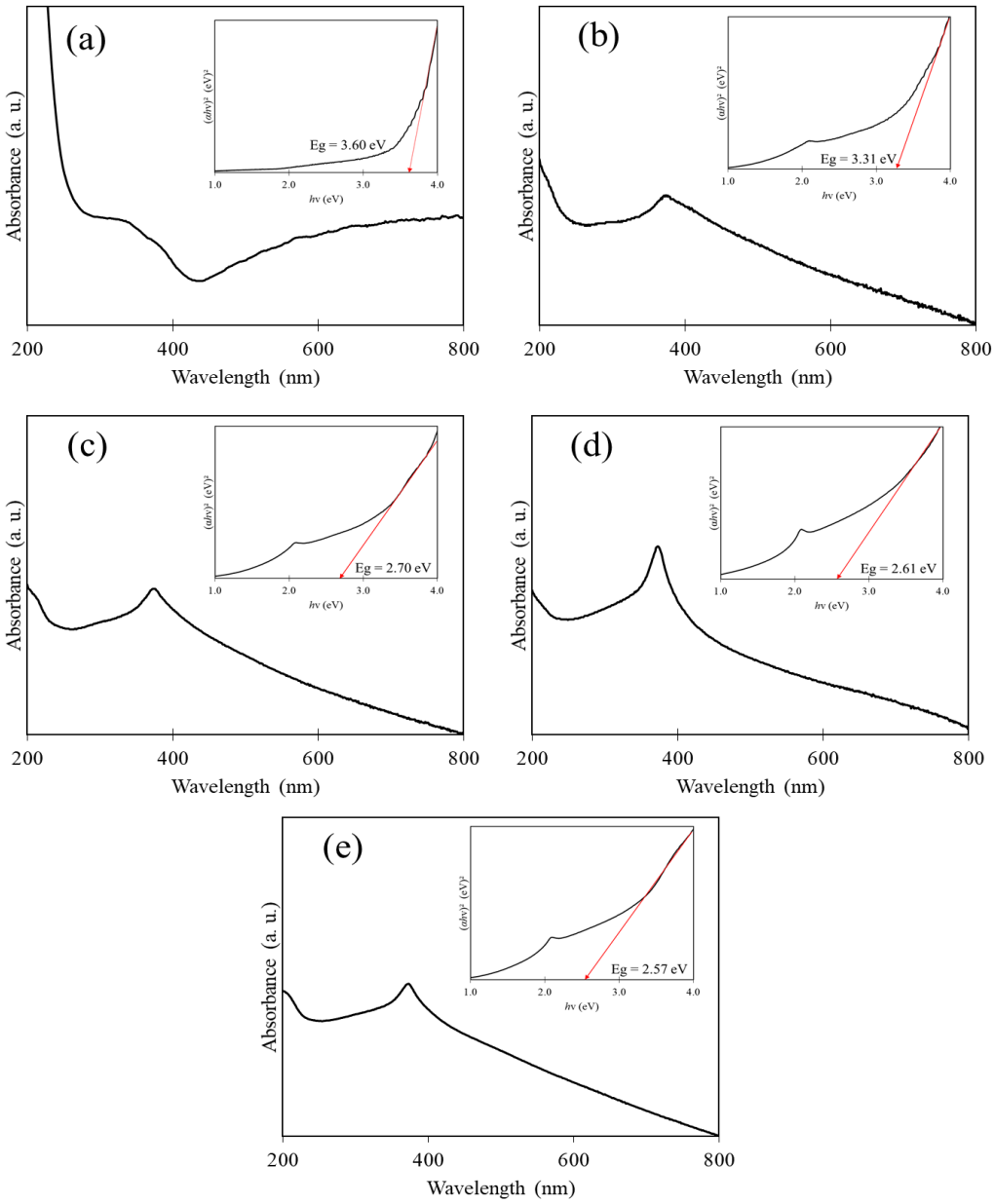

Figure 4.4: UV-Vis and Tauc's plot approach spectra of 70ZnO-30CuO NCs green synthesized using (a) 0.01 g/mL, (b) 0.02 g/mL, (c) 0.03 g/mL, (d) 0.04 g/mL and (e) 0.05 g/mL of MLE calcinated at 500°C for 2 h.

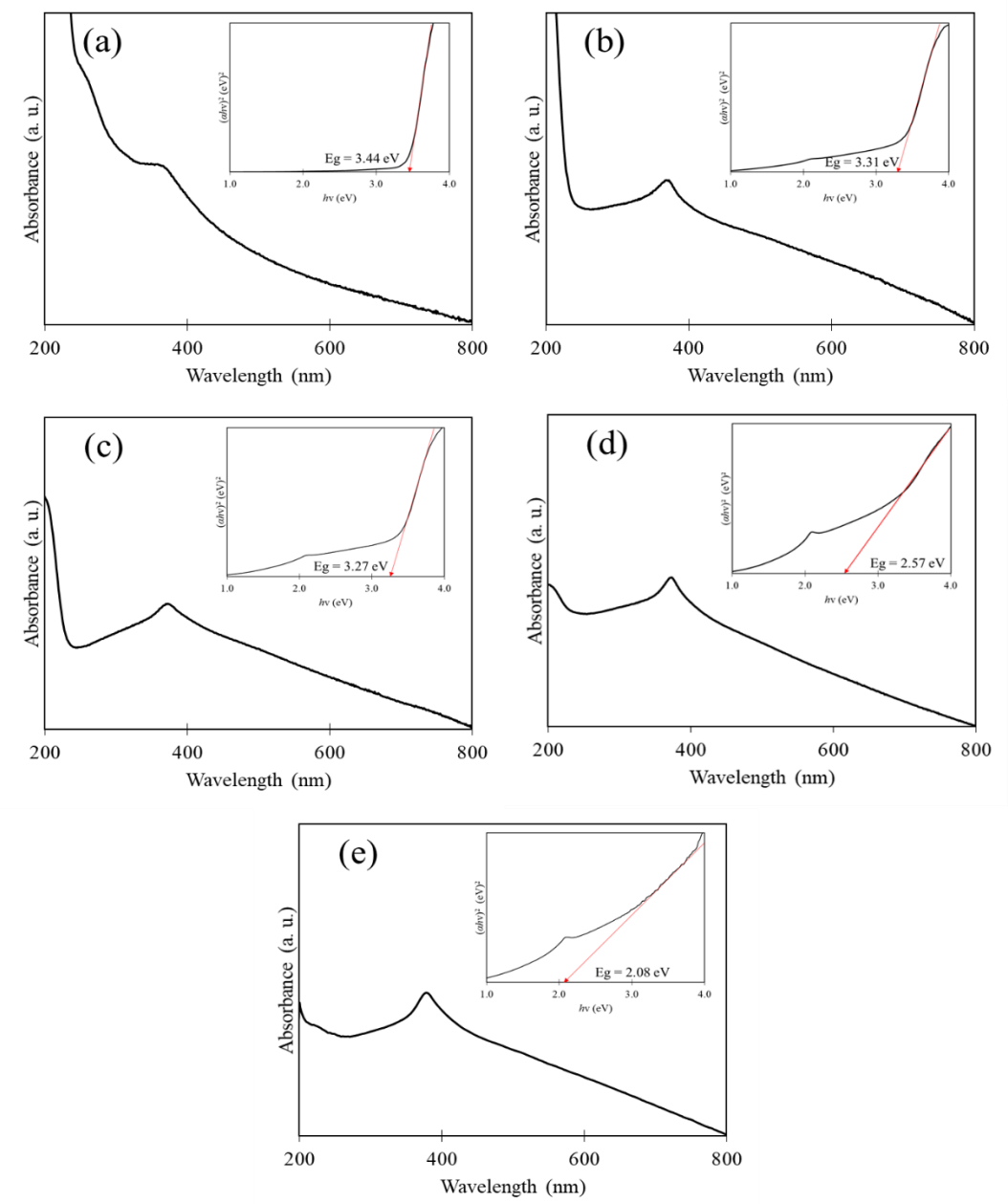

Figure 4.5: UV-Vis and Tauc's plot approach spectra of 70ZnO-30CuO NCs green synthesized using (a) 200ºC, (b) 300ºC, (c) 400ºC, (d) 500ºC and (e) 600ºC of 0.05 g/mL of MLE calcinated for 2 h.

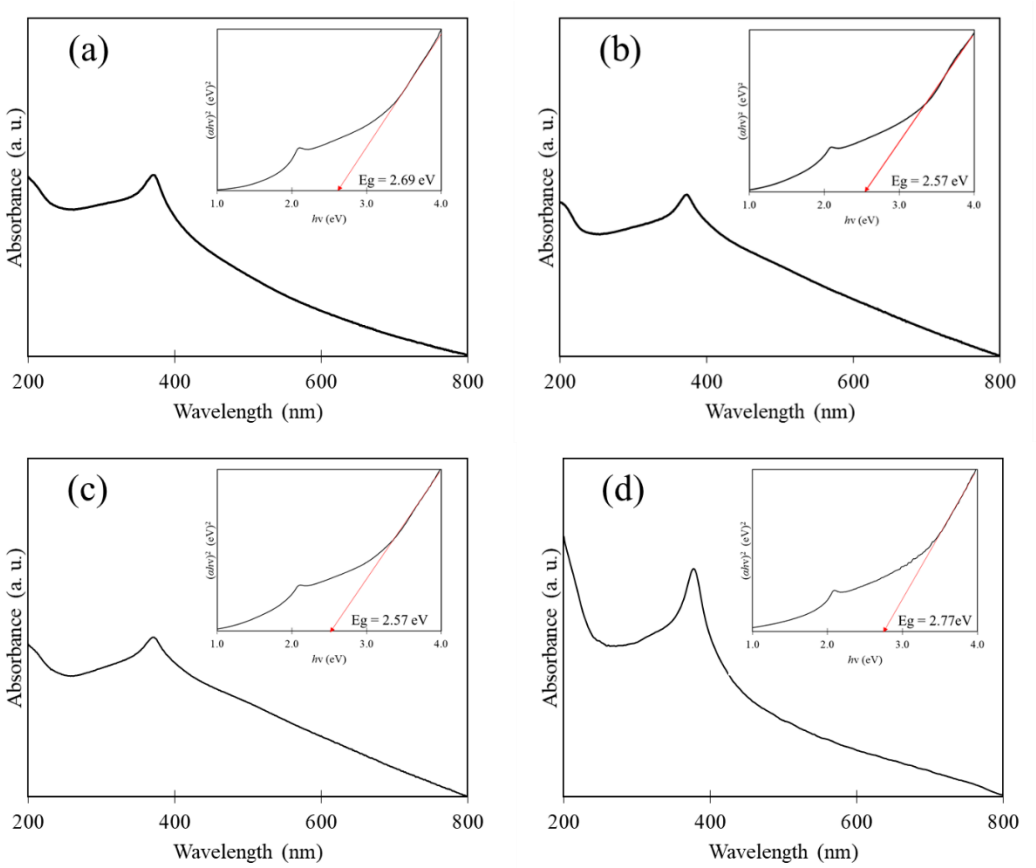

Figure 4.6: UV-Vis and Tauc's plot approach spectra of ZnO-CuO NCs green synthesized using (a) 80:20, (b) 70:30, (c) 60:40 and (d) 50:50 of ZnO-to-CuO ratio using 0.05 g/mL of MLE calcinated at 500ºC for 2 h.

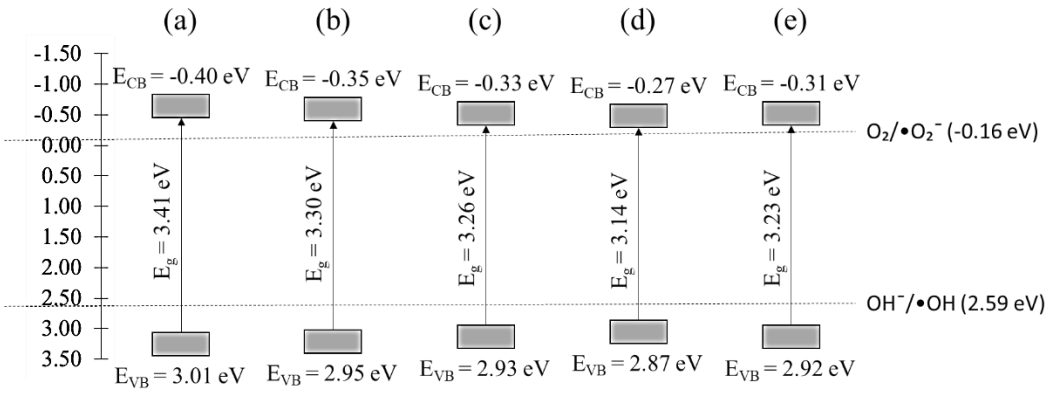

Figure 4.7: Calculated E_{CB} and E_{VB} (against NHE) of CuO NPs green synthesized calcinated (a) 200ºC, (b) 300ºC, (c) 400ºC, (d) 500ºC and (e) 600ºC for 2 h using 0.05 g/mL of MLE.

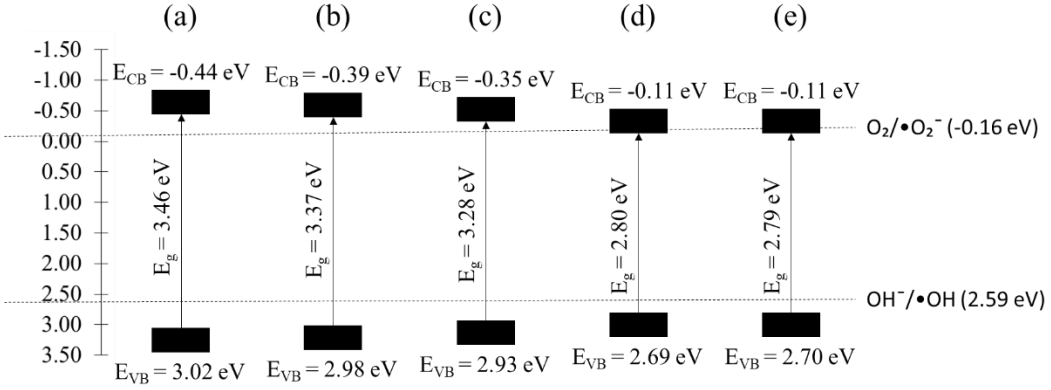

Figure 4.8: Calculated E_{CB} and E_{VB} (against NHE) of ZnO NPs green synthesized calcinated (a) 200ºC, (b) 300ºC, (c) 400ºC, (d) 500ºC and (e) 600ºC for 2 h using 0.04 g/mL of MLE.

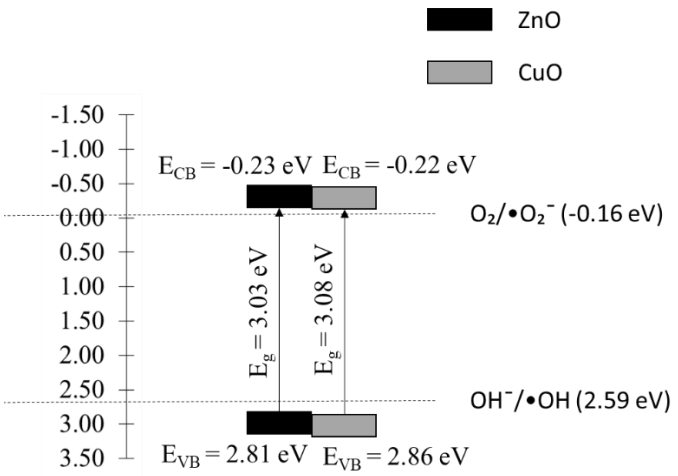

Figure 4.9: Calculated E_{CB} and E_{VB} (against NHE) of 70ZnO-30CuO NCs green synthesized using 0.05 g/mL of MLE calcinated at 500°C for 2 h.

4.1.2 FT-IR Analysis

The detected MLE's functional groups was shown in **Table 4.3**, while its FT-IR spectrum was shown in **Figure 4.10**. The 3410 cm^{-1} and 2929 cm^{-1} were corresponded to *v*(O-H) and *v*(C-H sp^3) bands, respectively. Moreover, 1731 cm^{-1} and 1619 cm^{-1} were corresponded to *v*(C=O) and *v*(C=C) bands, respectively. Furthermore, 1526 cm^{-1} and 1444 cm^{-1} were corresponded to *v*(C=C aromatic) and *v*($C-H_2$) bands, respectively. Besides, 1375 cm^{-1} and 1314 cm^{-1} were corresponded to *v*($C-H_3$) and *v*(O-H) bands, respectively. The 1284 cm^{-1}, 1246 cm^{-1}, 1203 cm^{-1}, 1158 cm^{-1}, 1105 cm^{-1} and 1062 cm^{-1} were corresponded to *v*(C-O-C) bands. Meanwhile, 894 cm^{-1}, 821 cm^{-1} and 780 cm^{-1} were corresponded to *v*(C-H).

Table 4.3: Summarization of functional group bands' locations of MLE.

Functional group	Compound class	Band location (cm^{-1})
v(O-H)	Alcohols, phenols, carboxylic acids,	3410
v(C-H sp^3)	Alkanes	2929
v(C=O)	Carbonyl groups	1731
v(C=C)	Alkenes	1619
v(C=C aromatic)	Polyphenols skeletal	1526
v(C-H_2)	Alkanes	1444
v(C-H_3)	Alkanes	1375
v(O-H)	Phenols	1314
v(C-O-C)	Aromatic esters	1284
v(C-O-C)	Alkyl aryl ethers	1246
v(C-O-C)	Alkyl aryl ethers	1203
v(C-O-C)	Ethers or esters	1158
v(C-O-C)	Ethers or esters	1105
v(C-O-C)	Ethers or esters	1062
v(C-H)	1,3-disubstituted	894
v(C-H)	1,4-disubstituted	821
v(C-H)	1,2,3-trisubstituted	780

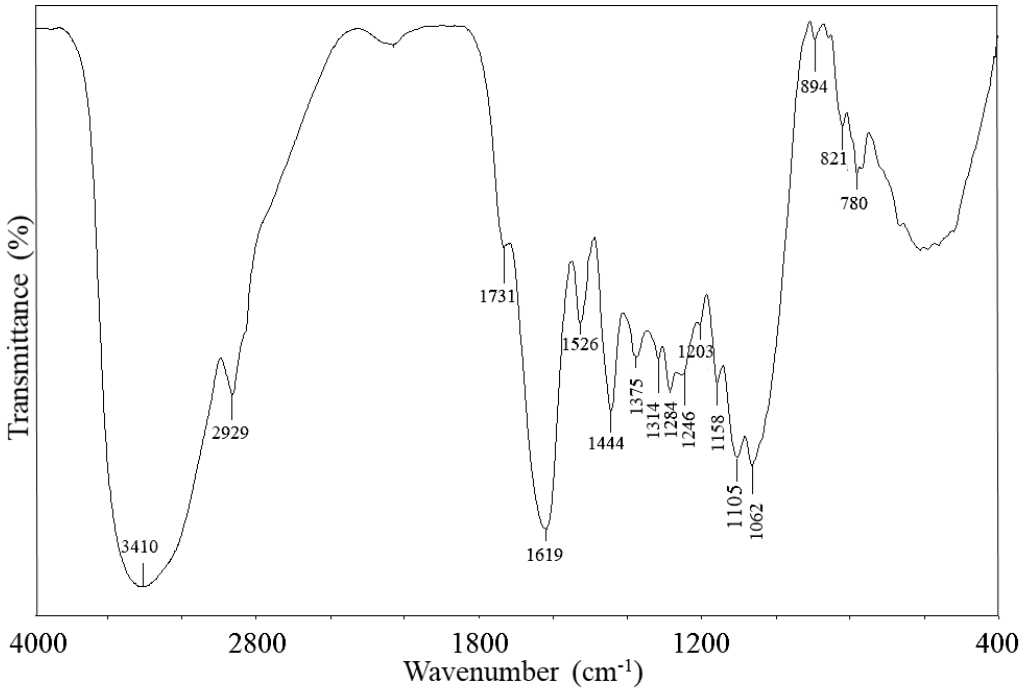

Figure 4.10: FT-IR spectrum of MLE.

Functional groups' bands location detected on the surface of nanomaterials was summarized in **Table 4.4** and **Table 4.5**. On the other hand, the FT-IR spectra of synthesized nanomaterials were shown in **Figures 4.11 – 4.15**. The 3392 – 3436 cm^{-1} and 1628 – 1640 cm^{-1} were corresponded to *v*(O-H) and *v*(C=C) bands, respectively. Moreover, bands located at 1383 – 1384 cm^{-1} and 1104 – 1124 cm^{-1} were corresponded to *v*(C-H_3) and *v*(C-O-C), respectively. Specifically, CuO NPs calcinated at 200^{o}C had the extra bands located at 2341 cm^{-1}, 1422 cm^{-1}, 1317 cm^{-1}, 1046 cm^{-1} and 814 cm^{-1} which were corresponded to *v*(O=C=O), *v*(C-H_2), *v*(O-H), *v*(C-O) and *v*(C-H) bands, respectively. Moreover, 1048 cm^{-1} was corresponded to *v*(C-O) band in CuO NPs calcinated at 600^{o}C. On the other hand, 70ZnO-30CuO NCs green synthesized using 0.01 g/mL MLE calcinated at 500^{o}C had a split bands located at 1618 cm^{-1} which was corresponded to *v*(C=C) with its FT-IR spectrum

dropped off at the percentage of transmittance. Furthermore, 70ZnO-30CuO NCs green synthesized using 0.05 g/mL calcinated at 200^{o}C had the bands located at 2426 cm^{-1} and 2341 cm^{-1}, 1319 cm^{-1}, 1033 cm^{-1} and 1020 cm^{-1}, and 822 cm^{-1} and 723 cm^{-1} which were corresponded to *v*(O=C=O), *v*(O-H), *v*(C-O) and *v*(C-H), respectively.

Meanwhile, the *v*(M-O) bands of ZnO-CuO NCs (452 – 524 cm^{-1}) were in between CuO NPs (504 – 538 cm^{-1}) and ZnO NPs (455 – 460 cm^{-1}) . Particularly, *v*(M-O) band of ZnO-CuO NCs shifted to higher wavenumber when ratio of CuO in ZnO-CuO NCs increased.

The transmittance of *v*(C=C) and *v*(C-O-C) bands increased, while *v*(C-H_3) band's transmittance decreased on CuO NPs surface at elevated calcination temperature. However, ZnO NPs, transmittance of *v*(C-H_3) and *v*(C-O-C) dropped when the applied calcination temperature rose. On the other hand, on 70ZnO-30CuO NCs surface, transmittance of *v*(C-H_3) and *v*(C-O-C) bands increased as the applied MLE concentration increased. Meanwhile, its transmittance of *v*(C-H_3) band decreased while *v*(C-O-C) band increased at the elevated calcination temperature. Interestingly, transmittance of *v*(C-O-C) band decreased while *v*(C-H_3) band increased when CuO ratio in the ZnO-CuO NCs increased.

Table 4.4: Summarization of functional group bands' locations on the surface of CuO NPs and ZnO NPs green synthesized at different calcination temperatures.

Nanomaterials	Parameters					Wavenumber (cm^{-1})				
	MLE concentrations (g/mL)	Calcination temperatures (^oC)	Zn precursor loadings (g)	Cu precursor loadings (g)	Zn-to-Cu ratios	*v*(O-H)	*v*(C=C)	*v*(C-H_3)	*v*(C-O-C)	[3]*v*(M-O)
CuO NPs	0.05	[1]200	-	2.0	-	3436	1628	1384	1111	504
	0.05	300	-	2.0	-	3435	1633	1384	1096	536
	0.05	400	-	2.0	-	3413	1632	1384	1100	534
	0.05	500	-	2.0	-	3434	1634	1384	1099	538
	0.05	[2]600	-	2.0	-	3400	1633	1384	1097	536
ZnO NPs	0.04	200	4.0	-	-	3435	1633	1384	1120	455
	0.04	300	4.0	-	-	3431	1633	1384	1115	456
	0.04	400	4.0	-	-	3436	1634	1384	1124	456
	0.04	500	4.0	-	-	3435	1633	1384	1110	456
	0.04	600	4.0	-	-	3401	1633	1383	1113	460

[1]Also consists of *v*(O=C=O), *v*(C-H_2), *v*(O-H), *v*(C-O) and *v*(C-H) bands located at 2341 cm^{-1}, 1422 cm^{-1}, 1317 cm^{-1}, 1046 cm^{-1} and 814 cm^{-1}, respectively.
[2]Also consists of *v*(C-O) bands located at 1048 cm^{-1}.
[3]*v*(M-O) refers to Cu-O or Zn-O bond vibration, depends on the respective nanomaterials.

Table 4.5: Summarization of functional group bands' locations on the surface of ZnO-CuO NCs green synthesized at different conditions.

Nanomaterials	Parameters					Wavenumber (cm^{-1})				
	MLE concentrations (g/mL)	Calcination temperatures (^oC)	Zn precursor loadings (g)	Cu precursor loadings (g)	Zn-to-Cu ratios	*v*(O-H)	*v*(C=C)	*v*(C-H_3)	*v*(C-O-C)	[6]*v*(M-O)
ZnO-CuO NCs	[1]0.01	500	2.8	1.2	70:30	3410	1638	1383	-	489
	0.02	500	2.8	1.2	70:30	3436	1636	1384	1114	452
	0.03	500	2.8	1.2	70:30	3435	1636	1384	1108	455
	0.04	500	2.8	1.2	70:30	3435	1636	1384	1108	485
	[2]0.05	500	2.8	1.2	70:30	3435	1636	1384	1108	486
	0.05	[3]200	2.8	1.2	70:30	3434	1640	1384	1123	493
	0.05	300	2.8	1.2	70:30	3436	1633	1384	1099	498
	0.05	400	2.8	1.2	70:30	3435	1636	1384	1108	486
	0.05	[2]500	2.8	1.2	70:30	3435	1636	1384	1108	486
	0.05	600	2.8	1.2	70:30	3392	1633	1384	1104	514
	0.05	500	3.2	0.8	80:20	3400	1635	1384	1108	494

Continue

Nanomaterials	Parameters					Wavenumber (cm^{-1})				
	MLE concentrations (g/mL)	Calcination temperatures (^oC)	Zn precursor loadings (g)	Cu precursor loadings (g)	Zn-to-Cu ratios	*v*(O-H)	*v*(C=C)	*v*(C-H_3)	*v*(C-O-C)	[4]*v*(M-O)
ZnO-CuO NCs	0.05	500	2.8	1.2	[2]70:30	3435	1636	1384	1108	486
	0.05	500	2.4	1.6	60:40	3431	1636	1384	1106	513
	0.05	500	2.0	2.0	50:50	3401	1635	1384	1109	524

[1]Also consists of *v*(C=C) bands located at 1618 cm^{-1}.
[2]ZnO-CuO NCs green synthesized in same conditions.
[3]Also consists of *v*(O=C=O), *v*(O-H), *v*(C-O) and *v*(C-H) bands located at 2426 cm^{-1} and 2341 cm^{-1}, 1319 cm^{-1}, 1033 cm^{-1} and 1020 cm^{-1}, and 822 cm^{-1} and 723 cm^{-1}, respectively.
[4]*v*(M-O) refers to Zn-O-Cu bond vibration.

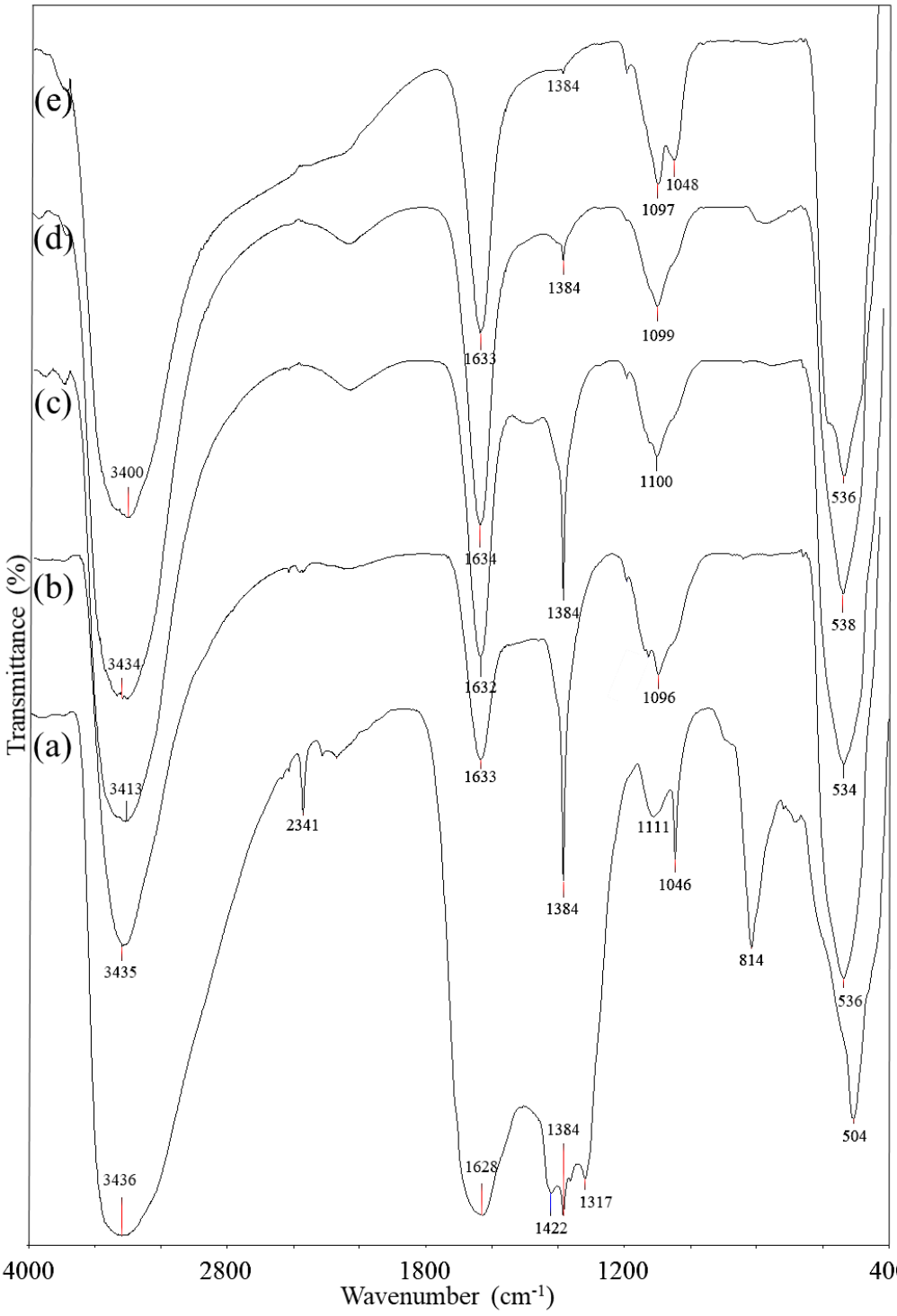

Figure 4.11: FT-IR spectra of CuO NPs green synthesized calcinated (a) 200^{o}C, (b) 300^{o}C, (c) 400^{o}C, (d) 500^{o}C and (e) 600^{o}C for 2 h using 0.05 g/mL of MLE.

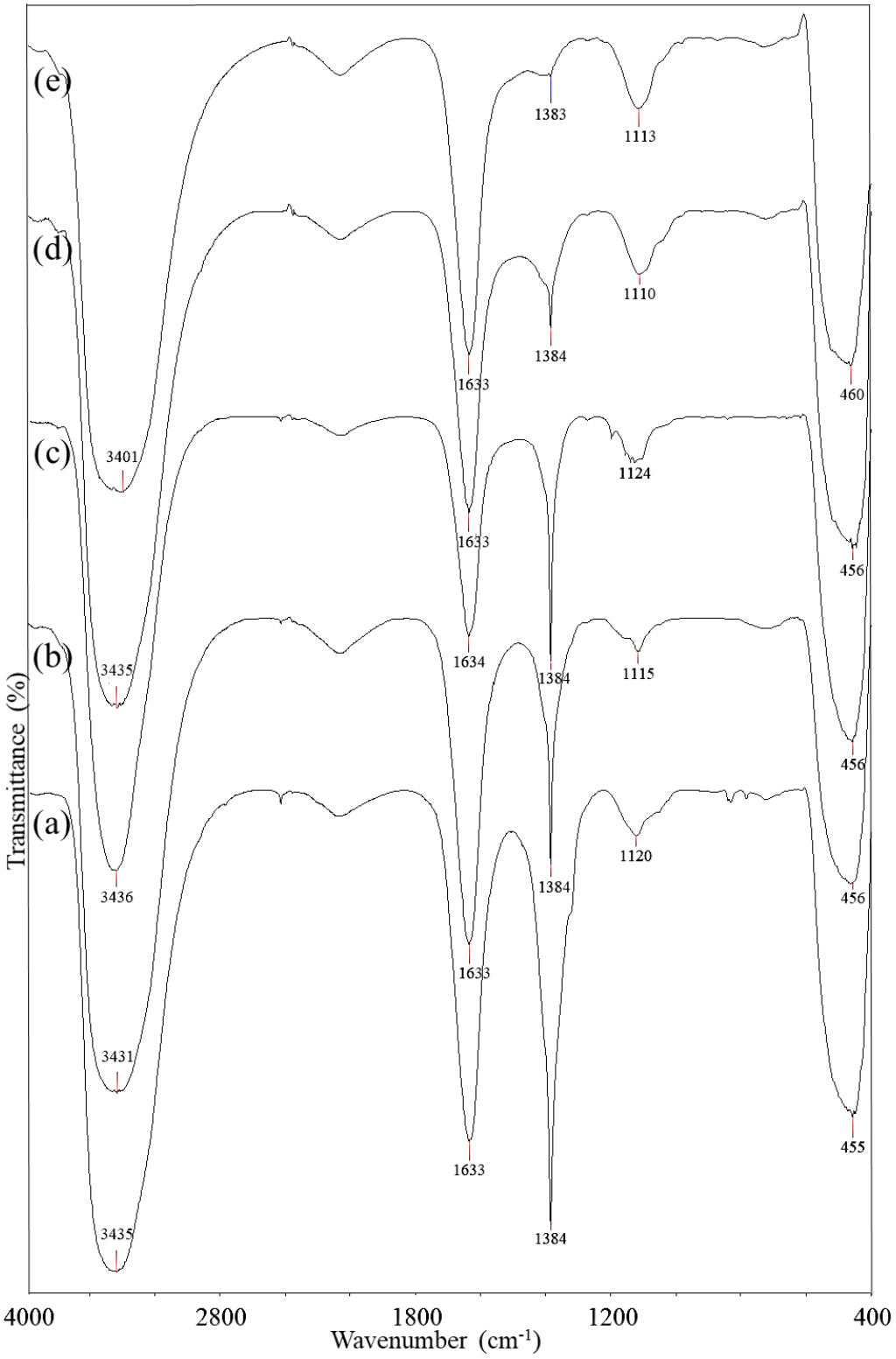

Figure 4.12: FT-IR spectra of ZnO NPs green synthesized calcinated (a) 200°C, (b) 300°C, (c) 400°C, (d) 500°C and (e) 600°C for 2 h using 0.04 g/mL of MLE.

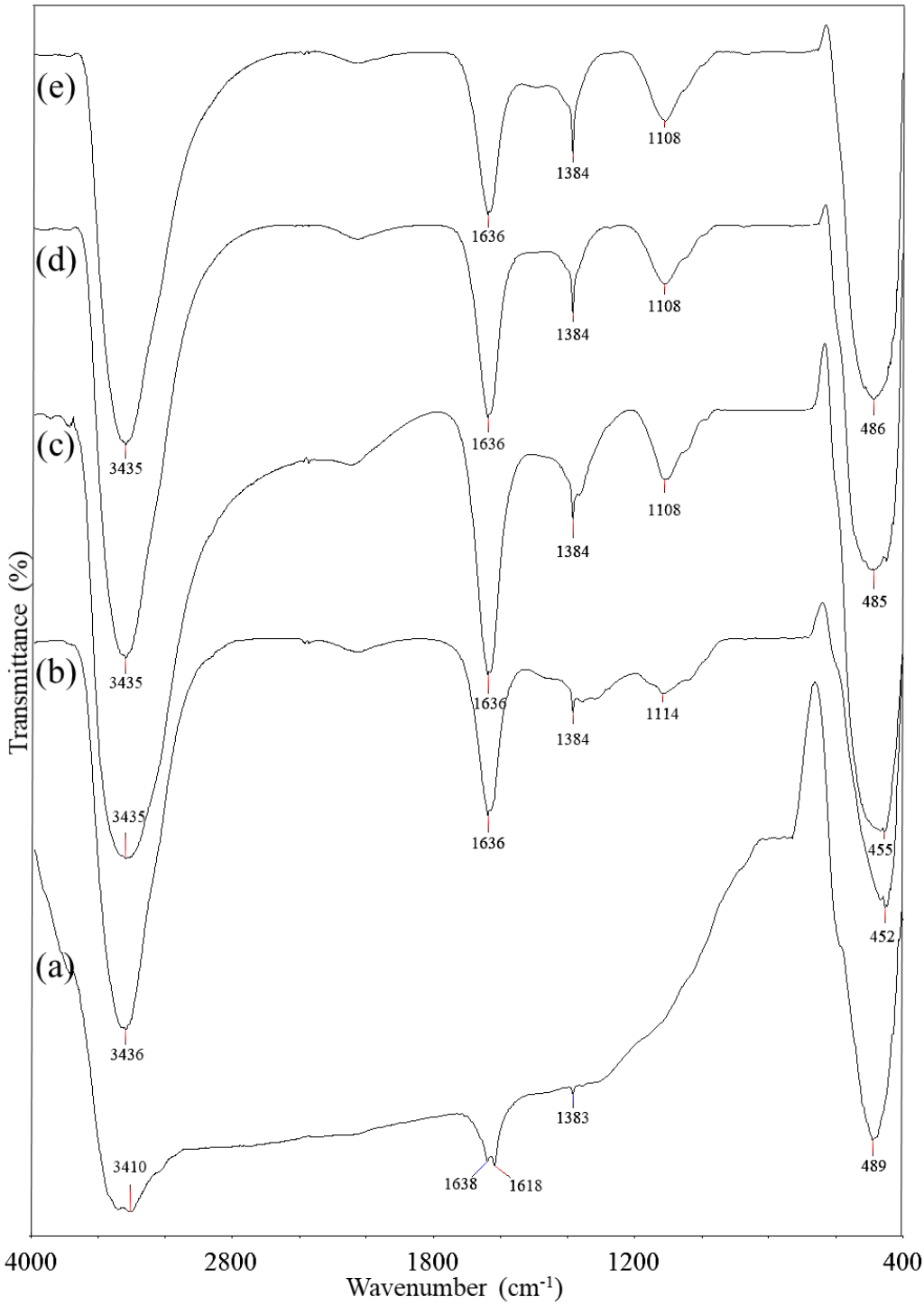

Figure 4.13: FT-IR spectra of 70ZnO-30CuO NCs green synthesized using (a) 0.01 g/mL, (b) 0.02 g/mL, (c) 0.03 g/mL, (d) 0.04 g/mL and (e) 0.05 g/mL of MLE calcinated at 500^{o}C for 2 h.

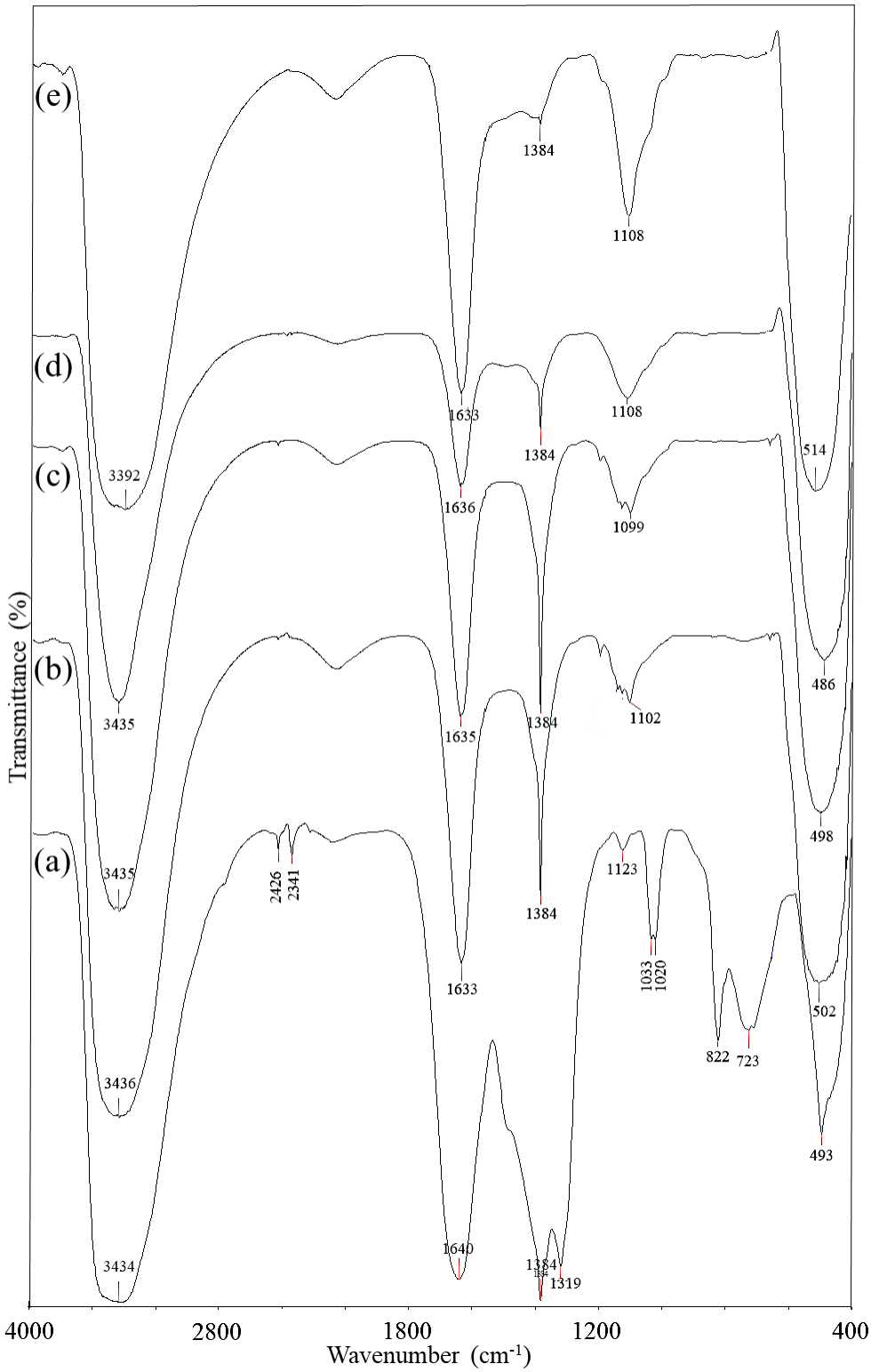

Figure 4.14: FT-IR spectra of 70ZnO-30CuO NCs green synthesized calcinated (a) 200ºC, (b) 300ºC, (c) 400ºC, (d) 500ºC and (e) 600ºC for 2 h using 0.05 g/mL of MLE.

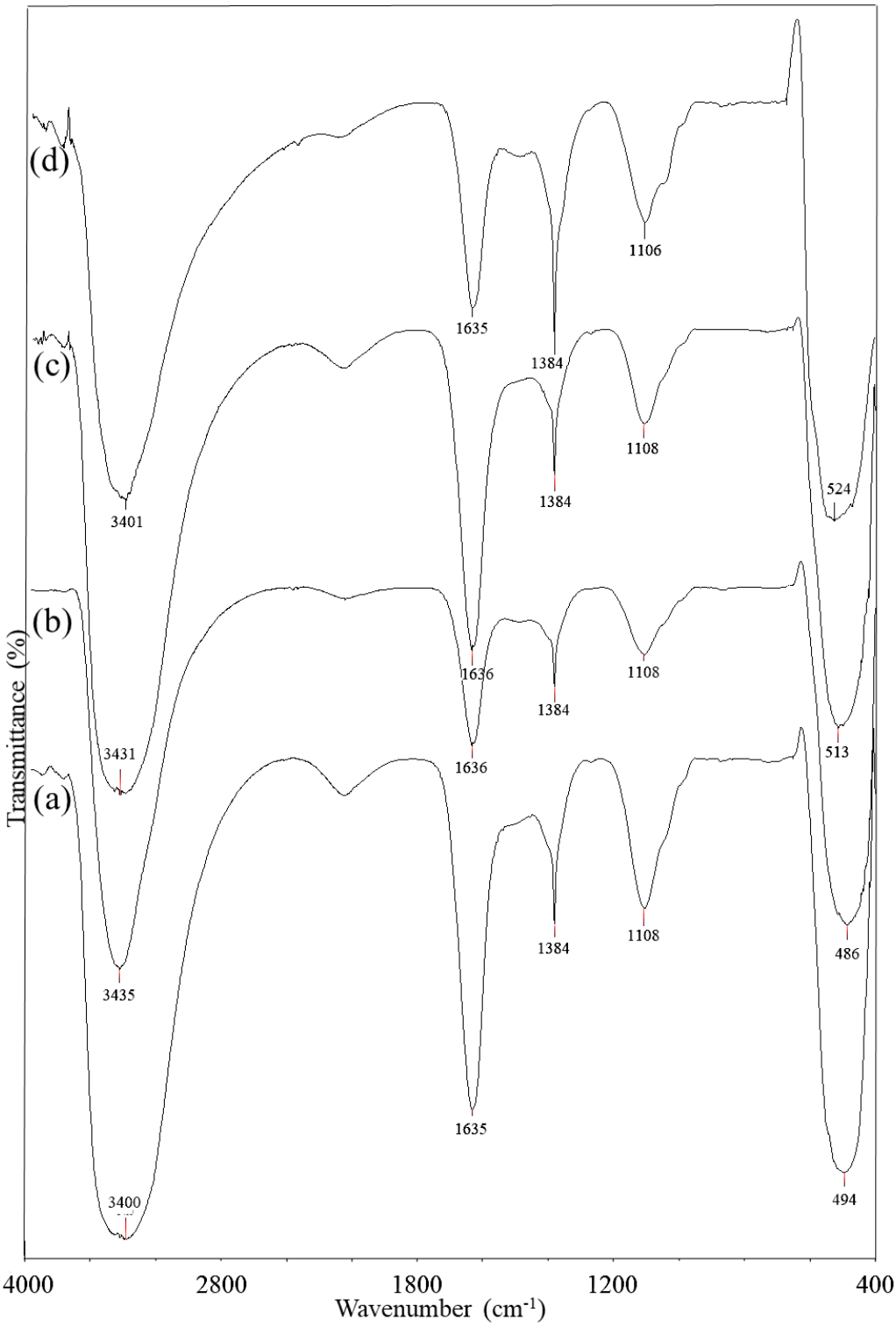

Figure 4.15: FT-IR spectra of ZnO-CuO NCs green synthesized using (a) 80:20, (b) 70:30, (c) 60:40 and (d) 50:50 of ZnO-to-CuO ratio using 0.05 g/mL of MLE calcinated at 500^{o}C for 2 h.

4.1.3 XRD Analysis

CuO NPs were in monoclinic-tenorite phase with their space group in C*2*/*c* and their unit cells at a = 4.6790Å, b = 3.4314Å and c = 5.1975Å. The CuO NPs were in good agreement with ICDD 00-045-0937 with the diffraction peaks at 2θ values of 3.246, 35.40, 38.48, 48.89, 61.46 and 67.90^{o}, indexed as (- 1 1 0), (0 0 2), (1 1 1), (-2 0 2), (-1 1 3), (0 0 2) and (-2 2 0), respectively (**Figure 4.16**). In contrast, ZnO NPs were in hexagonal-wurzite phase with their space group in P63*mc* and their unit cells at a = 3.2459Å and c = 5.1975Å. The ZnO NPs were in good agreement with ICDD 01-079-0208 with the diffraction peaks at 2θ values of 31.62, 34.30, 36.11, 47.25, 56.33, 62.61, 67.90 and 68.97^{o}, indexed as (1 0 0), (0 0 2), (1 0 1), (1 0 2), (1 1 0), (1 0 3), (1 1 2) and (2 0 1), respectively (**Figure 4.17**). Similar to ZnO NPs, 70ZnO-30CuO NCs were in hexagonal-wurzite phase with their space group in P63*mc* and their unit cells at a = 3.2459Å and c = 5.1975Å. The 70ZnO-30CuO NCs were in good agreement with ICDD 01-081-9217. The diffraction peaks at 2θ values of 31.74, 34.41, 36.22, 47.57, 56.58, 62.90, 68.01 and 69.03^{o} matched with ZnO phase indexed as (1 0 0), (0 0 2), (1 0 1), (1 0 2), (1 1 0), (1 0 3), (1 1 2) and (2 0 1), respectively. On the other hand, those 2θ values of 32.60, 35.58, 38.80, 4859, 61.57, 66.30 and 68.01^{o} matched with CuO phase were indexed as (-1 1 0), (0 0 2), (1 1 1), (-2 0 2), (-1 1 3), (0 2 2) and (-2 2 0), respectively (**Figures 4.18 – 4.20**).

The peaks became sharper and more intense as the less concentrated MLE and elevated calcination temperature applied during the green synthesis of

nanomaterials. Moreover, XRD patterns' were more well-defined, intense and narrow diffraction peaks when using less concentrated MLE in green synthesizing 70ZnO-30CuO NCs at 500^{o}C. Meanwhile, the XRD patterns of ZnO-CuO NCs did not affected by their CuO ratio. Among the detected peaks in XRD patterns, intensities of (0 0 2) and (1 1 1) peaks' intensities in CuO NPs, whereas (1 0 0), (0 0 2) and (1 0 1) peaks in ZnO NPs, were found stronger than other. For ZnO-CuO NCs, ZnO phase intensities of (1 0 0), (0 0 2) and (1 0 1) peaks were found stronger than other peaks. Meanwhile, their CuO phase intensities of (-1 1 0) and (0 0 2) were improved when higher calcination temperature or ratio of Cu was applied.

As shown in **Table 4.6**, CuO NPs crystalline size increased (from 13.42 nm to 29.50 nm) when higher calcination temperature applied. In contrast, the crystalline sizes of ZnO NPs decreased (from 17.77 nm to 16.67 nm) when higher calcination temperature applied. However, there was an increased in crystalline size when ZnO NPs calcinated at 300^{o}C, 400^{o}C and 500^{o}C. Similar results were obtained for 70ZnO-CuO NCs (**Table 4.7**) green synthesized at higher MLE concentrations (from 35.21 nm to 18.17 nm) and calcination temperatures (from 28.27 nm to 18.17 nm). But, its crystalline size increased when 70ZnO-30CuO NCs calcinated at 600^{o}C using 0.05 g/mL of MLE. On the other hand, Cu ratio in ZnO-CuO NCs did not significantly affect their crystalline sizes (20.66 – 22.31 nm), except for 70ZnO-30CuO NCs had the smallest (18.17 nm).

Dislocation density and micro strain calculated form nanomaterials were in opposite trend to their crystalline sizes, as shown in **Table 4.6** and **Table 4.7**.

Table 4.6: Summarization of crystalline properties of CuO NPs and ZnO NPs green synthesized at different calcination temperatures.

Nanomaterials	Parameters					Crystalline properties		
	MLE concentrations (g/mL)	Calcination temperatures (^oC)	Zn precursor loadings (g)	Cu precursor loadings (g)	Zn-to-Cu ratios	Crystalline size (nm)	Dislocation density ($\times 10^{14}$ cm^{-1})	Micro strain ($\times 10^{-4}$)
CuO NPs	0.05	200	-	2.0	-	13.42	96.29	3.14
	0.05	300	-	2.0	-	14.39	57.66	2.55
	0.05	400	-	2.0	-	18.60	32.42	1.94
	0.05	500	-	2.0	-	19.55	29.18	1.84
	0.05	600	-	2.0	-	29.50	12.47	1.21
ZnO NPs	0.04	200	4.0	-	-	17.77	34.13	2.00
	0.04	300	4.0	-	-	16.71	38.62	2.13
	0.04	400	4.0	-	-	16.79	38.98	2.13
	0.04	500	4.0	-	-	16.99	36.54	2.08
	0.04	600	4.0	-	-	16.67	37.65	2.11

Table 4.7: Summarization of crystalline properties of ZnO-CuO NCs green synthesized at different conditions.

Nanomaterials	Parameters					Crystalline properties		
	MLE concentrations (g/mL)	Calcination temperatures (^oC)	Zn precursor loadings (g)	Cu precursor loadings (g)	Zn-to-Cu ratios	Crystalline size (nm)	Dislocation density ($\times 10^{14}$ cm^{-1})	Micro strain ($\times 10^{-4}$)
ZnO-CuO NCs	0.01	500	2.8	1.2	70:30	35.21	10.48	1.08
	0.02	500	2.8	1.2	70:30	28.51	17.05	1.35
	0.03	500	2.8	1.2	70:30	26.95	15.00	1.32
	0.04	500	2.8	1.2	70:30	25.32	16.81	1.40
	[1]0.05	500	2.8	1.2	70:30	18.17	161.37	2.77
	0.05	200	2.8	1.2	70:30	28.27	43.73	1.97
	0.05	300	2.8	1.2	70:30	22.25	25.35	1.69
	0.05	400	2.8	1.2	70:30	20.23	30.90	1.86
	0.05	[1]500	2.8	1.2	70:30	18.17	161.37	2.77
	0.05	600	2.8	1.2	70:30	22.25	20.85	1.57
	0.05	500	3.2	0.8	80:20	22.31	23.33	1.63

[1]ZnO-CuO NCs green synthesized in same conditions.

Continue

Nanomaterials	Parameters					Crystalline properties		
	MLE concentrations (g/mL)	Calcination temperatures (^{o}C)	Zn precursor loadings (g)	Cu precursor loadings (g)	Zn-to-Cu ratios	Crystalline size (nm)	Dislocation density ($\times 10^{14}$ cm^{-1})	Micro strain ($\times 10^{-4}$)
ZnO-CuO NCs	0.05	500	2.8	1.2	[1]70:30	18.17	161.37	2.77
	0.05	500	2.4	1.6	60:40	20.66	29.35	1.80
	0.05	500	2.0	2.0	50:50	22.29	23.29	1.63

[1]ZnO-CuO NCs green synthesized in same conditions.

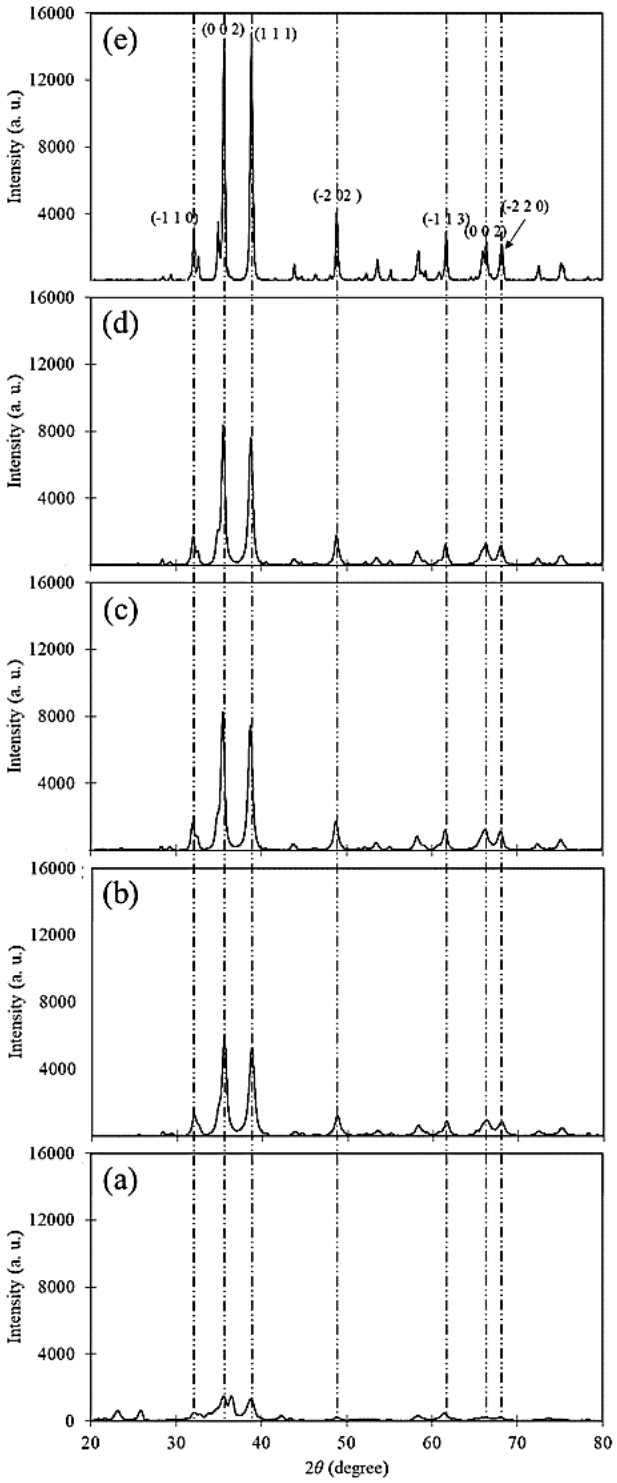

Figure 4.16: XRD patterns of CuO NPs green synthesized calcinated (a) 200ºC, (b) 300ºC, (c) 400ºC, (d) 500ºC and (e) 600ºC for 2 h using 0.05 g/mL of MLE. The Miller indexes were represented in (e).

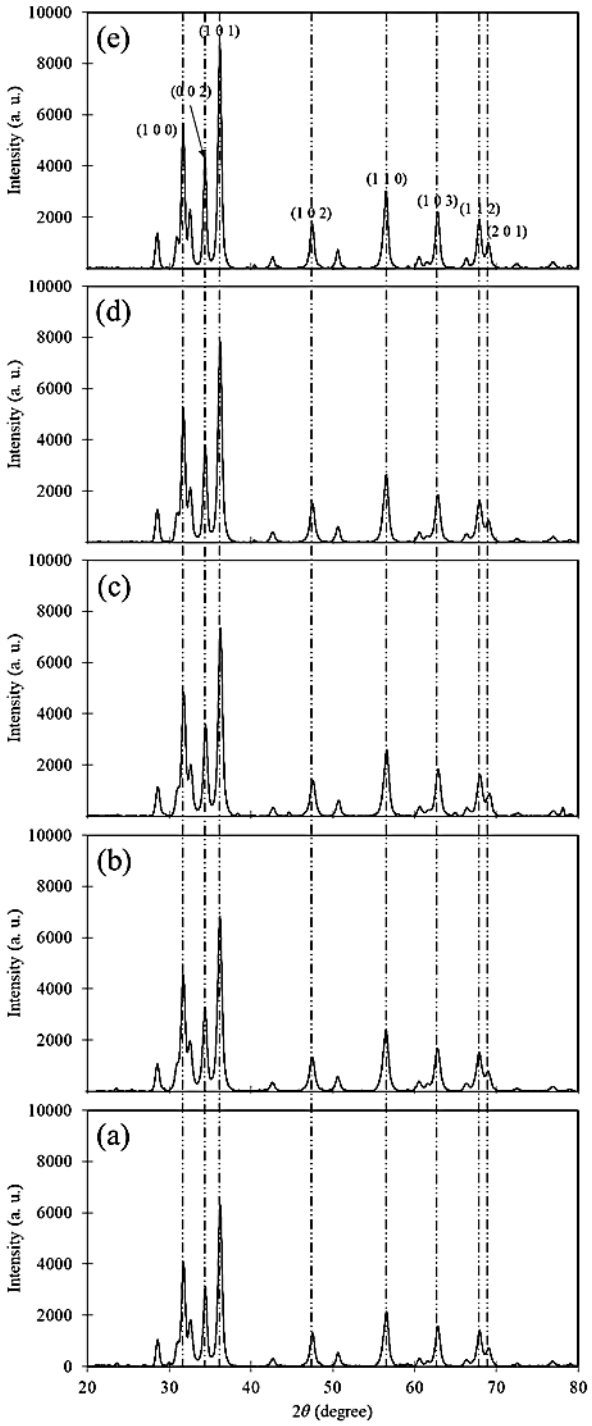

Figure 4.17: XRD patterns of ZnO NPs green synthesized calcinated (a) 200ºC, (b) 300ºC, (c) 400ºC, (d) 500ºC and (e) 600ºC for 2 h using 0.04 g/mL of MLE. The Miller indexes were represented in (e).

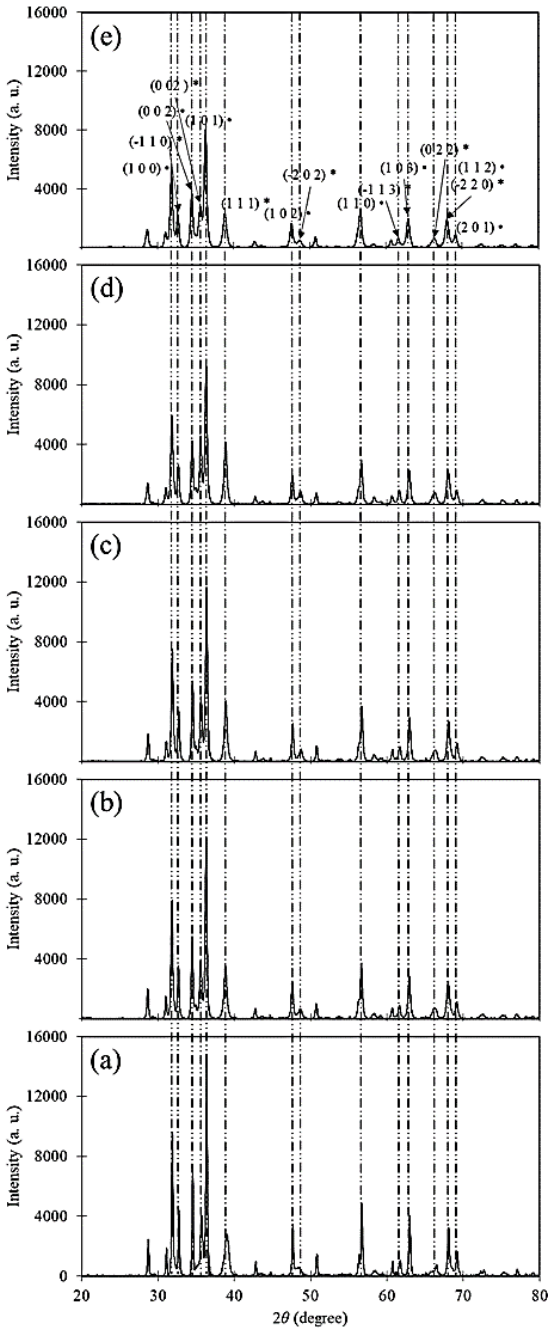

Figure 4.18: XRD pattern of 70ZnO-30CuO NCs green synthesized using (a) 0.01 g/mL, (b) 0.02 g/mL, (c) 0.03 g/mL, (d) 0.04 g/mL and (e) 0.05 g/mL of MLE calcinated at 500ºC for 2 h. The Miller indexes were represented in (e) and note that "•" represents ZnO diffraction peaks, while "*" represents CuO diffraction peaks.

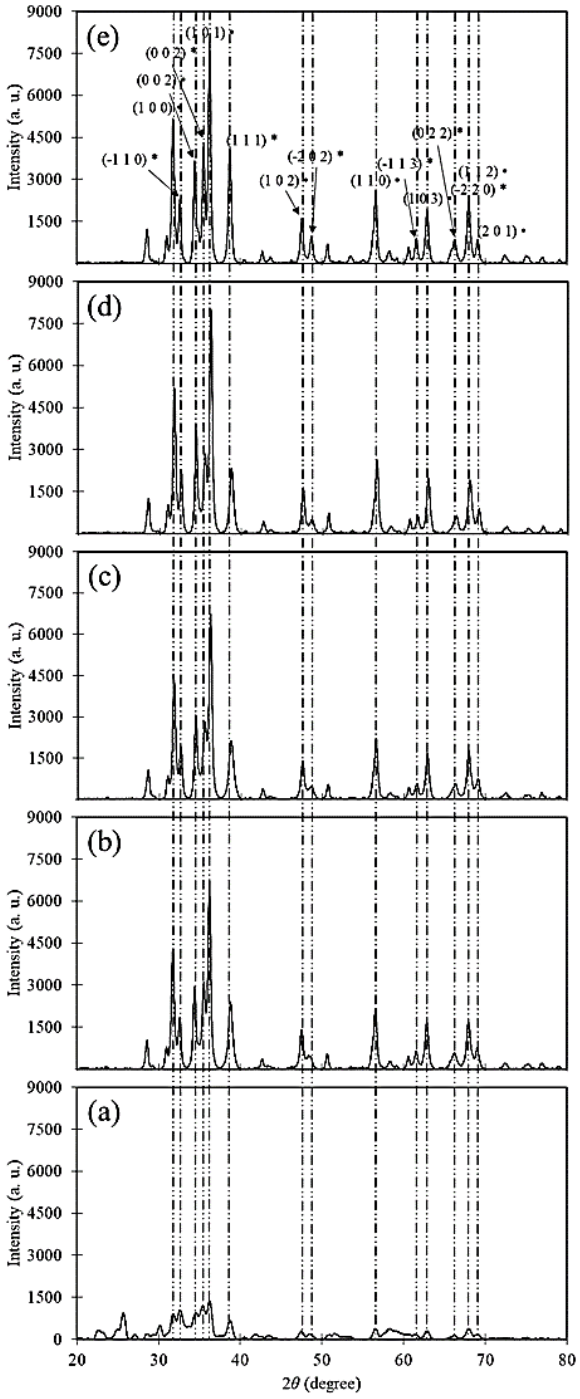

Figure 4.19: XRD patterns of 70ZnO-30CuO NCs green synthesized calcinated (a) 200ºC, (b) 300ºC, (c) 400ºC, (d) 500ºC and (e) 600ºC for 2 h using 0.05 g/mL of MLE. The Miller indexes were represented in (e) and note that "•" represents ZnO diffraction peaks, while "*" represents CuO diffraction peaks.

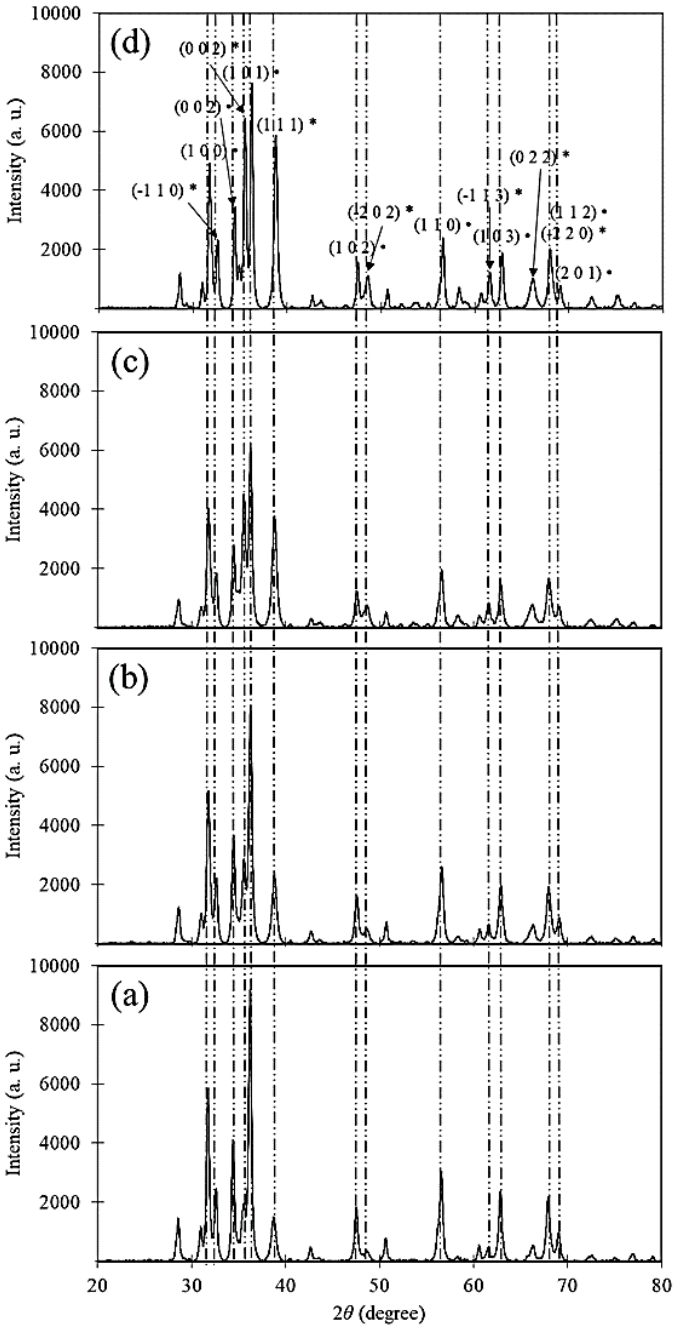

Figure 4.20: XRD patterns of ZnO-CuO NCs green synthesized using (a) 80:20, (b) 70:30, (c) 60:40 and (d) 50:50 of ZnO-to-CuO ratio using 0.05 g/mL of MLE calcinated at 500^{o}C for 2 h. The Miller indexes were represented in (d) and note that "•" represents ZnO diffraction peaks, while "*" represents CuO diffraction peaks.

4.1.4 FE-SEM with EDX and HR-TEM Analyses

Smooth spherical structure with agglomeration was observed in most nanomaterials at different synthesis conditions (**Table 4.8** and **Table 4.9**). Particularly, the nanomaterials became more spherical when higher MLE concentration or calcination temperature was applied. However, CuO NPs became bulky rectangular shaped when calcinated at 600^{o}C (**Figure 4.21**). Interestingly, porosity was found in ZnO NPs when higher calcination temperature was utilized (**Figure 4.22**). Nevertheless, 70ZnO-30CuO NCs forming spherical structure progressively when higher MLE concentration was applied (**Figure 4.23**). As shown in **Figure 4.24**, bulky structure was also found in 70ZnO-30CuO NCs calcinated at 600^{o}C by using 0.05 g/mL of MLE. In **Figure 4.25** shown that different ratios of Zn-to-Cu did not change the spherical structure of the ZnO-CuO NCs green synthesized by using 0.05 g/mL of MLE and calcinated at 500^{o}C.

Table 4.8: Summarization of morphological of CuO NPs and ZnO NPs green synthesized at different calcination temperatures.

Nanomaterials	Parameters					Morphologies
	MLE concentrations (g/mL)	Calcination temperatures (^oC)	Zn precursor loadings (g)	Cu precursor loadings (g)	Zn-to-Cu ratios	
CuO NPs	0.05	200	-	2.0	-	Flake
	0.05	300	-	2.0	-	Flake
	0.05	400	-	2.0	-	Quasi-spherical
	0.05	500	-	2.0	-	Spherical
	0.05	600	-	2.0	-	Mixture of spherical and bulky rectangular
ZnO NPs	0.04	200	4.0	-	-	Spherical
	0.04	300	4.0	-	-	Spherical
	0.04	400	4.0	-	-	Spherical
	0.04	500	4.0	-	-	Spherical
	0.04	600	4.0	-	-	Spherical

Table 4.9: Summarization of morphological of ZnO-CuO NCs green synthesized at different conditions.

Nanomaterials	Parameters					Morphologies
	MLE concentrations (g/mL)	Calcination temperatures (^oC)	Zn precursor loadings (g)	Cu precursor loadings (g)	Zn-to-Cu ratios	
ZnO-CuO NCs	0.01	500	2.8	1.2	70:30	Mixture of bulky and nano quasi-spherical
	0.02	500	2.8	1.2	70:30	Spherical
	0.03	500	2.8	1.2	70:30	Quasi-spherical
	0.04	500	2.8	1.2	70:30	Lobed
	[1]0.05	500	2.8	1.2	70:30	Spherical
	0.05	200	2.8	1.2	70:30	Irregular
	0.05	300	2.8	1.2	70:30	Quasi-spherical
	0.05	400	2.8	1.2	70:30	Spherical
	0.05	[1]500	2.8	1.2	70:30	Spherical
	0.05	600	2.8	1.2	70:30	Bulky spherical
	0.05	500	3.2	0.8	80:20	Mixture of spherical and robe

[1]ZnO-CuO NCs green synthesized in same conditions.

Continue

Nanomaterials	Parameters					Morphologies
	MLE concentrations (g/mL)	Calcination temperatures (^{o}C)	Zn precursor loadings (g)	Cu precursor loadings (g)	Zn-to-Cu ratios	
ZnO-CuO NCs	0.05	500	2.8	1.2	[1]70:30	Spherical
	0.05	500	2.4	1.6	60:40	Spherical
	0.05	500	2.0	2.0	50:50	Spherical

[1]ZnO-CuO NCs green synthesized in same conditions.

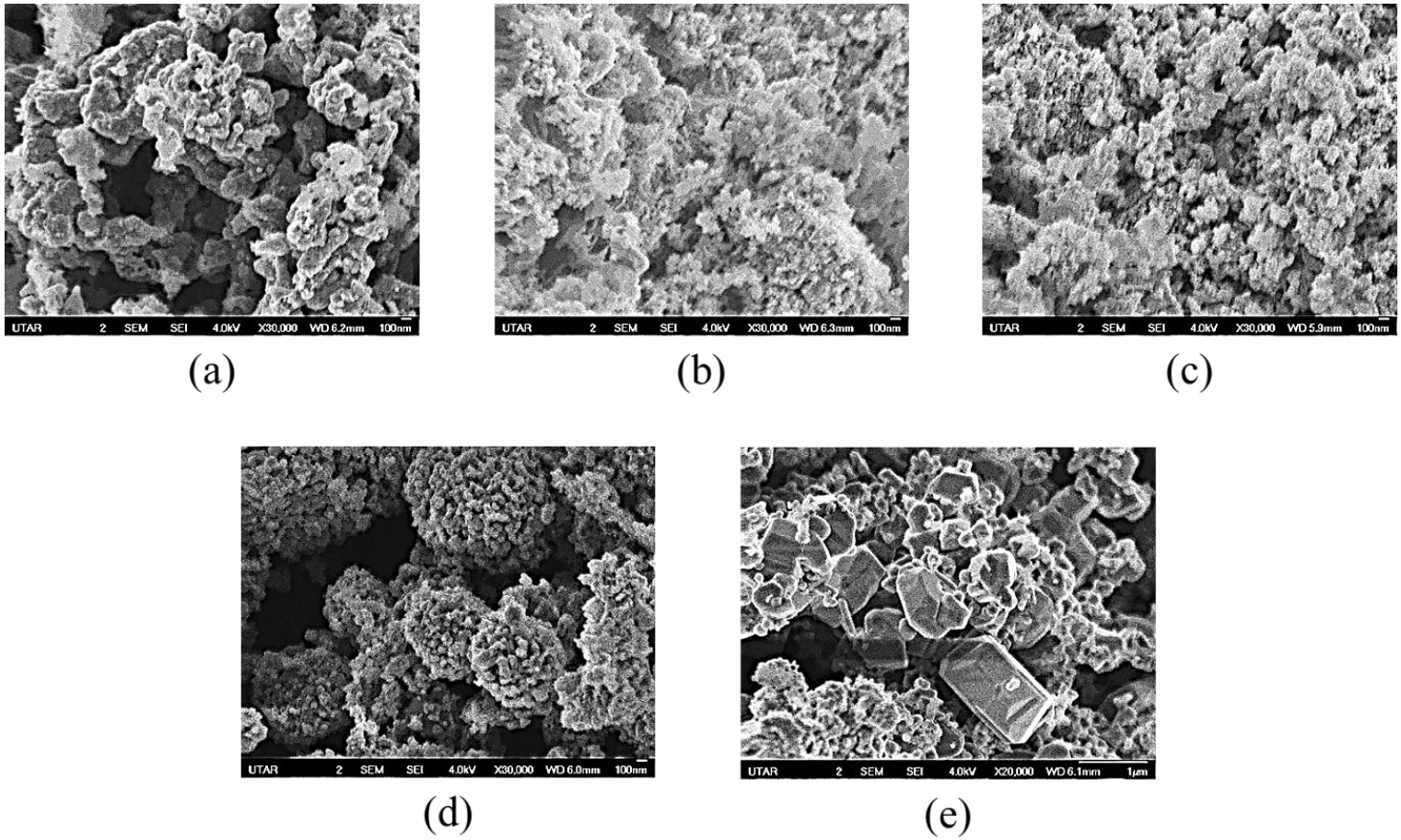

Figure 4.21: FE-SEM images of CuO NPs green synthesized calcinated (a) 200^{o}C, (b) 300^{o}C, (c) 400^{o}C, (d) 500^{o}C and (e) 600^{o}C for 2 h using 0.05 g/mL of MLE.

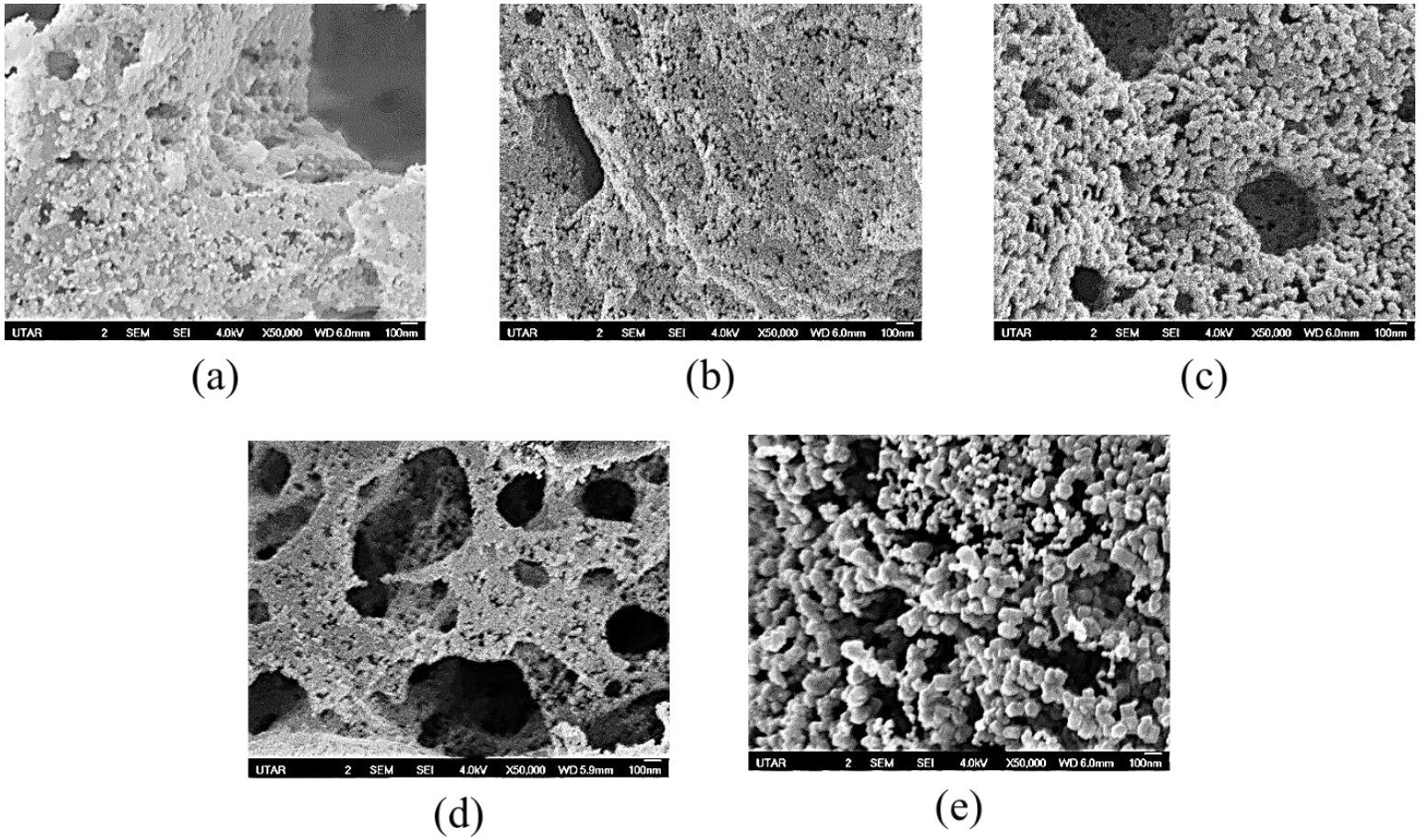

Figure 4.22: FE-SEM images of ZnO NPs green synthesized calcinated (a) 200^{o}C, (b) 300^{o}C, (c) 400^{o}C, (d) 500^{o}C and (e) 600^{o}C for 2 h using 0.04 g/mL of MLE.

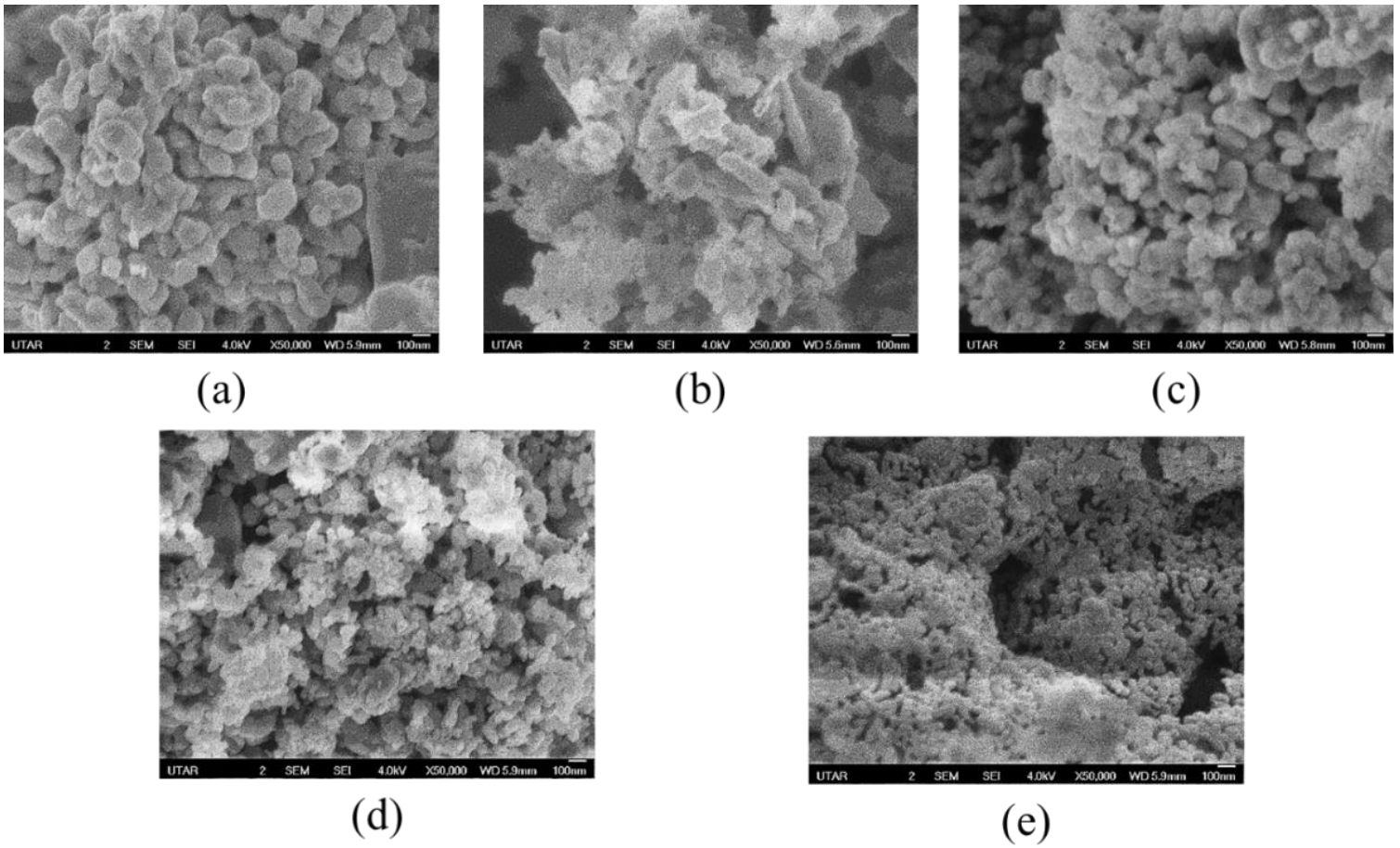

Figure 4.23: FE-SEM images of 70ZnO-30CuO NCs green synthesized using (a) 0.01 g/mL, (b) 0.02 g/mL, (c) 0.03 g/mL, (d) 0.04 g/mL and (e) 0.05 g/mL of MLE calcinated at 500^{o}C for 2 h.

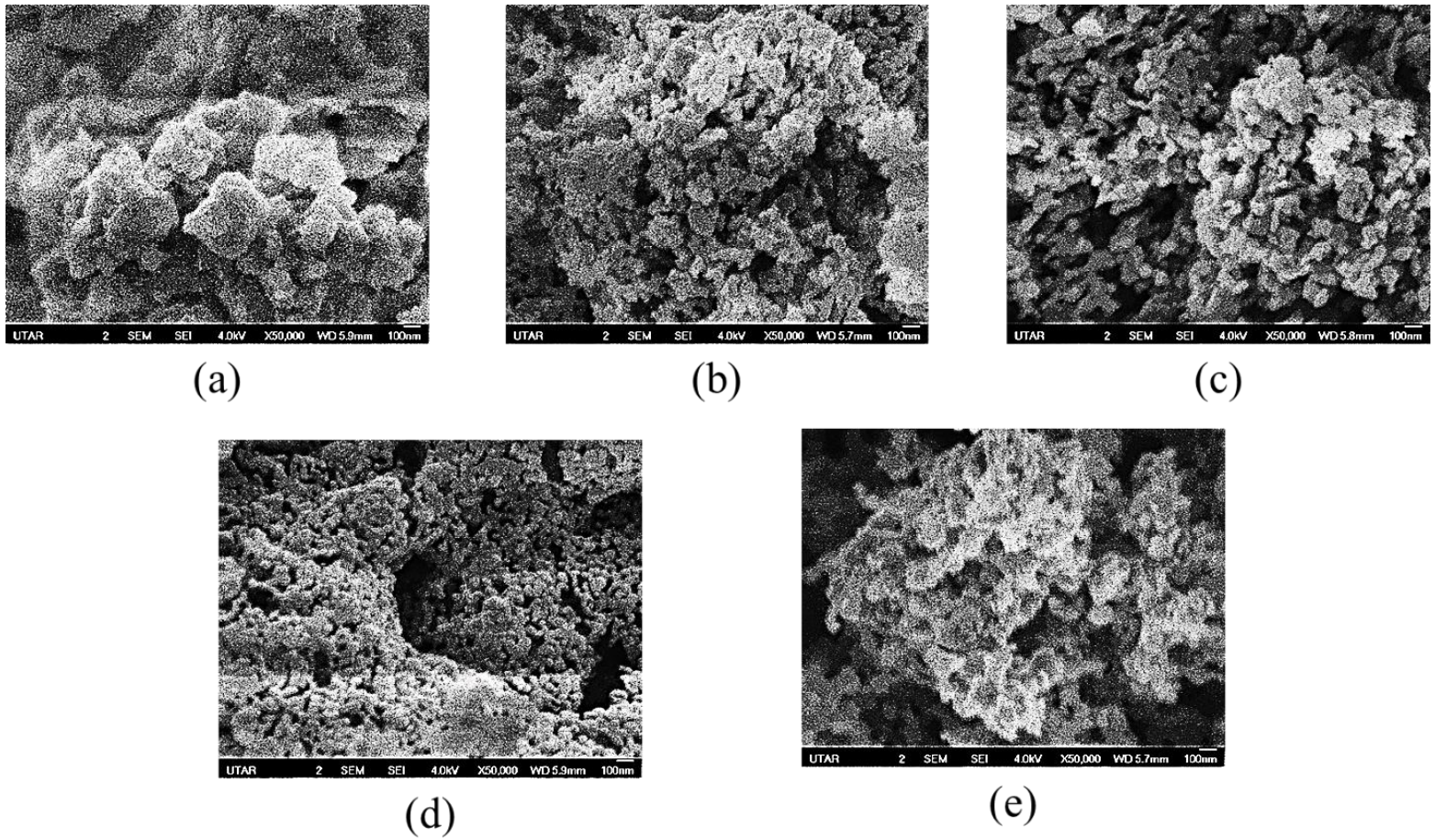

Figure 4.24: FE-SEM images of 70ZnO-30CuO NCs green synthesized calcinated (a) 200^{o}C, (b) 300^{o}C, (c) 400^{o}C, (d) 500^{o}C and (e) 600^{o}C for 2 h using 0.05 g/mL of MLE.

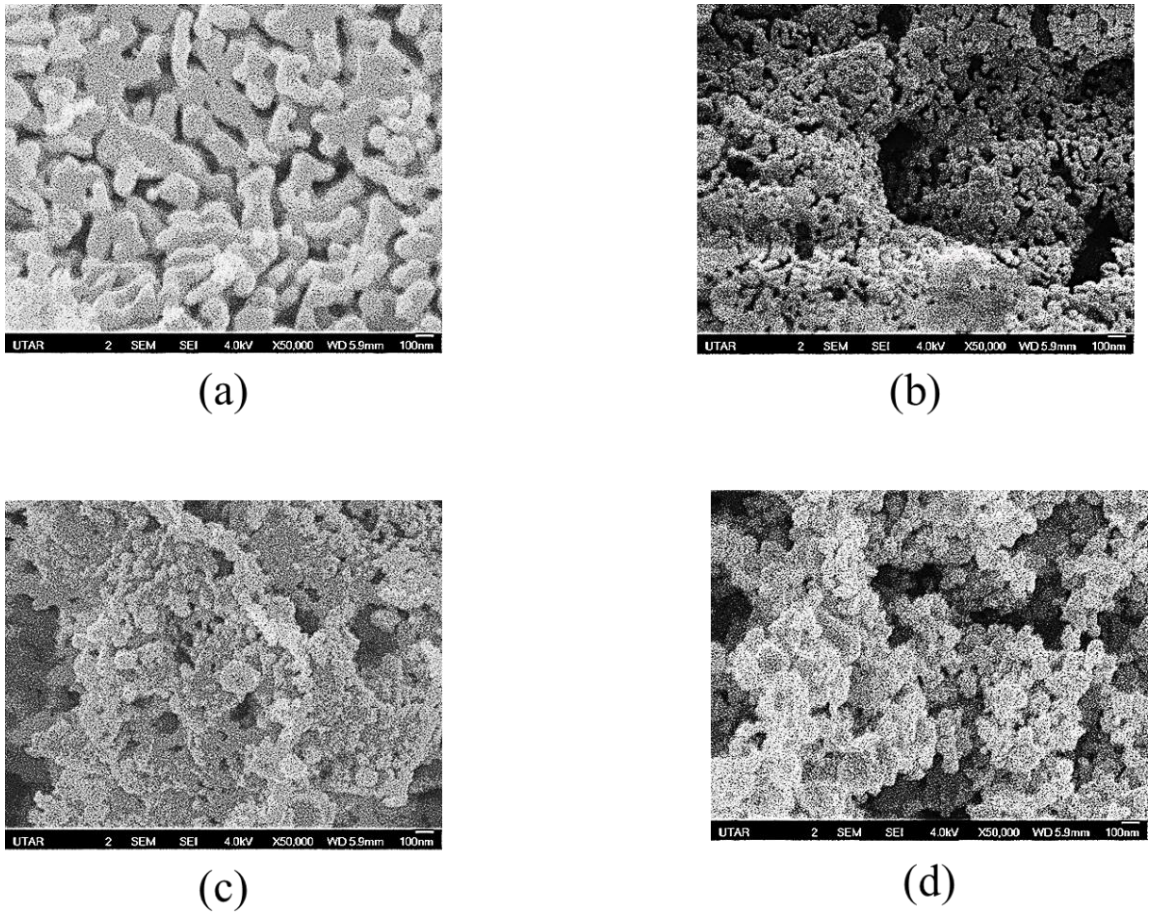

Figure 4.25: FE-SEM images of ZnO-CuO NCs green synthesized using (a) 80:20, (b) 70:30, (c) 60:40 and (d) 50:50 of ZnO-to-CuO ratio using 0.05 g/mL of MLE calcinated at 500^{o}C for 2 h.

In the EDX analysis, the synthesized nanomaterials were confirmed in oxidized form (**Figures 4.26** – **4.30**). Weight percentage of Cu-to-oxygen and Zn-to-O ratios were nearly 1:1 for synthesized CuO NPs and ZnO NPs, respectively. Similarly, the Zn-to-Cu ratios in ZnO-CuO NCs were similar to the weight ratio of salt precursors added. Detail weight percentage of elements was shown in **Table 4.10** and **Table 4.11**. Significant weight percentage of carbon was detected in the range of 16.10 – 31.91% in all nanomaterials. However, C could not be detected in 70ZnO-30CuO NCs green synthesized by using 0.01 g/mL and 0.02 g/mL calcinated at 500^{o}C due to low concentration of MLE were used.

Table 4.10: Summarization of elemental compositions of CuO NPs and ZnO NPs green synthesized at different calcination temperatures.

Nanomaterials	Parameters					Elemental compositions (%weight)			
	MLE concentrations (g/mL)	Calcination temperatures (^oC)	Zn precursor loadings (g)	Cu precursor loadings (g)	Zn-to-Cu ratios	C	O	Cu	Zn
CuO NPs	0.05	200	-	2.0	-	21.46	37.88	40.66	-
	0.05	300	-	2.0	-	21.13	32.90	45.97	-
	0.05	400	-	2.0	-	24.10	33.02	42.88	-
	0.05	500	-	2.0	-	28.00	30.45	41.55	-
	0.05	600	-	2.0	-	22.32	32.10	45.58	-
ZnO NPs	0.04	200	4.0	-	-	30.44	38.43	-	31.13
	0.04	300	4.0	-	-	31.91	36.63	-	31.46
	0.04	400	4.0	-	-	24.36	32.86	-	42.78
	0.04	500	4.0	-	-	30.00	34.17	-	33.83
	0.04	600	4.0	-	-	22.85	40.46	-	36.69

Table 4.11: Summarization of elemental compositions of ZnO-CuO NCs green synthesized at different conditions.

Nanomaterials	Parameters					Elemental compositions (%weight)			
	MLE concentrations (g/mL)	Calcination temperatures (^oC)	Zn precursor loadings (g)	Cu precursor loadings (g)	Zn-to-Cu ratios	C	O	Cu	Zn
ZnO-CuO NCs	0.01	500	2.8	1.2	70:30	-	28.43	28.20	43.37
	0.02	500	2.8	1.2	70:30	-	29.22	24.27	46.91
	0.03	500	2.8	1.2	70:30	18.10	21.17	20.20	40.53
	0.04	500	2.8	1.2	70:30	18.10	20.97	20.32	40.61
	[1]0.05	500	2.8	1.2	70:30	16.10	22.97	20.32	40.61
	0.05	200	2.8	1.2	70:30	20.21	40.86	18.08	30.85
	0.05	300	2.8	1.2	70:30	20.00	16.24	24.21	39.55
	0.05	400	2.8	1.2	70:30	18.31	18.27	20.85	42.57
	0.05	[1]500	2.8	1.2	70:30	16.10	22.97	20.32	40.61
	0.05	600	2.8	1.2	70:30	18.49	20.42	21.22	39.87

[1]ZnO-CuO NCs green synthesized in same conditions.

Continue

Nanomaterials	Parameters					Elemental compositions (%weight)			
	MLE concentrations (g/mL)	Calcination temperatures (^{o}C)	Zn precursor loadings (g)	Cu precursor loadings (g)	Zn-to-Cu ratios	C	O	Cu	Zn
ZnO-CuO NCs	0.05	500	3.2	0.8	80:20	23.33	18.60	13.44	44.63
	0.05	500	2.8	1.2	[1]70:30	16.10	22.97	20.32	40.61
	0.05	500	2.4	1.6	60:40	16.12	18.79	23.91	38.18
	0.05	500	2.0	2.0	50:50	17.00	20.18	31.94	30.88

[1]ZnO-CuO NCs green synthesized in same conditions.

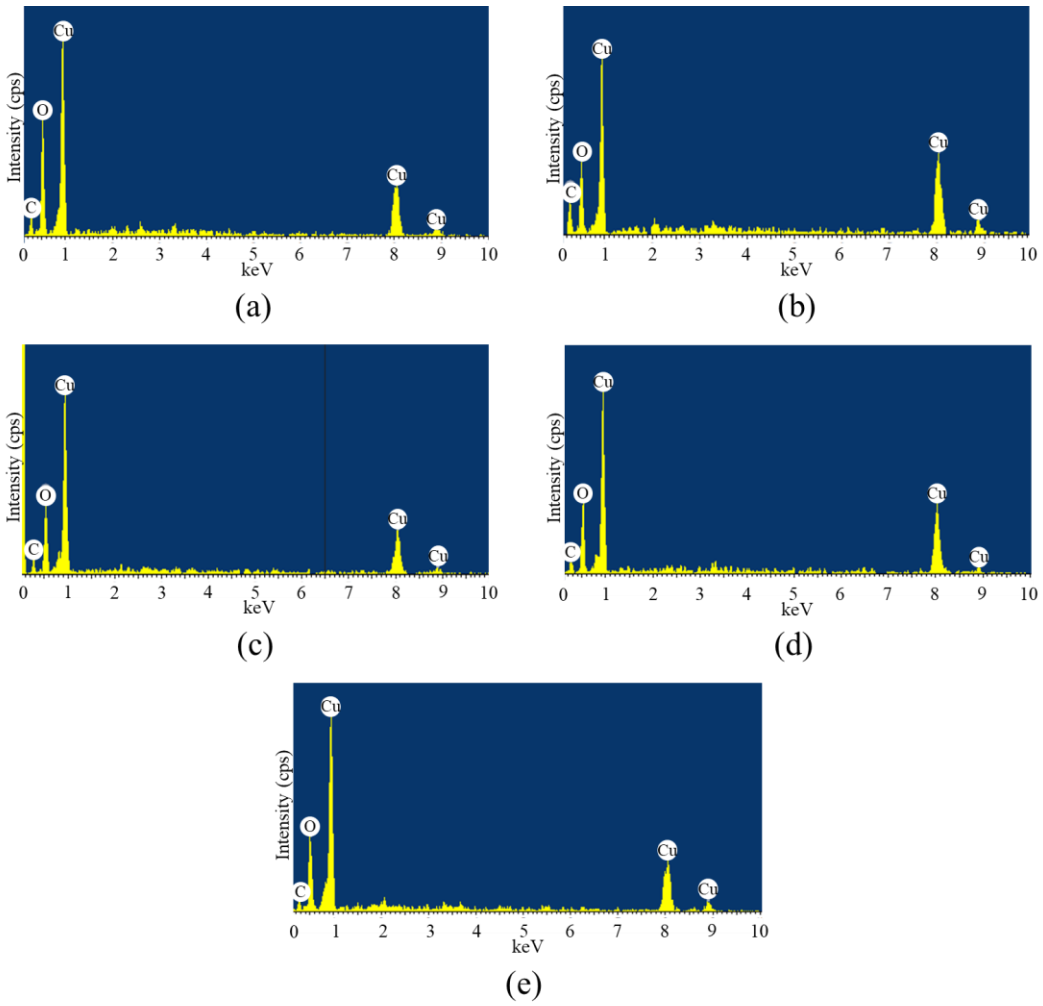

Figure 4.26: EDX spectra of CuO NPs green synthesized calcinated (a) 200^{o}C, (b) 300^{o}C, (c) 400^{o}C, (d) 500^{o}C and (e) 600^{o}C for 2 h using 0.05 g/mL of MLE.

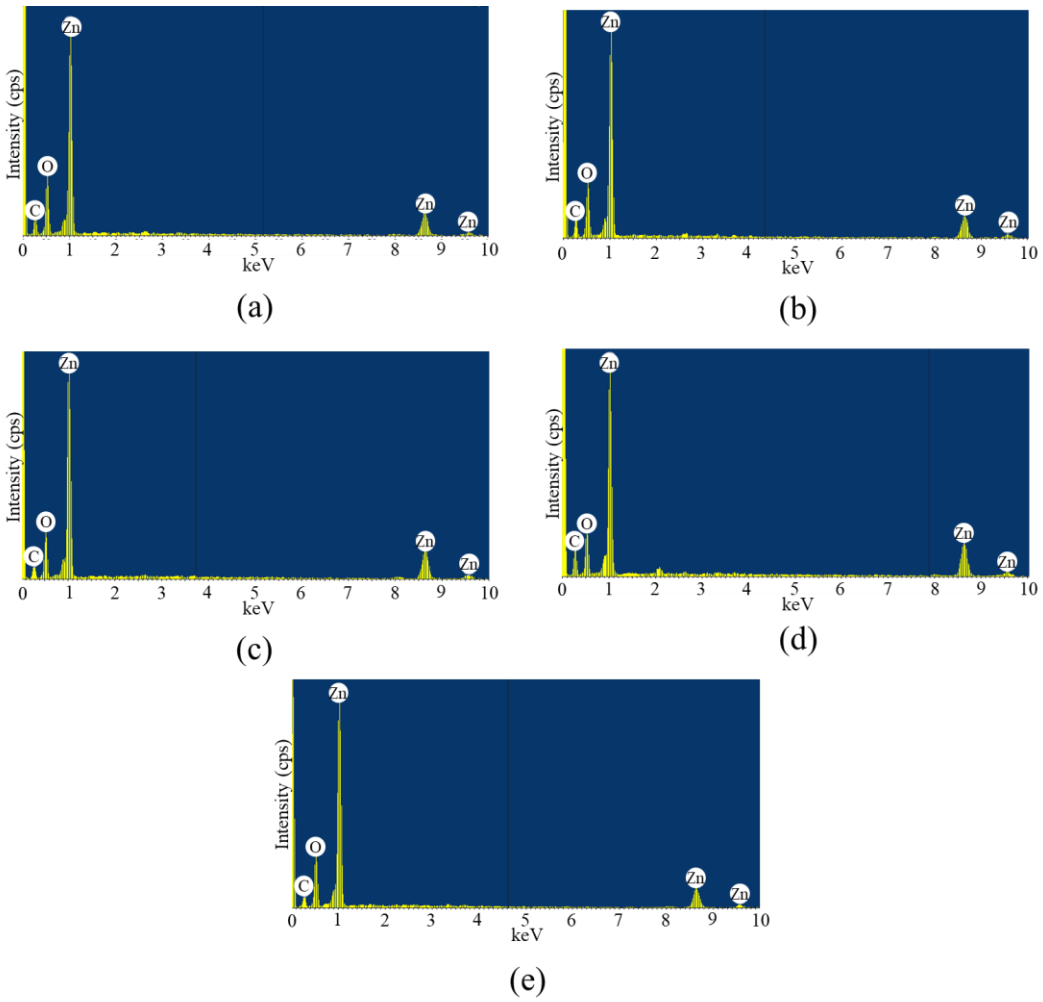

Figure 4.27: EDX spectra of ZnO NPs green synthesized calcinated (a) 200ºC, (b) 300ºC, (c) 400ºC, (d) 500ºC and (e) 600ºC for 2 h using 0.04 g/mL of MLE.

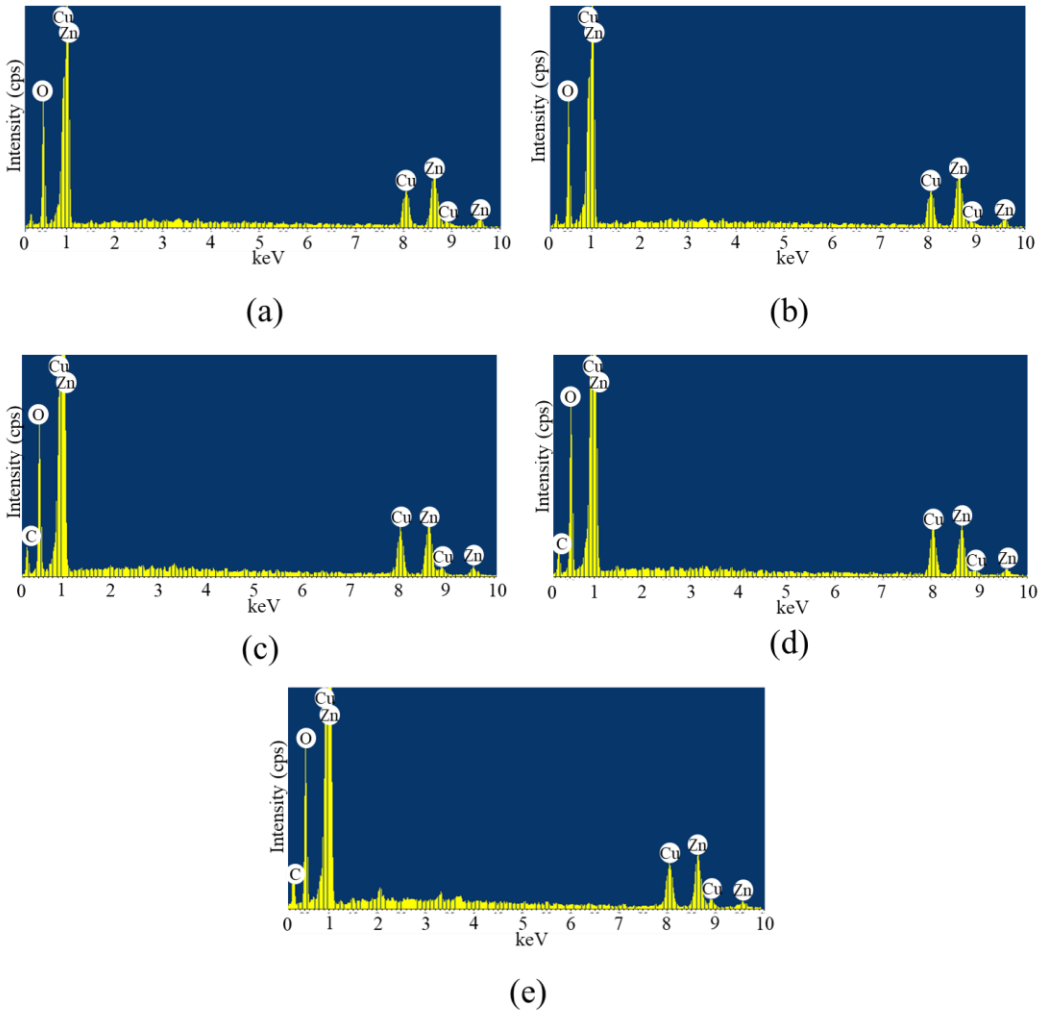

Figure 4.28: EDX spectra of 70ZnO-30CuO NCs green synthesized using (a) 0.01 g/mL, (b) 0.02 g/mL, (c) 0.03 g/mL, (d) 0.04 g/mL and (e) 0.05 g/mL of MLE calcinated at 500^{o}C for 2 h.

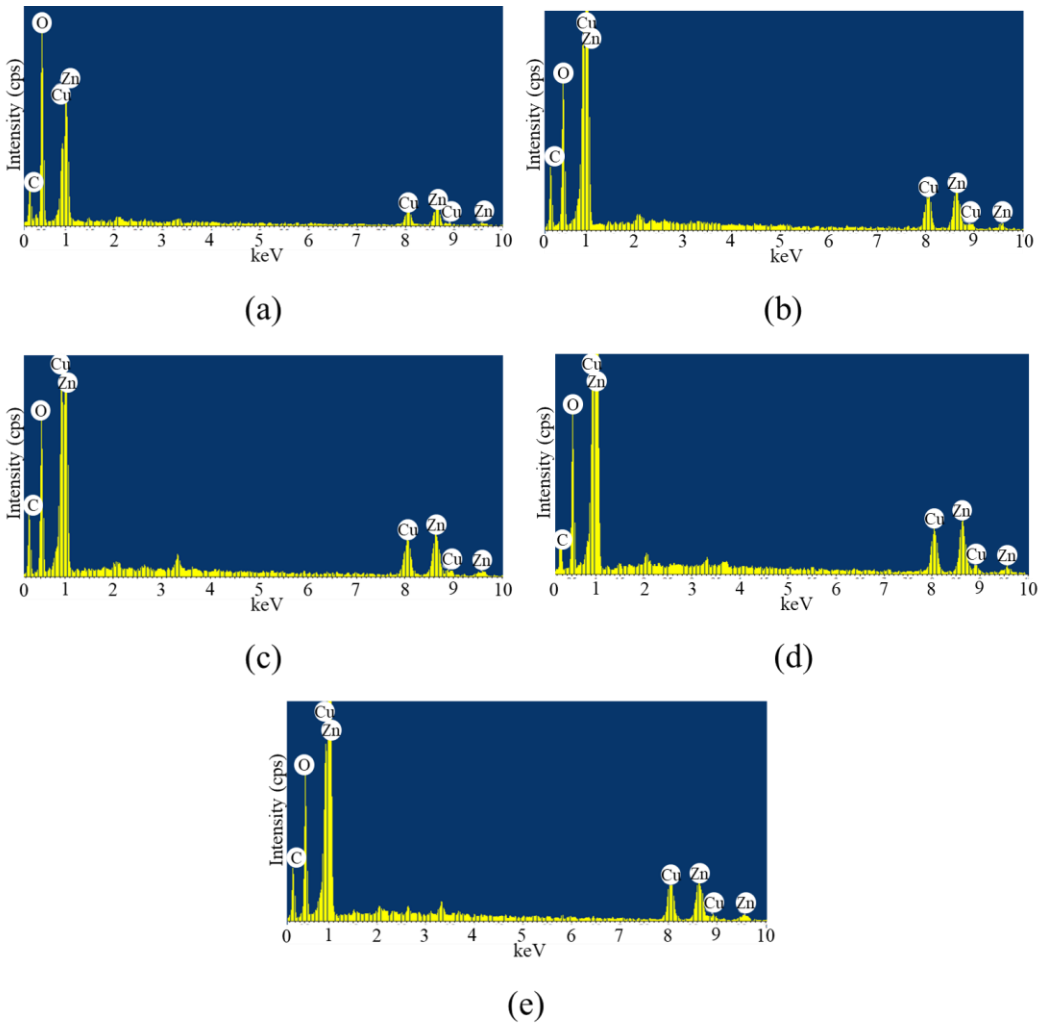

Figure 4.29: EDX spectra of 70ZnO-30CuO NCs green synthesized calcinated (a) 200ºC, (b) 300ºC, (c) 400ºC, (d) 500ºC and (e) 600ºC for 2 h using 0.05 g/mL of MLE.

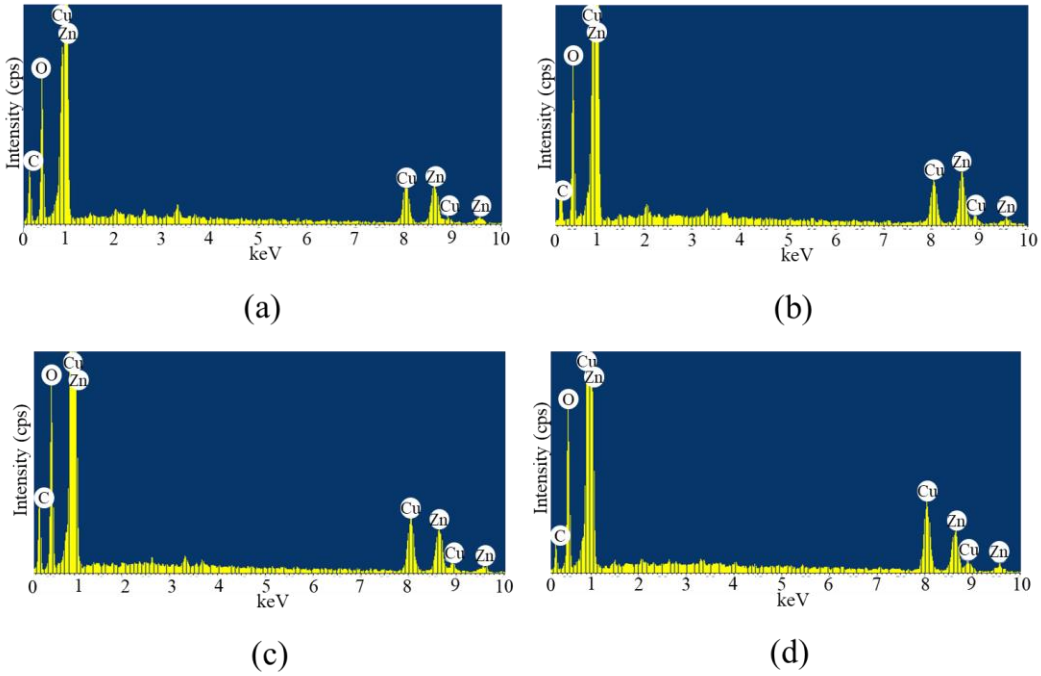

Figure 4.30: EDX spectra of ZnO-CuO NCs green synthesized using (a) 80:20, (b) 70:30, (c) 60:40 and (d) 50:50 of ZnO-to-CuO ratio using 0.05 g/mL of MLE calcinated at 500^{o}C for 2 h.

HR-TEM images (**Figures 4.31** – **4.33**) shown that selected nanomaterials was similar to the FE-SEM images. CuO NPs calcinated at 500^{o}C was in mixture of quasi-spherical and spherical nanostructures, ZnO NPs calcinated at 500^{o}C was in spherical nanostructure, whereas 70ZnO-30CuO NCs by using 0.05 g/mL calcinated at 500^{o}C was in mixture of hexagonal and spherical nanostructures. In particle means size, CuO NPs was found biggest (29.61 nm ± 12.573), followed by 70ZnO-30CuO NCs (23.09 nm ± 10.656) and ZnO NPs was the smallest (14.31 nm ± 5.368) among the nanomaterials.

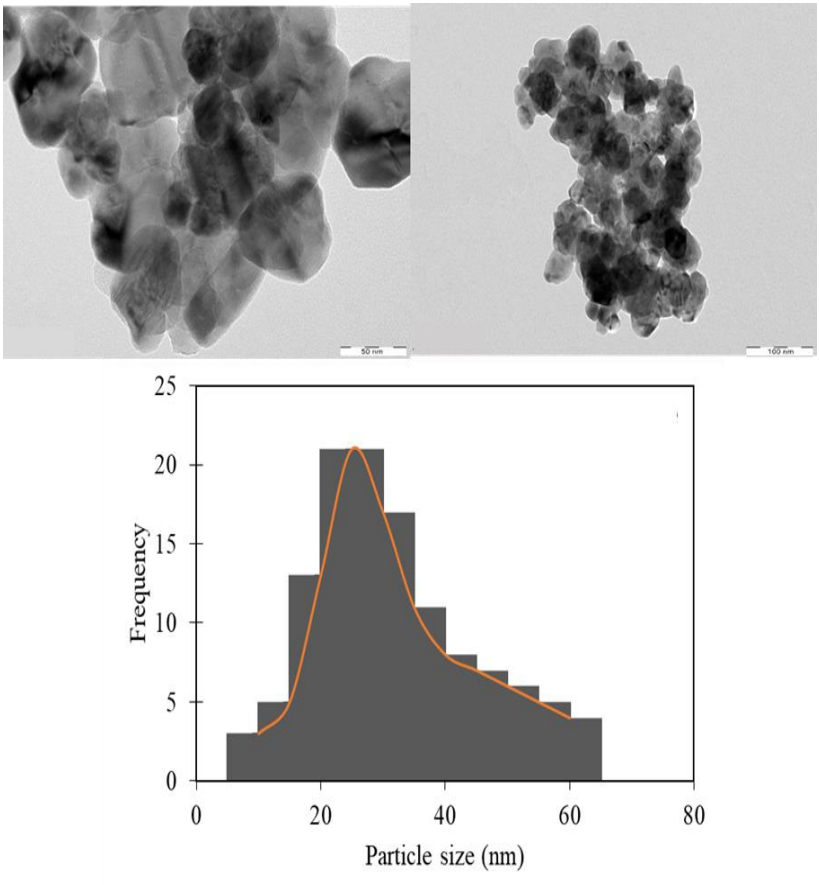

Figure 4.31: HR-TEM micrographs and histogram of particle size distribution CuO NPs green synthesized using 0.05 g/mL of MLE calcinated at 500^{o}C for 2 h.

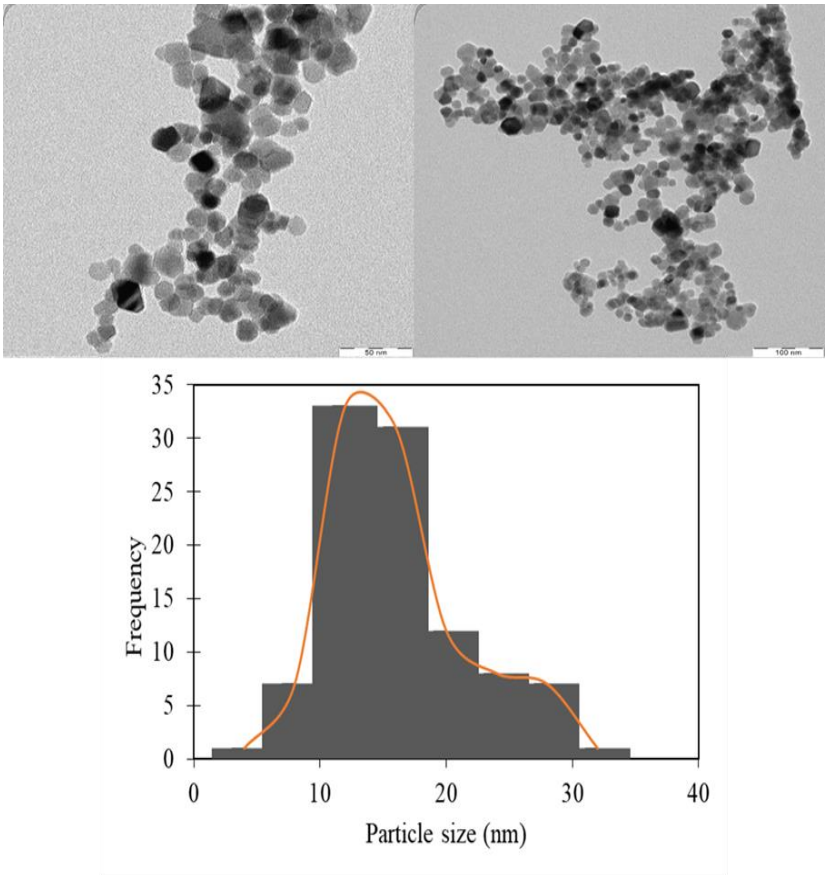

Figure 4.32: HR-TEM micrographs and histogram of particle size distribution of ZnO NPs green synthesized using 0.04 g/mL of MLE calcinated at 500^{o}C for 2 h.

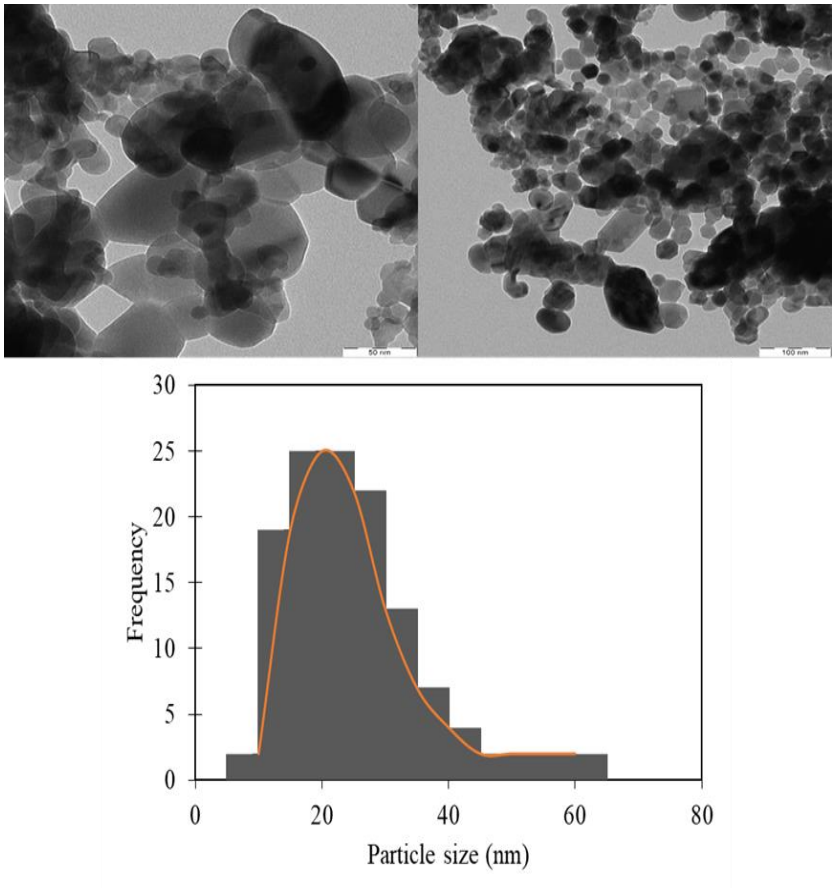

Figure 4.33: HR-TEM micrographs and histogram of particle size distribution of 70ZnO-30CuO NCs green synthesized using 0.05 g/mL of MLE calcinated at 500ºC for 2 h.

4.1.5 XPS Analysis

XPS measurements of CuO NPs calcinated at 500^{o}C was shown in **Figure 4.34**. Two Cu 2*p* peaks were detected at 933.56 eV and 953.81 eV which were corresponding to Cu $2p_{3/2}$ and Cu $2p_{1/2}$, respectively. Meanwhile, three satellite peaks were detected at 941.81 eV, 943.43 eV and 962.43 eV. On the other hand, O 1*s* and absorbed O peaks were located at 529.43 eV and 531.18 eV. For ZnO NPs calcinated at 500^{o}C, two Zn 2*p* peaks were detected at 1017.55 eV and 1040.65 eV which were corresponding to Zn $2p_{3/2}$ and Zn $2p_{1/2}$, respectively. Moreover, O 1*s* and absorbed O peaks were located at 526.45 eV and 528.25 eV, respectively in **Figure 4.35**. On the other hand, 70ZnO-30CuO NCs green synthesized using 0.05 g/mL calcinated at 500^{o}C shown two Zn 2*p* peaks were detected at 1018.95 eV and 1042.05 eV which were corresponding to Zn $2p_{3/2}$ and Zn $2p_{1/2}$, respectively in **Figure 4.36**, which was similar to aforementioned in ZnO NPs. Additionally, Cu 2*p* peaks detected was similar to early mentioned in CuO NPs. 70ZnO-30CuO NCs had the Cu $2p_{3/2}$ and Cu $2p_{1/2}$ were located at 930.25 eV and 950.35 eV with three satellite peaks (938.35 eV, 940.25 eV and 958.45 eV), whereas three satellite peaks were detected at 941.81 eV, 943.43 eV and 962.43 eV. On the other hand, O 1*s* was located at 527.95 eV.

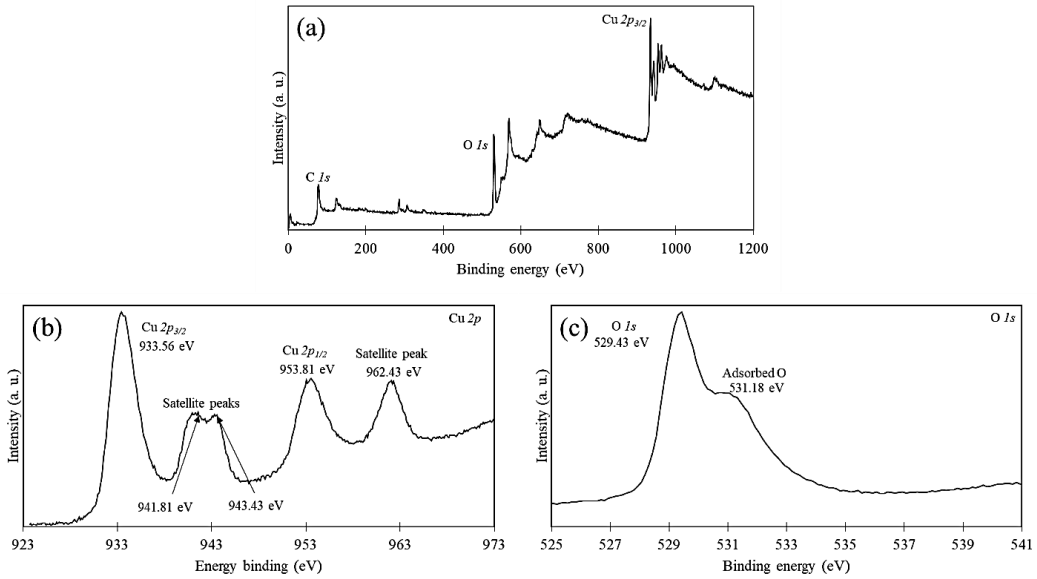

Figure 4.34: XPS measurement of (a) of CuO NPs green synthesized using 0.05 g/mL of MLE calcinated at 500ºC for 2 h, (b) high resolution Cu 2*p* peaks and (c) O 1*s* peaks.

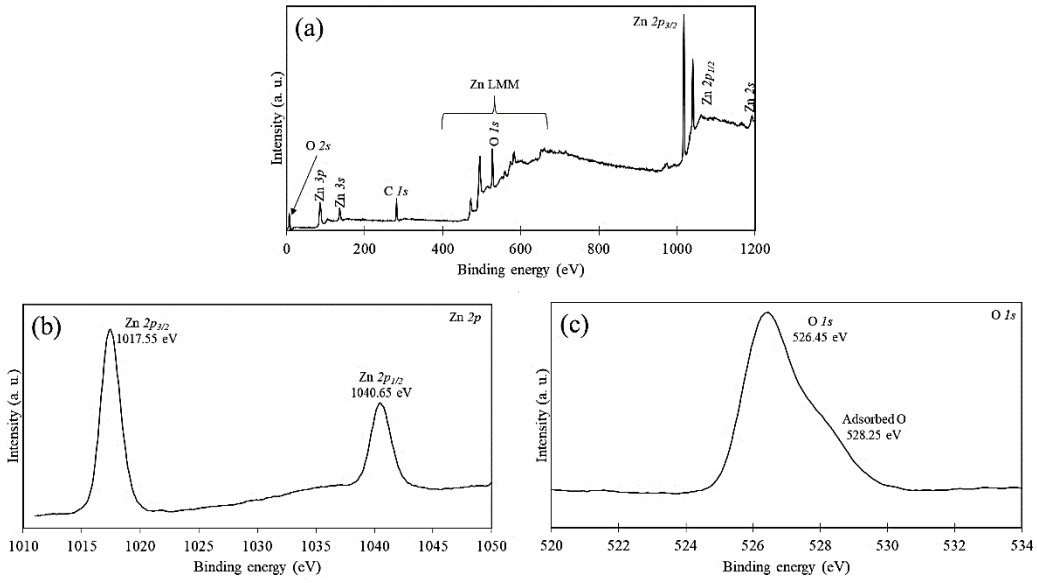

Figure 4.35: XPS measurement of (a) of ZnO NPs green synthesized using 0.04 g/mL of MLE calcinated at 500ºC for 2 h, (b) high resolution Zn 2*p* peaks and (c) O 1*s* peaks.

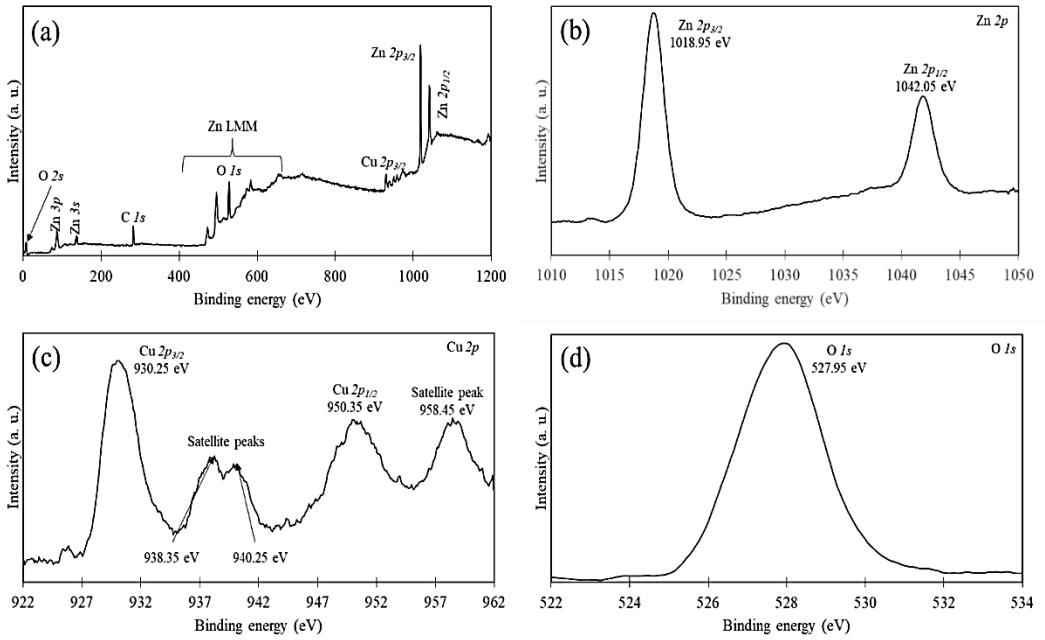

Figure 4.36: XPS measurement of (a) of 70ZnO-30CuO NCs green synthesized using 0.05 g/mL of MLE calcinated at 500°C for 2 h, (b) high resolution Zn 2*p* peaks, (c) Cu 2*p* peaks and (d) O 1*s* peaks.

4.2 Preliminary *in vitro* Antibacterial Activity

Both CuO NPs and ZnO NPs calcinated at 500°C, and 70ZnO-30CuO NCs green synthesized using 0.05 g/mL of MLE calcinated at 500°C, were used in preliminary *in vitro* antibacterial study. They were chosen due to they have relative good physicochemical properties, while ampicillin was used as positive control.

Ampicillin, CuO NPs, ZnO NPs and 70ZnO–30CuO NCs exhibited lower MIC values against Gram-positive bacteria (*S. aureus* and *B. subtilis*) than those against Gram-negative bacteria (*E. coli* and *K. pneumoniae*). The MIC results, as illustrated in **Figure 4.37** (Gram-positive bacteria) and **Figure 4.38** (Gram-negative bacteria), were employed to rank the sensitivity of the tested bacteria to the antibacterial effects, arranged from most to least sensitive as follows. Generally,

ampicillin was more effective in suppressing the growth of bacteria compared to the nanomaterials. However, less concentrated of ZnO NPs (15.63 μg/mL) was needed to suppress the growth of *B. subtilis* compared to ampicillin (25.00 μg/mL). Among the nanomaterials, least amount of ZnO NPs was required to inhibit the bacteria growth, followed by 70ZnO-30CuO NCs and CuO NPs. **Table 4.12** tabulates the MIC results of the synthesized nanomaterials.

- For Ampicillin (as positive control):

  S. aureus (1.56 μg/mL) > *B. subtilis* (25.00 μg/mL) > *E. coli* = *K. pneumoniae* (50.00 μg/mL)

- For ZnO NPs:

  S. aureus = *B. subtilis* (15.63 μg/mL) > *E. coli* (62.50 μg/mL) > *K. pneumoniae* (125.00 μg/mL)

- For CuO NPs:

  B. subtilis = *E. coli* (125.00 μg/mL) > *S. aureus* (250.00 μg/mL) > *K. pneumoniae* (500.00 μg/mL)

- For 70ZnO–30CuO NCs:

  S. aureus = *B. subtilis* (62.50 μg/mL) > *K. pneumoniae* (125.00 μg/mL) > *E. coli* (250.00 μg/mL)

Table 4.12: MIC values of Ampicillin (positive control), ZnO NPs, CuO NPs and 70ZnO-30CuO NCs in different tested bacteria.

Nanomaterials	MIC (μg/mL)			
	S. aureus	*B. subtilis*	*E. coli*	*K. pneumoniae*
Ampicillin (Positive control)	*1.56	*25.00	50.00	50.00
CuO NPs	*250.00	125.00	125.00	*500.00
ZnO NPs	15.63	15.63	*62.50	*125.00
70ZnO-30CuO NCs	62.50	62.50	*250.00	*125.00

"*" represent significant difference at $p < 0.05$.

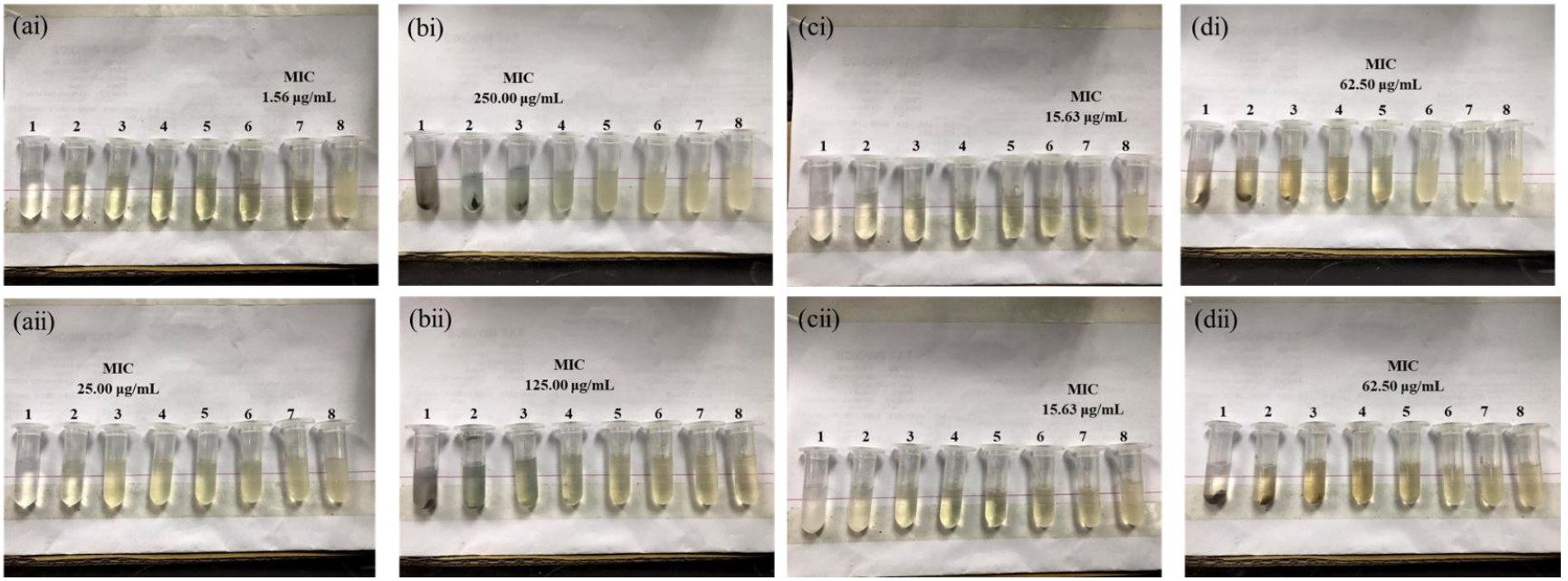

Figure 4.37: Observation of turbidity changes of *in vitro* antibacterial activity of (a) Ampicillin (positive control), (b) CuO NPs, (c) ZnO NPs and (d) 70ZnO-30CuO NCs by using broth macrodilution assay. Note that, images labelled with "i" and "ii" was using *S. aureus* and *B. subtilis*, respectively, in determining ampicillin and nanomaterials antibacterial activity. The concentration of ampicillin in each tubes was as follow: tube 1 = 100.00 µg/mL, tube 2 = 50.00 µg/mL, tube 3 = 25.00 µg/mL, tube 4 = 12.50 µg/mL, tube 5 = 6.25 µg/mL, tube 6 = 3.13 µg/mL, tube 7 = 1.56 µg/mL and tube 7 = 0.00 µg/mL. Meanwhile, the concentration of nanomaterials in each tubes was as follow: tube 1 = 1000.00 µg/mL, tube 2 = 500.00 µg/mL, tube 3 = 250.00 µg/mL, tube 4 = 125.00 µg/mL, tube 5 = 62.50 µg/mL, tube 6 = 31.25 µg/mL, tube 7 = 15.63 µg/mL and tube 7 = 0.00 µg/mL.

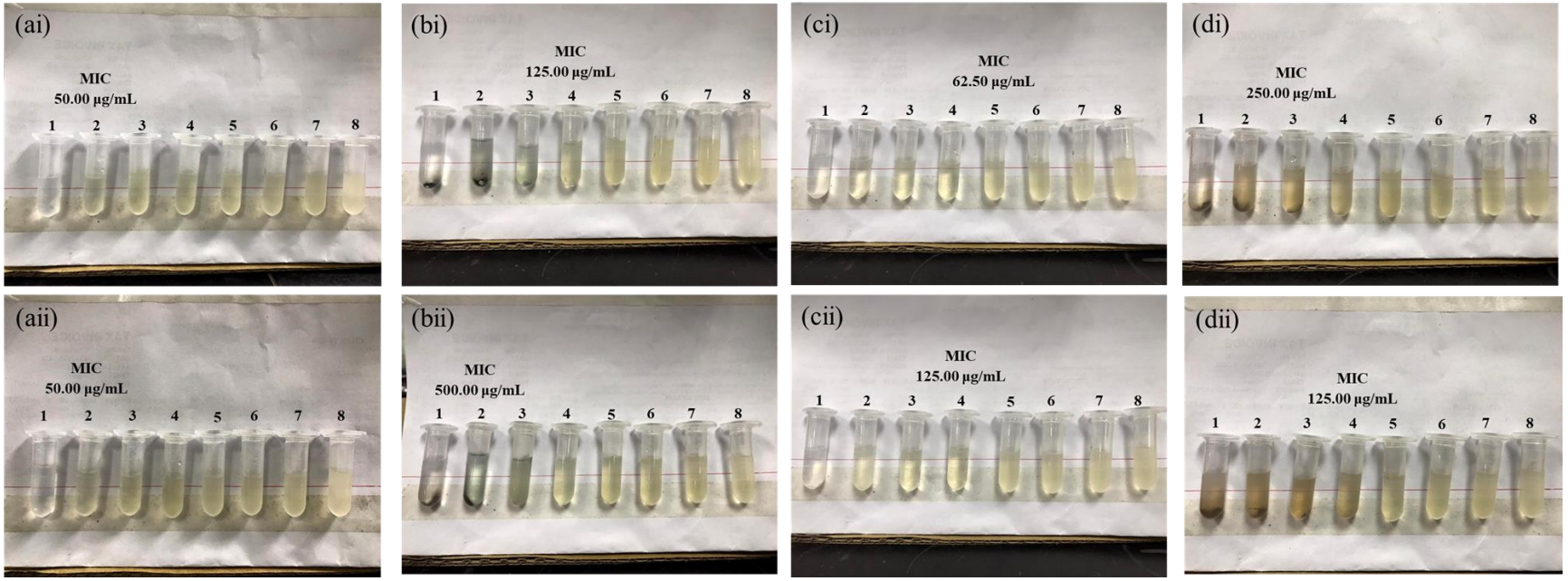

Figure 4.38: Observation of turbidity changes of *in vitro* antibacterial activity of (a) Ampicillin (positive control), (b) CuO NPs, (c) ZnO NPs and (d) 70ZnO-30CuO NCs by using broth macrodilution assay. Note that, images labelled with "i" and "ii" was using *E. coli* and *K. pneumoniae*, respectively, in determining ampicillin and nanomaterials antibacterial activity. The concentration of ampicillin in each tubes was as follow: tube 1 = 100.00 µg/mL, tube 2 = 50.00 µg/mL, tube 3 = 25.00 µg/mL, tube 4 = 12.50 µg/mL, tube 5 = 6.25 µg/mL, tube 6 = 3.13 µg/mL, tube 7 = 1.56 µg/mL and tube 7 = 0.00 µg/mL. Meanwhile, the concentration of nanomaterials in each tubes was as follow: tube 1 = 1000.00 µg/mL, tube 2 = 500.00 µg/mL, tube 3 = 250.00 µg/mL, tube 4 = 125.00 µg/mL, tube 5 = 62.50 µg/mL, tube 6 = 31.25 µg/mL, tube 7 = 15.63 µg/mL and tube 7 = 0.00 µg/mL.

4.3 Photocatalytic Performance in POME Treatment

Photocatalytic performance in POME treatment was conducted using selected nanomaterials, including CuO NPs calcinated at 500°C, ZnO NPs calcinated at 400°C, and 70ZnO-30CuO NCs green synthesized using 0.05 g/mL of MLE calcinated at 500°C, based on their calculated E_{CB} and E_{VB} location against NHE which were separated by minimum energy bandgap to generate radicals.

4.3.1 Selection of LEDs

The light intensity of blue and white LEDs were 0.2 mW/cm^2. Compared to exposure of white LED, 100 mg of nanomaterials performed well in reducing COD and AN values under blue LED for 2 h in 200 mL of 12.5 × diluted POME (**Table 4.13** and **Figure 4.39**). Under blue LED irradiation, nanomaterials had 32.99 – 82.62% higher reduction rate in reducing organic matters, whereas 15.12 – 33.94% higher reduction rate in degrading nitrogenous compounds, compared to white LED exposure. Therefore, blue LED was chosen as the light source in treating POME by using nanomaterials.

Under blue LED irradiation, 70ZnO-30CuO NCs had the highest reduction rate in removing organic compared to CuO NPs and ZnO NPs. The 70ZnO-30CuO NCs recorded 81.76% ± 0.02 in organic matters reduction rate, followed by CuO NPs (79.66% ± 0.04) and ZnO NPs (66.73% ± 0.03). In contrast, the nitrogenous compounds reduction rates were similar among the nanomaterials, which was

accounted for 41.23% ± 0.01 – 44.78% ± 0.01. Instead of CuO NPs had the highest reduction rate (65.08% ± 0.01), similar reduction rate in organic matters using ZnO NPs (44.19% ± 0.05) and 70ZnO-30CuO NCs (45.25% ± 0.04) were obtained under white LED exposure. On the other hand, CuO NPs and ZnO NPs had similar reduction rate in nitrogenous compounds, which were accounted for 38.03% ± 0.02 and 34.22% ± 0.02, respectively. However, 70ZnO-30CuO NCs had the lowest reduction rate (29.78% ± 0.02) in reducing nitrogenous compounds.

Table 4.13: The COD and AN removal efficiencies by 100 mg of CuO NPs, ZnO NPs and 70ZnO-30CuO NCs under blue and white LEDs for 2 h in 200 mL of POME diluted to 12.5 ×.

Light sources	COD			AN		
	CuO NPs	ZnO NPs	70ZnO-30CuO NCs	CuO NPs	ZnO NPs	70ZnO-30CuO NCs
Blue	79.66% ± 0.04	*66.73% ± 0.03	81.76% ± 0.02	44.71% ± 0.02	*41.23% ± 0.01	44.78% ± 0.01
White	*65.08% ± 0.01	44.19% ± 0.05	45.25% ± 0.04	*38.03% ± 0.02	*34.22% ± 0.02	*29.78% ± 0.02

"*" represent significant difference at $p < 0.05$.

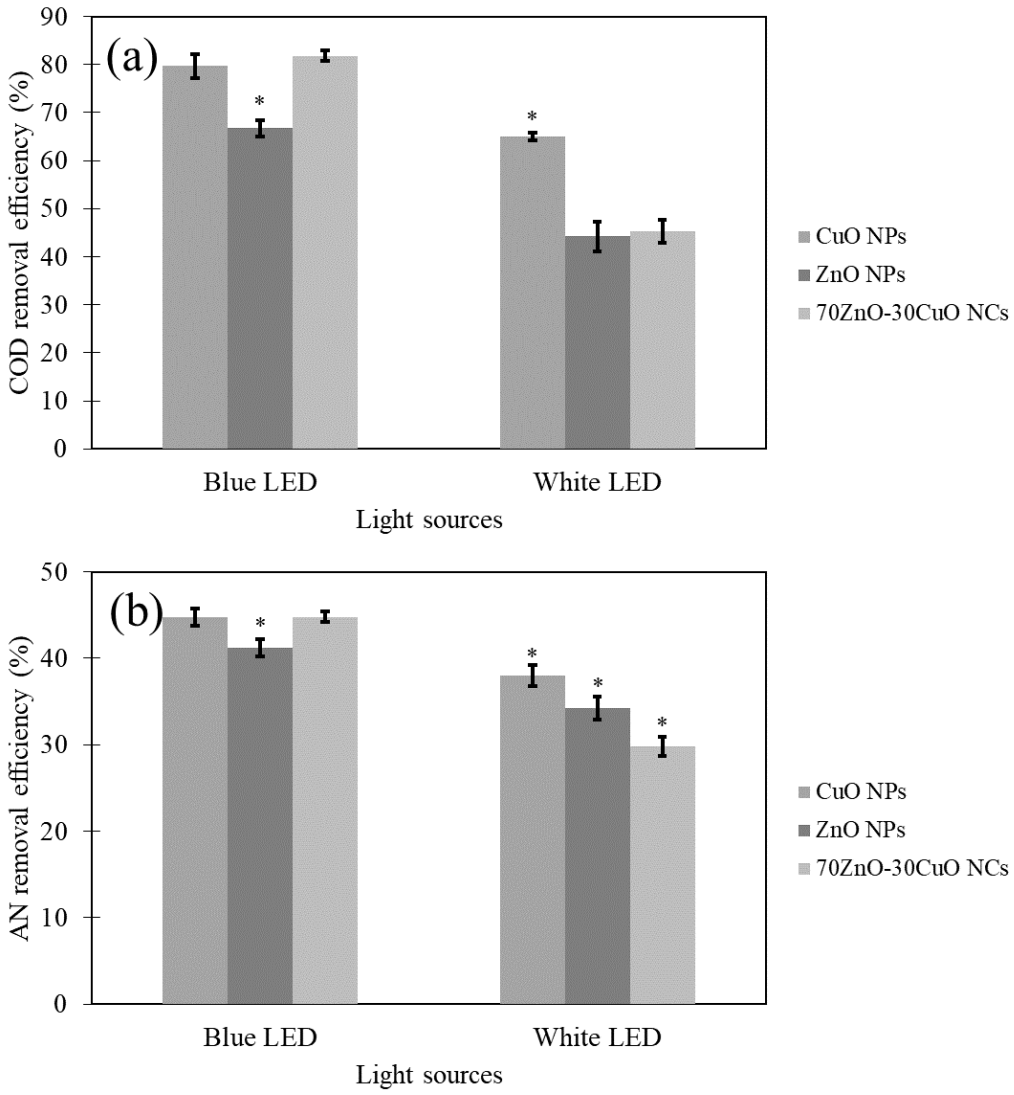

Figure 4.39: The removal efficiency of (a) COD and (b) AN was evaluated using 100 mg of nanomaterials under blue and white LEDs for 2 h with 200 mL of POME diluted to 12.5 ×. Note that "*" represent significant difference at $p < 0.05$.

4.3.2 Nanomaterial Loadings

Lesser ZnO NPs was used in in treating 200 mL of 12.5 × diluted POME under 2 h of blue LED irradiation to achieve highest reduction rate in reducing organic and nitrogenous compounds compared to CuO NPs and 70ZnO-30CuO

NCs (**Figure 4.40**). Under the same conditions, 50 mg of ZnO NPs was able to achieve highest reduction rate in reducing organic (78.55% ± 0.03) and nitrogenous (47.24% ± 0.02) compounds. Meanwhile, 100 mg of CuO NPs and 70ZnO-30CuO NCs were needed to have similar effect as ZnO NPs. Their organic matters reduction rate were able to reach 79.66% ± 0.04 and 81.76% ± 0.02 as well as nitrogenous compounds reduction rate at 44.71% ± 0.02 and 44.78% ± 0.01, respectively. The reduction rate of pollutants decreased when higher amount of nanomaterials utilized in treating POME. Therefore, 50 mg of ZnO NPs, and 100 mg of CuO NPs and 70ZnO-30CuO NCs were utilized in optimizing 12.5 × diluted POME volume under blue LED irradiation for 2 h. The pollutants removal efficiencies by different nanomaterials loadings were tabulated at **Table 4.14**.

Table 4.14: The COD and AN removal efficiencies were assessed using varying loadings of CuO NPs, ZnO NPs and 70ZnO-30CuO NCs under blue LED for 2 h with 200 mL of POME diluted to 12.5 ×.

Nanomaterial loadings (mg)	COD (%)			AN (%)		
	CuO NPs	ZnO NPs	70ZnO-CuO 30NCs	CuO NPs	ZnO NPs	70ZnO-CuO 30NCs
50	*56.51 ± 0.03	*78.55 ± 0.03	*44.13 ± 0.03	*31.39 ± 0.01	*47.24 ± 0.02	*29.24 ± 0.02
100	79.66 ± 0.04	*66.73 ± 0.03	81.76 ± 0.02	44.71 ± 0.02	*41.23 ± 0.01	44.78 ± 0.01
150	*64.02 ± 0.02	*46.27 ± 0.02	*61.33 ± 0.02	*36.12 ± 0.02	*38.70 ± 0.01	*40.32 ± 0.01
200	45.75 ± 0.02	42.54 ± 0.04	*55.40 ± 0.01	*15.82 ± 0.02	*37.08 ± 0.02	*35.49 ± 0.02

"*" represent significant difference at $p < 0.05$.

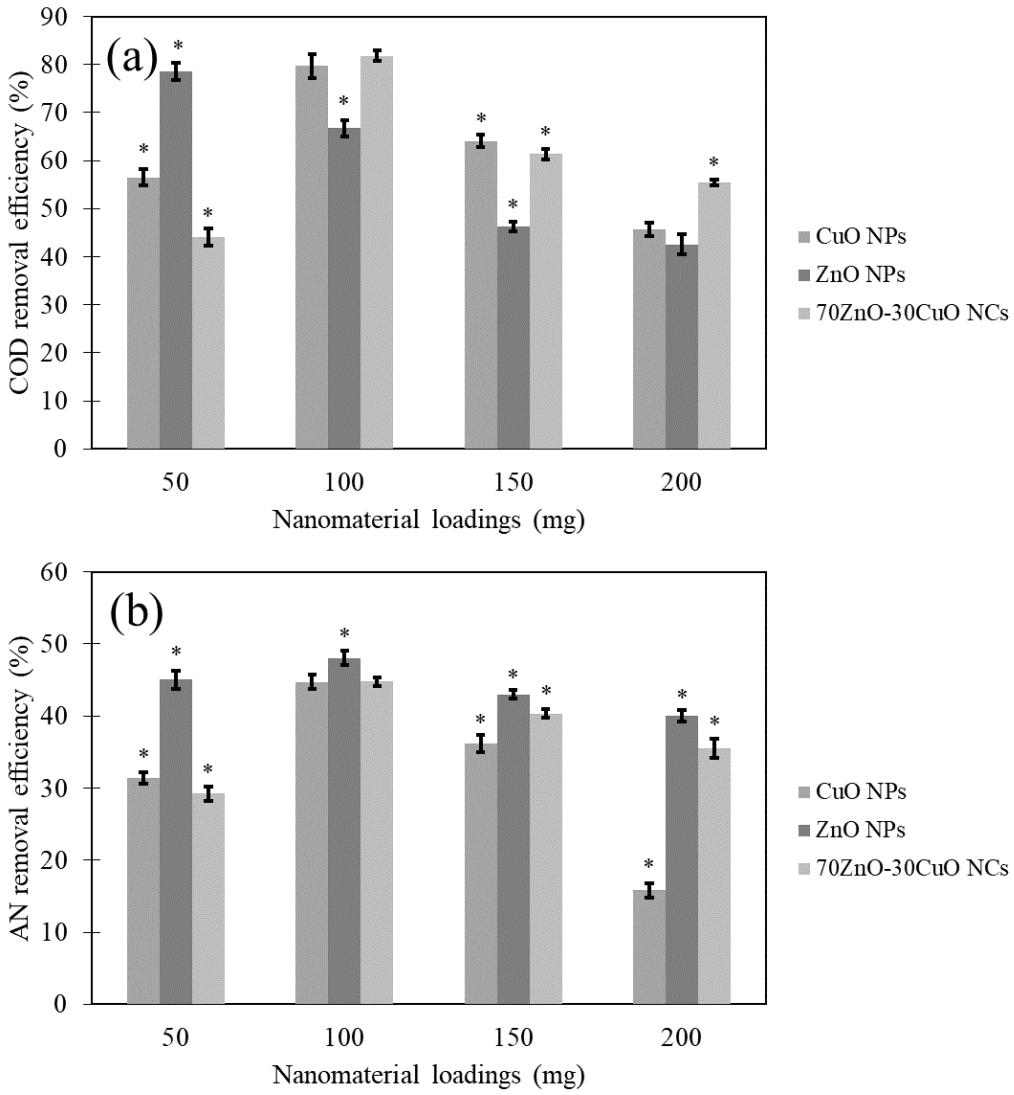

Figure 4.40: The removal efficiency of (a) COD and (b) AN was evaluated using varying loadings of nanomaterials with 200 mL of POME diluted to 12.5 × under blue LED for 2 h. Note that "*" represent significant difference at $p < 0.05$.

4.3.3 POME Volumes

For ZnO NPs 100 mL, 200 mL and 300 mL had the similar pollutants reduction rates as shown in **Table 4.15** and **Figure 4.41**. Highest reduction rate of organic (79.10% ± 0.04) and nitrogenous (48.49% ± 0.03) compounds were recorded utilized in 300 mL of 12.5 × diluted POME volume under blue LED irradiation for 2 h, by using 50 mg of ZnO NPs. Comparatively, lower POME volume (200 mL) was recorded for 100 mg of CuO NPs and 70ZnO-30CuO NCs to achieve highest organic and nitrogenous compounds reduction rates (same results mentioned in **Section 4.3.2**). The reduction rate of pollutants decreased when higher POME's volume was utilized in treating POME. Therefore, 50 mg of ZnO NPs, and 100 mg of CuO NPs and 70ZnO-30CuO were utilized in optimizing POME concentrations at 300 mL and 200 mL, respectively under blue LED irradiation for 2 h.

Table 4.15: The COD and AN removal efficiencies were assessed using CuO NPs, ZnO NPs and 70ZnO-30CuO NCs under blue LED for 2 h with varying volumes of POME diluted to 12.5 ×.

POME volume	COD (%)			AN (%)		
(mL)	[1]CuO NPs	[2]ZnO NPs	[1]70ZnO-30CuO NCs	[1]CuO NPs	[2]ZnO NPs	[1]70ZnO-30CuO NCs
100	59.22 ± 0.04	72.63 ± 0.02	44.12 ± 0.02	*18.37 ± 0.02	45.98 ± 0.02	*21.23 ± 0.02
200	*79.66 ± 0.04	78.55 ± 0.03	*81.76 ± 0.02	*44.71 ± 0.02	47.24 ± 0.02	44.78 ± 0.01
300	65.05 ± 0.01	79.10 ± 0.04	*63.48 ± 0.02	32.02 ± 0.01	48.49 ± 0.03	40.89 ± 0.02
400	61.87 ± 0.03	*42.99 ± 0.01	48.91 ± 0.01	28.57 ± 0.01	*38.65 ± 0.03	*32.31 ± 0.02

[1]100 mg of CuO NPs and 70ZnO-30CuO NCs were used, respectively.
[2]50 mg of ZnO NPs was used.
"*" represent significant difference at $p < 0.05$.

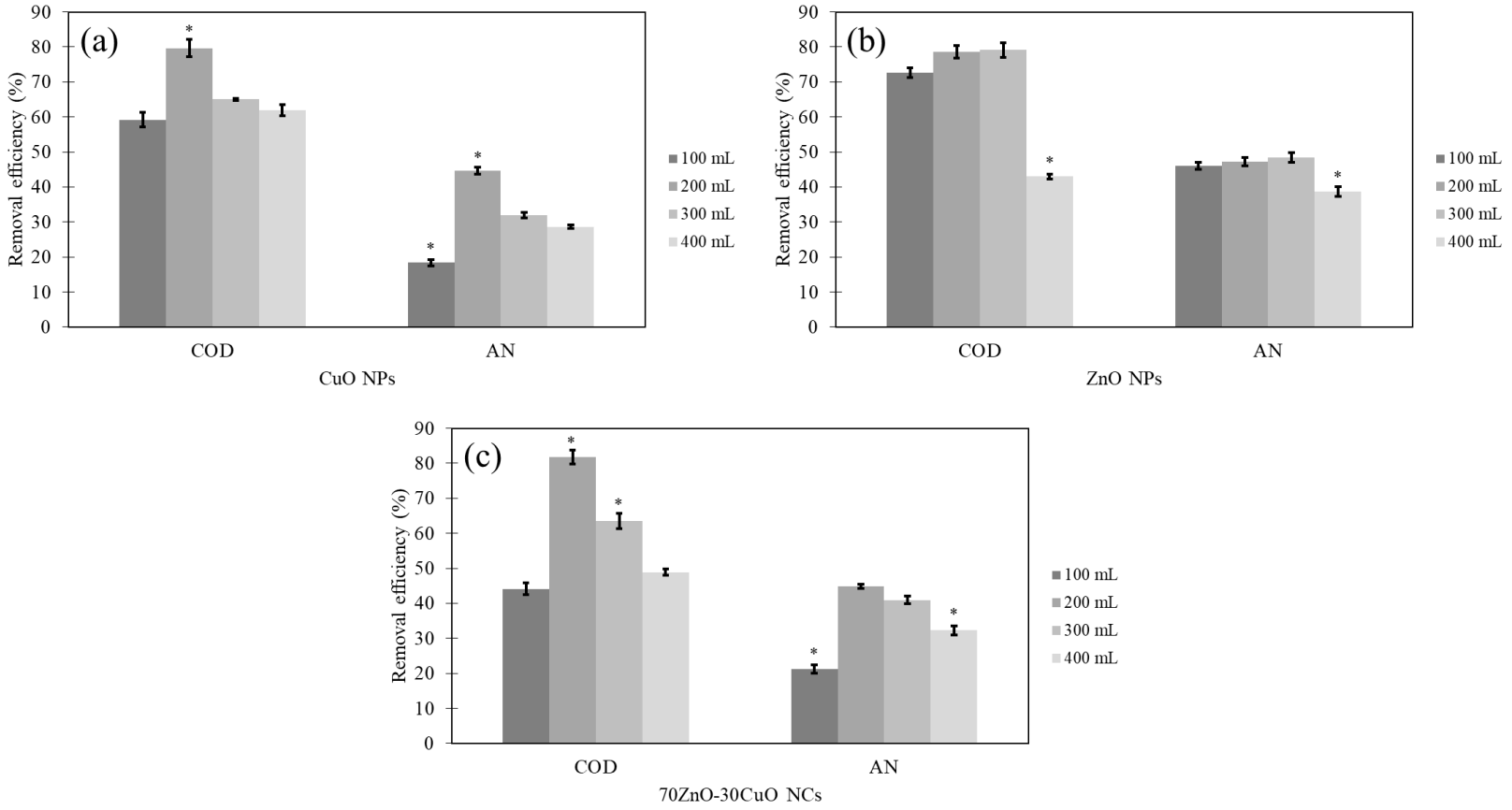

Figure 4.41: The removal efficiency of COD and AN was evaluated using (a) 100 mg of CuO NPs, (b) 50 mg of ZnO NPs and (c) 100 mg of 70ZnO-30CuO NCs with varying volumes of POME diluted to 12.5 × under blue LED for 2 h. Note that "*" represent significant difference at $p < 0.05$.

4.3.4 POME Concentrations

Nanomaterials' reduction rate in harmful compounds were gradually increased and achieved highest effectiveness when least concentrated POME (12.5 × diluted) was used in respective nanomaterials loadings and POME volume (**Table 4.16** and **Figure 4.42**). Interestingly, the treated 3.1 × diluted POME in all nanomaterials were at discharge passing edge set by Department of Environment Malaysia regulation. The treated 3.1 × diluted POME by CuO NPs, ZnO NPs and 70ZnO-30CuO NCs were 107.67 mg/L ± 5.13, 94.67 mg/L ± 5.67 and 107.00 mg/L ± 4.58, respectively. Therefore, 3.1 × diluted POME was carried forward to extend the photo-degradation duration (up to 3 h) to determine the ability of nanomaterials in degrading pollutants in fulfilling the Department of Environment Malaysia regulation.

Table 4.16: The COD and AN removal efficiencies were assessed using 100 mg of CuO NPs, 50 mg of ZnO NPs and 100 mg of 70ZnO-30CuO NCs under blue LED for 3 h at varying concentrations of POME.

POME concentration (× diluted)	COD (%)			AN (%)		
	[1]CuO NPs	[2]ZnO NPs	[1]70ZnO-30CuO NCs	[1]CuO NPs	[2]ZnO NPs	[1]70ZnO-30CuO NCs
1.6	*22.33 ± 0.01	*45.66 ± 0.02	*38.22 ± 0.02	*8.54 ± 0.01	*18.94 ± 0.01	*8.34 ± 0.01
3.1	*47.74 ± 0.02	*54.05 ± 0.03	*48.06 ± 0.02	*27.38 ± 0.00	*38.72 ± 0.04	*15.03 ± 0.01
6.3	72.74 ± 0.02	*69.16 ± 0.03	*69.17 ± 0.04	*36.76 ± 0.01	44.69 ± 0.04	*26.95 ± 0.01
12.5	79.66 ± 0.04	*79.10 ± 0.04	*81.76 ± 0.02	*44.71 ± 0.02	48.49 ± 0.03	*44.78 ± 0.01

[1]200 mL of 3.1 × diluted POME was used.
[2]300 mL of 3.1 × diluted POME was used.
"*" represent significant difference at $p < 0.05$.

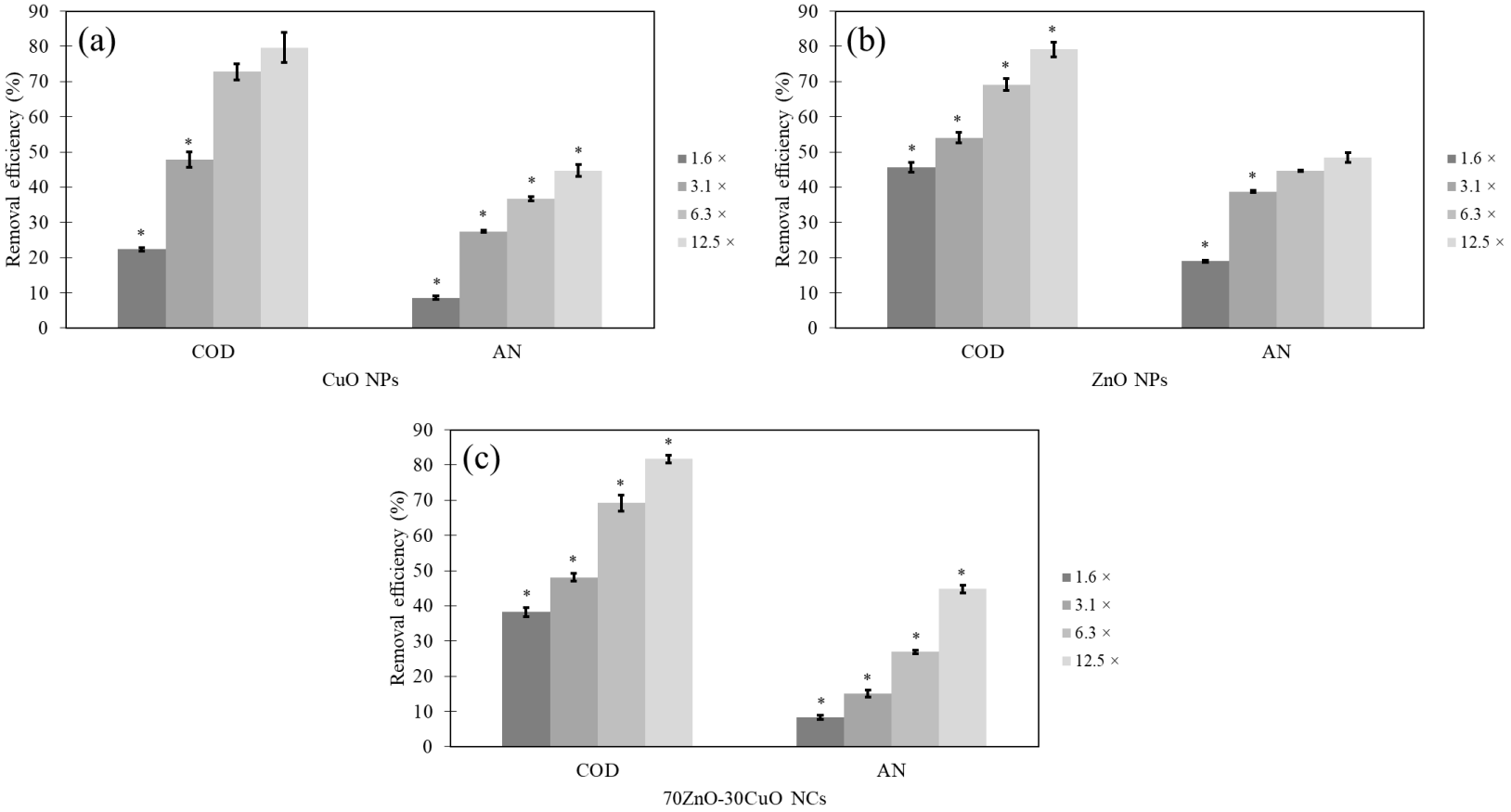

Figure 4.42: The removal efficiency of COD and AN was evaluated using (a) 100 mg of CuO NPs of 200 mL of POME, (b) 50 mg of ZnO NPs at 300 mL of POME and (c) 100 mg of 70ZnO-30CuO NCs in 200 mL of POME at varying concentrations under blue LED for 2 h. Note that "*" represent significant difference at $p < 0.05$.

4.3.5 Photodegradation Durations

The 100 mg of CuO NPs and 70ZnO-30CuO NCs in 200 mL of 3.1 × diluted POME were improved to 58.58% ± 0.02 (85.33 mg/L ± 4.04) and 59.72% ± 0.02 (83.00 mg/L ± 5.20), respectively as well as nitrogenous compounds reduction rate increased to 38.86% ± 0.01 (1.44 mg/L ± 0.03) and 27.80% ± 0.01 (1.70 mg/L ± 0.05), under blue LED for 150 min. However, their effectiveness in degrading pollutants dropped at 180 min. In contrast, the effectiveness of 50 mg ZnO NPs in reducing harmful compounds in 300 mL of 3.1 × diluted POME did not improve after 120 min of blue LED exposure (**Table 4.17** and **Table 4.18**). Its reduction rates dropped slightly and remained similar after 120 min. Their results were shown in **Figure 4.43** and **Figure 4.44**.

Table 4.17: The COD and AN removal efficiencies were assessed using 100 mg of CuO NPs, 50 mg of ZnO NPs and 100 mg of 70ZnO-30CuO NCs under blue LED for 3 h at POME diluted to 3.1 ×.

Duration	COD (%)			AN (%)		
(min)	[1]CuO NPs	[2]ZnO NPs	[1]70ZnO-30CuO NCs	[1]CuO NPs	[2]ZnO NPs	[1]70ZnO-30CuO NCs
0	*0.00 ± 0.00	*0.00 ± 0.00	*0.00 ± 0.00	0.00 ± 0.00	*0.00 ± 0.00	0.00 ± 0.00
30	*15.21 ± 0.01	*15.21 ± 0.02	*16.67 ± 0.02	1.00 ± 0.01	*3.24 ± 0.01	0.71 ± 0.00
60	*23.63 ± 0.01	*29.78 ± 0.01	*25.41 ± 0.02	*3.68 ± 0.01	*12.61 ± 0.01	*1.40 ± 0.02
90	*30.10 ± 0.01	*40.13 ± 0.01	*39.81 ± 0.02	*13.74 ± 0.01	*24.10 ± 0.01	*3.82 ± 0.01
120	*47.74 ± 0.02	*54.05 ± 0.03	48.06 ± 0.02	*27.38 ± 0.00	*38.72 ± 0.00	15.03 ± 0.01
150	*58.58 ± 0.02	48.06 ± 0.02	*59.72 ± 0.02	*38.86 ± 0.01	37.85 ± 0.01	*27.80 ± 0.01
180	*53.40 ± 0.01	48.87 ± 0.01	45.95 ± 0.00	*30.49 ± 0.00	38.43 ± 0.01	16.59 ± 0.01

[1]200 mL of 3.1 × diluted POME was used.
[2]300 mL of 3.1 × diluted POME was used.
"*" represent significant difference at $p < 0.05$.

Table 4.18: The COD and AN removal efficiencies were assessed using 100 mg of CuO NPs, 50 mg of ZnO NPs and 100 mg of 70ZnO-30CuO NCs under blue LED for 3 h at POME diluted to 3.1 × diluted POME in C_t/C_i.

Duration	COD			AN		
(min)	[1]CuO NPs	[2]ZnO NPs	[1]70ZnO-30CuO NCs	[1]CuO NPs	[2]ZnO NPs	[1]70ZnO-30CuO NCs
0	*1.00 ± 0.00	*1.00 ± 0.00	*1.00 ± 0.00	1.00 ± 0.00	*1.00 ± 0.00	1.00 ± 0.00
30	*0.85 ± 0.01	*0.85 ± 0.02	*0.83 ± 0.02	0.99 ± 0.01	*0.97 ± 0.01	0.99 ± 0.00
60	*0.76 ± 0.01	*0.70 ± 0.01	*0.75 ± 0.02	*0.96 ± 0.01	*0.87 ± 0.01	*0.99 ± 0.02
90	*0.70 ± 0.01	*0.60 ± 0.01	*0.60 ± 0.02	*0.86 ± 0.01	*0.76 ± 0.01	*0.96 ± 0.01
120	*0.52 ± 0.02	*0.46 ± 0.03	0.52 ± 0.02	*0.73 ± 0.00	*0.61 ± 0.00	0.85 ± 0.01
150	*0.41 ± 0.02	0.52 ± 0.02	*0.40 ± 0.02	*0.61 ± 0.01	0.62 ± 0.01	*0.72 ± 0.01
180	*0.47 ± 0.01	0.51 ± 0.01	0.54 ± 0.00	*0.70 ± 0.00	0.62 ± 0.01	0.83 ± 0.01

[1]200 mL of 3.1 × diluted POME was used.
[2]300 mL of 3.1 × diluted POME was used.
"*" represent significant difference at $p < 0.05$.

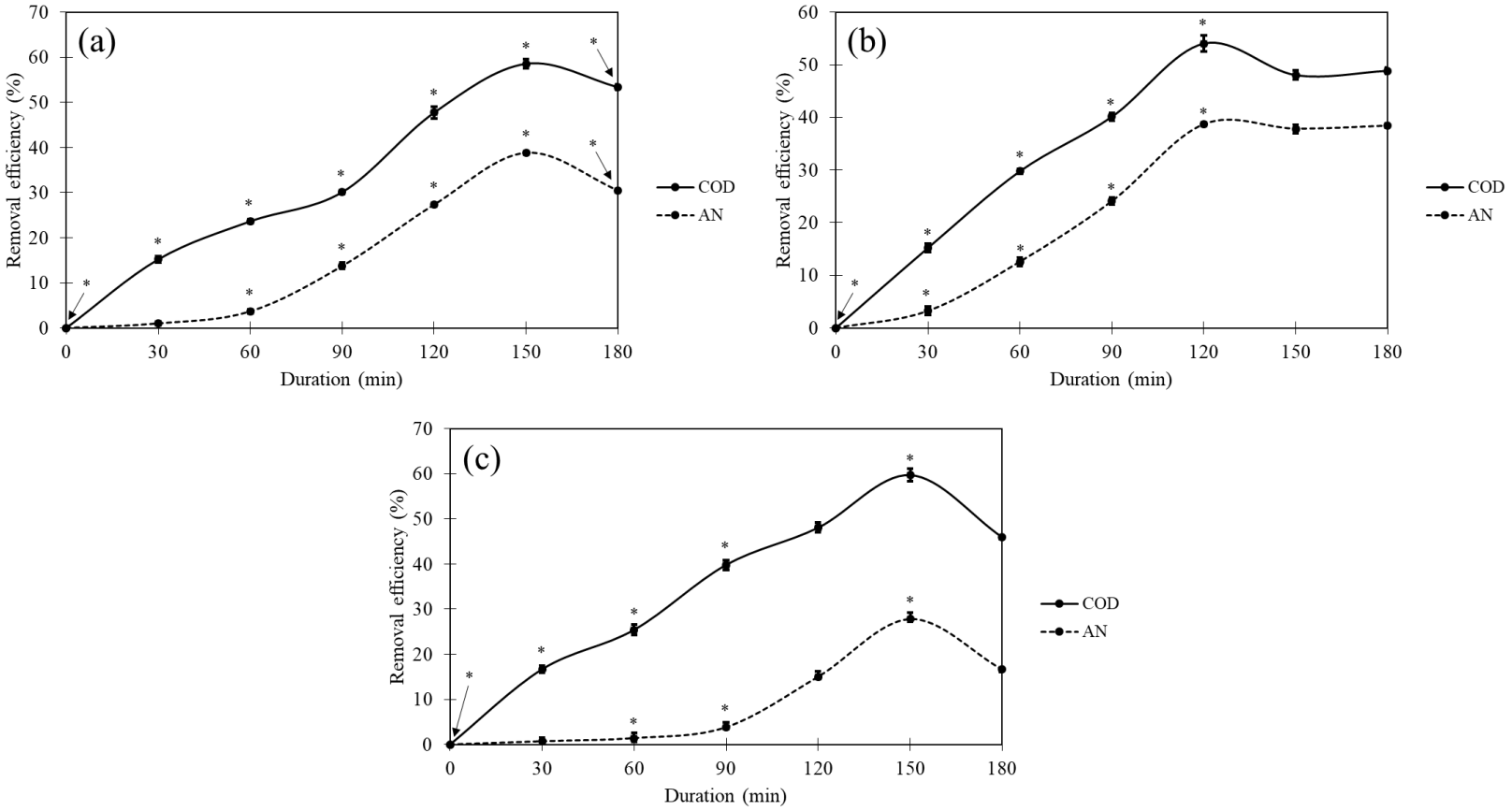

Figure 4.43: The removal efficiency of COD and AN was evaluated using (a) 100 mg of CuO NPs of 200 mL of POME, (b) 50 mg of ZnO NPs at 300 mL of POME and (c) 100 mg of 70ZnO-30CuO NCs at 200 mL of POME diluted to 3.1 × diluted under blue LED for 3 h. Note that "*" represent significant difference at $p < 0.05$.

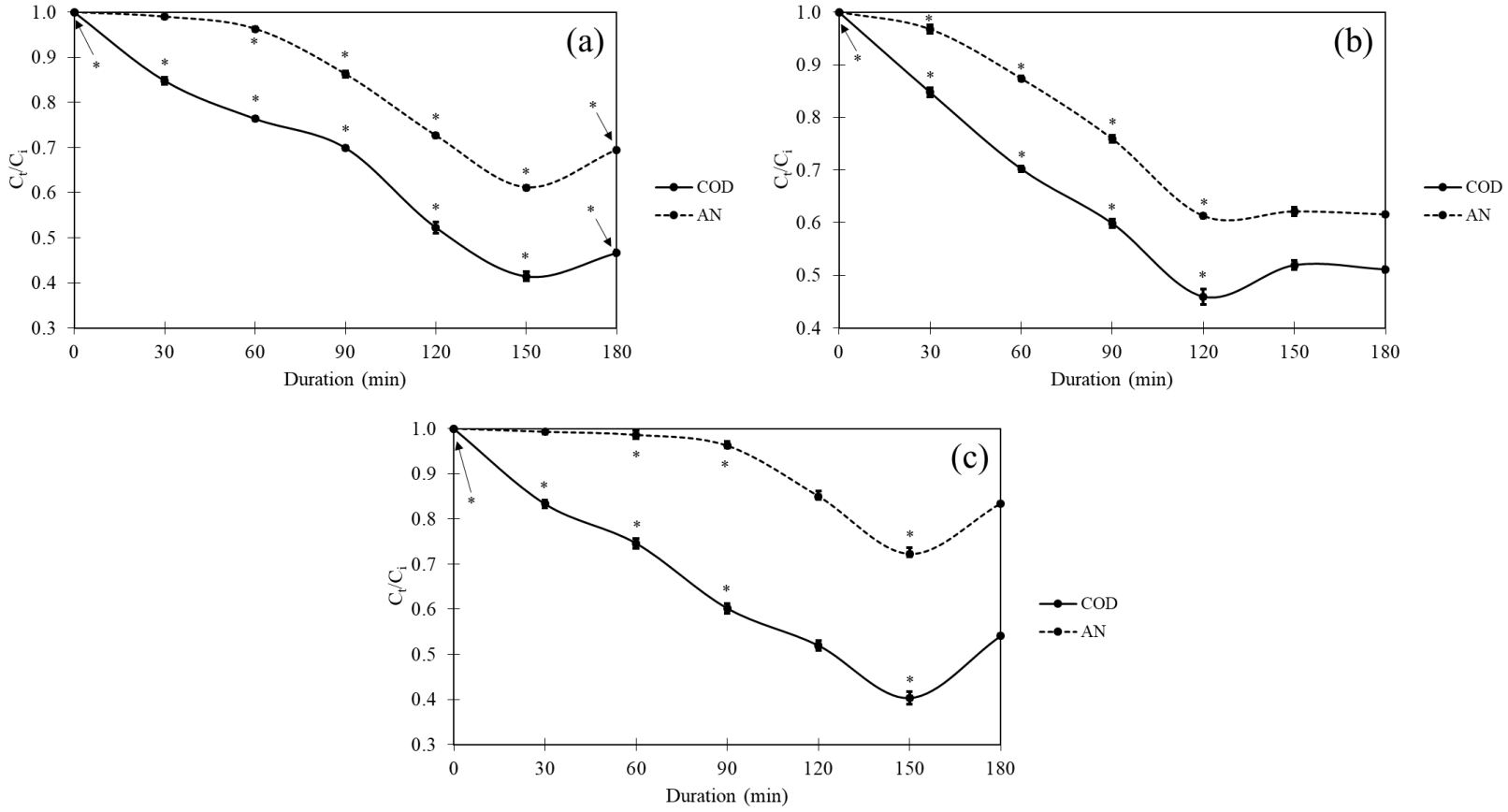

Figure 4.44: The C_t/C_i of COD and AN was evaluated using (a) 100 mg of CuO NPs of 200 mL of POME, (b) 50 mg of ZnO NPs at 300 mL of POME and (c) 100 mg of 70ZnO-30CuO NCs at 200 mL of POME diluted to 3.1 × under blue LED for 3 h. Note that "*" represent significant difference at $p < 0.05$.

4.3.6 Phytotoxicity Study

As shown in **Table 4.19**, the mung bean seeds' germination rate in 70ZnO-30CuO NCs was 60.00%, higher than CuO NPs (50.00%) and ZnO NPs (50.00%) in 12.5 × diluted POME. Comparatively, untreated 12.5 × diluted POME had the lowest mung bean seeds' germination rate at 40.00%, while tap water (as control) had 90.00% of mung bean seeds' germination rate. Additionally, mean shoot length germinated at tap water was 9.79 cm ± 3.21, shorter than nanomaterials treated 12.5 × diluted POME. Particularly, 70ZnO-30CuO NCs treated 12.5 × diluted POME had the longest mean shoot length (10.68 cm ± 4.35), followed by CuO NPs treated (10.52 cm ± 4.64) and ZnO NPs (9.84 cm ± 5.52). In contrast, untreated 12.5 × diluted POME had the shortest mean shoot length recorded at 6.83 cm ± 1.19. In SHSI analysis, nanomaterials treated 12.5 × diluted POME exceeded 100.00% (100.52 – 109.14%), while untreated one was 69.72%. Similarly, nanomaterials treated 12.5 × diluted POME did not inhibit the growth of shoot (negative shoot phytotoxicity percentage from -0.52% to -9.14%), but untreated one shown 30.28% of shoot inhibition. **Figures 4.45** and **4.46** shown the mung bean seeds germination rate and mean shoot length, respectively, at different treatment conditions after seven day. Meanwhile, **Figure 4.47** shown the growth of mung bean seed with their shoot length in tap water (positive control), treated and untreated 12.5 × diluted POME.

Table 4.19: Phytotoxicity study untreated and treated 12.5 × diluted POME by using mung bean seeds.

Samples	Germination rate (%)	Mean shoot length (cm)	SHSI (%)	Shoot phytotoxicity (%)
Tap water (Positive control)	*90.00 ± 0.10	9.79 ± 3.21	100.00	0.00
Untreated	40.00 ± 0.10	6.83 ± 1.19	69.72	30.28
CuO NPs	50.00 ± 0.10	10.52 ± 4.64	107.47	-7.47
ZnO NPs	50.00 ± 0.10	9.84 ± 5.52	100.52	-0.52
70ZnO-30CuO NCs	60.00 ± 0.10	10.68 ± 4.35	109.14	-9.14

"*" represent significant difference at $p < 0.05$.

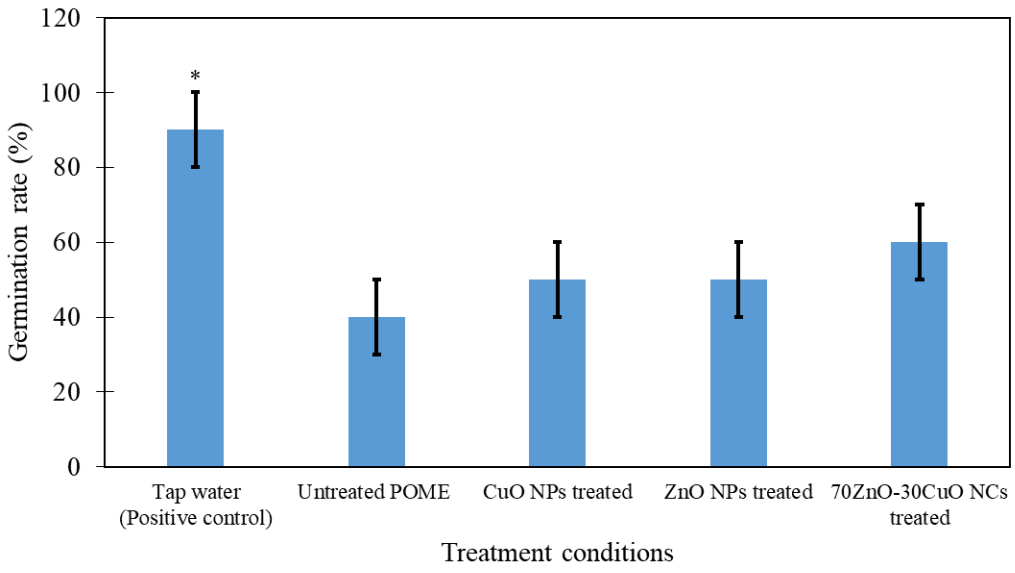

Figure 4.45: Germination rate of mung bean seeds in untreated and 12.5 × diluted POME-treated conditions after seven days. Note that "*" represent significant difference at $p < 0.05$.

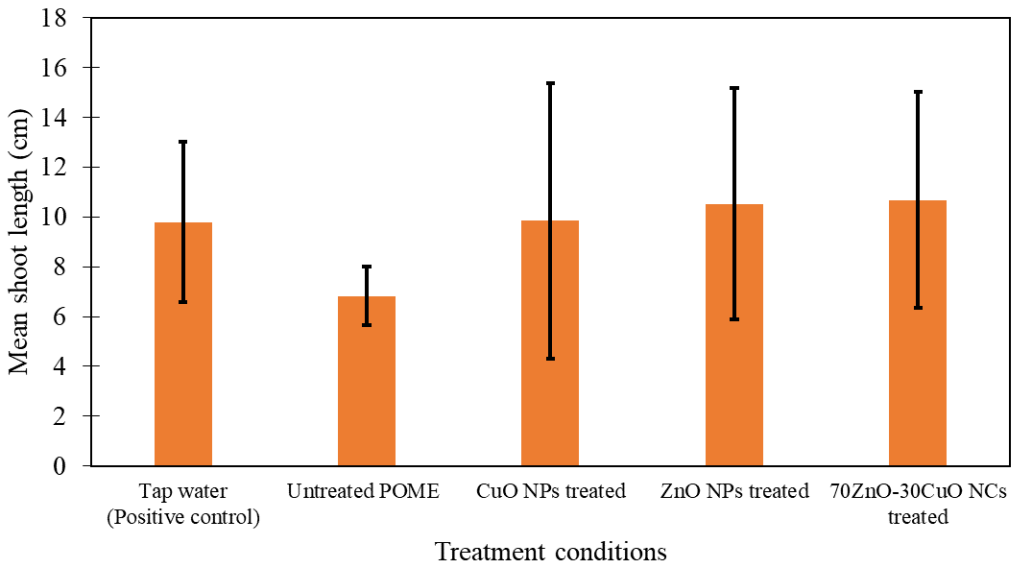

Figure 4.46: Mean shoot length of mung bean seeds in untreated and 12.5 × diluted POME-treated conditions after seven days.

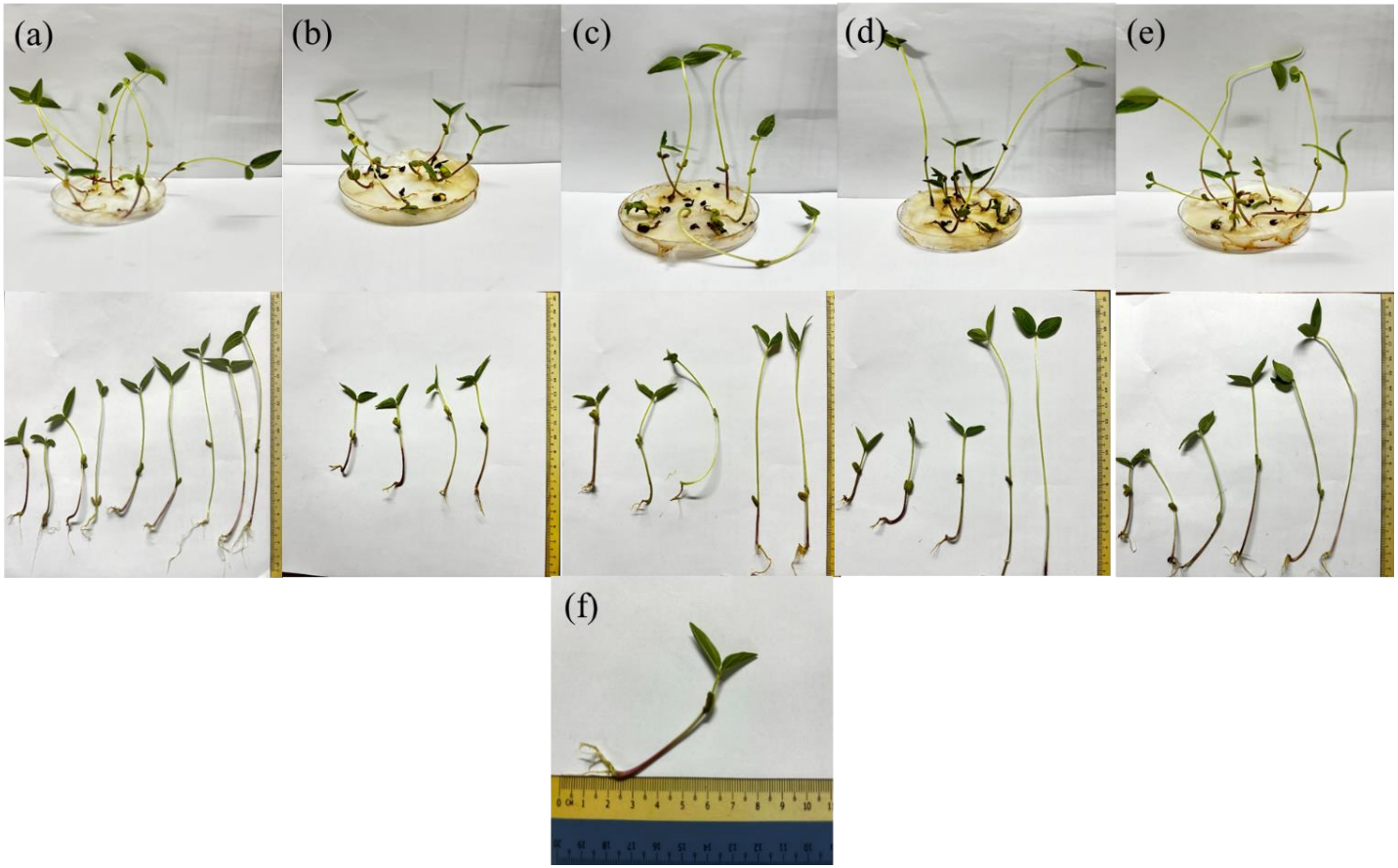

Figure 4.47: Growth of mung bean seeds was evaluated in (a) tap water (positive control), (b) untreated 12.5 × diluted POME, (c) CuO NPs treated 12.5 × diluted POME, (d) ZnO NPs treated 12.5 × diluted POME, (e) ZnO-CuO NCs treated 12.5 × diluted POME and (f) measurement of shoot length.

CHAPTER 5

DISCUSSION

5.1 Physicochemical Properties of Nanomaterials

The effect of different parameters during green synthesis on nanomaterials physicochemical properties were discussed as below.

5.1.1 UV-Vis Analysis and Energy Bandgap Study

The appearance of absorption peak in MLE (**Figure 4.1**) was due to the $\pi \rightarrow \pi^*$ transitions of phytochemicals (Rajendran et al., 2021). The formation of nanomaterials was confirmed by the colour changes of the MLE (Georgia et al., 2023). After adding $Cu(NO_3)_2 \cdot 3H_2O$ and/or $Zn(NO_3)_2 \cdot 6H_2O$ to MLE, the light brown plant extract immediately changed to brownish, revealed the formation of Zn^0 and Cu^0 after the Zn^{2+} and Cu^{2+} reduction by the presence of phytochemicals in the MLE. Consequently, the Zn^0 and Cu^0 were oxidized into ZnO, CuO and ZnO-CuO, respectively. The nanomaterials' absorption peaks were detected when electrons were transferred from the valance band to the conduction band in nanomaterials (Senthilkumar et al., 2017b) due to the occurrence of SPR phenomena at specific wavelength (Basit et al., 2023; Georgia et al., 2023; Kureshi

et al., 2021; Sivakavinesan et al., 2021; Takele et al., 2023; Trang et al., 2021). The SPR occurred when incident electromagnetic radiation wavelength was larger than size of particle and related to the collective oscillation of electromagnetically induced free conduction band electrons in nanomaterials (Basit et al., 2023). Thus, differences in crystallinity, crystalline size, morphology and presence of defects explained the different wavelength detected in nanomaterials (Mrabet et al., 2023). The bathochromic shifting of the nanomaterials' absorption peaks were also caused by the non-bonding electrons of phytochemicals to metal's unoccupied *d*-orbital and resulting in simplified electrons transitions (Khan et al., 2020) as shown in **Figures 4.2** – **4.6** compared to MLE (**Figure 4.1**). The bathochromic shift of ZnO-CuO NCs also caused by the generation of O vacancies and localized energy states in ZnO (Dien et al., 2023).

The dropping in energy bandgap when utilizing concentrated MLE was supported by other studies due to the presence of distinct phytochemicals (Demissie et al., 2020; Soto-Robles et al., 2019). Additionally, increased in concentration of localized states in the band structure and width due to the increment in surface dangling bond counts, resulted in decreasing energy bandgap of nanomaterials at elevated calcination temperature (Bano and Pillai, 2020). The presence of CuO as an impurity in reducing energy bandgap of ZnO-CuO NCs (Elemike et al., 2019; Yulizar et al., 2018) is due to the occurrence of bandgap narrowing effect when the impurity band is formed by the overlapped impurity states (Ayalew, 2004). The energy bandgap decrement effect became significant at more concentrated MLE concentration, higher calcination temperature and lower Zn-to-Cu ratio applied.

The increment in energy bandgap in 50ZnO-50CuO NCs could be explained by the degeneracy effect in heavily percentage of impurity in the NCs (Harmon et al., 1994).

Energy bandgap in CuO NPs greater than its bulk size was explained by the quantum confinement effect, which happened when the crystalline size was lower than the excited e^-/h^+ pair Bohr radius. This led to an increase in energy bandgap as particle size decreased (Mrabet et al., 2023). In contrast, more O deficiency, higher lattice strain, smaller grain size and greater surface roughness explained smaller energy bandgap in ZnO NPs compared to CuO NPs (Jaithon et al., 2024). By comparing the energy bandgap of nanomaterials at different calcination temperature, the strong ionicity between cation and anion caused the splitting of dangling bond orbitals resulted in a large energy bandgap in pure MO NPs. In contrast, in heterojunction NCs, the additional of impurities resulted in secondary bonding-antibonding interaction and removal of dangling bonds, gave rose by the extra interactions with occupied or unoccupied orbitals (Lany, 2015). The electrons transferred from occupied valence band to the defects' energy level rather than transition of electrons form occupied valence band to empty conduction band (Mrabet et al., 2023). Additionally, it was widely known that the splitting of each level to sub-levels equal to the number of interacting atoms could cause band overlap in hetero-structured NCs. Therefore, in accordance with the energy bandgap theory, NC's energy bandgap ought to rise or fall (Rao and Ravikumar, 2020). Consequently, low energy states and ionization energies in synthesized ZnO-CuO NCs was caused by strong interfaces between CuO and ZnO. The

interactions between band electrons in the NCs and electrons in the localized *d*-orbital of Cu ions, which are replacing Zn ions, could potentially be the another reason for the significantly small energy bandgap in synthesized ZnO-CuO NCs (M. I. Khan et al., 2021).

The selected nanomaterials have the good charge separation and transferring due to their inner electric field (Dien et al., 2023; Li et al., 2023; Mrabet et al., 2023). They were thermodynamically favoured to the formation of •OH and $\bullet O_2^-$ radicals (Nguyen et al., 2023) as shown in **Figures 4.7 – 4.9**. Moreover, crystalline size of nanomaterials below 20 nm has distinct physical properties from its bulk which results in great research interest in various applications, including photodegradation (Kumar and Pandey, 2017).

5.1.2 FT-IR Analysis

The detected functional groups on MLE (**Figure 4.10**) was originated from its phytochemicals, such as xanthones, flavonoids, tannins and terpenes (Andani et al., 2021; Diniatik and Anggraeni, 2021; Jassim et al., 2021; Septiningrum et al., 2024; Tran et al., 2021). The broad band at 3410 cm^{-1} indicating the presence of hydroxyl groups in alcohols, phenols or carboxylic acids. The absorption band at 2929 cm^{-1}, 1444 cm^{-1} and 1375 cm^{-1} suggesting the presence of alkanes. A band at 1731 cm^{-1} purposing the presence of carbonyl groups in xanthones or flavonoids. The sharp band at 1619 cm^{-1} and 1526 cm^{-1} support the presence of unsaturated hydrocarbons and aromatic rings associated with polyphenols, respectively. The

band at 1314 cm^{-1} shows the presence of hydroxyl group further supports the presence of phenol. Additionally, the bands between 1200 – 1300 cm^{-1} and 1000 – 1100 cm^{-1} indicating ether or ester linkages in flavonoids or tannins. The bands between 750 – 900 cm^{-1} show substituted aromatic rings further supporting the presence of polyphenolic compounds (Jassim et al., 2021; Marcorius et al., 2022; Septiningrum et al., 2024). In **Figures 4.11 – 4.15**, the changes in the transmittance of the bands in synthesized nanomaterials may be attributed to the variations in the interaction of functional groups from the MLE under different controlled parameters. On the other hand, the bands remain unchanged, showing the suggested phytochemicals' functional groups were responsible for stabilizing nanomaterials during green synthesis primarily through electrostatic and steric mechanism (Chan et al., 2023; Chan et al., 2022; Jaithon et al., 2024; Jassim et al., 2021; Yusefi et al., 2021).

Generally, the MOs bands were located at fingerprint region (below 1000 cm^{-1}), which caused by interatomic vibrations (Nguyen et al., 2023). The position of Cu-O bond vibration (**Figure 4.11**) suggested the lack of Cu_2O (Siddiqui, Ansari, Ansari, et al., 2021) and supported by other studies (Amin et al., 2021; Phang et al., 2021; Ramzan et al., 2021; Selvanathan et al., 2021; Shammout and Awwad, 2021; Sharma et al., 2021; Siddiqui, Ansari, Chauhan, et al., 2021; Veisi et al., 2021). In **Figure 4.12**, the sharp *v*(M-O) indicated strong hexagonal-wurtzite single phase of ZnO NPs (Kaningini et al., 2022) and similar to literature reviews (Abbes et al., 2021; Rajendran et al., 2021; Sajjad et al., 2021). The calculated *v*(M-O) detected in CuO NPs and ZnO NPs were 814 cm^{-1} and 813 cm^{-1}, respectively, higher than

the corresponding experimental values. Similarly, *v*(M-O) frequency in cm^{-1}, ZnO-CuO NCs was 814 cm^{-1} higher than experimental bands location (**Figures 4.13** – **4.15**). The experimental values were different from calculated frequencies due to the presence of resonance, hybridization (Pavia et al., 2015), electron correlation effects and basis set deficiencies (Suresh et al., 2015) in nanomaterials. This also explained the shifting of *v*(M-O) in ZnO-CuO NCs to higher wavenumber in higher ratio of CuO in NCs. The location of Zn-O-Cu bands were supported by other literatures (Basit et al., 2023; Nguyen et al., 2023; Rajith Kumar et al., 2020; Takele et al., 2023).

5.1.3 XRD Analysis

The XRD patterns shown in **Figures 4.16** – **4.20** confirmed the successful of green synthesis of CuO NPs, ZnO NPs and ZnO-CuO NCs, respectively.

Monoclinic-tenorite phase is a mineral that consists of Cu and O and can be obtained by calcinating the Cu minerals at high temperature (Ratnawulan et al., 2017) but seldom reported in other studies (Habibi and Karimi, 2014; Ratnawulan et al., 2017). In contrast, hexagonal-wurzite phase is the most stable and commonly found ZnO NPs state at ambient conditions due to its iconicity was exactly in between covalent and ionic materials (Baharudin et al., 2018; Mansoor Al-Saeedi et al., 2022; Nguyen et al., 2023) and reported in other studies (Abbes et al., 2021; Narath et al., 2021; Sajjad et al., 2021). In hexagonal-wurzite phase, each anion was surrounded by four cations at the tetrahedron corners and shown a tetrahedron

coordination, which was responsible for piezoelectricity and pyroelectricity (Shaba et al., 2021). Consequently, ZnO is in a non-centrosymmetric structure and exhibited sp^3 covalent bonding with a polar surface (Baharudin et al., 2018). On the other hand, according to earlier findings, NCs with lower Cu contents showed a one-phase oxide phase that resembled as wurtzite-like $Cu_xZn_{1-x}O$, but NCs with greater Cu contents showed an oxide phase that resembled as tenorite-like, $Zn_xCu_{1-x}O$ (Adeyemi et al., 2022; Elemike et al., 2019). Thus the ZnO-CuO NCs synthesized were in hexagonal-wurzite phase and similar reported by other researchers (Hitkari et al., 2022).

More well-defined, higher intensity and narrower diffraction peaks indicated the synthesized nanomaterials were well crystalline. This is expected as the removal of organic materials was more effective at elevated calcination temperature. Consequently, the nanomaterials' crystallinity improved at higher calcination temperature (Chan et al., 2022). Moreover, less organic materials content in dilute MLE contributed in boosting 70ZnO-30CuO NCs' crystallinities (G. C. Park et al., 2017). In the synthesized nanomaterials, CuO NPs were preferential crystal planes at (0 0 2) and (1 1 1) (Habibi and Karimi, 2014), whereas strong intensities at (1 0 0), (0 0 2) and (1 0 1) peaks shown that they were preferential crystal planes of ZnO NPs (Yusoff et al., 2020). Specifically, strong intensity at (1 0 1) and (0 0 2) peaks corresponded to a ZnO crystal structure grown in *a*-direction (Mansoor Al-Saeedi et al., 2022) and *c*-axis (Mrabet et al., 2023), respectively. For ZnO-CuO NCs, higher ZnO peaks intensity compared to CuO peaks indicated higher ZnO in ZnO-CuO NCs (Adeyemi et al., 2022) due to the

role of ZnO as a coating material led to lower peaks crystallization of CuO (Cao et al., 2021). The intensities of indexed CuO peaks were improved as Cu ratio was increased in ZnO-CuO NCs reflecting the contribution of Cu in the formation of heterojunction nanomaterials (Bekru et al., 2022; Hitkari et al., 2022; Fouda et al., 2020) and its higher weight percentage in the formation of NCs (Mohammadi-Aloucheh et al., 2018a; Mohammadi-Aloucheh et al., 2018b).

The decreased in ZnO NPs' crystalline size at elevated calcination temperature could be explained by the effective of phytochemicals in capping and stabilizing nanomaterials (Demissie et al., 2020). Additionally, decrement crystalline size in 70ZnO-30CuO NCs at increasing MLE concentration or calcination temperature was due to the successful cooperation of CuO and ZnO during the green synthesis (Kaningini et al., 2022). The mismatch in the sizes of Zn and Cu atoms resulting in non-uniform lattice distortion and crystal phase dislocation (Hitkari et al., 2022; Siddiqui, Ansari, Ansari, et al., 2021). Thus, high number of interfaces in each nanomaterial's volume led to small NC's crystalline size (Chan et al., 2022) and increase in micro strain level (Siddiqui, Ansari, Ansari, et al., 2021). However, slight increment in the crystalline size of 70ZnO-30CuO NCs calcinated at 600^{o}C was observed due to the tendency for minimization of the interfacial surface energy (Oh et al., 2007). At elevated calcination temperature, the diffusion of atom in nanomaterials resulted in the increasing nuclei formation with the grain boundary separated by pores. However, when the calcination temperature constantly increased, the grain boundary finally disappeared resulted in crystalline size increased (Kim et al., 2021; Ratnawulan et al., 2017). Moreover, the process

such as agglomeration, re-crystallization, aggregation and particles' growth at high calcination temperature can cause the increased in nanomaterials' crystalline size (Bano and Pillai, 2020; Saravanan and Sivasankar, 2016). This phenomena indicated the stability of nanomaterials' crystals improved at high calcination temperature (Hamid et al., 2021). The aforementioned explanations were same applied in explaining the increasing crystalline size in CuO NPs at elevated temperature in this study. On the other hand, the relative similar crystalline sizes of ZnO-CuO NCs in different Zn-to-Cu ratios (expect 70ZnO-30CuO NCs) was different from those reported in Fouda et al. study (2020). The crystalline sizes of ZnO-CuO NCs decreased with the addition of more Cu precursor (Kaningini et al., 2022) during their synthesis (Fouda et al., 2020).

Dislocation densities and micro strains of nanomaterials are related to their crystalline sizes (Chan et al., 2023; Chan et al., 2022). The number of interfaces in a given volume is greater in smaller crystalline size (Velsankar et al., 2020) which implies more flaws (Chan, Aminuzzaman, Khalilur Rahman, et al., 2024). Similarly, micro strain can give information about the defects present in the lattice. Lower micro strain indicated less defects in the nanomaterials (Bano and Pillai, 2020).

5.1.4 FE-SEM with EDX and HR-TEM Analyses

The single phase of nanomaterials explained the monodispersed smooth surface of CuO NPs, ZnO NPs and ZnO-CuO NCs (Ahn et al., 2022) as shown in **Figures 4.21** – **4.25**. High viscosity of plant extract (Siddiqui, Ansari, Chauhan, et

al., 2021), surface physicochemical characteristics (Phang et al., 2021; Sajjad et al., 2021; Sharma et al., 2021; You et al., 2021), strong force of attraction (Aminuzzaman et al., 2021; Yusefi et al., 2021), MO nanomaterials oxidation (Ramzan et al., 2021) and occurrence of isotropic aggregation at isoelectric point (Mrabet et al., 2023; You et al., 2021), kept the synthesized nanomaterials firmly bound together to form a nanostructure that was almost spherical (Kaningini et al., 2022). This explained spherical structure formed in nanomaterials, especially at higher MLE concentration or calcination temperature. Moreover, green-synthesized nanomaterials aggregation potentially caused by nucleation of Zn and Cu ions during the reduction of salt precursors by the phytochemicals from the MLE (M. I. Khan et al., 2021). This proved the capping and reducing properties and ability of phytochemicals during the green synthesis of nanomaterials. Additionally, the aggregation of synthesized nanomaterials might be caused by the excess hydrogen cations from the moisture surface of nanomaterials (Ahn et al., 2022). Additionally, the escaping of gases at higher calcination temperature contributed to the pore development in ZnO NPs (Basavalingiah et al., 2019), which was similar to other findings (Mfon et al., 2020; Y. Wang et al., 2021). Disappearance of the grain boundary area of particles resulted in crystal surface energy decrement during the aggregation under high calcination temperature. As a result, pore volume in particles decreased and resulted in compact shrinkage. Consequently, bulky structure was observed at high calcination temperature (Baharudin et al., 2018; Oh et al., 2007).

The presence of Zn, Cu and oxygen peaks in CuO NPs, ZnO NPs and ZnO-CuO NCs in the EDX spectra (**Figures 4.26** – **4.30**) indicated the purity of green-synthesized nanomaterials (Adeyemi et al., 2022). Oxygen signal in the EDX spectra provided proof that the nanomaterials were in oxidized form (Adeyemi et al., 2022). The weight percentage of Zn-to-Cu ratio detected in ZnO-CuO NCs were comparable to the Zn and Cu precursors added during the green synthesis, revealed the cooperation of CuO within ZnO in desired ratio (Das and Srivastava, 2017). Meanwhile, the weak signal of C was due to the burning of organic materials during the calcination and the soot was left over as impurities (Siddiqi and Husen, 2020). On the other hand, organic materials were suggested totally burnt using less concentrated MLE in green synthesizing nanomaterials due to its lower content of phytochemicals.

The successful of cooperation of CuO into ZnO (as explained in **Section 5.1.3**) pores interfered the particle size by increasing the particle size of selected ZnO-CuO NCs, resulted in bigger particle size than selected ZnO NPs but smaller particle size than selected CuO NPs (**Figures 4.31** – **4.33**).

5.1.5 XPS Analysis

The detection of Cu $2p_{3/2}$ and Cu $2p_{1/2}$ correlated to the Cu^{2+} valence state, while the 20.25 eV (CuO NPs) and 20.10 eV (ZnO-CuO NCs) difference of both peaks matches with other studies. Moreover, the appearance of satellite peaks confirmed the presence of the d^9 Cu^{2+} fingerprint caused by the relaxation

circumstance of the strong alignment interaction in the final state revealed that they were the shake-up satellites of Cu^{2+} (Phang et al., 2021; Selvanathan et al., 2021). On the other hand, for ZnO NPs and ZnO-CuO NCs, the presence of binding energies of Zn $2p_{3/2}$ and Zn $2p_{1/2}$ indicated the presence of Zn^{2+}. Furthermore, the difference of the peaks (23.1 eV) represented the Zn 2*p* spin-orbit splitting energy (Chan, Aminuzzaman, Khalilur Rahman, et al., 2024). Nonetheless, the lower binding energy of O 1*s* indicated O^{2-} the presence of M-O bonding, whereas higher binding energy revealed adsorbed O on the MO surface (**Figures 4.34** – **4.36**). Hence, the presence of zinc hydroxide, Cu (I) oxide and Cu hydroxide were excluded in the nanomaterials (Narath et al., 2021; Phang et al., 2021; Selvanathan et al., 2022; Selvanathan et al., 2021; Y. Wang et al., 2021).

5.2 Preliminary *in vitro* Antibacterial Activity

The antibacterial activity of nanomaterials are intricately influenced by their physicochemical properties, including the generation of ROS, surface area, particle size, solubility, surface charge and more (Masri et al., 2022; Rajith Kumar et al., 2020). These unique properties of MO nanomaterials, such as their small particle size, nanomaterial stability, Van der Waals forces, hydrophobic interactions and electrostatic attraction, contribute to their antibacterial activity through various mechanisms (Niño-Martínez et al., 2019). The structural differences between Gram-positive and Gram-negative bacteria are responsible for this variation in susceptibility; Gram-positive bacteria have simpler and thinner cell walls, which

makes them more vulnerable to antibacterial agents (Silhavy et al., 2010). The results indicated that ZnO NPs exhibited the most potent antibacterial activity among the synthesized nanomaterials, possibly attributed to the presence of porosity in ZnO NPs, which provided a high surface-to-volume ratio for effective interaction with the tested bacteria. Additionally, it was suggested by Govindasamy et al. (2020) that Zn^{2+} ions diffused more readily into the medium compared to Cu^{2+} ions, which could explain the prolonged duration required for Cu^{2+} to diffuse out from CuO NPs into the medium to exert antibacterial effects (Govindasamy et al., 2020).

5.3 Photocatalytic Performance in POME Treatment

The removal efficiency of organic matters (represented by COD) and nitrogenous compounds (represented by AN) by selected nanomaterials, including CuO NPs calcinated at 500ºC, ZnO NPs calcinated at 400ºC and 70ZnO-30CuO NCs green synthesized using 0.05 g/mL of MLE calcinated at 500ºC, at different treatment parameters were discussed as below.

5.3.1 Selection of LEDs

The e^-/h^+ formation is predominant and its recombination is negligible at low light intensity (0 – 20 mW/cm^2) (Kumar and Pandey, 2017) and this explained nanomaterials were able to well-degrade pollutants at blue and white LEDs

exposure, respectively. Generally, to create most white light diodes, an LED that emits light at a short wavelength is combined with a wavelength converter to create a longer wavelength secondary emission (Davidson, n.d.). As a result, monochromatic blue LED provided higher photon energy than polychromatic white LED. Consequently, lower pollutants removal efficiency was recorded using nanomaterials under polychromatic white LED compared to monochromatic blue LED (**Figure 4.39**). Narrow energy bandgap and existence of O vacancies found in heterojunction NCs contributed in high pollutant removal efficiency. The combination of wide energy bandgap of ZnO in synthesized 70ZnO-30CuO NCs prevented the recombination of e^-/h^+ pair. Thus, *n*-ZnO and *p*-CuO in the heterojunction NCs improved the e^-/h^+ pair separation by charge transfer mechanism and intercalation and enhancing the pollutant degradation (Basit et al., 2023; Dien et al., 2023; Li et al., 2023; Mrabet et al., 2023; Nguyen et al., 2023) in POME under LEDs irradiation. Additionally, the recombination of e^-/h^+ was also prevented by the packed structure in synthesized 70ZnO-30CuO NCs that to speed up the electrons flow between the surface (Basit et al., 2023; Dien et al., 2023). Moreover, the addition of CuO in 70ZnO-30CuO NCs enhanced the photocatalytic performance by increasing the carrier trapping sites, resulting in charge separation improvement and extending the carrier lifetime (Dien et al., 2023). On the other hand, lower energy bandgap in CuO NPs was easier to form e^-/h^+ pair in particles and degrade pollutants easily compared to ZnO NPs with larger energy bandgap (Fatima et al., 2017).

5.3.2 Nanomaterial Loadings

As shown in **Figure 4.40**, when the dosage of nanomaterial was increased, more active sites became available resulted in higher rate in photo-excitation and fast generation of •OH and superoxide radicals (Kumar and Pandey, 2017; Tan et al., 2014), which improved the effectiveness of removing pollutants. This was only true when there were free active sites for the adsorption of contaminants. However, with subsequent increased in the dosage of nanomaterial employed, the active sites were completely occupied and the removal efficiency was marginally decreased (Ismail et al., 2023; Sidik et al., 2023). This is because nanomaterial was difficult to move in solutions (Shadi et al., 2020), which led to aggregation and a reduction in the surface area available for pollutant linkage (Ismail et al., 2023; Mrabet et al., 2021; Tan et al., 2014). Additionally, when a greater dosage of nanomaterial was given and reached saturation phase (Sidik et al., 2023), there was insufficient light penetration to reach the nanomaterial due to an increase in solution turbidity (Kashitarash et al., 2012; Kumar and Pandey, 2017; Shahmoradi et al., 2018; Sidik et al., 2023; Tan et al., 2014; Zandsalimi et al., 2019). The amount of photons striking a nanomaterial's surface controls the rate of reaction, thus the surface morphology of the nanomaterial affects the pollutants removal efficiency (Kumar and Pandey, 2017). As aforementioned in ZnO NPs morphological properties, the presence of pores helps in increasing the light dispersion and strengthen the photocatalytic performance (Dien et al., 2023; Estrada-Flores et al., 2020), resulted

in using less dosage of nanomaterial to achieve comparable pollutants removal efficiency with CuO NPs and 70ZnO-30CuO NCs.

5.3.3 POME Volumes

The effect of POME volumes on the photocatalytic performance are rarely discussed by researchers. Its impact on the photocatalytic performance could be related to the increment in POME volume reduced the vacancy nanomaterial's active sites rapidly as more pollutants were adsorbed on the nanomaterial's surface (**Figure 4.41**).

5.3.4 POME Concentrations

Brownish intensity of POME causes by the dissolved organics could affect the photo-degradation process and toxic to receiving water bodies (Aqilah Mohd Razali et al., 2020). The brownish intensity decreased as the POME was more diluted by distilled water. The nanomaterial's active sites in diluted POME were fully exposed to LED irradiation and were not covered by POME molecules, which caused an increase in the production of oxidants on the surface of the nanomaterials to break down the pollutants (Kumar and Pandey, 2017; Shahmoradi et al., 2018; Zandsalimi et al., 2019). Furthermore, because there were more active sites available on the surface of nanomaterial, the adsorption of contaminants increased in diluted POME (Hamadamin et al., 2023). Additionally, when POME was diluted,

less light was absorbed by the POME itself, improving the effectiveness of organic and nitrogenous compounds removal (Shahmoradi et al., 2018). The results were shown in **Figure 4.42**.

5.3.5 Photodegradation Durations

The prolonged reaction time between nanomaterial and pollutants led to an improvement in efficiency as degradation duration increased (Pavithra et al., 2020; Zandsalimi et al., 2019) as shown in **Figures 4.43** and **4.44**. However, the active sites of nanomaterial decreased with irradiation time (Putri et al., 2022; Saputera, Amri, Mukti, et al., 2021). Nanomaterials' pores first were clogged with contaminants due to strong driving force (Ismail et al., 2023). Additionally, more active sites on the nanomaterial enable quick removal effectiveness during the initial degradation time (Ismail et al., 2023; Mrabet et al., 2021; Singh et al., 2021). The consumption of produced oxidants during the pollutants' breakdown or the inhibitory reaction by nanomaterial caused the pollutants removal to stabilize and slow down with irradiation time (Mrabet et al., 2021). Moreover, the competition of degradation might happened between nanomaterial and intermediate products as irradiation time grew (Kumar and Pandey, 2017). Additionally, the pollutants filled the nanomaterial’s active sites as the contact period grew and approached equilibrium, creating forces of repulsion between the two materials (Ismail et al., 2023; Mrabet et al., 2021; Aqilah Mohd Razali et al., 2020; Singh et al., 2021).

5.3.6 Phytotoxicity Study

Soils micronutrients were improved, particularly for phosphorus, calcium, magnesium, sodium, nitrogen, organic Cu, iron and lead, Zn and potassium, after the application of liquid POME (Amirul Alam et al., 2022; Loh et al., 2019; Maliki et al., 2020; Pujono et al., 2021; Variyani et al., 2020). Organic C quantity also enhanced after applying POME to the soil as nutrient to plant (Pujono et al., 2021). Although it has been reported that POME consists of high nutrient content, POME needs to be treated before being utilized as fertilizer (Mohd Hashim and Zaharah, 1994) *via* anaerobic digestion and composting because of the treated POME still consists of significant amount of mineral elements needed for plant growth (Loh et al., 2019). Improvement in plant growth by using treated POME was reported in several studies. In Amirul Alam et al. study (2022), the Brazilian spinach height by using 70% of POME with 15% of cocopeat and 15% of sand was found taller (30.68 cm) than less POME applied soils (28.48 cm and 30.38 cm) and vegetable plant in normal soil had the shorted plant height (27.40 cm). Their vegetable's growth rate also found highest in 70% POME soil (78.00%) compared to others (58.00 – 65.00%) (Amirul Alam et al., 2022). Moreover, kangkung growth was improved by using mixture of treated POME with chicken manure compared to its raw POME mixture and control in Loh et al. study (2019). In their study, high ratio of POME affected the kangkung growth resulted in lower growth than control (Loh et al., 2019). Additionally, tomato plant height was improved by adding more POME to the soil (from 36.67 – 40.45 cm to 55.81 – 59.36 cm) in Maliki et al. study in 2020

(Maliki et al., 2020). Furthermore, oil palm planted in POME applied land was found increased in crude palm oil level of oil palm compared to non-POME applied land in Pujono et al. study (2021) (Pujono et al., 2021).

5.4 Proposed Mechanisms

Mechanisms in green synthesizing nanomaterials, photocatalytic performance in degrading POME by nanomaterials and nanomaterials' antibacterial activity were proposed in below sections.

5.4.1 Green Synthesis of Nanomaterials

The exact route(s) of synthesis nanomaterials is based on phytochemicals, it is hypothesized that nanomaterials were green synthesized *via* bio-reduction. Three stages were involved in green synthesizing nanomaterials through bio-reduction: (1) activation, (2) growth and (3) termination phases. During the activation step, zinc (II) (Zn^{2+}) and copper (II) (Cu^{2+}) ions were released from their own precursors when dissolved in mangosteen leaf aqueous extract. The metal divalent ions were forming metal complexes with the phytochemicals (Chan et al., 2023; Selvanathan et al., 2022) through hydrogen bonding and electrostatic attraction forces (Septiningrum et al., 2024). Consequently, the metal divalent ions decrease to metallic form, indicated by the rapid colour change in mangosteen leaf extract after the addition of precursors. They would instantly oxidized to MO

nanomaterials during the calcination process by the oxygen from the atmosphere or the breakdown of phytochemicals attaches itself to the metals by electrostatic attraction resulting in nanomaterials before the development and stabilization phase because of the increased chemical reactivity of the exposed nanoscale metal surface. Throughout the growth and termination stages, the remaining phytochemicals in mangosteen leaf aqueous extract would cause the MO nanomaterials to aggregate and stabilise (Chan et al., 2023; Parapat et al., 2022). Literature also reported the smaller nearby particles adhered to low-energy faces and crystallize to produce bigger, thermodynamically stable nanomaterials due to the occurrence of Ostwald ripening. The adsorbed phytochemicals were interacted with the metal complexes crystal's facets to produce certain crystal facets that have reduced surface tension and interfacial energy. As a result, the adsorbed phytochemicals altered the surface characteristics of the crystal facets, resulting in an orientation changed and the assembly of the following growth. Thus, the crystal growth in planes of preference and frequent morphologies from green synthesized nanomaterials are wires, cubes, hexagons, pentagons, rods, spheres and triangles (Cao et al., 2019; Fawcett et al., 2017; Jeevanandam et al., 2016; Shah et al., 2015; Singh et al., 2018; Sharma et al., 2019).

In the synthesis of ZnO-CuO NCs, there is no any conclusion was drawn for the formation NCs. After the formation of MOs synthesized through the aforementioned mechanisms, it was hypothesized that coordinate covalent bonds were formed in between ZnO and CuO using the lone-pair electron from their own

oxygen atom to bond the MOs together in forming ZnO-CuO NCs (Chan et al., 2023). The proposed mechanism was shown in **Figure 5.1**.

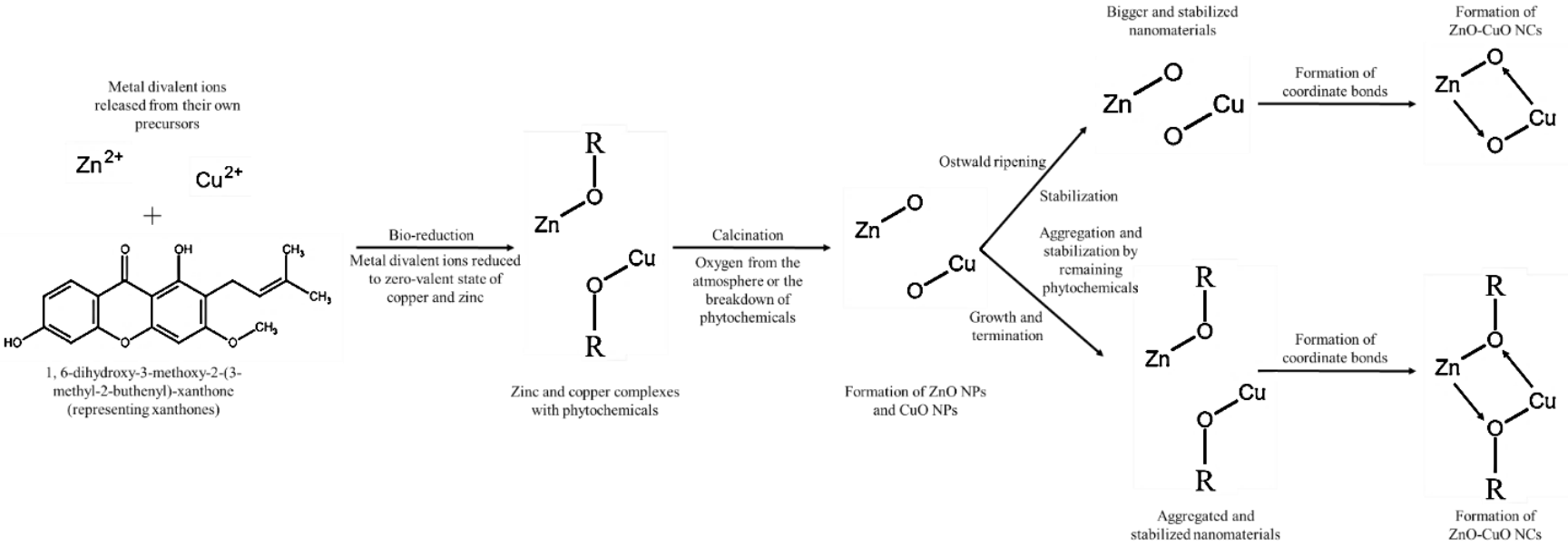

Figure 5.1: Hypothesized mechanisms in green synthesizing nanomaterials using MLE *via* bio-reduction. R was representing 1, 6-dihydroxy-3-methoxy-2-(3-methyl-2-buthenyl) xanthone (xanthone found in mangosteen leaves) in demonstrating the hypothesized mechanisms in green synthesizing nanomaterials. The Zn^{2+} and Cu^{2+} were released upon precursors added to the MLE. During the calcination process, the MOs nanomaterials were formed instantly by reacting with oxygen from atmosphere or the breakdown from phytochemicals. Subsequently, the MOs nanomaterials were also aggregated and stabilized by the presence of remaining phytochemicals in bio-reduction mechanism. Also, the MOs nanomaterials were stabilized and became bigger due to the occurrence of Ostwald ripening. For the formation of ZnO-CuO NCs, the coordinate covalent bond are further formed using the oxygen atoms lone pair in the nano-sized ZnO and CuO to bond themselves resulted in NCs.

5.4.2 Preliminary *in vitro* Antibacterial Activity

Although a definitive antibacterial mechanism for MO nanomaterials remains elusive, it is widely believed that the antibacterial effects stem from direct interactions with bacterial cell membranes, ROS generation and the release of free metal ions from nano-MOs (Amaro et al., 2021; Masri et al., 2022; Shabatina et al., 2022).

As shown in **Figure 5.2**, taking ZnO NPs as an example in the first prepared mechanism, these NPs accumulate in the outer membrane or cytoplasm of bacterial cells, potentially triggering the release of Zn^{2+} ions that attach to biomolecules in the bacterial cell membrane *via* electrostatic forces. This leads to depolarization of the bacterial cell membrane, resulting in cellular leakage. Moreover, an excess of ROS is induced by the formation of metal ions, which penetrate the bacterial cell membrane, causing denaturation in proteins and lipids, genomic instability, disruption of mitochondrial function, interference with bacterial cell metabolic activity and ultimately apoptosis (Cuong et al., 2022; Waris et al., 2020; Xu et al., 2021).

Interestingly, particularly in the case of Cu-containing nanomaterials, it has been reported that the contribution of dissolved metal ions to antibacterial activity is relatively minor. In the second prepared mechanism, the presence of water and oxygen can only dissolve a small amount of Cu^{2+} from CuO NPs. However, more free radicals are promoted and the NPs are converted into metal ions once they enter the acidic lysosomal environment. This process, often referred to as the "Trojan horse mechanism", promotes the formation of intracellular ROS, disrupting the

bacterial cell mitochondrial membrane potential and degrading deoxyribonucleic acid (DNA), ultimately leading to bacterial cell death (Applerot et al., 2012; Cuong et al., 2022; Ma et al., 2022).

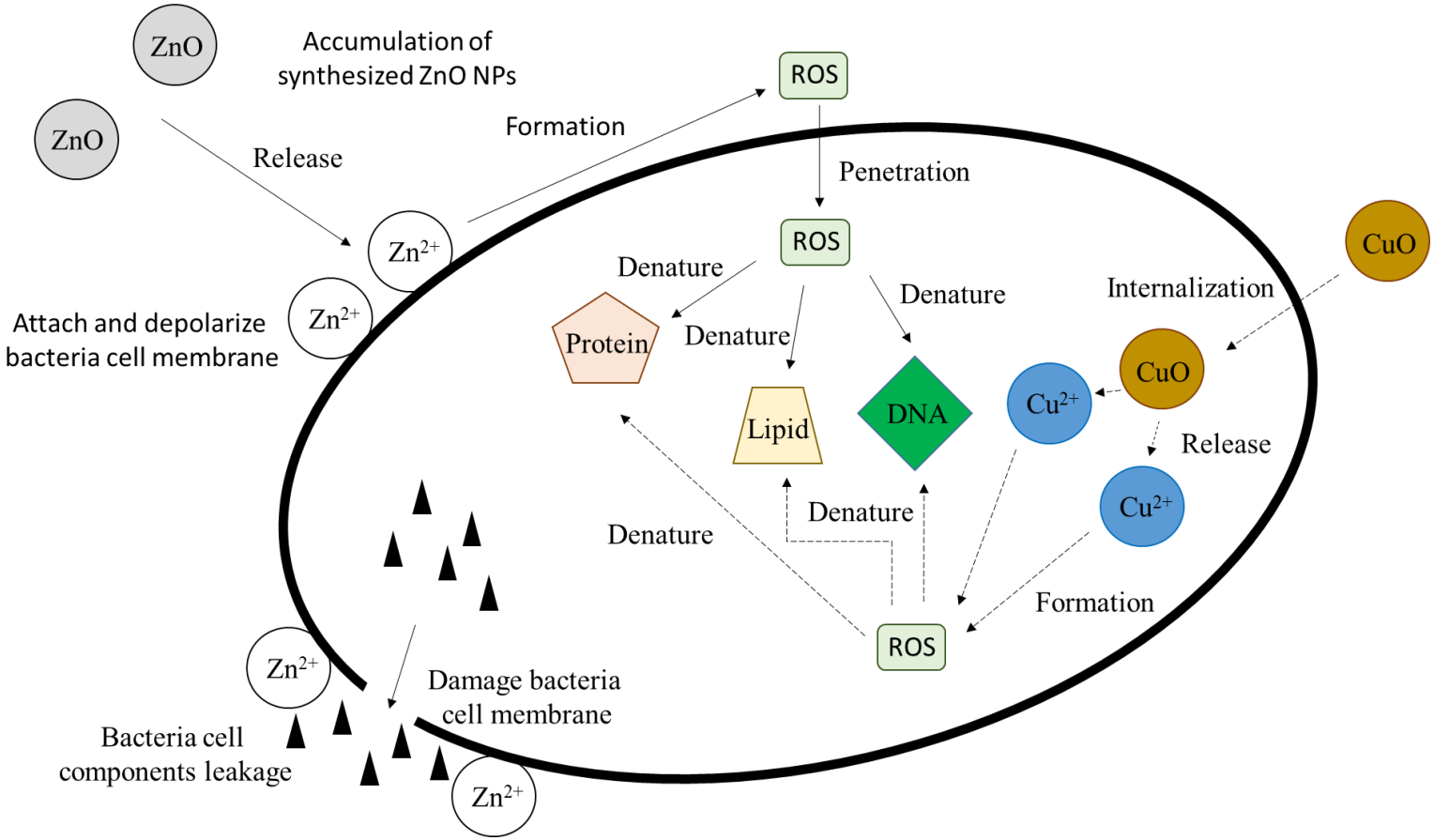

Figure 5.2: Proposed antibacterial mechanisms which include direct contact of bacteria cell membrane, generation of ROS and release of free metal ion from ZnO NPs and CuO NPs. The antibacterial mechanism of ZnO-CuO NCs was suggested is the combination of the above-mentioned mechanism in the scheme (Chan, Aminuzzaman, Khalilur Rahman, et al., 2024).

5.4.3 Photocatalytic Performance in Degrading POME

The band alignment in nanomaterial influences the photocatalytic activity (**Figures 4.7** – **4.9**). The proposed photocatalytic performance mechanism on POME degradation for CuO NPs and ZnO NPs was similar to ZnO-CuO NCs without the inter-transferred of electrons and holes to other particles. Indeed, the holes were intra-transferred within the particle from valance band to conduction band (**Figure 5.3**). During exposure to light, the electrons were promoted to conduction band (CB) and left the holes n the valance band (VB) when energy exceeded the MO bandgap. The electrons in the CB acted as reductants, while the holes in the VB acted as oxidants. Thus, both electrons and holes were taking part in generating ROS by having reaction with oxygen and other species in solution. For example, ROS (•OH and $\bullet O_2^-$) were formed on MO NPs with energy bandgap lower than 3.4 eV when irradiated by UV (365 nm) which carry photon energy of 3.4 eV. As a result, the organic pollutants in wastewater were oxidized. The possible mechanism in degrading organic pollutants by using MO NPs under light exposure was shown in **Equations 17** – **26** (Agustina et al., 2021; Cheng et al., 2021; Dien et al., 2023; Elleuch et al., 2020; Kessler et al., 2022; Li et al., 2023; Mrabet et al., 2021; Nguyen et al., 2023; Saputera, Amri, Daiyan, et al., 2021; Saputera, Amri, Mukti, et al., 2021).

The electrons and holes were formed when light was irradiated on MO NPs.

$$\mathrm{MO} \rightarrow e^- + h^+ \qquad (17)$$

In VB, adsorbed water or hydroxide ion (OH^-) was oxidized by h^+ and •OH was formed. Note that, the water molecule will be dissociated into ion in the presence of high concentration of OH^-.

$$h^+ + H_2O \rightarrow \bullet OH + H^+ \quad (18)$$

$$h^+ + OH^- \rightarrow \bullet OH \quad (19)$$

$$H_2O \rightarrow OH^- + H^+ \quad (20)$$

Meanwhile, oxygen was reduced into $\bullet O_2^-$ by accepting electrons in CB. The generation of oxygen vacancies played the roles in trapping electron and active sites to enhance photocatalytic activity by improving e^-/h^+ pair separation Later, the hydrogen ion (H^+) was reacted with $\bullet O_2^-$ to form hydroperoxyl radical ($\bullet HO_2$) and further forming hydrogen peroxide (H_2O_2). After the formation of H_2O_2, it was photo-converted into •OH.

$$e^+ + O_2 \rightarrow \bullet O_2^- \quad (21)$$

$$\bullet O_2^- + H^+ \rightarrow \bullet HO_2 \quad (22)$$

$$\bullet O_2^- + \bullet HO_2 + H^+ \rightarrow H_2O_2 + O_2 \quad (23)$$

$$H_2O_2 \rightarrow 2 \bullet OH \quad (24)$$

Finally, the generated •OH was responsible in oxidizing adsorbed organic pollutants on the MO NPs' surface into less harmful products. The •OH is very effective in degrading organic pollutants into mineral acids, such as carbon dioxide and water (Chan, Aminuzzaman, Win, et al., 2024). On the other hand, nitrogenous compounds were degraded into nitrogen, nitrate ions and nitrite ions by •OH (Zhang et al., 2024).

$$\bullet OH + \text{Organic pollutants} \rightarrow CO_2 + H_2O + \text{Intermediates} \quad (25)$$

$$\bullet\ OH + \text{Ammonia} - \text{nitrogen} \rightarrow N_2 + NO_3^- + NO_2^- + \text{Intermediates} \quad (26)$$

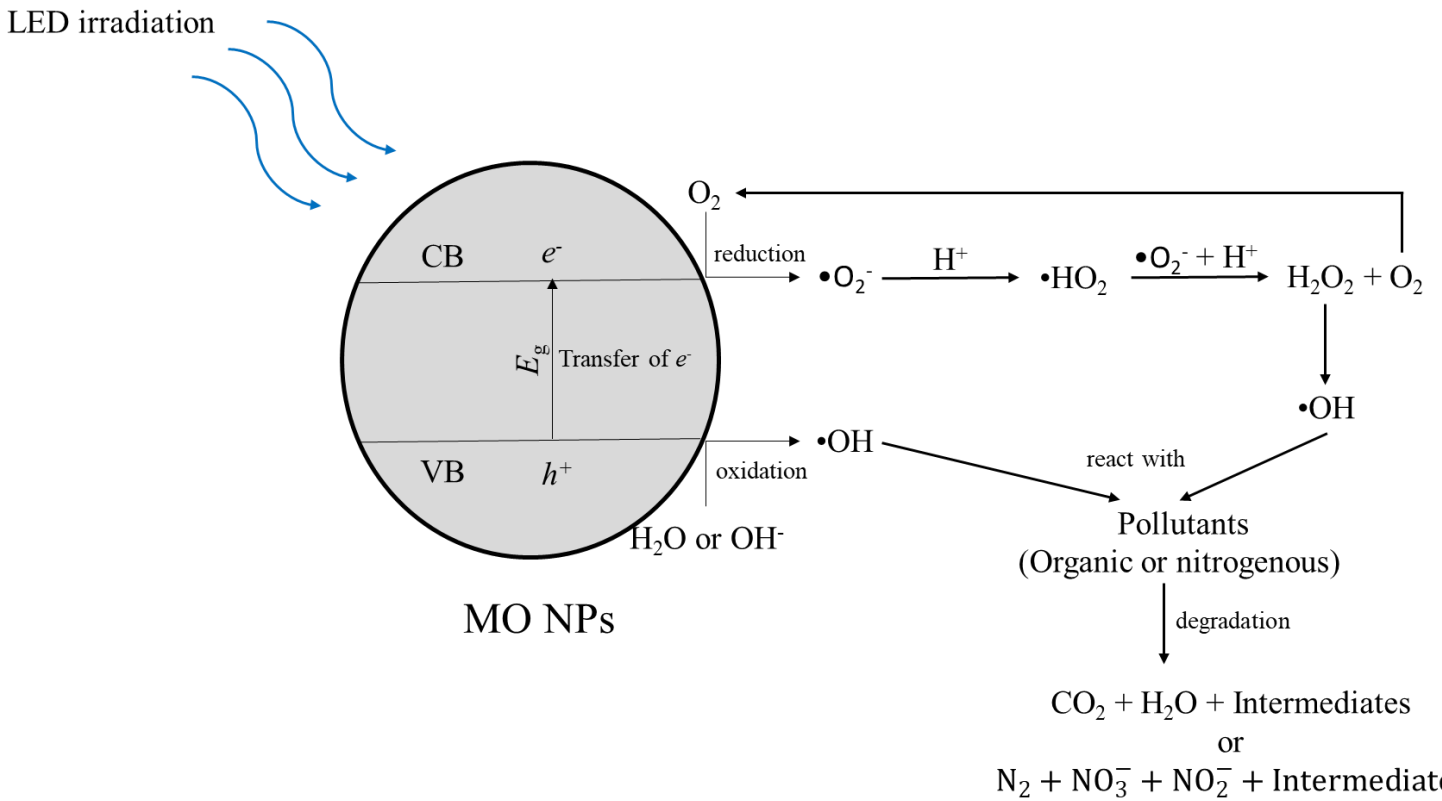

Figure 5.3: Possible mechanism involved in degrading pollutants in POME by using MO NPs. The e^-/h^+ pair was formed at VB and CB when light irradiated on the MO NPs surface. The •OH and $\bullet O_2^-$ were then generated by redox reaction by involving water and oxygen in CB and VB, respectively. For organic compounds, carbon dioxide and water were finally produced with the pollutants intermediates after degraded by •OH. Meanwhile, nitrogenous compounds were degraded into nitrogen, nitrate ions, nitrite ions and intermediates after reacted with •OH.

In ZnO-CuO NCs, the conduction and valance band locations of ZnO NPs was -0.23 and 2.81 eV, respectively, while CuO NPs was -0.22 eV and 2.86 eV, respectively. Considering the redox potential of hydroxyl radicals (•OH, 2.59 eV) and superoxide radicals ($\bullet O_2^-$, -0.16 eV) (Nguyen et al., 2023), it could be concluded that the generation of radicals were thermodynamically favored to ZnO NPs and CuO NPs as their E_{CB} and E_{VB} met the energy requirements. As exposing synthesized ZnO-CuO NCs under LEDs, the formation of holes at valence band (h_{VB}^+) of CuO NPs migrated to ZnO NPs valance band and reacted with water to produce •OH. On the other hand, the electrons in conduction band (e_{CB}^-) of ZnO NPs with high energy migrated to CuO NPs conduction band. The electrons reacted with the absorbed oxygen to form $\bullet O_2^-$. The generation of oxygen vacancies played the roles in trapping electrons and active sites to enhance photocatalytic activity by improving e^-/h^+ pair separation. Eventually, the highly reactive •HO and $\bullet O_2^-$ radicals degraded the pollutants in POME into carbon dioxide, water and intermediate (**Figure 5.4**). The proposed mechanism was supported by Mubeen et al. study in 2023 (Mubeen et al., 2023). The transfer of electrons and holes were in reverse direction in other studies due to their energy bandgap of ZnO was larger than CuO in their green-synthesized ZnO-CuO NCs (Dien et al., 2023; Li et al., 2023; Mrabet et al., 2023).

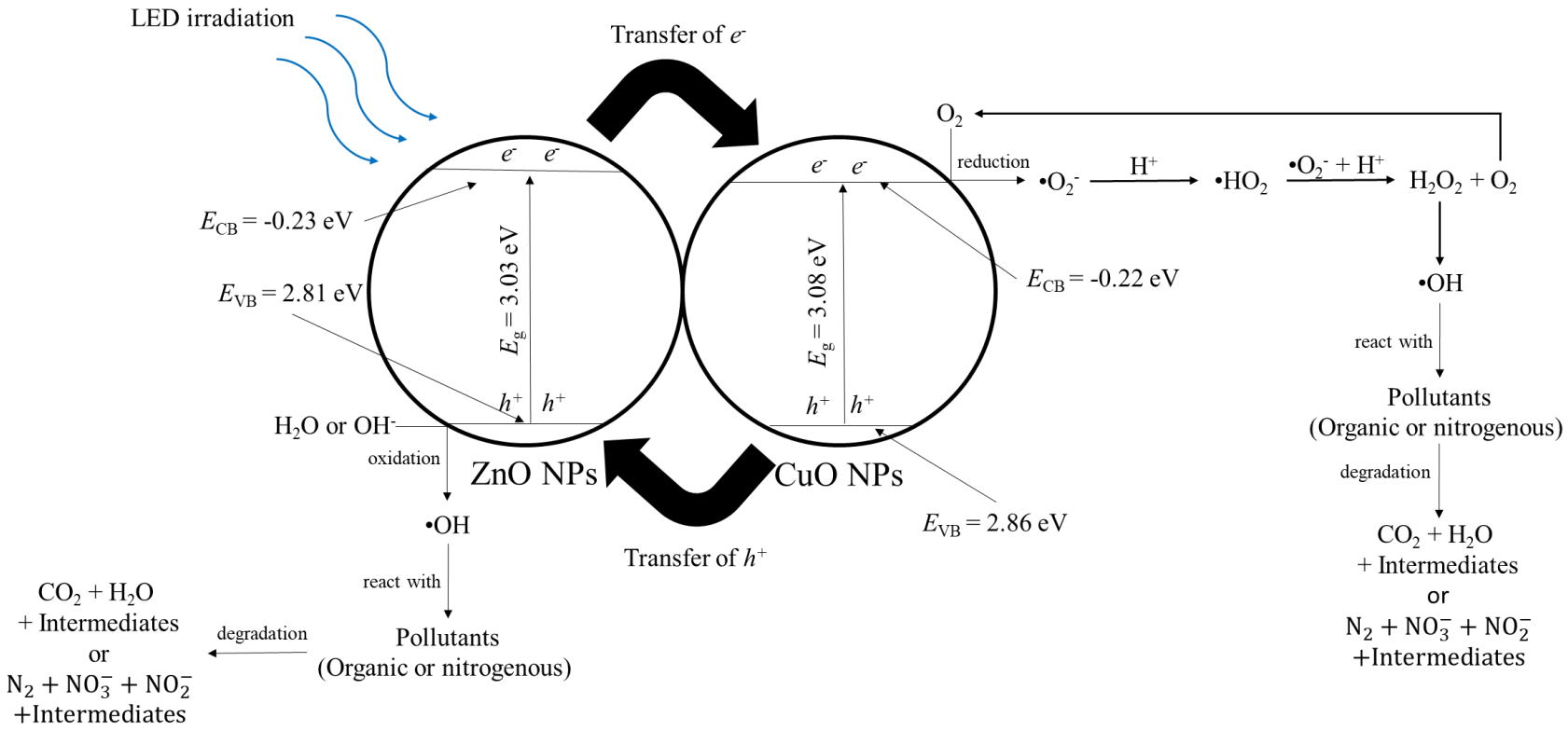

Figure 5.4: Proposed photo-degradation mechanism of ZnO-CuO NCs. Under exposure of LEDs, the holes were migrated to ZnO, while electrons migrated to CuO due to their band alignments in thermodynamically favored in generating ROS (•OH and $•O_2^-$). In ZnO, the water or OH^- was oxidized at VB, while oxygen was reduced at CB, to produce •OH and $•O_2^-$, respectively. The organic pollutants in POME reacted with produced ROS and eventually degraded into carbon dioxide, water and intermediates. Meanwhile, nitrogenous compounds were degraded into nitrogen, nitrate ions, nitrite ions and intermediates. Bottom conduction band energy, top valance band energy and energy bandgap of the synthesized ZnO-CuO NCs were represented by E_{CB}, E_{VB} and E_g, respectively, in the figure.

CHAPTER 6

CONCLUSION

This study successfully demonstrated an eco-friendly method for synthesizing CuO, ZnO and ZnO-CuO nanomaterials using plant extracts. These nanomaterials were evaluated for their antibacterial efficacy and ability to photodegrade POME.

The study focused on CuO NPs, ZnO NPs and ZnO-CuO NCs. The ZnO NPs exhibited the lowest MIC against both Gram-positive and Gram-negative bacteria, showing higher sensitivity to Gram-positive bacteria due to their simpler cell membrane structure.

In POME degradation, the optimized calcination temperatures were identified to be 500°C for CuO NPs and 400°C for ZnO NPs and 70ZnO-30CuO NCs for its thermodynamic properties and band alignment. Blue LED light was more effective than white LED for photodegradation. ZnO NPs showed better COD and AN removal efficiency to CuO NPs and the ZnO-CuO NCs. Although the nanomaterial-treated POME resulted in lower mung bean germination rates, it improved seedling growth compared to untreated POME and tap water.

The mechanisms of antibacterial activity and photodegradation were linked to the generation of ROS, membrane disruption, and pollutant breakdown. The

green synthesis process relied on plant phytochemicals to reduce metal ions, forming MO, which displayed promising antibacterial and photocatalytic properties.

In conclusion, the green synthesis of CuO, ZnO and ZnO-CuO nanomaterials offers a sustainable and cost-effective alternative to conventional methods. These nanomaterials not only demonstrate effectiveness in antibacterial applications and POME treatment but also show potential for broader applications, including energy harvesting systems (like solar cells) and optical sensors. Further research could explore their potential in targeted drug delivery systems, leveraging their biocompatibility and ROS generating capabilities. This study not only advances green nanotechnology but also highlights the versatility of these nanomaterials for addressing global challenges in healthcare, environmental sustainability and renewable energy.

REFERENCES

Abbes, N., Bekri, I., Cheng, M., Sejri, N., Cheikrouhou, M. and Xu, J., 2021. Green Synthesis and characterization of zinc oxide nanoparticles using mulberry fruit and their antioxidant activity. *Materials Science*, 28(2), pp.144–150.

Abdumutalovna, M.S. and Urmanovna, M.D., 2021. Technology of *in vitro* propagation of mangosteen in the climatic conditions of Uzbekistan. *Natural Volatiles & Essential Oils*, 8(4), pp.5610–5617.

Adeyemi, J.O., Onwudiwe, D.C. and Oyedeji, A.O., 2022. Biogenic synthesis of CuO, ZnO, and CuO–ZnO nanoparticles using leaf extracts of *Dovyalis caffra* and their biological properties. *Molecules*, 27(10), pp.3206–3220.

Agustina, L., Suprihatin, Romli, M. and Suryadarma, P., 2021. Processing of palm mill oil effluent using photocatalytic: A literature review. *Journal of Ecological Engineering*, 22(11), pp.43–52.

Ahn, E.-Y., Shin, S.-W., Kim, K. and Park, Y., 2022. Facile green synthesis of titanium dioxide nanoparticles by upcycling mangosteen (*Garcinia mangostana*) pericarp extract. *Nanoscale Research Letters*, 17(1), pp.40–51.

Aizat, W.M., Ahmad-Hashim, F.H. and Syed Jaafar, S.N., 2019. Valorization of mangosteen, "The Queen of Fruits," and new advances in postharvest and in food and engineering applications: A review. *Journal of Advanced Research*, 20, pp.61–70.

Akbarian, M., Mahjoub, S., Elahi, S.M., Zabihi, E. and Tashakkorian, H., 2019. Appraisal of biological aspect of zinc oxide nanoparticles prepared using extract of *Camellia sinensis* L. *Materials Research Express*, 6(9).

Akhbari, A., Kutty, P.K., Chuen, O.C. and Ibrahim, S., 2020. A study of palm oil mill processing and environmental assessment of palm oil mill effluent treatment. *Environmental Engineering Research*, 25(2), pp.212–221.

Akpomie, K.G., Conradie, J., Adegoke, K.A., Oyedotun, K., Ighalo, J.O., Amaku, J.F., Olisah, C., Adeola, A.O. and Iwuozor, K.O., 2023. Adsorption mechanism and modeling of radionuclides and heavy metals onto ZnO nanoparticles: A review. *Applied Water Science*, 13(1).

Alavi, M., Karimi, N. and Valadbeigi, T., 2019. Antibacterial, antibiofilm, antiquorum sensing, antimotility, and antioxidant activities of green fabricated Ag, Cu, TiO_2, ZnO, and Fe_3O_4 NPs *via Protoparmeliopsis muralis* lichen aqueous extract against multi-drug-resistant bacteria. *ACS Biomaterials Science and Engineering*, 5(9), pp.4228–4243.

Alkhuriji, A.F., Majrashi, N.A., Alomar, S., El-Khadragy, M.F., Awad, M.A., Khatab, A.R. and Yehia, H.M., 2020. The beneficial effect of eco-friendly green nanoparticles using *Garcinia mangostana* peel extract against pathogenicity of *Listeria monocytogenes* in female BALB/c mice. *Animals*, 10(4), pp.573–586.

Amaro, F., Morón, Á., Díaz, S., Martín-González, A. and Gutiérrez, J.C., 2021. Metallic nanoparticles—friends or foes in the battle against antibiotic-resistant bacteria? *Microorganisms*, 9(2), pp.364–373.

Amin, F., Fozia, Khattak, B., Alotaibi, A., Qasim, M., Amad, I., Ullah, R., Bourhia, M., Gul, A., Zahoor, S. and Ahamd, R., 2021. Green synthesis of copper oxide nanoparticles using *Aerva javanica* leaf extract and their characterization and investigation of *in vitro* antimicrobial potential and cytotoxic activities. *Evidence-based Complementary and Alternative Medicine*, 2021, pp.1–12.

Aminuzzaman, M., Chong, C.-Y., Goh, W.-.S., Phang, Y.-K., Tey, L.-H., Chee, S.-Y., Akhtaruzzaman, Md., Ogawa, S. and Watanabe, A., 2021. Biosynthesis of NiO nanoparticles using soursop (*Annona muricata* L.) fruit peel green waste and their photocatalytic performance on crystal violet dye. *Journal of Cluster Science*, 32(4), pp.949–958.

Aminuzzaman, M., Ng, P.S., Goh, W.-S., Ogawa, S. and Watanabe, A., 2019. Value-adding to dragon fruit (*Hylocereus polyrhizus*) peel biowaste: Green synthesis of ZnO nanoparticles and their characterization. *Inorganic and Nano-Metal Chemistry*, 49(11), pp.401–411.

Aminuzzaman, M., Lim, P.Y., Goh, W.S. and Watanabe, A., 2018. Green synthesis of zinc oxide nanoparticles using aqueous extract of *Garcinia mangostana* fruit pericarp and their photocatalytic activity. *Bulletin of Materials Science*, 41(2), pp.50–59.

Amirian, P., Bazrafshan, E. and Payandeh, A., 2017. Optimisation of chemical oxygen demand removal from landfill leachate by sonocatalytic degradation in the presence of cupric oxide nanoparticles. *Waste Management and Research*, 35(6), pp.636–646.

Amirul Alam, Md., Rahmat, N.A., Mijin, S., Sajedur Rahman, Md. and Hasan, M.M., 2022. Influence of palm oil mill effluent (POME) on growth and yield performance of Brazilian spinach (*Alternanthera sissoo*). *Journal of Agrobiotechnology*, 13(1), pp.40–49.

Ammulu, M.A., Vinay Viswanath, K., Giduturi, A.K., Vemuri, P.K., Mangamuri, U. and Poda, S., 2021. Phytoassisted synthesis of magnesium oxide nanoparticles from *Pterocarpus marsupium* rox.b heartwood extract and its biomedical applications. *Journal of Genetic Engineering and Biotechnology*, 19(1), pp.21–38.

Amouei, A., Pouramir, M., Asgharnia, H., Mehdinia, M., Shirmardi, M., Fallah, H., Khalilpour, A. and Tabarinia, H., 2021. Evaluation of the efficiency of electrocoagulation process in removing cyanide, nitrate, turbidity, and chemical oxygen demand from landfill leachate. *Environmental Health Engineering and Management Journal*, 8(3), pp.237–244.

Andani, R., Fajrina, A., Asra, R. and Eriadi, A., 2021. Antibacterial activity test of mangosteen plants (*Garcinia mangostana* L.): A review. *Asian Journal of Pharmaceutical Research and Development*, 9(1), pp.164–171.

Applerot, G., Lellouche, J., Lipovsky, A., Nitzan, Y., Lubart, R., Gedanken, A. and Banin E., 2012. Understanding the antibacterial mechanism of CuO nanoparticles: Revealing the route of induced oxidative stress. *Small*, 8(21), pp.3326–3337.

Aqilah Mohd Razali, N., Norharyati Wan Salleh, W., Rosman, N., Hafiza Ismail, N., Zu Nurain Ahmad, S., Aziz, F., Jye, L.W. and Fauzi Ismail, A., 2020. Palm oil mill effluent treatment using tungsten trioxide: Adsorption and photocatalytic degradation. *Materials Today: Proceedings*, 42, pp.22–27.

Ayalew, T., 2004. *SiC Semiconductor Devices Technology, Modeling, and Simulation*. Technical University of Vienna.

Azadi, S., Karimi-Jashni, A., Javadpour, S. and Mahmoudian-Boroujerd, L., 2020. Photocatalytic landfill leachate treatment using *p*-type TiO_2 nanoparticles under visible light irradiation. *Environment, Development and Sustainability*, 23(4), pp.6047–6065.

Baharudin, K.B., Abdullah, N. and Derawi, D., 2018. Effect of calcination temperature on the physicochemical properties of zinc oxide nanoparticles synthesized by coprecipitation. *Materials Research Express*, 5(12), pp.125018–125024.

Balakrishnan, G., Velavan, R., Mujasam Batoo, K. and Raslan, E.H., 2020. Microstructure, optical and photocatalytic properties of MgO nanoparticles. *Results in Physics*, 16, pp.103013–103016.

Bandekar, S.S. Hosamane, S.N., Patil, C., Yaragatti, A., Hukerikar, A., Patil, S. and Chachadi, P., 2020. ZnO-CuO nanocomposites: Synthesis, characterization and antibacterial activity. *Journal of Physics: Conference Series*, 1706, pp.012018–012023.

Bano, S. and Pillai, S., 2020. Green synthesis of calcium oxide nanoparticles at different calcination temperatures. *World Journal of Science, Technology and Sustainable Development*, 17(3), pp.283–295.

Basavalingiah, K.R., Harishkumar, S., Udayabhanu, Nagaraju, G., Rangappa, D. and Chikkahanumantharayappa, 2019. Highly porous, honeycomb like Ag–ZnO nanomaterials for enhanced photocatalytic and photoluminescence studies: Green synthesis using *Azadirachta indica* gum. *SN Applied Sciences*, 1(8), pp.935–947.

Basit, R.A., Abbasi, Z., Hafeez, M., Ahmad, P., Khan, J., Khandaker, M.U., Al-Mugran, K.S. and Khalid, A., 2023. Successive Photocatalytic degradation of methylene blue by ZnO, CuO and ZnO/CuO synthesized from *Coriandrum sativum* plant extract *via* green synthesis technique. *Crystals*, 13(2), pp.281–294.

Bekru, A.G., Tufa, L.T., Zelekew, O.A., Goddati, M., Lee, J. and Sabir, F.K., 2022. Green synthesis of a CuO–ZnO nanocomposite for efficient photodegradation of methylene blue and reduction of 4-nitrophenol. *ACS Omega*, 7(35), pp.30908–30919.

Benitha, J.G., Pratibha Ramani, Rajeshkumar, S., Gheena, S., Abhilasha, R. and Reshma, K., 2021. Antibacterial and antioxidant activity of *Garcinia mangostana* mediated selenium induced nanoparticles: An *in vitro* study. *Journal of Pharmaceutical Research International*, 33(62A), pp.490–500.

Cao, D., Gong, S., Shu, X., Zhu, D. and Liang, S., 2019. Preparation of ZnO nanoparticles with high dispersibility based on oriented attachment (OA) process. *Nanoscale Research Letters*, 14(1), pp.1–11.

Cao, Y., Dhahad, H.A., El-Shorbagy, M.A., Alijani, H.Q., Zakeri, M., Heydari, A., Bahonar, E., Slouf, M., Khatami, M., Naderifar, M., Iravani, S., Khatami, S. and Dehkordi, F.F., 2021. Green synthesis of bimetallic ZnO–CuO nanoparticles and their cytotoxicity properties. *Scientific Reports*, 11(1).

Chai, H.Y., Lam, S.M. and Sin, J.C., 2019. Green synthesis of ZnO nanoparticles using *Hibiscus rosa-sinensis* leaves extracts and evaluation of their photocatalytic activities. *International Symposium on Green and Sustainable Technology (ISGST2019)*. 2019 AIP Conference Proceedings, Kampar.

Chan, Y.B., Aminuzzaman, M., Khalilur Rahman, Md., Win, Y.F., Sultana, S., Cheah, S.-Y., Watanabe, A., Wong, L.S., Guha, S.K., Djearamane, S., Rajendran, V., Akhtaruzzaman, Md. and Tey, L.-H., 2024. Green synthesis of ZnO nanoparticles using the mangosteen (*Garcinia mangostana* L.) leaf extract: Comparative preliminary *in vitro* antibacterial study. *Green Processing and Synthesis*, 13(1), pp.20230251–20230270.

Chan, Y.B., Aminuzzaman, M., Tey, L.-H., Win, Y.F., Watanabe, A., Djearamane, S. and Aktharuzzaman, Md., 2023. Impact of diverse parameters on the physicochemical characteristics of green-synthesized zinc oxide–copper oxide nanocomposites derived from an aqueous extract of *Garcinia mangostana* L. leaf. *Materials*, 16(15), pp.5421–5439.

Chan, Y.B., Aminuzzaman, M., Win, Y.F., Djearamane, S., Wong, L.S., Guha, S.K., Almohammadi, H., Aktharuzzaman, Md. and Tey, L.-H., 2024. *Garcinia mangostana* L. leaf-extract-assisted green synthesis of CuO, ZnO and CuO-ZnO nanomaterials for the photocatalytic degradation of palm oil mill effluent (POME). *Catalysts*, 14(8), pp.486–503.

Chan, Y.B., Selvanathan, V., Tey, L.-H., Aktharuzzaman, Md., Anur, F.H., Djearamane, S., Watanabe, A. and Aminuzzaman, M., 2022. Effect of calcination temperature on structural, morphological and optical properties of copper oxide nanostructures derived from *Garcinia mangostana* L. leaf extract. *Nanometerials*, 12(20), pp.3589–3607.

Charles, A. and Chin, K.C., 2018. Recent advances in photocatalytic treatment of palm oil mill effluent (POME): A review. *International Journal of Engineering & Technology*, 7(4.34), pp.389–393.

Cheng, Y.W., Chong, C.C., Lam, M.K., Ayoub, M., Cheng, C.C., Lim, J.W., Yusup, S., Tang, Y. and Bai, J., 2021. Holistic process evaluation of non-conventional palm oil mill effluent (POME) treatment technologies: A conceptual and comparative review. *Journal of Hazardous Materials*, 409, pp.124964–124996.

Cuong, H.N., Pansambal, S., Ghotekar, S., Oza, R., Hai, N.T.T., Viet, N.M. and Nguyen, V-H., 2022. New frontiers in the plant extract mediated biosynthesis of copper oxide (CuO) nanoparticles and their potential applications: A review. *Environmental Research*, 203, pp.111858–111881.

Das, S. and Srivastava, V.C., 2017. Synthesis and characterization of ZnO/CuO nanocomposite by electrochemical method. *Materials Science in Semiconductor Processing*, 57, pp.173–177.

Dauthal, P. and Mukhopadhyay, M., 2016. Noble metal nanoparticles: Plant-mediated synthesis, mechanistic aspects of synthesis, and applications. *Industrial and Engineering Chemistry Research*, 55(36).

Davidson, M.W., *Fundamentals of Light-Emitting Diodes (LEDs)* [Online]. Available at: https://zeiss-campus.magnet.fsu.edu/print/lightsources/leds-print.html#:~:text=However%2C most white light diodes,emission at a longer wavelength. [Accessed: 9 January 2024].

Dawadi, S., Gupta, A., Khatri, M., Budhathoki, B., Lamichhan, G. and Parajuli, N., 2020. Manganese dioxide nanoparticles: Synthesis, application and challenges. *Bulletin of Materials Science*, 43, pp.277–286.

Demissie, M.G., Sabir, F.K., Edossa, G.D. and Gonfa, B.A., 2020. Synthesis of zinc oxide nanoparticles using leaf extract of *Lippia adoensis* (Koseret) and evaluation of its antibacterial activity. *Journal of Chemistry*, 2020, pp.1–9.

Dien, N.D., Ha, P.T.T., Vu, X.H., Trang, T.T., Giang, T.D.T. and Dung, N.T., 2023. Developing efficient CuO nanoplate/ZnO nanoparticle hybrid photocatalysts for methylene blue degradation under visible light. *Royal Society of Chemistry Adavnces*, 13(35), pp.24505–24518.

Diniatik and Anggraeni, R.S., 2021. Antibacterial (*Staphylococcus aureus* and *Escherichia coli*) and antifungal (*Saccharomyces cerevisiae*) activity assay on nanoemulsion formulation of ethanol extract of mangosteen leaves (*Garcinia mangostana* L.) as fruit preservative. *Journal of Food and Pharmaceutical Sciences*, 9(1), pp.351–365.

Droepenu, E.K., Wee, B.S., Chin, S.F., Kok, K.Y. and Maligan, M.F., 2022. Zinc oxide nanoparticles synthesis methods and its effect on morphology: A review. *Biointerface Research in Applied Chemistry*, 12(3), pp.4261–4292.

Efenberger-Szmechtyk, M., Nowak, A. and Czyzowska, A., 2020. Plant extracts rich in polyphenols: antibacterial agents and natural preservatives for meat and meat products. *Critical Reviews in Food Science and Nutrition*, 61(1), pp.149–178.

Elemike, E.E., Onwudiwe, D.C. and Singh, M., 2019. Eco-friendly synthesis of copper oxide, zinc oxide and copper oxide–zinc oxide nanocomposites, and their anticancer applications. *Journal of Inorganic and Organometallic Polymers and Materials*, 30(2), pp.400–409.

Elleuch, L., Messaoud, M., Djebali, K., Attafi, M., Cherni, Y., Kasmi, M., Elaoud, A., Trabelsi, I. and Chatti, A., 2020. A new insight into highly contaminated landfill leachate treatment using Kefir grains pre-treatment combined with Ag-doped TiO_2 photocatalytic process. *Journal of Hazardous Materials*, 382, pp.121119–121129.

Estrada-Flores, S., Martínez-Luévanos, A., Perez-Berumen, C.M., García-Cerda, L.A. and Flores-Guia, T.E., 2020. Relationship between morphology, porosity, and the photocatalytic activity of TiO_2 obtained by sol–gel method assisted with ionic and nonionic surfactants. *Boletin de la Sociedad Espanola de Ceramica y Vidrio*, 59(5), pp.209–218.

European Committee for Antimicrobial Susceptibility Testing of the European Society of Clinical Microbiology and Infectious Diseases, 2003. Determination of minimum inhibitory concentrations (MICs) of antibacterial agents by broth dilution. *Clinical Microbiology and Infection*, 9(8), pp.1–7.

Fardood, S.T. and Ramazani, A., 2018. Black tea extract mediated green synthesis of copper oxide nnaoparticles. *Journal of Applied Chemical Research*, 12(2), pp.8–15.

Fardood, S.T. and Ramazani, A., 2016. Green synthesis and characterization of copper oxide nanoparticles using coffee powder extract. *Journal of Nanostructures,* 6(2), pp.167–171.

Fatima, S., Infan Ali, S., Iqbal, M.Z. and Rizwan, S., 2017. The high photocatalytic activity and reduced band gap energy of La and Mn co-doped $BiFeO_3$/graphene nanoplatelet (GNP) nanohybrids. *Royal Society of Chemistry Adavnces*, 7(57), pp.35928–35937.

Fawcett, D.,Verduin, J.J., Shah, M., Sharma, S.B. and Poinern, G.E.J., 2017. A review of current research into the biogenic synthesis of metal and metal oxide nanoparticles *via* marine algae and seagrasses. *Journal of Nanoscience*, 2017, pp.1–15.

Fouda, A., Salem, S.S., Wassel, A.R., Hamza, M.F. and Shaheen, Th.I., 2020. Optimization of green biosynthesized visible light active CuO/ZnO nano-photocatalysts for the degradation of organic methylene blue dye. *Heliyon*, 6(9), pp.e04896–e04908.

Fredericks, J., Senapati, S. and Wannemuehler, M.J., 2020. Cytotoxic effects of manganese oxide nanoparticles in combination with microbial components on intestinal epithelial cells. *F1000Research*, 9, pp.975–989.

Gajic, I., Kabic, J., Kekic, D., Jovicevic, M., Milenkovic, M., Culafic, D.M., Trudic, A., Ranin, L. and Opavski, N., 2022. Antimicrobial susceptibility testing: A comprehensive review of currently used methods. *Antibiotics*, 11(4), pp.427–452.

Geerdink, R.B., Sebastiaan van den Hurk, R. and Epema, O.J., 2017. Chemical oxygen demand: Historical perspectives and future challenges. *Analytica Chimica Acta*, 961, pp.1–11.

Georgia, B.J., Gheena, S., Prathiba, R., Rajesh Kumar, S., Kartikeyan, R. and Abilasha, R., 2023. Anticancer activity of green synthesized selenium nanoparticles from *Garcinia mangostana* crude extract against MCF-7 Breast cancer cells. *Journal of Population Therapeutics and Clinical Pharmacology*, 30(6), pp.e74–e82.

Ghazali, S.S., Jusoh, R. and Shariffuddin, J.H., 2019. Parameter affecting photocatalytic degradation of POME using LaCa as photocatalyst. *Materials Today: Proceedings*, 19, pp.1173–1182.

Govindasamy, G.A., Mydin, R.B.S.M.N., Harun, N.H. and Sreekantan, S., 2020. Calcination temperatures, compositions and antimicrobial properties of heterostructural ZnO–CuO nanocomposites from *Calotropis gigantea* targeted for skin ulcer pathogens. *Research Square*, 11, pp.1–14.

Greene, A., Hashemi, J. and Kang, Y., 2020. Development of MnO_2 hollow nanoparticles for potential drug delivery applications. *Nanotechnology*, 32(2), pp.025713–025727.

Gupta, N., Gupta, C., Sharma, S., Sharma, R.K. and Bohidar, H.B., 2015. Comparative study of antibacterial activity of standard antibiotic with silver nanoparticles synthesized using *Ocimum tenuiflorum* and *Garcinia mangostana* leaves. *Chemical Biology Letters*, 2(2), pp.41–44.

Habibi, M.H. and Karimi, B., 2014. Effect of the annealing temperature on crystalline phase of copper oxide nanoparticle by copper acetate precursor and sol-gel method. *Journal of Thermal Analysis and Calorimetry*, 115(1), pp.419–423.

Hamadamin, S.I., Anwer, S.S., Sdiq, K.H. and Abdulkareem, P.M., 2023. Competence kinetic and thermodynamic studies between natural bio-adsorbent green microalgae and synthetic adsorbent magnetic nanoparticles for copper(II) ion in water. *Bulletin of the Chemical Society of Ethiopia*, 37(1), pp.183–195.

Hamid, A., Haq, S., Ur Rehman, S., Akhter, K., Rehman, W., Waseem, M., Ud Din, S., Zain-ul-Abdin, Hafeez, M., Khan, A. and Shah, A., 2021. Calcination temperature-driven antibacterial and antioxidant activities of *Fumaria indica* mediated copper oxide nanoparticles: Characterization. *Chemical Papers*, 75(8), pp.4189–4198.

Haneefa, M.M., Jayandran, M. and Balasubramanian, V., 2017. Green synthesis characterization and antimicrobial activity evaluation of manganese oxide nanoparticles and comparative studies with salicylalchitosan functionalized nanoform. *Asian Journal of Pharmaceutics*, 11(1), pp.65–74.

Harmon, E.S., Melloch, M.R. and Lundstrom, M.S., 1994. Effective band-gap shrinkage in GaAs. *American Institute of Physics*, 64(4), pp.502–504.

Hassan, S.E.-D., Fouda, A., Saied, E., Farag, M.M.S., Eid, A.M., Barghoth, M.G., Awad, M.A., Hamza, M.F. and Awad, M.F., 2021. *Rhizopus oryzae*-mediated green synthesis of magnesium oxide nanoparticles (MgO-NPs): A promising tool for antimicrobial, mosquitocidal action, and tanning effluent treatment. *Journal of Fungi*, 7(5), pp.372–396.

Helba, L., Kačániová, M., Petrová, J., Felšöciová, S., Pavelková, A. and Rovná, K., 2013. Antibacterial activity of some wild medical plants extract to antibiotic resistant *Escherichia coli*. *Journal of Microbiology, Biotechnology and Food Sciences*, 2(1), pp.1215–1224.

Hiew, C.-W., Lee, L.-J., Junus, S., Tan, Y.-N., Chai, T.-T. and Ee, K.-Y., 2021. Optimization of microwave-assisted extraction and the effect of microencapsulation on mangosteen (*Garcinia mangostana* L.) rind extract. *Food Science and Technology*, 42, pp.1–10.

Hitkari, G., Chowdhary, P., Kumar, V., Singh, S. and Motghare. A., 2022. Potential of copper-zinc oxide nanocomposite for photocatalytic degradation of Congo red dye. *Cleaner Chemical Engineering*, 1, pp.100003–100009.

Hoseinpour, V. and Ghaemi, N., 2018. Green synthesis of manganese nanoparticles: Applications and future perspective–A review. *Journal of Photochemistry and Photobiology B: Biology*, 189, pp.234–243.

Hoseinzadeh, E., Makhdoumi, P., Taha, P., Hossini, H., Pirsaheb, M., Rastegar, S.O. and Stelling, J., 2016. A review of available techniques for determination of nano-antimicrobials activity. *Toxin Reviews*, 36(1), pp.18–32.

Huang, X., Zhou, X., Dai, Q. and Qin, Z., 2021. Antibacterial, antioxidation, UV-blocking, and biodegradable soy protein isolate food packaging film with mangosteen peel extract and ZnO nanoparticles. *Nanomaterials*, 11(12), pp.3337–3352.

Igwe, J.C. and Onyegbado, C.C., 2007. A review of palm oil mill effluent (POME) water treatment. *Global Journal of Environmental Research*, 1(2), pp.54–62.

Imani, M.M. and Safaei, M., 2019. Optimized synthesis of magnesium oxide Nanoparticles as bactericidal agents. *Journal of Nanotechnology*, 2019.

Ingale, A.G. and Chaudhari, A.N., 2013. Biogenic synthesis of nanoparticles and potential applications: An eco-friendly approach. *Journal of Nanomedicine and Nanotechnology*, 4(2), pp.165–171.

Ismail, N., Imran, M., Ramzan, M., Anwar, A., Alsafari, I.A., Asgher, M. and Iqbal, H.M.N., 2023. Functionalized graphene oxide-zinc oxide hybrid material and its deployment for adsorptive removal of levofloxacin from aqueous media. *Environmental Research*, 217, pp.114958–114969.

Jaithon, T., Atichakaro, T., Phonphoem, W., T-Thienprasert, J., Sreewongchai, T. and T-Thienprasert, N.P., 2024. Potential usage of biosynthesized zinc oxide nanoparticles from mangosteen peel ethanol extract to inhibit *Xanthomonas oryzae* and promote rice growth. *Heliyon*, 10(1), pp.e24076–e24085.

Jameel, M.S., Aziz, A.A. and Dheyab, M.A., 2020. Green synthesis: Proposed mechanism and factors influencing the synthesis of platinum nanoparticles. *Green Processing and Synthesis*, 9, pp.386–398.

Jamila, N., Khan, N., Bibi, N., Waqas, M., Khan, S.N., Atlas, A., Amin, F., Khan, F. and Saba, M., 2021. Hg(II) sensing, catalytic, antioxidant, antimicrobial, and anticancer potential of *Garcinia mangostana* and α-mangostin mediated silver nanoparticles. *Chemosphere*, 272, pp.12974–12990.

Jassim, A.M.N., Shafy, G.M., Mohammed, M.T., Farhan, S.A. and Noori, O.M., 2021. Antioxidant, anti-inflammatory and wound healing of biosynthetic gold nanoparticles using mangosteen (*G. mangostona*). *Iraqi Journal of Industrial Research*, 8(2), pp.59–74.

Jeevanandam, J., Chan, Y.S. and Danquah, M.K., 2016. Biosynthesis of metal and metal oxide nanoparticles. *ChemBioEng Reviews*, 3(2), pp.55–67.

Jeong, H., Park, J. and Kim, H., 2013. Determination of $NH4^{+}$ in environmental water with interfering substances using the modified nessler method. *Journal of Chemistry*, 2013, pp.1–9.

de Jesus Matos Viégas, I., Cordeiro, R.A.M., de Almeida, G.M., Silva, D.A.S., da Silva, B.C., Okumura, R.S., da Silva Júnior, M.L., da Silva, S.P. and de Freitas, J.M.N., 2018. Growth and visual symptoms of nutrients deficiency in mangosteens (*Garcinia mangostana* L.). *American Journal of Plant Sciences*, 9(5), pp.1014–1028.

Jiang, J., Pi, J. and Cai, J., 2018. The advancing of zinc oxide nanoparticles for biomedical applications. *Bioinorganic Chemistry and Applications*, 2018, pp.1–19.

Jindaruk, A., Jaithon, T., T-Thienprasert, J. and T-Thienprasert, N.P., 2023. *In vitro* analysis of antibacterial activity against wound pathogens, potential for wound healing, and anti-melanoma properties of biosynthesized zinc oxide nanoparticles. *Micro and Nano Letters*, 18(9–12), pp.e12177–e12185.

Kanakaraju, D., Ahmad, N.L.B., Mohd Sedik, N.B., Long, S.G.H., Guan, T.M. and Chin, L.Y., 2017. Performance of solar photocatalysis and photo-fenton degradation of palm oil mill effluent. *Malaysian Journal of Analytical Sciences*, 21(5), pp.996–1007.

Kaningini, A.G., Azizi, S., Sintwa, N., Mokalane, K., Mohale, K.C., Mudau, F.N. and Maaza, M., 2022. Effect of optimized precursor concentration, temperature, and doping on optical properties of ZnO nanoparticles synthesized *via* a green route using bush tea (*Athrixia phylicoides* DC.) leaf extracts. *ACS Omega*, 7(36), pp.31658–31666.

Karthiga, P., 2018. Preparation of silver nanoparticles by *Garcinia mangostana* stem extract and investigation of the antimicrobial properties. *Biotechnology Research and Innovation*, 2(1), pp.30–36.

Karthiga, P., Rajeshkumar, S. and Annadurai, G., 2018. Mechanism of larvicidal activity of antimicrobial silver nanoparticles synthesized using *Garcinia mangostana* bark extract. *Journal of Cluster Science*, 29(6), pp.1233–1241.

Karthiga, P., Soranam, R. and Annadurai, G., 2012. Alpha-mangostin, the major compound from *Garcinia mangostana* Linn. responsible for synthesis of Ag nanoparticles: Its characterization and evaluation studies. *Research Journal of Nanoscience and Nanotechnology*, 2(2), pp.46–57.

Kashitarash, Z.E., Taghi, S.M., Kazem, N., Abbass, A. and Alireza, R., 2012. Application of iron nanaoparticles in landfill leachate treatment-case study: Hamadan landfill leachate. *Iranian Journal of Environmental Health Science and Engineering*, 9(1), pp.36–40.

Kessler, A., Hedberg, J., Blomberg, E. and Odnevall, I., 2022. Reactive oxygen species formed by metal and metal oxide nanoparticles in physiological media—A review of reactions of importance to nanotoxicity and proposal for categorization. *Nanomaterials*, 12(11), pp.1922–1945.

Khalafi, T., Buazar, F. and Ghanemi, K., 2019. Phycosynthesis and enhanced photocatalytic activity of zinc oxide nanoparticles toward organosulfur pollutants. *Scientific Reports*, 9(1), pp.6866–6875.

Khameneh, B., Iranshahy, M., Soheili, V. and Bazzaz, B.S.F., 2019. Review on plant antimicrobials: A mechanistic viewpoint. *Antimicrobial Resistance and Infection Control*, 8(1), pp.18–45.

Khan, A., Shabir, D., Ahmad, P., Khandaker, M.U., Faruque, M.R.I. and Ud Din, I., 2021. Biosynthesis and antibacterial activity of MgO-NPs produced from *Camellia-sinensis* leaves extract. *Materials Research Express*, 8(1), pp.015402–015411.

Khan, M.I., Fatima, N., Shakil, M., Tahir, M.B., Riaz, K.N., Rafique, M., Iqbal, T. and Mahmood, K., 2021. Investigation of in-vitro antibacterial and seed germination properties of green synthesized pure and nickel doped ZnO nanoparticles. *Physica B: Physics of Condensed Matter*, 601.

Khan, S.A., Shahid, S., Shahid, B., Fatima, U. and Abbasi, S.D., 2020. Green synthesis of MnO nanoparticles using *Abutilon indicum* leaf extract for biological, photocatalytic, and adsorption activities. *Biomolecules*, 10(5), pp.785–803.

Khan, S.A., Noreen, F., Kanwal, S., Iqbal, A. and Hussain, G., 2017. Green synthesis of ZnO and Cu-doped ZnO nanoparticles from leaf extracts of *Abutilon indicum*, *Clerodendrum infortunatum*, *Clerodendrum inerme* and investigation of their biological and photocatalytic activities. *Materials Science and Engineering C*, 82, pp.46–59.

Khatoon, U.T., Velidandi, A. and Nageswara Rao, G.V.S., 2023. Copper oxide nanoparticles: Synthesis *via* chemical reduction, characterization, antibacterial activity, and possible mechanism involved. *Inorganic Chemistry Communications*, 149, pp.110372–11084.

Kim, M.G., Kang, J.M., Lee, J.E., Kim, K.S., Kim, K.H., Cho, M. and Lee, S.G., 2021. Effects of calcination temperature on the phase composition, photocatalytic degradation, and virucidal activities of TiO_2 nanoparticles. *ACS Omega*, 6(16), pp.10668–10678.

Kolb, M., Bahadir, M. and Teichgräber, B., 2017. Determination of chemical oxygen demand (COD) using an alternative wet chemical method free of mercury and dichromate. *Water Research*, 122, pp.645–654.

Koopi, H. and Buazar, F., 2018. A novel one-pot biosynthesis of pure alpha aluminum oxide nanoparticles using the macroalgae *Sargassum ilicifolium*: A green marine approach. *Ceramics International*, 44(8), pp.8940–8945.

Kumar, A. and Pandey, G., 2017. A review on the factors affecting the photocatalytic degradation of hazardous materials. *Material Science & Engineering International Journal*, 1(3), pp.106–114.

Kumar, H., Bhardwaj, K., Dhanjal, D.S., Nepovimova, E., Şen, F., Regassa, H., Singh, R., Verma, R., Kumar, V., Kumar, D., Bhatia, S.K. and Kŭca. K., 2020. Fruit extract mediated green synthesis of metallic nanoparticles: A new avenue in pomology applications. *International Journal of Molecular Sciences*, 21(22), pp.8458–8475.

Kumar, I., Mondal, M. and Sakthivel, N., 2019. Green synthesis of phytogenic nanoparticles. In: Shukla, A.K. and Iravani, S., (eds.) *Green Synthesis, Characterization and Applications of Nanoparticles*. Elsevier Inc., pp. 37–73.

Kumar, V., Singh, K., Panwar, S. and Mehta, S.K., 2017. Green synthesis of manganese oxide nanoparticles for the electrochemical sensing of *p*-nitrophenol. *International Nano Letters*, 7(2), pp.123–131.

Kureshi, A.A., Vaghela, H.M., Kumar, S., Singh R. and Kumari P., 2021. Green synthesis of gold nanoparticles mediated by *Garcinia* fruits and their biological applications. *Pharmaceutical Sciences*, 27(2), pp.238–250.

Kuruppu, K.A.S.S., Perera, K.M.K.G., Chamara, A.M.R. and Thiripuranathar, G., 2020. Flower shaped ZnO—NPs; phytofabrication, photocatalytic, fluorescence quenching, and photoluminescence activities. *Nano Express*, 1(2), pp.020020–020037.

Lam, S.-M., Wong, K.-A. and Sin, J.-C., 2018. Fabrication of flower-like ZnO micro/nanostructures for photodegradation of pre-treated palm oil mill effluent. *IOP Conference Series: Earth and Environmental Science*, 112, pp.012003–012007.

Lany, S., 2015. Semiconducting transition metal oxides. *Journal of Physics: Condensed Matter*, 27(28), p.283203.

Le, N.T.T., Thi, T.T.H., Ching, Y.C., Nguyen, N.H., Nguyen, D.Y.P., Truong, Q.M. and Nguyen, D.H., 2021. *Garcinia mangostana* shell and *Tradescantia spathacea* leaf extract-mediated one-pot synthesis of silver nanoparticles with effective antifungal properties. *Current Nanoscience*, 17(5), pp.762–771.

Lee, K.X., Shameli, K., Miyake, M., Ahmad Khairudin, N.B.B., Mohamad, S.E.B., Hara, H., Mad Nordin, M.F.B. and Yew, Y.P., 2017. Gold nanoparticles biosynthesis: A simple route for control size using waste peel extract. *IEEE Transactions on Nanotechnology*, 16(6), pp.954–957.

Lee, K.X., Shameli, K., Miyake, M., Kuwano, N., Ahmad Khairudin, N.B.B., Mohamad, S.E.B. and Yew, Y.P., 2016. Green synthesis of gold nanoparticles using aqueous extract of *Garcinia mangostana* fruit peels. *Journal of Nanomaterials*, 2016, pp.1–7.

Lee, K.X., Shameli, K., Mohamad, S.E., Yew, Y.P., Isa, E.D.M., Yap, H.-.Y., Lim, W.L. and Teow, S.-Y., 2019. Bio-mediated synthesis and characterisation of silver nanocarrier, and its potent anticancer action. *Nanomaterials*, 9(10), pp.1423–1441.

Lee, K.X., Shameli, K., Yew, Y.P., Teow, S.-Y., Jahangirian, H., Rafiee-Moghaddam, R. and Webster, T.J., 2020. Recent developments in the facile bio-synthesis of gold nanoparticles (AuNPs) and their biomedical applications. *International Journal of Nanomedicine*, 15, pp.275–300.

Lei, C., Pi, M., Jiang, C., Cheng, B. and Yu, J., 2017. Synthesis of hierarchical porous zinc oxide (ZnO) microspheres with highly efficient adsorption of Congo red. *Journal of Colloid and Interface Science*, 490, pp.242-251.

Li, H., Ma, W., Zeng, X., Liu, S., Xiao, L., Zheng F., Feng, Y., Yang, M., Zhu, H., Yang, Y. and Liu, H., 2023. ZnO/CuO piezoelectric nanocatalysts for the degradation of organic pollutants. *ACS Applied Nano Materials*, 6(22), pp.21113–21122.

Li, J., Luo, G., He, L., Xu, J. and Lyu, J., 2017. Analytical Approaches for determining chemical oxygen demand in water bodies: A review. *Critical Reviews in Analytical Chemistry*, 48(1), pp.47–65.

Loh, S.K., Lai, M.E. and Ngatiman, M., 2019. Vegetative growth enhancement of organic fertilizer from anaerobically-treated palm oil mill effluent (POME) manure in food-energy-water nexus challenge supplemented with chicken. *Food and Bioproducts Processing*, 117, pp.95–104.

Ma, X., Zhou, S., Xu, X. and Du, Q., 2022. Copper-containing nanoparticles: Mechanism of antimicrobial effect and application in dentistry-A narrative review. *Frontiers in Surgery*, 9, pp.1–21.

Mahmod, S.S., Arisht, S.N., Jahim, J.Md., Takriff, M.S., Tan, J.P., Luthfi, A.A.I. and Abdul, P.M., 2021. Enhancement of biohydrogen production from palm oil mill effluent (POME): A review. *International Journal of Hydrogen Energy*, 47(96), pp.40637–40655.

Mahmod, S.S., Takriff, M.S., Al-Rajabi, M.M., Abdul, P.M., Gunny, A.A.N., Silvamany, H. and Jahim, J.Md., 2023. Water reclamation from palm oil mill effluent (POME): Recent technologies, by-product recovery, and challenges. *Journal of Water Process Engineering*, 52, pp.103488–103502.

Maliki, M., Ikhuoria, E.U., Omorogbe, S.O. and Ekebafe, M.O., 2020. Comparative study on nutrient availability and growth of tomato (*Lycopersicon esculentum*) seedlings in soils amended with palm oil mill effluent and rubber processing effluents. *Cogent Food and Agriculture*, 6(1), pp.1738199–1738209.

Mallikarjunaswamy, C., Lakshmi Ranganatha, V., Ramith Ramu, Udayabhanu and Nagaraju, G., 2020. Facile microwave-assisted green synthesis of ZnO nanoparticles: Application to photodegradation, antibacterial and antioxidant. *Journal of Materials Science: Materials in Electronics*, 31(2), pp.1004–1021.

Manju, M., Elsa Rose, P.J., Arunima, F., Grace, M.B. and Anila, W., 2021. Green synthesis of silver nanoparticles from fruit rind extract of *Garcinia mangostana* L. and evaluation of antibacterial properties. *Plant Archives*, 21(2), pp.279–283.

Mansoor Al-Saeedi, A.M., Mohamad, F.K. and Ridha, N.J., 2022. Synthesis and characterization CuO-ZnO binary nanoparticles. *Journal of Nanostructures*, 12(3), pp.686–696.

Marcorius, A., Sulaeman, U., Afif, M., Nurfiah, S., Khanifudin, K. and Afifah, K., 2022. The enhanced photocatalytic properties of silver phosphate synthesized under mangosteen peel extract solution. *Jurnal Teknologi*, 84(1), pp.21–27.

Masri, A., Brown, D.M., Smith, D.G.E., Stone, V. and Johnston, H.J., 2022. Comparison of *in vitro* approaches to assess the antibacterial effects of nanomaterials. *Journal of Functional Biomaterials*, 13(4), pp.255–274.

Mazli, S.R.A., Yusoff, H.M. and Idris, N.H., 2020. Synthesis of zinc oxide nanoparticles by using *Aloe vera* leaf extract as pontential anode material in lithium ion battery. *Universiti Malaysia Terengganu Journal of Undergraduate Research*, 2(2), pp.1–8.

Mfon, R.E., Hall, S.R. and Sarua, A., 2020. Effect of *Ocimum gratissimum* plant leaf extract concentration and annealing temperature on the structure and optical properties of synthesized zinc oxide nanoparticles. *EDUCATUM Journal of Science, Mathematics And Technology*, 7(1), pp.1–13.

Mohammadi-Aloucheh, R., Habibi-Yangjeh, A., Bayrami, A., Latifi-Navid, S. and Asadi, A., 2018a. Enhanced anti-bacterial activities of ZnO nanoparticles and ZnO/CuO nanocomposites synthesized using *Vaccinium arctostaphylos* L. fruit extract. *Artificial Cells, Nanomedicine and Biotechnology*, 46, pp.1200–1209.

Mohammadi-Aloucheh, R., Habibi-Yangjeh, A., Bayrami, A., Latifi-Navid, S. and Asadi, A., 2018b. Green synthesis of ZnO and ZnO/CuO nanocomposites in *Mentha longifolia* leaf extract: Characterization and their application as anti-bacterial agents. *Journal of Materials Science: Materials in Electronics*, 29(16), pp.13596–13605.

Mohd Basri, M.S., Ren, B.L.M., Talib, R.A., Zakaria, R. and Kamarudin, S.H., 2021. Novel mangosteen-leaves-based marker ink color lightness, viscosity, optimized composition, and microstructural analysis. *Polymers*, 13(10), pp.1581–1598.

Mohd Hashim, T. and Zaharah, A.R., 1994. Nitrogen contribution by palm oil mill effluent to young oil palm (*Elaeis guineensis* Jacq.) as measured by 15N isotope dilution technique. *Pertanika Journal Tropical Agriculture Science*, 17(2), pp.81–87.

Mojiri, A., Zhou, J.L., Ratnaweera, H., Ohashi, A., Ozaki, N., Kindaichi, T. and Asakura, H., 2020. Treatment of landfill leachate with different techniques: An overview. *Journal of Water Reuse and Desalination*, 11(1), pp.66–96.

Mrabet, C., Jaballah, R., Mahdhi, N., Boukhachem, A. and Amlouk, M., 2023. CuO-ZnO nanocomposites-based thin films: Characterization, physical properties and sunlight photocatalytic degradation of organic pollutants. *Journal of Alloys and Compounds*, 968, pp.172252–172266.

Mrabet, I.E., Bellouk, H., Bencheqroun, Z., Nawdali, M. and Zaitan, H., 2021. Treatment of stabilized landfill leachate using coupled Fenton-like and adsorption process onto Moroccan bentonite clay. *Desalination and Water Treatment*, 240, pp.43–54.

Mubeen, K., Irshad, A., Safeen, A., Aziz, U., Safeen, K., Ghani, T., Khan, K., Ali, Z., ul Haq, I. and Shah, A., 2023. Band structure tuning of ZnO/CuO composites for enhanced photocatalytic activity. *Journal of Saudi Chemical Society*, 27(3), pp.101639–101651.

Mulyono, D., Irawati, Y. and Syah, M.J.A., 2021. Identification morphological variability of six mangosteen (*Garcinia mangostana* L.) as a conservation strategy for local varieties. *IOP Conference Series: Earth and Environmental Science*. 2021 IOP Publishing, pp. 012076–017082.

Mutlu, H. and Barner, L., 2022. Getting the terms right: Green, sustainable, or circular chemistry? *Macromolecular Chemistry and Physics*, 223(13), pp.1–7.

Narath, S., Koroth, S.K. and Shankar, S.S., 2021. *Cinnamomum tamala* leaf extract stabilized zinc oxide nanoparticles: A promising photocatalyst for methylene blue degradation. *Nanomaterials*, 11(6), pp.1558–1574.

Naseer, M., Aslam, U., Khalid, B. and Chen, B., 2020. Green route to synthesize zinc oxide nanoparticles using leaf extracts of *Cassia fistula* and *Melia azadarach* and their antibacterial potential. *Scientific Reports*, 10(1), pp.9055–9064.

Ng, K.H., Yuan, L.S., Cheng, C.K., Chen, K. and Fang, C., 2019. TiO_2 and ZnO photocatalytic treatment of palm oil mill effluent (POME) and feasibility of renewable energy generation: A short review. *Journal of Cleaner Production*, 233, pp.209–225.

Nguyen, T.T.T., Nguyen, Y.N.N., Tran, X.T., Nguyen, T.T.T. and Tran, T.V., 2023. Green synthesis of CuO, ZnO and CuO/ZnO nanoparticles using *Annona glabra* leaf extract for antioxidant, antibacterial and photocatalytic activities. *Journal of Environmental Chemical Engineering*, 11, pp.111003–111016.

Niño-Martínez, N., Orozco, M.F.S., Martínez-Castañón, G.-.A., Méndez, F.T. and Ruiz, F., 2019. Molecular mechanisms of bacterial resistance to metal and metal oxide nanoparticles. *International Journal of Molecular Sciences*, 20(11), pp.2808–2822.

Nishanthi, R., Malathi, S., Paul, S.J. and Palani, P., 2019. Green synthesis and characterization of bioinspired silver, gold and platinum nanoparticles and evaluation of their synergistic antibacterial activity after combining with different classes of antibiotics. *Materials Science and Engineering C*, 96, pp.693–707.

Nishanthi, R. and Palani, P., 2016. Green synthesis of gold nanoparticles from the rind extract of *Garcinia mangostana* and its synergistic effect with antibiotics against human pathogenic bacteria. *Proceedings of the 16th International Conference on Nanotechnology*. 2016 Sendai, Japan, pp. 431–434.

Nisticò, R., 2023. New advances into nanostructured oxides. *Inorganics*, 11(3), pp.130–134.

Nithya, K., Yuvasree, P., Neelakandeswari, N., Rajasekaran, N., Uthayarani, K., Chitra, M. and Sathiesh Kumar, S., 2014. Preparation and characterization of copper oxide nanoparticles. *International Journal of ChemTech Research*, 6(3), pp.2220–2222.

Nithya, K. and Kalyanasundharam, S., 2019. Effect of chemically synthesis compared to biosynthesized ZnO nanoparticles using aqueous extract of *C. halicacabum* and their antibacterial activity. *OpenNano*, 4, pp.100024.

Obayomi, K.S., Lau, S.Y., Danquah, M.K., Zhang, J., Chiong, T., Takeo, M. and Jeevanandam, J., 2023. Novel concepts for graphene-based nanomaterials synthesis for phenol removal from palm oil mill effluent (POME). *Materials*, 16(12), pp.4379–4395.

Obolskiy, D., Pischel, I., Siriwatanametanon, N. and Heinrich, M., 2009. *Garcinia mangostana* L.: A phytochemical and pharmacological review. *Phytotherapy Research*, 23, pp.1047–1065.

Ogunyemi, S.O., Zhang, M., Abdallah, Y., Ahmed, T., Qiu, W., Arshad Ali, Md., Yan, C., Yang, Y., Chen, J. and Li, B., 2020. The bio-synthesis of three metal oxide nanoparticles (ZnO, MnO_2, and MgO) and their antibacterial activity against the bacterial leaf blight pathogen. *Frontiers in Microbiology*, 11, pp.1–14.

Oh, S.W., Bang, H.J., Bae, Y.C. and Sun, Y., 2007. Effect of calcination temperature on morphology, crystallinity and electrochemical properties of nano-crystalline metal oxides (Co_3O_4, CuO, and NiO) prepared via ultrasonic spray pyrolysis. *Journal of Power Sources*, 173, pp.502–509.

Osaigbovo, A.U., Orhue, E.R. and Popor, U., 2007. Effects of palm oil mill effluent on some soil chemical properties and the growth of maize (*Zea mays* L.). *African Journal of Biotechnology*, 3(1), pp.43–48.

Osman, N.A., Ujang, F.A., Roslan, A.M., Ibrahim, M.F. and Hassan, M.A., 2020. The effect of palm oil mill effluent final discharge on the characteristics of *Pennisetum purpureum*. *Scientific Reports*, 10, pp.6613–6622.

Oudah, M.H., Hasan, M.H. and Abd, A.N., 2020. Synthesis of copper oxide thin films by electrolysis method based on porous silicon for solar cell applications. *IOP Conference Series: Materials Science and Engineering*. 2020 IOP Publishing, pp. 012051–012057.

Panawala, L., 2017, *Difference between Gram positive and Gram negative bacteria* [Online]. Available at: http://pediaa.com/difference-between-gram-positive-and-gram-negative-bacteria/ [Accessed: 6 May 2022].

Parapat, R.Y., Schwarze, M., Ibrahim, A., Tasbihi, M. and Schomäcker, R., 2022. Efficient preparation of nanocatalysts. Case study: Green synthesis of supported Pt nanoparticles by using microemulsions and mangosteen peel extract. *Royal Society of Chemistry Adavnces*, 12(53), pp.34346–34358.

Park, G.C., Seo, T.Y., Park, C.H., Lim, J.H. and Joo, J., 2017. Effects of calcination temperature on morphology, microstructure, and photocatalytic performance of TiO_2 mesocrystals. *Industrial and Engineering Chemistry Research*, 56(29), pp.8235–8240.

Park, J.S., Ahn, E.Y. and Park, Y., 2017. Asymmetric dumbbell-shaped silver nanoparticles and spherical gold nanoparticles green-synthesized by mangosteen (*Garcinia mangostana*) pericarp waste extracts. *International Journal of Nanomedicine*, 12, pp.6895–6908.

Patil, P.B., Bhandari, V.M. and Ranade, V.V, 2021. Improving efficiency for removal of ammoniacal nitrogen from wastewaters using hydrodynamic cavitation. *Ultrasonics - Sonochemistry*, 70, pp.105306–10315.

Patra, J.K. and Baek, K.H., 2014. Green nanobiotechnology: Factors affecting synthesis and characterization techniques. *Journal of Nanomaterials*, 2014, pp.1–12.

Pavia, D.L., Lampman, G.M., Kriz, G.S. and Vyvyan, J.R., 2015. *Introduction to spectrometry* Fifth., Nelson Education, Ltd, Stamford, USA.

Pavithra, M.P., Pushpa, L., Dhruthi, N.S. and Shivaraj, D., 2020. Treatment of landfill leachate by using nano particals of titanium oxide. *International Journal of Future Generation Communication and Networking*, 13(4), pp.2936–2945.

Perera, K.M.K.G., Kuruppu, K.A.S.S., Chamara, A.M.R. and Thiripuranathar, G., 2020. Characterization of spherical Ag nanoparticles synthesized from the agricultural wastes of *Garcinia mangostana* and *Nephelium lappaceum* and their applications as a photo catalyzer and fluorescence quencher. *SN Applied Sciences*, 2(12), pp.1974–1997.

Phang, Y.-K., Aminuzzaman, M., Akhtaruzzaman, Md., Muhammad, G., Ogawa, S., Watanabe, A. and Tey, L.-H., 2021. Green synthesis and characterization of CuO nanoparticles derived from papaya peel extract for the photocatalytic degradation of palm oil mill effluent (POME). *Sustainability*, 13(2), pp.796–810.

Prasanth, R., Dinesh Kumar, S., Jayalakshmi, A., Singaravelu, G., Govindaraju, K. and Ganesh Kumar, V., 2019. Green synthesis of magnesium oxide nanoparticles and their antibacterial activity. *Indian Journal of Geo Marine Sciences*, 48(8), pp.1210–1215.

Puasa, N.A., Hairon, N.H.H., Dzinun, H., Madon, R.H., Ahmad, N.S., Sidik, D.A.B. and Rahman Azmi, A.A.A., 2021. Photocatalytic degradation of palm oil mill secondary effluent in presence of zinc oxide nanoparticles. *Environmental Nanotechnology, Monitoring and Management*, 15, pp.100413–100418.

Pujono, H.R., Kukuh, S., Evizal, R., Afandi and Rahmat, A., 2021. The effect of POME application on production and yield components of oil palm in Lampung, Indonesia. *IOP Conference Series: Earth and Environmental Science*, 648(1), pp.012058–012064.

Putri, R.M., Almunadya, N.S., Amri, A.F., Afnan, N.T., Nurachman, Z., Devianto, H. and Saputera, W.H., 2022. Structural characterization of polycrystalline titania nanoparticles on *C. striata* biosilica for photocatalytic POME degradation. *ACS Omega*, 7(48), pp.44047–44056.

Qamar, H., Rehman, S., Chauhan, D.K., Tiwari, A.K. and Upmanyu, V., 2020. Green synthesis, characterization and antimicrobial activity of copper oxide nanomaterial derived from *Momordica charantia*. *International Journal of Nanomedicine*, 15, pp.2541–2553.

Rajakannu, S., Shankar, S., Perumal. S., Subramanian, S. and Dhakshinamoorthy, G.P., 2015. Biosynthesis of silver nanoparticles using *Garcinia mangostana* fruit extract and their antibacterial, antioxidant activity. *International journal of Current Microbiology and Applied Sciences*, 4(1), pp.944–952.

Rajendran, N.K., George, B.P., Houreld, N.N. and Abrahamse, H., 2021. Synthesis of zinc oxide nanoparticles using *Rubus fairholmianus* root extract and their activity against pathogenic bacteria. *Molecules*, 26(10), pp.3029–3039.

Rajith Kumar, C.R., Betageri, V.S., Nagaraju, G., Pujar, G.H., Onkarappa, H.S. and Latha, M.S., 2020. One-pot green synthesis of ZnO-CuO nanocomposite and their enhanced photocatalytic and antibacterial activity. *Advances in Natural Sciences: Nanoscience and Nanotechnology*, 11(1), pp.015009–015017.

Ramzan, M., Obodo, R.M., Mukhtar, S., Ilyas, S.Z., Aziz, F. and Thovhogi, N., 2021. Green synthesis of copper oxide nanoparticles using *Cedrus deodara* aqueous extract for antibacterial activity. *Materials Today: Proceedings*, 36, pp.576–581.

Ranjith Kumar, R., Hanumantha Rao, P. and Arumugam, M., 2015. Lipid extraction methods from microalgae: A comprehensive review. *Frontiers in Energy Research*, 2(61).

Rao, G.T. and Ravikumar, R.V.S.S.N., 2020. Novel Fe-doped ZnO-CdS nanocomposite with enhanced visible light-driven photocatalytic performance. *Materials Research Innovations*, 25(4), pp.215–220.

Ratnasari, A., Zaidi, N.S., Syafiuddin, A., Boopathy, R., Kueh, A.B.H., Amalia, R. and Prasetyo, D.D., 2021. Prospective biodegradation of organic and nitrogenous pollutants from palm oil mill effluent by acidophilic bacteria and archaea. *Bioresource Technology Reports*, 15, pp.100809–100819.

Ratnawulan, Fauzi, A. and Ae, S.H., 2017. Effect of calcination temperature on phase transformation and crystallite size of copper oxide (CuO) powders. *The 4th International Conference on Research, Implementation, and Education of Mathematics and Science*. 2017 AIP Publishing.

Ruda, D.A., Al-Karam, L.Q. and Ghadhban, E., 2019. The effect of calcination temperature and solvent on the synthesis of CuO nanoparticles and assessment as an anti-leishmania agent. *Technologies and Materials for Renewable Energy, Environment and Sustainability*. 2019 AIP Publishing.

Sabir, S., Arshad, M. and Chaudhari, S.K., 2014. Zinc oxide nanoparticles for revolutionizing agriculture: Synthesis and applications. *The Scientific World Journal*, 2014.

Sajjad, A., Bhatti, S.H., Ali, Z., Jaffari, G.H., Khan, A.N., Rizvi, Z.F. and Zia, M., 2021. Photoinduced fabrication of zinc oxide nanoparticles: Transformation of morphological and biological response on light irradiance. *ACS Omega*, 6(17), pp.11783–11793.

Sakib, A.A.M., Masum, S.Md., Hoinkis, J., Islam, R. and Ashraful Islam Molla, Md., 2019. Synthesis of CuO/ZnO nanocomposites and their application in photodegradation of toxic textile dye. *Journal of Composites Science*, 3(3), pp.91–103.

Salayová, A., Bedlovičová, Z., Daneu, N., Baláž, M., Bujňáková, Z.L., Balážová, Ľ. and Tkáčiková Ľ., 2021. Green synthesis of silver nanoparticles with antibacterial activity using various medicinal plant extracts: Morphology and antibacterial efficacy. *Nanomaterials*, 11(4), pp.1005–1024.

Sana, S.S., Kumbhakar, D.V., Pasha, A., Pawar, S.C., Grace, A.N., Singh, R.P., Nguyen, V.-H., Le, Q.V. and Peng, W., 2020. *Crotalaria verrucosa* leaf extract mediated synthesis of zinc oxide nanoparticles: Assessment of antimicrobial and anticancer activity. *Molecules*, 25(21), pp.4896–4916.

Saputera, W.H., Amri, A.F., Mukti, R.R., Suendo, V., Devianto, H. and Sasongko, D., 2021. Photocatalytic degradation of palm oil mill effluent (POME) waste using $BiVO_4$ based catalysts. *Molecules*, 26(20), pp.6225–6239.

Saputera, W.H., Amri, A.F., Daiyan, R. and Sasongko, D., 2021. Photocatalytic technology for palm oil mill effluent (POME) wastewater treatment: Current progress and future perspective. *Materials*, 14(11), pp.2846–2880.

Saravanan, S. and Sivasankar, T., 2016. Effect of ultrasound power and calcination temperature on the sonochemical synthesis of copper oxide nanoparticles for textile dyes treatment. *Environmental Progress & Sustainable Energy*, 35(3), pp.669–679.

Selvanathan, V., Aminuzzaman, M., Tan, L.X., Win, Y.F., Cheah, E.S.G., Heng, M.H., Tey, L.-H., Arullappan, S., Algethami, N., Alharthi, S.S., Sultana, S., Shahiduzzaman, Md., Abdullah, H. and Akhtaruzzaman, Md., 2022. Synthesis, characterization, and preliminary *in vitro* antibacterial evaluation of ZnO nanoparticles derived from soursop (*Annona muricata* L.) leaf extract as a green reducing agent. *Journal of Materials Research and Technology*, 20, pp.2931–2941.

Selvanathan, V., Aminuzzaman, M., Tey, L.-H., Razali, S.A., Althubeiti, K., Alkhammash, H.I., Guha, S.K., Ogawa, S., Watanabe, A., Shahiduzzaman, Md. and Akhtaruzzaman, Md., 2021. *Muntingia calabura* leaves mediated green synthesis of CuO nanorods: Exploiting phytochemicals for unique morphology. *Materials*, 14(21), pp.6379–6390.

Sen, S.K., Jha, S. and Mandal, P., 2016. Evaluation of phytotoxicity of mung bean genotypes against salinity stress. *International Journal of Scientific and Research Publications*, 6(12), pp.1–6.

Senthilkumar, N., Nandhakumar, E., Priya, P., Soni, D., Vimalan, M. Vetha Potheher, I., 2017a. Synthesis, anti-bacterial, anti-arthritic, anti-oxidant and *in-vitro* cytotoxicity activities of ZnO nanoparticles using leaf extract of *Tectona grandis*(L.). *New Journal of Chemistry*, 41(18), pp.1–12.

Senthilkumar, N., Nandhakumar, E., Priya, P., Soni, D., Vimalan, M. Vetha Potheher, I., 2017b. Synthesis of ZnO nanoparticles using leaf extract of *Tectona grandis* (L.) and their anti-bacterial, anti-arthritic, anti-oxidant and *in vitro* cytotoxicity activities. *New Journal of Chemistry*, 41(18), pp.10347–10356.

Sepahvand, M., Buazar, F. and Sayahi, M.H., 2020. Novel marine-based gold nanocatalyst in solvent-free synthesis of polyhydroquinoline derivatives: Green and sustainable protocol. *Applied Organometallic Chemistry*, 34(12), pp.1–11.

Septiningrum, F., Yuwono, A.H., Maulana, F.A., Nurhidayah, E., Dhaneswara, D., Sofyan, N., Hermansyah, H. and Purwanto, W.W., 2024. Mangosteen pericarp extract mediated synthesis of Ag/TiO_2 nanocomposite and its application on organic pollutant degradation by adsorption-photocatalytic activity. *Current Research in Green and Sustainable Chemistry*, 8, pp.100394–100404.

Shaba, E.Y., Jacob, J.O., Tijani, J.O. and Suleiman, M.A.T., 2021. A critical review of synthesis parameters affecting the properties of zinc oxide nanoparticle and its application in wastewater treatment. *Applied Water Science*, 11(2), pp.48–88.

Shabatina, T., Vernaya, O., Shumilkin, A., Semenov, A. and Melnikov, M., 2022. Nanoparticles of bioactive metals/metal oxides and their nanocomposites with antibacterial drugs for biomedical applications. *Materials*, 15(10), pp.3602–3621.

Shadi, A.M.H., Kamaruddin, M.A., Niza, N.M., Emmanuel, M.I., Sohrab Hossain, Md. and Ismail, N., 2020. Efficient treatment of raw leachate using magnetic ore iron oxide nanoparticles Fe_2O_3 as nanoadsorbents. *Journal of Water Process Engineering*, 38, pp.101637–101645.

Shah, M., Fawcett, D., Sharma, S., Tripathy, S.K. and Poinern, G.E.J., 2015. Green synthesis of metallic nanoparticles *via* biological entities. *Materials,* 8(11), pp.7278–7308.

Shahmoradi, B., Yavari, S., Zandsalim, Y., Shivaraju, H.P., Negahdari, M., Maleki, A., Gordon Mckay, Pawar, R.R. and Lee, S.-M., 2018. Optimization of solar degradation efficiency of bio-composting leachate using Nd: ZnO nanoparticles. *Journal of Photochemistry and Photobiology A: Chemistry*, 356, pp.201–211.

Shammout, M.W. and Awwad, A.M., 2021. A novel route for the synthesis of copper oxide nanoparticles using *Bougainvillea* plant flowers extract and antifungal activity evaluation. *International Scientific Organization,* 7(1), pp.71–78.

Sharma, D., Kanchi, S. and Bisetty, K., 2019. Biogenic synthesis of nanoparticles: A review. *Arabian Journal of Chemistry*, 12(8), pp.3576–3600.

Sharma, S., Yadav, D.K., Chawla, K., Lai, N. and Lai, C., 2021. Synthesis and characterization of CuO nanoparticles by *Aloe barbadensis* leaves. *Quantum Journal of Engineering, Science and Technology*, 2(5), pp.1–9.

Siddiqi, K.S. and Husen, A., 2020. Current status of plant metabolite-based fabrication of copper/copper oxide nanoparticles and their applications: A review. *Biomaterials Research,* 24(1), pp.1–15.

Siddiqi, K.S., ur Rahman, A., Tajuddin and Husen, A., 2018. Properties of zinc oxide nanoparticles and their activity against microbes. *Nanoscale Research Letters*, 13(1).

Siddiqui, V.U., Ansari, A., Taazeem Ansari, M., Khursheed Akram, Md., Siddiqi, W.A., Alosaimi, A.M., Hussein, M.A. and Rafatullah, M., 2021. Optimization of facile synthesized ZnO/CuO nanophotocatalyst for organic dye degradation by visible light irradiation using response surface methodology. *Catalysts*, 11(12), pp.1509–1533.

Siddiqui, V.U., Ansari, A., Chauhan, R. and Siddiqi, W.A., 2021. Green synthesis of copper oxide (CuO) nanoparticles by *Punica granatum* peel extract. *Materials Today: Proceedings*, 36, pp.751–755.

Sidik, D.A.B., Hairom, N.H.H., Rozman, A.I., Johari, M.J.S. and Muhammad, A., 2023. The photocatalytic activity of green zinc oxide nanoparticles in the treatment of aerobically palm oil mill effluent. *Journal of Science and Technology*, 15(1), pp.7–15.

Silhavy, T.J., Kahne, D. and Walker, S., 2010. The bacterial cell envelope. *Cold Spring Harb Perspect Biol*, 2, pp.a000414–a000429.

Sin, J.-C., Chin, Y.-H. and Lam, S.-M., 2019. WO_3/Nb_2O_5 nanoparticles-decorated hierarchical porous ZnO microspheres for enhanced photocatalytic degradation of palm oil mill effluent and simultaneous production of biogas. *Key Engineering Materials*, 821, pp.379–385.

Singh, A., Gautam, P.K., Verma, A., Singh, V., Shivapriya, P.M., Shivalkar, S., Sahoo, A.K. and Samanta, S.K., 2020. Green synthesis of metallic nanoparticles as effective alternatives to treat antibiotics resistant bacterial infections: A review. *Biotechnology Reports*, 25, pp.e00427–e00437.

Singh, J., Dutta, T., Kim, K.-H., Rawat, M., Samddar, P. and Kumar, P., 2018. "Green" synthesis of metals and their oxide nanoparticles: Applications for environmental remediation. *Journal of Nanobiotechnology*, 16, pp.84–107.

Singh, K., Lohchab, R.K., Kumari, M. and Beniwal, V., 2021. Potential of TiO_2 loaded almond shell derived activated carbon for leachate treatment: Isotherms, kinetics, and Response Surface Methodology. *International Journal of Environmental Analytical Chemistry*, pp.1–22.

Sivakavinesan, M., Vanaja, M. and Annadurai, G., 2021. Dyeing of cotton fabric materials with biogenic gold nanoparticles. *Scientific Reports*, 11(1), pp.13249–13259.

Sivakumar, P., Lee, M., Kim, Y.S. and Shim, M.S., 2018. Photo-triggered antibacterial and anticancer activities of zinc oxide nanoparticles. *Journal of Materials Chemistry B*, 6(30), pp.4852–4871.

Slavin, Y.N., Asnis, J., Häfeli, U.O. and Bach, H., 2017. Metal nanoparticles: Understanding the mechanisms behind antibacterial activity. *Journal of Nanobiotechnology*, 15(1).

Slobodchikov, A.A., Nekrasov, I.A., Begunovich, L.V., Makarov, I.A., Korshunov, M.M. and Ovchinnikov, S.G., 2023. Electronic structure and minimal models for flat and corrugated CuO monolayers: An ab initio study. *Materials*, 16(2), pp.658–667.

Sobańska, Z., Roszak, J., Kowalczyk, K. and Stępnik, M., 2021. Applications and biological activity of nanoparticles of manganese and manganese oxides in *in vitro* and in vivo models. *Nanomaterials*, 11, pp.1084–1099.

Soto-Robles, C.A., Luque, P.A., Gómez-Gutiérrez, C.M., Nava, O., Vilchis-Nestor, A.R., Lugo-Medina, E., Ranjithkumar, R. and Castro-Beltrán, A., 2019. Study on the effect of the concentration of *Hibiscus sabdariffa* extract on the green synthesis of ZnO nanoparticles. *Results in Physics*, 15, p.102807.

Souri, M., Hoseinpour, V., Ghaemi, N. and Shakeri, A., 2019. Procedure optimization for green synthesis of manganese dioxide nanoparticles by *Yucca gloriosa* leaf extract. *International Nano Letters*, 9(1), pp.73–81.

Steward, K., 2019, *Gram positive vs Gram negative* [Online]. Available at: https://www.technologynetworks.com/immunology/articles/gram-positive-vs-gram-negative-323007 [Accessed: 6 May 2022].

Suresh, S., Gunasekaran, S. and Srinivasan, S., 2015. Vibrational spectra (FT-IR, FT-Raman), frontier molecular orbital, first hyperpolarizability, NBO analysis and thermodynamics properties of Piroxicam by HF and DFT methods. *Spectrochimica Acta - Part A: Molecular and Biomolecular Spectroscopy*, 138, pp.447–459.

Swarnakar, A., 2020. Phytotoxicity of arsenite on early seedling growth of mung bean: A Threat to potential pulse cultivation. *Advances in Zoology and Botany*, 8(2), pp.69–73.

Syahputra, M.R., Setiado, H., Siregar, L.A.M. and Damanik, R.I., 2021. Morphological characteristics of mangosteen plants (*Garcinia mangostana* L.) in Langkat District, North Sumatera, Indonesia. *IOP Conference Series: Earth and Environmental Science*. 2021 IOP Publishing, pp. 042056–042062.

Takele, E., Bogale, R.F., Shumi, G. and Kenasa, G., 2023. Green synthesis, characterization, and antibacterial activity of CuO/ZnO nanocomposite using *Zingiber officinale* rhizome extract. *Journal of Chemistry*, 2023, pp.1–15.

Tan, Y.H., Goh, P.S., Lai, G.S., Lau, W.J. and Ismail, A.F., 2014. Treatment of aerobic treated palm oil mill effluent (AT-POME) by using TiO_2 photocatalytic process. *Jurnal Teknologi*, 70(2), pp.61–63.

Tran, V.A., Thi Vo, T.-T., Thi Nguyen, M.-N., Dat, N.D., Doan, V.-D., Nguyen, T.-Q., Vu, Q.H., Le, V.T. and Tong, T.D., 2021. Novel α-mangostin derivatives from mangosteen (*Garcinia mangostana* L.) peel extract with antioxidant and anticancer potential. *Journal of Chemistry*, 2021, pp.1–12.

Trang, N.L.N., Hoang, V.-T., Dinh, N.X., Tam, L.T., Le, V.P., Linh, D.T., Cuong, D.M., Khi, N.T., Anh, N.H., Nhung, P.T. and Le, A.-T., 2021. Novel eco-friendly synthesis of biosilver nanoparticles as a colorimetric probe for highly selective detection of Fe (III) ions in aqueous solution. *Journal of Nanomaterials*, 2021, pp.1–17.

Utomo, W.P., Wu, H. and Ng, Y.H., 2023. Quantification methodology of ammonia produced from electrocatalytic and photocatalytic nitrogen/nitrate reduction. *Energies*, 16(1), pp.27–48.

Vaidh, S., Parekh, D., Patel, D. and Vishwakarma, G.S., 2022. Leachate treatment potential of nanomaterial based assemblies: A systematic review on recent development. *Water Science and Technology*, 85(11), pp.3285–3300.

Varghese, A.P., Neppolian, B. and Lakhera, S.K., 2023. Pitfalls of using Nessler's reagent for ammonia detection in photocatalytic nitrogen fixation studies: Leveraging 1H NMR for enhanced accuracy and precision. *Industrial and Engineering Chemistry Research*, 62(32), pp.12530–12537.

Variyani, I.V., Ardi, A., Syahrin, A.A., Samudra, T.T. and Suyono, E.A., 2020. The usage of palm oil mill effluent as a cultivation medium of *Arthrospira maxima* Setchell *et* Gardner. *AIP Conference Proceedings*, 2260, pp.030014–030022.

Vaseem, M., Umar, A. and Hahn, Y.B., 2010. ZnO nanoparticles: Growth, properties, and applications. In: Umar, A. and Hahn, Y.B., (eds.) *Metal oxide nanostructures and their applications*. American Scientific Publishers, pp. 1–36.

Veerasamy, R., Xin, T.Z., Gunasagaran, S., Xiang, T.F.W., Yang, E.F.C., Jeyakumar, N. and Dhanaraj, S.A., 2011. Biosynthesis of silver nanoparticles using mangosteen leaf extract and evaluation of their antimicrobial activities. *Journal of Saudi Chemical Society*, 15(2), pp.113–120.

Veisi, H., Karmakar, B., Tamoradi, T., Hemmati, S., Hekmati, M. and Hamelian, M., 2021. Biosynthesis of CuO nanoparticles using aqueous extract of herbal tea (*Stachys lavandulifolia*) flowers and evaluation of its catalytic activity. *Scientific Reports*, 11(1), pp.1983–1995.

Velsankar, K., Sudhahar, S., Parvathy, G. and Kaliammal, R., 2020. Effect of cytotoxicity and antibacterial activity of biosynthesized of ZnO hexagonal shaped nanoparticles by *Echinochloa frumentacea* grains extract as a reducing agent. *Materials Chemistry and Physics*, 239, pp.121976–121988.

Verma, R.P. and Khan, F., 2019. Green approach for biofabrication of CuO nanoparticles from *Prunus amygdalus* pericarp extract and characterization. *Inorganic and Nano-Metal Chemistry*, 49(3), pp.69–74.

Vibitha, B.V., Anitha, B. and Tharayil, N.J., 2020. Green synthesis of ZnO: CuO nanocomposites by *Aloe barbadansis* leaf extract: Structure and photo catalytic properties. *International Conference on Energy and Environment 2019*. 2020 AIP Conference Proceedings, pp. 020031–1–020031–5.

Vijayaraghavan, K. and Ashokkumar, T., 2017. Plant-mediated biosynthesis of metallic nanoparticles: A review of literature, factors affecting synthesis, characterization techniques and applications. *Journal of Environmental Chemical Engineering*, 5(5), pp.4866–4883.

Vindhya, P.S. and Kavitha, V.T., 2023. Effect of cobalt doping on antimicrobial, antioxidant and photocatalytic activities of CuO nanoparticles. *Materials Science and Engineering B*, 289, pp.116258–116270.

Vladimirovna Zaitseva, N. and Alexandrovna Zemlyanova, M., 2020. Toxicologic characteristics of nanodisperse manganese oxide: Physical-chemical properties, biological accumulation, and morphological-functional properties at various exposure types. In: Nduka, J.K. and Rashed, M.N., (eds.) *Heavy metal toxicity in public health*. InTechOpen.

Wang, H., Zhou, Y., Sun, Q., Zhou, C., Hu, S., Lenahan, C., Xu, W., Deng, Y., Li, G. and Tao, S., 2021. Update on nanoparticle-based drug delivery system for anti-inflammatory treatment. *Frontiers in Bioengineering and Biotechnology*, 9, pp.1–9.

Wang, L., Hu, C. and Shao, L., 2017. The antimicrobial activity of nanoparticles: Present situation and prospects for the future. *International Journal of Nanomedicine*, 12, pp.1227–1249.

Wang, Y., Hu, K., Yang, Z., Ye, C., Li, X. and Yan, K., 2021. Facile synthesis of porous ZnO nanoparticles efficient for photocatalytic degradation of biomass-derived bisphenol a under simulated sunlight irradiation. *Frontiers in Bioengineering and Biotechnology*, 8, pp.1–11.

Waris, A., Din, M., Ali, A., Ali, M., Afridi, S., Baset, A. and Khan, A.U., 2020. A comprehensive review of green synthesis of copper oxide nanoparticles and their diverse biomedical applications. *Inorganic Chemistry Communications*, 123.

Wiyantoko, B., Rahmadani, N., Kurniawati, P. and Purbaningtias, T.E., 2020. Method verification of chemical oxygen demand (COD) and total suspended solid (TSS) analysis from Mentaya River. *Proceedings of the 3rd International Seminar on Metallurgy and Materials (ISMM2019): Exploring New Innovation in Mettallurgy and Materials*. 2020

Xu, J., Huang, Y., Zhu, S., Abbes, N., Jing, X. and Zhang, L., 2021. A review of the green synthesis of ZnO nanoparticles using plant extracts and their prospects for application in antibacterial textiles. *Journal of Engineered Fibers and Fabrics*, 16, pp.1–14.

You, W., Ahn, J.C., Boopathi, V., Arunkumar, L., Rupa, E.J., Akter, R., Kong, B.M., Lee, G.S., Yang, D.C., Kang, S.C. and Liu, J., 2021. Enhanced antiobesity efficacy of tryptophan using the nanoformulation of *Dendropanax morbifera* extract mediated with ZnO nanoparticle. *Materials*, 14(4), pp.824–838.

Yulizar, Y., Bakri, R., Apriandanu, D.O.B. and Hidayat, T., 2018. ZnO/CuO nanocomposite prepared in one-pot green synthesis using seed bark extract of *Theobroma cacao*. *Nano-Structures and Nano-Objects*, 16, pp.300–305.

Yusefi, M., Shameli, K., Yee, O.S., Teow, S.-Y., Hedayatnasab, Z., Jahangirian, H., Webster, T.J. and Kuča, K., 2021. Green synthesis of Fe_3O_4 nanoparticles stabilized by a *Garcinia mangostana* fruit peel extract for hyperthermia and anticancer activities. *International Journal of Nanomedicine*, 16, pp.2515–2532.

Yusoff, H.M., Idris, N.H., Hipul, N.F., Yusoff, N.F.M., Izham, N.Z.M. and Ui Haq Bhat, I., 2020. Green synthesis of zinc oxide nanoparticles using black tea extract and its potential as anode material in sodium-ion batteries. *Malaysian Journal of Chemistry*, 22(2), pp.43–51.

Zainal, N.H., Jalani, N.F., Mamat, R. and Astimar, A.A., 2017. A review on the development of palm oil mill effluent (POME) final discharge polishing treatments. *Journal of Oil Palm Research*, 29(4), pp.528–540.

Zandsalimi, Y., Rezaee, R., Ghahramani, E. and Moradi, M., 2019. Photocatalytic efficiency of molybdenum-doped zinc oxide nanoparticles in treating landfill leachate. *Journal of Advances in Environmental Health Research*, 7(1), pp.25–31.

Zelekew, O.A., Haitosa, H.H., Chen, X. and Wu, Y.-N., 2023. Recent progress on plant extract-mediated biosynthesis of ZnO-based nanocatalysts for environmental remediation: Challenges and future outlooks. *Advances in Colloid and Interface Science*, 317, pp.102931–102951.

Zhang, H., Cao, Y., Wang, S., Tang, Y., Tian, L., Cai, W., Wei, Z., Wu, Z., Zhu, Y. and Guo, Q., 2024. Photocatalytic removal of ammonia nitrogen from water: investigations and challenges for enhanced activity. *Environmental Science and Pollution Research*, 31(29), pp.41824–41843.

Zhang, X. and Xiao, C., 2018. Biofabrication of silver nanoparticles and their combined effect with low intensity ultrasound for treatment of lung cancer. *Journal of Photochemistry and Photobiology B: Biology*, 181, pp.122–126.

Appendix A

UV-Vis spectra and energy bandgap (Tauc's plot approach) of (a) ZnO NPs by using 2.8 g of $Zn(NO_3)_2 \cdot 6H_2O$ and (b) CuO NPs by using 1.2 g of $Cu(NO_3)_2 \cdot 3H_2O$, respectively, by utilizing 0.05 g/mL of MLE calcinated at 500°C.

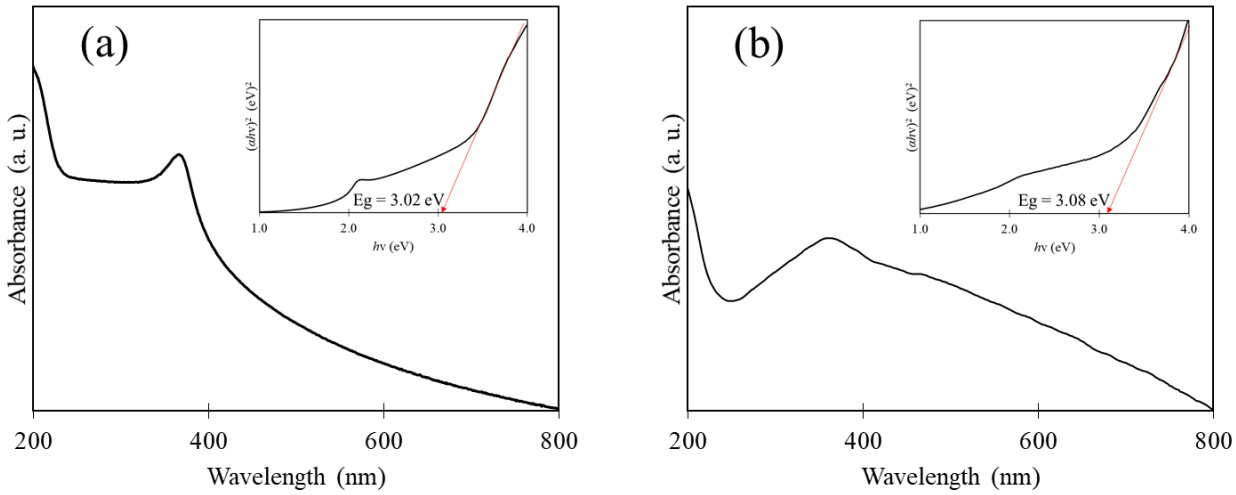

The determined energy bandgap were used in predict the band alignments of 70ZnO-30CuO NCs by using 0.05 g/mL MLE calcinated at 500°C.

Appendix B

List of Publication

(a) **Chan, Y. B.**, Aminuzzaman, M., Win, Y. F., Djearamane, S., Wong, L. S., Guha, S. K., Almohammadi, H., Akhtaruzzaman, Md. and Tey, L.-H., 2024. *Garcinia mangostana* L. leaf-extract-assisted green synthesis of CuO, ZnO and CuO-ZnO nanomaterials for the photocatalytic degradation of palm oil mill effluent (POME). Catalysts, 14(8), pp.486–503.

(b) **Chan, Y.B.**, Aminuzzaman, M., Khalilur Rahman, Md., Win, Y.W., Sultana, S., Cheah, S.-Y., Watanabe, A., Wong, L.S., Guha, S.K., Djearamane, S., Rajendran, V., Akhtaruzzaman, Md. and Tey, L.-H., 2024. Green synthesis of ZnO nanoparticles using the mangosteen (*Garcinia mangostana* L.) leaf extract: Comparative preliminary *in vitro* antibacterial study. *Green Processing and Synthesis*, 13(1), pp.20230251–20230270.

(c) Cheah, S.-Y., Tey, L.-H., Aminuzzaman, M., Phang, Y.-K., **Chan, Y.B.**, Djearamane, S., Wong, L.-S. and Watanabe, A., 2023. Green synthesis and characterizations of chromium oxide nanoparticles (Cr_2O_3 NPs) derived from pomegranate husk and its α-amylase inhibitory and antioxidant properties. *Nano Hybrids and Composites*, 39, pp.51–55.

(d) **Chan, Y.B.**, Aminuzzaman, M., Tey, L.-H., Win, Y.F., Watanabe, A., Djearamane, S. and Akhtaruzzaman, Md., 2023. Impact of diverse parameters on the physicochemical characteristics of green-synthesized zinc oxide–copper oxide nanocomposites derived from

an aqueous extract of *Garcinia mangostana* L. leaf. *Materials*, 16(15), pp.5421–5439.

(e) **Chan, Y.B.**, Selvanathan, V., Tey, L.-H., Akhtaruzzaman, Md., Anur, F.H., Djearamane, S., Watanabe, A. and Aminuzzaman, M., 2022. Effect of calcination temperature on structural, morphological and optical properties of copper oxide nanostructures derived from *Garcinia mangostana* L. leaf extract. *Nanometerials*, 12(20), pp.3589–3607.